Top quark interactions in the Standard Model Effective Field Theory

Hesham El Faham
September 2022

Jury Members	
Prof. Jorgen D'HONDT (VUB)	Promotor
Dr. Andrea Giammanco (UCLouvain)	Promotor
Prof. Fabio Maltoni (UCLouvain)	President
Prof. Alberto Mariotti (VUB)	Secretary
Prof. Céline Degrande (UCLouvain)	
Prof. Christoph Englert (University of Glasgow)	
Dr. Denise Müller (VUB)	
Dr. Eleni Vryonidou (University of Manchester)	

A dissertation submitted to the Catholic University of Louvain and Vrije Universiteit Brussel in fulfilment of the requirements for the degree of Doctor of Sciences

Acknowledgements

Firstly, I would like to express my sincere gratitude to my supervisors, Jorgen D'Hondt and Andrea Giammanco, for their continuous support throughout my PhD. Thank you to Andrea for his great help while I worked on the experiment and for his encouragement and backing over the last four years that made it all possible. I use this acknowledgement to express appreciation for my supervisors' benevolence in accommodating my aspiration to change my research line from experiment to theory. Of course, such a change could have never been successful without the support of Fabio Maltoni. Words can not express my gratitude to Fabio for involving me in his team. His guidance has supported me in all my research, and his discernment made completing my thesis possible. I could not have envisioned having a better advisor and mentor for my PhD study.

Besides my advisors, I would like to thank the rest of my thesis committee: Alberto Mariotti, Céline Degrande, Christoph Englert, Denise Müller, and Eleni Vryonidou, for their insightful comments, which have not only improved this thesis but have also widened my viewpoint to my research.

My sincere thanks also go to the CMS team at CP3, particularly Pietro Vischia, whose hands-on guidance has assisted me throughout my time working within CMS. Without such support, conducting this research would not have been possible.

I am lucky to have worked with Rafael Aoude, Ken Mimasu, Eleni Vryonidou, and Marco Zaro. Their knowledge, patience, and invaluable assistance were essential in completing Refs. [1] and [2]. Working with such incredible people has undoubtedly shaped my experience as a PhD student and prepared me for post-PhD life.

I thank Marco Drewes and Jan Hajer for involving me in their research. In particular, I am grateful for Jan's patience and support during our discussions, from which I learned a great deal of C++.

I thank the IT team at CP3 for their continuous support during my studies. A similar thanks to Olivier Mattelaer for his support along the way with MadGraph-related issues. I appreciate the time Pietro Vischia and Rafael Aoude put into proofreading parts of this thesis in its early stages.

I thank my good old friends for their spiritual support. And my new friends, for all the joyful time we have spent together that motivated me to keep going and for creating all those memories that will last forever.

Lastly, my family deserves endless gratitude: I thank my parents, sister and brother for their support throughout the journey. To my family, I give everything, including this.

Abstract

The enormous amount of data gathered by the LHC has put the SM under severe tests, proving it the most successful theory in particle physics. Despite such success, the SM is an inherently incomplete theory. The current challenges facing the SM have led to the proposals that new physics must exist. This new physics beyond the SM may not be necessarily evident in the resonant production of new particles at the LHC. An effective field theory approach (EFT) can be used as a framework to parameterise possible deviations from the SM due to the presence of such new states that can not be probed directly with the current reach of our colliders. One possible EFT approach is the Standard Model EFT (SMEFT), which we adopt throughout this thesis. One of many possible probes of new physics is the top quark. The motivation behind the vigorous effort put into probing top quark processes is its high mass and strong coupling to the Higgs boson. This original work in this thesis explores the use of SMEFT in the search for new physics beyond the SM, focusing on top quark interactions in three different processes.

Firstly, the thesis presents the CMS measurement of the rate of the Higgs boson production in association with two top quarks in multilepton final states at the LHC. In the attempts to measure the $t\bar{t}H$ cross-section through the reconstruction of relevant differential observables, the quality of such reconstruction was computed in response matrices, allowing the quantification of the inefficiencies originating from imperfect lepton and jet assignments and missing energies in the final state. The EFT effects from the relevant operators modifying the interaction vertices in the $t\bar{t}H$ process were studied and parametrised. This differential study provided constraints on the coefficients of the relevant operators to the $t\bar{t}H$ production process.

Secondly, the thesis presents the single top quark production associated with a WZ pair at the LHC in the context of the SM and the SMEFT. The uniqueness of the tWZ processes is manifested in its sensitivity to unitarity-violating behaviour induced in its sub-amplitudes through modified electroweak interactions. At NLO in QCD, tWZ interferes with $t\bar{t}Z$ and $t\bar{t}$, necessitating the employment of a method to separate it from these overlapping processes meaningfully. We used diagram-removal procedures to define the tWZ production at NLO accuracy in a suitably defined phase-space region, obtaining reliable total rates and differential results in the SM and the SMEFT. Our analysis also included matching NLO predictions to parton showers.

The final presentation is that of the four top quark production at the LHC in the context of the SMEFT. We analysed all possible QCD- and EW-couplings orders and relevant dimension-six operators. We found several cases where formally subleading terms in the cross-section expansion provided significant contributions, enhancing the sensitivity to a broad class of operators. Inclusive and differential predictions are presented for the LHC and the future proton-proton circular collider, FCC-hh. We carried out a projection study through which we assessed the EFT sensitivity at different collider energies for all the relevant operators. Moreover, we performed a simplified chi-square fit to set limits on SMEFT Wilson coefficients. In so doing, we assessed the importance of including subleading terms and differential information in constraining new physics contributions. Finally, we computed the SMEFT predictions for the double insertion of dimension-six operators and scrutinised the possible enhancements to the sensitivity induced by a specific class of higher order terms in the EFT series.

Declaration

This dissertation is the result of the author's work, except where explicit reference is made to the work of others. The dissertation has not been submitted for another qualification to this or any other university.

The material presented in Chap. 4 is based on work done in collaboration with the CMS experiment.

The material in Chap. 5 is based on work done in collaboration with Fabio Maltoni, Ken Mimasu, and Marco Zaro. This work is published in Ref. [1].

The material in Chap. 6 is based on work done in collaboration with Rafael Aoude, Fabio Maltoni, and Eleni Vryonidou. This work is published in Ref. [2].

The author's contribution to the material presented in Chap. 4- 6 is specified in a dedicated declaration at the beginning of each chapter.

The material in Chap. 3 is written by the author based on articles cited in the text, and does not contain any contributions from the author himself. Chapters 1, 2 are introductory chapters written by the author based on articles cited in the text.

Contents

Chapter 1.

The Standard Model of Particle Physics

The theoretical formulation of the Standard Model of particle physics (SM) over the last century has revolutionised our understanding of nature's fundamental building blocks and provided an accurate description of the interactions among them. Those fundamental interactions described by the SM constitute three out of nature's four known fundamental interactions, namely, electromagnetic, weak and strong force. Despite the astounding precision by which the SM has been verified against a wide range of experimental measurements, many questions and challenges remain open. These challenges drive our perception of the SM as an effective field theory (EFT) and that perhaps a more general theory can answer our most fundamental questions. To set the stage for discussing EFTs in the next chapter, here I first present the SM and the motivations behind pursuing physics beyond the SM (BSM) in the first place. In the following, it is assumed that the reader has had a first graduate-level course in quantum field theory (QFT) or particle physics. Throughout the thesis, and unless otherwise specified, the use of natural units, i.e. $\hbar = c = 1$, is assumed. I relied mainly on Ref. [3] in writing Sec. 1.2 and on Ref. [4] in writing Sec. 1.3.

1.1. The fundamental blocks of nature

The SM is a QFT classifying all the known elementary particles and describing their fundamental interactions. The elementary particles in the SM fall under two main classes, fermions and bosons. Fermions, and their corresponding antiparticles, are half-integer spin particles obeying Fermi-Dirac statistics, while bosons are integer spin particles obeying the Bose-Einstein statistics. Fermions are further classified into quarks and leptons. Bosons in the SM are classified into spin-1 gauge bosons, the so-called force carriers, and spin-0 scalar bosons. The SM has one scalar boson, the Higgs boson, H.

Fermions The SM fermions are classified into six quarks (up, down, charm, strange, top, bottom) and six leptons (electron, electron neutrino, muon, muon neutrino, tau, tau neutrino). Quarks are distinguished through their colour charge, allowing them to participate in strong interactions, while leptons have no colour charge and therefore do not undergo strong interactions. At low energies, quarks exhibit the phenomenon of colour confinement which renders them strongly bonded to one another, forming composite colour-neutral particles called hadrons. These composite states can either be made of a quark and an antiquark (mesons) or three (anti)quarks, the so-called (anti)baryons. Protons and neutrons are the lightest baryons in the SM. All quarks, as well as the electron (e), muon (μ), and tau (τ), carry an electric charge and weak isospin, which allow them to interact with the other fermions via electromagnetism and the weak interactions. On the other hand, the three neutrinos do not carry an electric charge, so their motion is only influenced by the weak force in the SM[1]. Fermions are classified into three generations; each generation member has greater mass than the corresponding particle of any generation before it. The first-generation particles are the building blocks of ordinary matter. Second- and third-generation particles, on the other hand, decay with very short half-lives and are observed only in very high-energy environments. Neutrinos in all three generations do not decay; they "oscillate". Neutrino oscillation is a phenomenon in which a neutrino of a specific lepton flavour, i.e. electron, muon, or tau, can later be measured to have a different flavour, hence the term "oscillation".

Gauge vector bosons Gauge vector bosons are spin-1 particles and are the force carriers mediating the electromagnetic, weak and strong interactions. A photon, γ, is a massless gauge vector boson and is the mediator of the electromagnetic force between electrically charged particles. The theory of quantum electrodynamics (QED) describes photons. The $W^{\pm}$ and Z massive vector gauge bosons mediate the weak interactions between fermions. The W bosons carry an electric charge of +1 or -1. The Z boson is electrically neutral. These three gauge bosons and the photon grouped collectively mediate the electroweak (EW) interactions described by the EW theory. The gluons, g, are massless vector gauge bosons that mediate the strong interactions between colour-charged particles, i.e. quarks and gluons. The theory of quantum chromodynamics (QCD) describes gluons and their interactions.

[1] Neutrinos are massless in the SM. However, from neutrino oscillation experiments, we know they have masses, albeit very light, so their motion must be influenced by gravity too. This is one of the SM's shortcomings.

The Higgs boson Finally, the Higgs particle (usually referred to as the "Higgs") is a massive scalar elementary particle and is considered the vital building block of the SM. The Higgs particle is a spin-0 particle, hence is classified as a scalar boson. The Higgs boson plays a unique role in the SM by explaining mass generation for all the massive elementary particles. The Higgs boson was discovered at the Large Hadron Collider (LHC) experiment at CERN in 2012 [5,6].

Gauge symmetries of the SM The SM is an $\mathrm{SU}(3)_\mathrm{c} \times \mathrm{SU}(2)_\mathrm{L} \times \mathrm{U}(1)_\mathrm{Y}$ non-abelian gauge theory. Moreover, the SM is chiral, meaning left- and right-handed fermions are in different representation of the gauge group. The weak interactions arise from the $\mathrm{SU}(2)_\mathrm{L}$ transformations, with three weak gauge bosons corresponding to the three generators of the symmetry. Weak interactions only couple to left-handed particles (hence the subscript L for left-handed). Therefore, the left-handed quarks and the left-handed leptons form *doublets* of the so-called weak isospin, i.e. they form a **2** representation of $\mathrm{SU}(2)_\mathrm{L}$. Two particles forming an $\mathrm{SU}(2)$ doublet means they transform to each other under an $\mathrm{SU}(2)$ transformation. The Higgs field is also in a doublet representation of $\mathrm{SU}(2)_\mathrm{L}$. On the other hand, right-handed quarks and right-handed leptons do not transform under $\mathrm{SU}(2)_\mathrm{L}$, or in other words, are weak isospin *singlets*. The charge[2] of the $\mathrm{U}(1)_\mathrm{Y}$ symmetry is the so-called weak hypercharge, Y_W, a quantum number relating the electric charge and (the third component of) the weak isospin. Quarks carry a colour charge and therefore transform as a *triplet* of $\mathrm{SU}(3)_\mathrm{c}$, i.e. in the **3** representation of $\mathrm{SU}(3)_\mathrm{c}$ (where the subscript c denotes "colour"), while leptons are singlets under $\mathrm{SU}(3)_\mathrm{c}$. The physical intuition is that if a quark field transforms in the fundamental representation of $\mathrm{SU}(3)$, i.e. the **3** representation, then the quarks come in three colours. The transformation properties of the SM fields under the SM gauge groups are presented in Tab. 1.1.

1.2. The theory of QCD

QCD is based on the $\mathrm{SU}(3)$ gauge group [7,8]. The special unitary group $\mathrm{SU}(\mathrm{N})$ has a degree n and elements as $n \times n$ unitary matrices[3] of determinant equals one. In the case of $\mathrm{SU}(3)$, there are a total of eight independent directions in this matrix space.

[2] In the context of symmetries, the "charge" is the generator of the symmetry.

[3] A matrix U is unitary if it satisfies the condition $UU^\dagger = \mathbb{1}$ where $U^\dagger$ is the hermitian adjoint of U and $\mathbb{1}$ is the identity matrix.

Field	$\mathbf{SU(3)_c}$	$\mathbf{SU(2)_L}$	$\mathbf{U(1)_Y}$
$Q_i = (u_L^i, d_L^i)^T$	**3**	**2**	1/6
$u_i = \{u_R, c_R, t_R\}$	**3**	**1**	2/3
$d_i = \{d_R, s_R, b_R\}$	**3**	**1**	-1/3
$L_i = (\nu_L^i, e_L^i)^T$	**1**	**2**	-1/2
$e_i = \{e_R, \mu_R, \tau_R\}$	**1**	**1**	-1
H	**1**	**2**	1/2

Table 1.1.: Transformation properties of the SM fields under the gauge groups. Q_i and L_i denote the left-handed (L) quarks and leptons doublets with the index $i \in \{1,2,3\}$ running over the three generations of fermions. u_i, d_i denote the right-handed (R) quarks, while e_i denote the right-handed leptons.

These independent directions represent the eight generators of the SU(3) group, which can further be thought of as the gauge transformations carried out by gluons in the colour space. Gluons live in the adjoint representation of SU(3), i.e. the **8** of SU(3). The dimension of the adjoint representation is equal to the number of generators of the group, $n^2 - 1$. In QCD, these eight generators are a set of eight traceless and hermitian matrices; the Gell-Mann matrices. These unitary matrices or the group's generators can act on one another as successive gauge transformations, or on quarks in colour space. The latter, and as mentioned before, is represented by a triplet, i.e. a three-component quantum field that transforms under the fundamental representation of $\mathrm{SU(3)_c}$, denoted by ψ_q or the conjugate field $\overline{\psi}_q$.

The QCD Lagrangian density describes the dynamics of the quarks and gluons,

$$\mathcal{L}_{\mathrm{QCD}} = -\frac{1}{4} G^a_{\mu\nu} G^{a\mu\nu} + \overline{\psi}^i_q (i\gamma^\mu)(D_\mu)_{ij} \psi^j_q - m_q \overline{\psi}^i_q \psi_{qi}, \tag{1.1}$$

where ψ^i_q denotes the quark field with colour index i, i.e. $\psi_q = (\psi_{qR}, \psi_{qG}, \psi_{qB})^T$, γ^μ is a Dirac matrix representing the vector nature of strong interactions, with μ being a Lorentz vector index, m_q is a parameter allowing for non-zero quark masses, $G^a_{\mu\nu}$ is the gluon field strength tensor with adjoint colour index a, $a \in [1, ..., 8]$, and D_μ is the covariant derivative in QCD,

$$(D_\mu)_{ij} = \delta_{ij}\partial_\mu - i g_s t^a_{ij} A^a_\mu, \tag{1.2}$$

where g_s is related to the coupling of the strong interaction, α_s, through $g_s^2 = 4\pi\alpha_s$, A^a_μ are the gluon fields, and $t^a_{ij} = \frac{1}{2}\lambda^a_{ij}$ with λ^a being the set of hermitian and traceless

Gell-Mann matrices representing the generators of the SU(3) group. The gluon field strength tensor is defined as follows:

$$G^a_{\mu\nu} = \partial_\mu A^a_\nu - \partial_v A^a_\mu + g_s f^{abc} A^b_\mu A^c_\nu, \tag{1.3}$$

where f^{abc} is the structure constant of the SU(3) group appearing in the non-abelian part of the field tensor.

1.2.1. Perturbative QCD

Perturbative QFT is the main tool for solving the QCD equations of motion at high energy scales, $Q \gg \Lambda_{\text{QCD}}$. Below the QCD scale parameter (referred to also the as the QCD confinement scale) $\Lambda_{\text{QCD}} \sim$ 200 MeV, where QCD becomes non-perturbative, the quarks, antiquarks, and gluons would no longer exist as separate components but as bound states, forming hadrons and mesons, and different tools would be needed to solve it, e.g. lattice QCD and chiral perturbation theory. The calculation of Matrix Elements at fixed order (FO) in strong coupling α_s is the starting point to solve QCD in the context of perturbative QFT. Calculations at the leading/lowest order in α_s (LO) have been highly automated through tools like `MadGraph5` [9, 10] and several others [11–19].

Factorisation Even though QCD high-energy scatterings can be solved using the methods of perturbative QFT, there arises a complexity for hadron-initiated scatterings, that is, hadrons in the initial state are composite. The compositeness of hadrons means there are partons within clouds of further partons, constantly being emitted and absorbed. Therefore, and besides perturbatively calculating the partonic scattering matrix elements, one must also address the partonic structure of the colliding hadrons. The Factorisation theorem [20] allows us to write the cross-section for hadron-initiated processes in which the assumed factorisable cross-section reads

$$d\sigma_{h1h2} = \sum_{i,j} \int_0^1 dx_i \int_0^1 dx_j \sum_f \int d\Phi_f f_{i/h_1}(x_i, \mu_F^2) f_{j/h_2}(x_j, \mu_F^2) \frac{d\hat{\sigma}_{ij\to f}}{dx_i dx_j d\Phi_f}, \tag{1.4}$$

where i and j are indices running over all possible parton types in the incoming hadrons, f enumerates all possible partonic final states, with Lorentz-invariant phase space, Φ_f. The parton density functions (PDFs), f_{i/h_1} and f_{j/h_2}, parameterise the distribution of partons inside the hadrons h_1 and h_2. PDFs are not a priori calculable

and must be constrained by fits to data. The fraction of the hadron momentum carried by parton i and j is x_i and x_j, respectively. The partonic cross-section, $d\hat{\sigma}$, is calculable within perturbation theory. The dividing line between the partonic cross-section and parton density functions is an arbitrary scale, μ_F, the so-called factorisation scale. In other words, factorisation in perturbative QCD separates the short- and the long-distance physics, with the associated scale μ_F corresponding to the resolution by which the hadron is being probed. It is worth noting, however, that μ_F is not physical. Therefore, ultimately, QCD predictions should have minimal dependence on this scale.

Running of QCD coupling Calculations in QCD can be dramatically complex, especially at higher orders in the strong coupling, α_s. The evaluation of the matrix elements can therefore give divergent results; non-physical infinities referred to as ultra-violet (UV) divergences. Dealing with these infinities require the absorption of the divergent terms into a redefinition of fields or parameters; this method is usually called renormalisation. Therefore, in perturbative QCD, predictions for observables are expressed in terms of the renormalised coupling $\alpha_s(\mu_R^2)$, where μ_R is some non-physical renormalisation scale. Since QCD is not a theory with a fixed coupling, that is, the coupling is not the same at all scales, taking μ_R close to the scale of the momentum transfer, Q, in a given process renders $\alpha_s(\mu_R^2 \simeq Q^2)$ indicative of the effective strength of the strong interaction in that process. The "running" coupling thus satisfies the renormalisation group equation (RGE),

$$\mu_R^2 \frac{d\alpha_s}{d\mu_R^2} = \beta(\alpha_s) = -\alpha_s^2(b_0 + ...), \tag{1.5}$$

where $b_0 = (33 - 2n_f)/(12/\pi)$ is referred to as the 1-loop beta function coefficient with n_f being the number of active quark flavours (effectively light, i.e. $m_q \ll Q$) considered. The minus sign in Eq. 1.5 signifies the asymptotic freedom of QCD, i.e. the strong coupling effectively decreases with energy, and consequently perturbation theory becomes better-behaved at higher energies. The dots on the r.h.s of Eq. 1.5 are in place of b_1, 2-loop beta-function coefficient, b_2, 3-loop coefficient, and so on, which are related to the UV divergences at each loop order.

In parallel to the arbitrariness in the choice of the factorisation scale, μ_F, the uncertainties associated with determining the renormalisation scale, μ_R, at which $\alpha_s(\mu_R^2)$ is to be evaluated is another key obstacle in making precise perturbative QCD predictions. One way of handling this is to fix μ_F and μ_R to some physically meaningful value related to the process being calculated and then performing a variation of μ_F

and μ_R around that central scale. This variation provides an envelope of the so-called QCD scale uncertainties around the calculated QCD predictions.

Fixed order QCD Considering the QCD production of some arbitrary final state, F, the all orders differential cross-section for an observable, $\mathcal{O}$, schematically reads (where PDF factors have been omitted for simplicity)

$$\frac{d\sigma_F}{d\mathcal{O}} = \sum_{k=0}^{\infty} \int d\Phi_{F+k} \left| \sum_{l=0}^{\infty} \mathcal{A}_{F+k}^{(l)} \right|^2 \delta(\mathcal{O} - \mathcal{O}(\Phi_{F+k})), \tag{1.6}$$

where the sum over k is a sum over additional final-state partons, $\mathcal{A}_{F+k}^{(l)}$ is the amplitude for producing F in association with k additional partons and l additional loops. The delta function ensures the formula gives the cross-section differentially in $\mathcal{O}$ and not the total integrated cross-section. The start of the sum at $k = 0$, $l = 0$ represent the leading order (LO) for producing F, while higher terms represent real and virtual next-to-leading order (NLO) corrections, with real emissions being additional legs in the amplitude and virtual ones are additional loops. For $k \geq 1$, the process under consideration is the F production + k jets, $F + k$. Integrating over all momenta implied by the $d\Phi_{F+k}$ factor in Eq. 1.6 would include configurations in which the extra k partons are collinear or soft leading to infrared (IR) QCD divergences. These divergences are usually regulated by selections on angles or energies that would cut away these regions in the phase space to make the FO QCD prediction reliable.

1.3. The EW theory and the Brout-Englert-Higgs (BEH) mechanism

The EW theory is a unified theory describing two of the four fundamental interactions in nature, electromagnetism and the weak interaction [21–23]. As mentioned before, weak interactions are mediated through the $W^{\pm}$ and Z massive vector gauge bosons, in parallel to the photon, γ, which is the electromagnetic force carrier. The EW theory is based on the $\mathrm{SU(2)_L} \times \mathrm{U(1)_Y}$ gauge group. In analogy to the discussion on QCD, here the SU(2) group gives rise to three generators named the weak isospin, T, while the U(1) group gives rise to one generator called the weak hypercharge, Y_W. The electric charge quantum number, Q, is defined as $T^3 + Y_W$, where T^3 is the third component

of the weak isospin[4]. The generators of the group formally dictate the gauge bosons of the theory. The three bosons of the weak isospin (W^1_μ,W^2_μ,W^3_μ) and the B_μ boson of the weak hypercharge are not physical unless EW symmetry breaking (EWSB) and the associated BEH mechanism [24,25] have taken place. After said EWSB and mass generation through the BEH mechanism, the first two bosons of the weak isospin become the $W^\pm$ massive vector gauge bosons, while the W^3_μ boson together with the B_μ boson "mix" to form the photon, γ, and the massive vector gauge boson, Z. Such mixing through the so-called weak mixing angle (or the Weinberg angle), θ_W, reads

$$\begin{pmatrix} \gamma \\ Z \end{pmatrix} = \begin{pmatrix} \cos\theta_W & \sin\theta_W \\ -\sin\theta_W & \cos\theta_W \end{pmatrix} \begin{pmatrix} B \\ W^3 \end{pmatrix}. \tag{1.7}$$

These mixing angles play an important role in relating the masses of the W and Z bosons, as later discussed.

The observation of nuclear β decays was the starting point of the theory of weak interactions. The Fermi theory of weak interactions (which is in the next chapter discussed as an EFT) attempted to explain the observed beta decays. In the original form of the theory, Fermi proposed the weak interaction has a general form of contact coupling between two vector currents,

$$\mathcal{H}_{Fermi} = \frac{G_F}{\sqrt{2}} \int d^3x \cdot j^\mu_H(x) \cdot j_{L\mu}(x), \quad j^\mu = \overline{\psi}\gamma^\mu\psi, \tag{1.8}$$

where G_F is the Fermi coupling constant, and j^μ_H and $j_{L\mu}$ are 4-dimensional current densities for hadrons and leptons, respectively. The Wu experiment conducted by Chien-Shiung Wu et al. in 1957, in which the beta decay of polarised Cobalt-60 nuclei was studied [26], led to the observation that electrons are emitted preferentially in the direction opposite to the applied field, showing that parity is maximally violated in weak interactions. Violation of parity necessitated that the interaction Hamiltonian should be modified as follows:

$$\mathcal{H}_{V-A} = \frac{G_F}{\sqrt{2}} \int d^3x \cdot \overline{\psi}_p\gamma^\mu(1-\gamma_5)\psi_n \cdot \overline{\psi}_e\gamma_\mu(1-\gamma_5)\psi_\nu, \tag{1.9}$$

in a structure merely dictated by phenomenology. This modification is the essence of the V-A theory (vector and axial-vector), originally formulated by Robert Marshak and

[4] This is called the "half-scale" definition. In this choice, the convention used by Peskin and Schroeder's "Introduction to QFT" [4] is followed. An alternative definition is $Q = T^3 + \frac{1}{2}Y_W$.

George Sudarshan in 1957 and publicised by Richard Feynman and Murray Gell-Mann in [27] in 1958, i.e. the weak interactions are produced by both vector and axial-vector currents. The maximal parity violation in weak interactions dictates the transformation of weakly interacting particles under the SU(2) gauge group: left-handed particles form doublets, while right-handed particles form singlets of $\mathrm{SU}(2)_\mathrm{L}$.

1.3.1. EW symmetry breaking in the SM

In QFT, the particle states are created from the vacuum, i.e. lowest possible energy state. For two physical states to be related by some symmetry, the vacuum must be invariant under such symmetry. Consider the two fields φ_1 and φ_2 being related by the action of some symmetry generated by the hermitian operator $\hat{Q}$, i.e. $\varphi_1 = i[\hat{Q}, \varphi_2]$. The corresponding creation and annihilation operators are therefore related in the same way, $a_1^\dagger = i[\hat{Q}, a_2^\dagger]$, expanding the latter reads

$$|1\rangle = a_1^\dagger|0\rangle = i\hat{Q}a_2^\dagger|0\rangle - ia_2^\dagger\hat{Q}|0\rangle = i\hat{Q}|2\rangle - ia_2^\dagger\hat{Q}|0\rangle. \tag{1.10}$$

Therefore, the particle states satisfy $|1\rangle = i\hat{Q}|2\rangle$ *only* if the vacuum is invariant, i.e. $\hat{Q}|0\rangle = 0$. If the vacuum is not invariant under the symmetry operation, i.e. $\hat{Q}|0\rangle \neq 0$, then the symmetry is spontaneously broken. A system is spontaneously broken if the vacuum acquires a non-trivial vacuum expectation value (vev). The Goldstone theorem states that for every spontaneously broken continuous symmetry, there is an induced massless scalar boson, Nambu-Goldstone boson (usually referred to as the Goldstone boson) for each broken generator [28].

Above the unification energy, on the order of $v \simeq 246$ GeV, both electromagnetism and weak forces merge into a single EW force which is described by the unbroken gauge group $\mathrm{SU}(2)_\mathrm{L} \times \mathrm{U}(1)_\mathrm{Y}$. In breaking the EW symmetry, the unified description of EW theory is broken down to electromagnetism,

$$\mathrm{SU}(2)_\mathrm{L} \times \mathrm{U}(1)_\mathrm{Y} \to \mathrm{U}(1)_\mathrm{EM}. \tag{1.11}$$

The EW Lagrangian, $\mathcal{L}_{EW}$, in the SM reads

$$\mathcal{L}_\mathrm{EW} = \mathcal{L}_K + \mathcal{L}_f + \mathcal{L}_H + \mathcal{L}_{Yukawa}, \tag{1.12}$$

where $\mathcal{L}_K$ denotes the kinetic terms of the $\mathrm{SU(2)_L}$ and $\mathrm{U(1)_Y}$ gauge fields with $W_{\mu\nu}$ and $B_{\mu\nu}$ being their field strength tensors, respectively,

$$\mathcal{L}_k = -\frac{1}{4}W^a_{\mu\nu}W^{a\mu\nu} - \frac{1}{4}B_{\mu\nu}B^{\mu\nu}. \tag{1.13}$$

The second term on the r.h.s of Eq. 1.12, $\mathcal{L}_f$, denotes the fermions dynamics,

$$\mathcal{L}_f = \overline{Q}_L(i\not{D})Q_L + \overline{u}_R(i\not{D})u_R + \overline{d}_R(i\not{D})d_R + \overline{L}_L(i\not{D})L_L + \overline{e}_R(i\not{D})e_R, \tag{1.14}$$

where Q_L and L_L are the quarks and leptons doublets, respectively. The EW covariant derivative, $\not{D}$, is defined as $\gamma^\mu D_\mu$ with D_μ reading

$$D_\mu = \partial_\mu - ig\sigma^a W^a_\mu - ig'YB_\mu, \tag{1.15}$$

where σ^a where $a = 1, 2, 3$ represent the three generators of the $\mathrm{SU(2)_L}$ group, and W^a_μ are the three associated gauge bosons. B_μ is the gauge boson associated with $\mathrm{U(1)_Y}$. The parameters g and g' are the $\mathrm{SU(2)_L}$ and $\mathrm{U(1)_Y}$ gauge coupling constants, respectively. The last two terms of Eq. 1.12 denote the Higgs and the Yukawa Lagrangians. The Higgs Lagrangian shown is written as follows,

$$\mathcal{L}_H = |D_\mu\Phi|^2 + \mu^2\Phi^\dagger\Phi - \lambda(\Phi^\dagger\Phi)^2, \tag{1.16}$$

where the first term is the kinetic term of the complex scalar field $\Phi = (\varphi^+\varphi^0)^T$, the second and the third terms form the most general renormalisable and $\mathrm{SU(2)}$ invariant potential allowed. The scalar field transforms as a doublet under the $\mathrm{SU(2)_L}$ group with weak hypercharge $Y_W(\Phi) = \frac{1}{2}$. The minimum of the potential for $\mu^2 < 0$ occurs at a non-zero value of $v \equiv \frac{\mu}{\sqrt{\lambda}}$ where v is the vev acquired by the complex field. The complex doublet Φ can be written in terms of its four fields and acted on by an $\mathrm{SU(2)}$ gauge transformation such that the upper component of the rotated doublet is zero, while the lower component is real and positive,

$$\Phi = \begin{pmatrix} \theta_2 + i\theta_1 \\ \frac{1}{\sqrt{2}}(v + H) - i\theta_3 \end{pmatrix} = \frac{1}{\sqrt{2}}e^{i\frac{\sigma^a\theta^a}{v}}\begin{pmatrix} 0 \\ v + H \end{pmatrix}, \tag{1.17}$$

where the exponential factor denotes the $\mathrm{SU(2)}$ transformation with θ^a being the three additional fields of the complex doublet. The lower real-valued component of the doublet field in Eq. 1.17 has now an arbitrary value given by the vev plus

some fluctuating real-valued field, H. In the unitary gauge, the field Φ can further be simplified as follows:

$$\Phi = \frac{1}{\sqrt{2}} \begin{pmatrix} 0 \\ v + H \end{pmatrix}, \tag{1.18}$$

where the the Goldstone bosons, θ^a, are *rotated away*, leaving only the H fluctuation in the spectrum after the spontaneous symmetry breaking induced by the non-zero vev, v, of the Φ field took place. This quantum of the H field is the Higgs boson.

1.3.2. The Higgs boson role in mass generation

The expansion of the kinetic terms in Eq. 1.16 using Eq. 1.18 induces the mass terms for the gauge bosons plus additional terms involving the Higgs scalar particle. On the other hand, expanding the potential term in Eq. 1.16 yields the Higgs boson mass term and terms involving Higgs self-coupling. Combining all the mass terms as a result of EWSB in $\mathcal{L}_{mass}$ reads

$$\mathcal{L}_{mass} = \frac{1}{2} m_W^2 W^{\mu +} W_\mu^- + \frac{1}{2} m_Z^2 Z^\mu Z_\mu - \frac{1}{2} m_h^2 H^2, \tag{1.19}$$

where the definitions that have been adopted in the expansion and the induced masses of the gauge bosons are as follows,

$$W_\mu^\pm = \frac{1}{\sqrt{2}} (W_\mu^1 \mp i W_\mu^2), \qquad m_W = g \frac{v}{2}. \tag{1.20}$$

$$Z_\mu = \frac{1}{\sqrt{g^2 + g'^2}} (g W_\mu^3 - g' B_\mu), \qquad m_Z = \sqrt{g^2 + g'^2} \frac{v}{2}. \tag{1.21}$$

The fourth vector field denoted as A_μ is the electromagnetic field vector potential, it remains massless and is defined as follows ,

$$A_\mu = \frac{1}{\sqrt{g^2 + g'^2}} (g' W_\mu^3 + g B_\mu). \tag{1.22}$$

The Higgs boson mass term, m_H, is a function of the vev, v, and some dimensionless coupling, λ, it reads

$$m_H = \sqrt{2}\mu^2 = \sqrt{\frac{\lambda}{2}}v. \tag{1.23}$$

Having discussed the generation of gauge bosons masses through the so-called BEH mechanism associated with EWSB, and before moving on the generation of fermion masses, it is instructive to summarise the previous discussion: we started with the complex scalar SU(2) doublet Φ with four degrees of freedom, a three SU(2) gauge fields, W^a_μ, each with two degrees of freedom; a total of six degrees of freedom, and one U(1) gauge field, B_μ, having two degrees of freedom, summing up to a total of twelve degrees of freedom. After the spontaneous symmetry breaking, there remains a massive scalar boson, H, with one degree of freedom, *massive* $W^\pm$ and Z bosons, each having three degrees of freedom; a total of nine degrees of freedom, and a massless photon with another two degrees of freedom. The total degrees of freedom is therefore conserved through the EWSB. The transformation of the scalar degrees of freedom from the complex scalar doublet Φ to the $\mathrm{SU(2)_L}$ and $\mathrm{U(1)_Y}$ gauge bosons gave rise to their *longitudinal* components, and so the massive $W^\pm$ and Z bosons.

We now turn to the mass generation of fermions. In the EW theory, fermions are better described in a chiral basis since, as already mentioned, left and right-handed fermions have different transformation properties under the $\mathrm{SU(2)_L} \times \mathrm{U(1)_Y}$ group, and so a direct mass term like

$$-m_\psi(\overline{\psi}_L\psi_R + \overline{\psi}_R\psi_L), \tag{1.24}$$

is forbidden to be written since it is not invariant under local gauge transformation. The Yukawa couplings of the fermions to the Higgs boson allow fermions masses to arise in a gauge-invariant way. The Yukawa Lagrangian from Eq. 1.12 can be compactly written for quarks as follows:

$$\Delta\mathcal{L}_{Yukawa} = -\lambda_d\overline{Q}_L\Phi d_R - \lambda_u\overline{Q}_L\Phi^c u_R + \text{h.c.}, \tag{1.25}$$

where $\Phi^c = -i\sigma^2\Phi^*$. The coupling generates the mass term for the down quark as follows:

$$-\lambda_d \frac{1}{\sqrt{2}}(\overline{u}_L \ \overline{d}_L)\begin{pmatrix} 0 \\ v+H \end{pmatrix} d_R \quad \rightarrow \lambda_d = \frac{m_d\sqrt{2}}{v}, \tag{1.26}$$

and in the same way for the up quark and for charged leptons. In general, the direct coupling of the Higgs boson to fermions is what gives rise to their masses. The coupling of the Higgs boson to fermions follows the relation:

$$\Delta\mathcal{L}_f = -m_f\overline{f}f\left(1+\frac{H}{v}\right), \tag{1.27}$$

where f stands for any quark or lepton flavour. The Lagrangian in Eq. 1.27 dictates the interaction strength of the Higgs boson to be proportional to the masses of the fermions. One experimental consequence of this relation is that the particles that are easily produced in an experiment have very weak coupling to the Higgs boson rendering them very difficult to observe.

Experimental consequences of the BEH mechanism In Eq. 1.7, the weak mixing angle was introduced in showing the mixing of the W^3_μ boson together with the B_μ boson to form the neutral Z and γ physical bosons. The weak mixing angle can be defined as follows:

$$\cos\theta_w = \frac{g}{\sqrt{g^2+g'^2}}, \quad \sin\theta_w = \frac{g'}{\sqrt{g^2+g'^2}}, \tag{1.28}$$

relating the masses of the W and Z bosons according to $m_W = m_Z\cos\theta_w$ which dictates the W boson mass to be smaller than the Z boson mass.

The W boson mass is measured to be 80.433 ± 0.009 GeV [29] and the Z boson mass is measured to be 91.1876 ± 0.0021 GeV [30]. The Higgs boson mass term in Eq. 1.23 is determined by a renormalisable coupling constant, λ, which acts as a free parameter in the theory. The parameter v is derived from the charged current of μ decay, $\mu \rightarrow e\overline{\nu}_e\nu_\mu$, of which the interaction strength (the so-called Fermi constant) is measured accurately to be $G_F = 1.1663787(6) \times 10^{-5}$ GeV $^{-2}$ and can be related to the parameter v following the relation $v = (\sqrt{2}G_F)^{-1/2} \simeq 246$ GeV. The Higgs boson mass in the SM is measured to be near 125 GeV, together with the precise measurement of v, the coupling constant λ in the SM can then be written as $\lambda_{SM} = m_h^2/2v^2$. The parameter λ_{SM} controls the

Higgs self-coupling and it has not been measured independently as of the time of writing, such measurement of the Higgs self-coupling is indeed needed to understand the EWSB fully.

The Higgs boson role in unitarity As previously discussed, and since the Goldstone bosons constitute the longitudinal polarisation of the massive physical gauge bosons, $W^{\pm}$ and Z. Therefore, the scattering $V_L V_L \to V_L V_L$ where V is W or Z bosons, puts the Goldstone dynamics into a direct test. Without considering the Higgs boson, the tree-level scattering amplitude would have the following form:

$$\mathcal{A}(W_L^+ W_L^- \to W_L^+ W_L^-) = \frac{s+t}{v^2} + \mathcal{O}\left(\frac{m_W}{\sqrt{s}}\right), \tag{1.29}$$

where s and t are the Mandelstam variables; numerical quantities encode the energy of scattering. The contribution s/v^2 implies an unacceptable violation of unitarity at high energies.

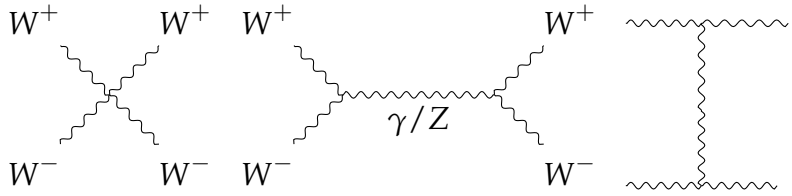

Figure 1.1.: Tree-level Feynman diagrams for the scattering of gauge bosons process $W_L W_L \to W_L W_L$ without the Higgs boson exchange.

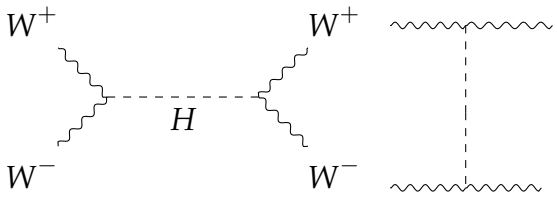

Figure 1.2.: Additional diagrams for the scattering of gauge bosons process, $W_L W_L \to W_L W_L$, mediated through the Higgs boson exchange.

The additional tree-level $W_L W_L \to W_L W_L$ contributions to the ones shown in Fig. 1.1 includes the Higgs boson exchange and are shown in Fig. 1.2. These additional contributions recover the correct high-energy unitary behaviour through intricate cancellation of the otherwise unphysical energy growth. The SM scattering amplitude

then reads

$$\mathcal{A}_{SM} = \frac{1}{v^2}\left(s + t - \frac{s^2}{s - m_h^2} - \frac{t^2}{t - m_h^2}\right) = -\frac{m_h^2}{v^2}\left(\frac{s}{s - m_h^2} - \frac{t}{t - m_h^2}\right). \tag{1.30}$$

Such intricate cancellation led to the understanding that any small deviation away from the SM Higgs dynamics would imply the presence of new-physics contributions to the $V_L V_L \to V_L V_L$ scattering amplitude for unitarity to remain restored.

1.4. The need for BSM physics

Despite the SM being the most successful theory in particle physics, it is inherently an incomplete one. Over the years, this has led to the proposals that BSM physics must exist to address these shortcomings of the existing theory. The shortcomings of the SM can arise in the form of non-explained phenomena or theoretical predictions that were not observed. The most recent contradiction to the SM is the anomalous mass of the W boson reported by the CDF Collaboration [29]. The result shows tension with the SM expectation [30] with a significance amounting to 7.0σ.

Moreover, there are several lingering non-explained phenomena that the SM, so far, has not been able to explain. Examples of these are gravity, dark matter and dark energy, neutrino masses, and the strong CP problem.

Gravity A significant fundamental physical phenomenon in nature that the SM has not been able to explain is gravity. It has been widely considered that the SM is incompatible with the theory of general relativity. This comes from the fact that incorporating a spin-2 gauge field acting as a graviton renders the SM not renormalisable.

Dark matter and dark energy Dark matter and dark energy are yet another manifestation of the SM limitations. Cosmological observations show that around 26% of our universe is dark matter while 69% is dark energy; this leaves around only 5% of the universe explained by the SM. Many ideas exist on the nature of dark matter as some new particles, some of which can be part of the SM, like neutrinos, while others are potentially not part of the SM, like weakly interacting massive particles (WIMPs). So far, none of the potential dark matter candidates has been observed, and so the question of dark matter remains open.

Neutrino masses Conversely to the SM predictions, neutrino oscillation experiments have shown that neutrinos do have masses. Adding neutrino mass terms for the SM to match the current evidence gives rise to new theoretical problems, for the generation of neutrino masses is not necessarily arising in the same way as the masses of other fundamental particles in the SM.

Strong CP problem CP-symmetry states that physics should be invariant to particles swapping with their antiparticles and then left-handed and right-handed particles also interchanging. The standing mathematical formulation of QCD hints at a violation of such CP-symmetry in strong interactions, yet no such violation of CP-symmetry has ever been observed in experiments involving only strong interactions. In the SM, the parameter controlling the amount of CP violation is the so-called CP-violating angle denoted by $\overline{\theta}$ which can can take any value between 0 and 2π. The measurement of the electron dipole moment [31] requires $\overline{\theta} < 10^{-10}$, a particularly small value hinting at a fine-tuning problem; the strong CP problem.

1.5. Towards an EFT approach

Theories extending the SM through novel explanations are derived to address current open questions and overcome existing challenges. However, the final word on whether one given proposal accurately describes experimental observation and thus can be regarded as a valid theory of nature belongs to the experiment. In the search for new physics beyond the SM, so far, high-energy experiments have found no indications of BSM particle production. One explanation for this lack of evidence is that the experimental reach may not have yet reached the kinematic range where these potential BSM particles can be produced in final states. This reasoning led to EFT approaches, a powerful tool by which potential new physics effects induced by said BSM particles, should we be unable to observe them directly, can be systematically parameterised and searched for *indirectly*.

Chapter 2.

The Standard Model Effective Field Theory

As discussed in the previous chapter, the proposal of the BEH mechanism resolved the mass-generation conundrum in the SM through the breaking of the EW symmetry. The main goal of the LHC was to reveal the $\mathrm{SU(2)_L \times U(1)_Y \to U(1)_{EM}}$ mechanism. In 2012, the LHC discovered a scalar boson consistent with the SM Higgs boson associated with the Higgs field from the BEH mechanism. The scarcity of additional new state discoveries at the LHC is unsurprising given the lack of statistically significant deviations from the SM predictions. This can be a result of a moderate degree of decoupling of physics at higher energy scales Λ; $\Lambda \gg m_W$ [32]. Assuming this is the case, an outstanding improvement in the theoretical predictions of experimental results will be required to *indirectly* search for physics beyond the SM. Knowledge attained through indirect methods using EFT techniques has historically led to indications of new states or theoretical frameworks. In this chapter, I relied mainly on two sources for the EFT introductory discussion, these were Ref. [33], and Ref. [34].

2.1. Fermi's theory as an illustration of EFTs

One famous example of EFTs is the Fermi theory which is treated here for illustration. The original framework introduced by Fermi was intended to describe the neutron decay. However, here the name is used to refer to the low-energy effective theory of the SM below the $W^{\pm}$ mass scale where the W, Z, Higgs boson and top quark are all *integrated out* of the theory. Considering a small subset of the Fermi theory where only muons, electrons and neutrinos exist, we treat the muon decay process,

$$\mu^-(p) \to e^-(k_1)\overline{\nu}_e(k_2)\nu_\mu(k_3), \tag{2.1}$$

with p and k referring to incoming and outgoing momenta, respectively. In the SM, this process is mediated by the W boson, where the interaction reads

$$\Delta\mathcal{L}_{SM} = \frac{g_L}{\sqrt{2}}(\overline{\nu}_\mu \sigma_\rho \mu + \overline{\nu}_e \sigma_\rho e) W^+_\rho + \text{h.c.}, \tag{2.2}$$

where $\sigma_\rho \equiv \gamma^\rho P_L$ with P_L being the left-handed projection operator. The muon decay amplitude $\mathcal{A}$ reads

$$\mathcal{A} = \frac{g_L^2}{2}\overline{x}(k_3)\sigma_\rho x(p)\frac{1}{q^2 - m_W^2}\overline{x}(k_1)\sigma_\rho y(k_2), \;\; q \equiv p - k_3, \tag{2.3}$$

where $m_W \approx 80\,\text{GeV}$, x and y are two-component spinor wave functions depending on the spin of the leptons. Considering the physical process of Eq. 2.1 in the kinematics of the $1 \to 3$ body decay. The exchange of momenta would be constrained to $0 \leq q^2 \leq m_\mu^2$ (in the limit where the electrons and neutrinos can be treated as massless) rendering $q^2/m_w^2 \lesssim 10^{-6}$. The consequence of the latter observation is the Taylor expansion of the amplitude:

$$\mathcal{A} \approx -\frac{g_L^2}{2m_W^2}[\overline{x}(k_3)\sigma_\rho x(p)\overline{x}(k_1)\sigma_\rho y(k_2)][1 + \mathcal{O}(q^2/m_W^2)], \tag{2.4}$$

where the amplitude no longer has a pole corresponding to the W boson propagation. Before continuing this example, let us pause and attempt to address the fundamental idea behind EFT in a brief interlude.

Interlude The fundamental idea behind EFT comes from the observation that the non-analytic structure of scattering amplitudes is due to intermediate propagation where physical particles can exist on-shell[1], i.e. $p^2 = m^2$. Therefore, having a QFT constructed for relatively light particles (what we did in the Fermi theory example), virtual heavy particles which can not be created at the energy scale of the problem can be Taylor expanded, e.g. $\mathcal{O}(q^2/m_W^2)$. EFT's power comes from the fact that Taylor expanded amplitudes can be computed from EFTs with only relatively light particles. The local interactions between the light particles encapsulate the "slight" effects potentially arising from the virtual heavy particle exchange. This is essentially due to the decoupling theorem [35]. The latter formalises how the non-analytic structure

[1] In this limit, amplitudes with propagators $1/\left(p^2 - m^2 + i\epsilon\right)$ become sensitive to $i\epsilon$.

of correlation functions due to heavy states are projected out when matching onto a low-energy EFT.
The EFT we can construct through Eq. 2.4 can be written as the following interaction term:

$$\Delta\mathcal{L}_{\text{EFT}} = \frac{c}{\Lambda^2}(\overline{\nu}_\mu\sigma_\rho\mu)(\bar{e}\sigma_\rho\nu_e) + \text{h.c.}, \tag{2.5}$$

where the expansion scale, Λ, and c, the so-called Wilson coefficient (WC) of the dimension-six[2] operator in Eq. 2.5, are defined as follows:

$$\Lambda = m_W, \;\; c = \frac{-g_L^2}{2}. \tag{2.6}$$

The parameter m_W marks the validity scale of the Fermi theory. Such procedure is the so-called *tree-level matching*. For the latter, one compares the EFT and full theory in the IR limit to *match* the WCs as shown in Eq. 2.6. The power of what we have accomplished here is manifested in the fact that Fermi's theory was used for weak decay calculations even when the scales m_W and m_Z were not known. Needless to say, for scattering energies close to or above m_W, the Fermi theory is no more useful since the EFT expansion will break down in this limit.

So far, we have reconstructed an EFT theory only in hindsight. After all, we already know that W and Z bosons exist. The above example was only intended to portray the Fermi theory as a low-energy limit of a UV theory, in such case, this UV theory was the SM (which we know). In this chapter, however, the aim is to discuss the SM itself as a low-energy limit of an even more complete UV theory (which we do not know). For this, we will have to construct the EFT Lagrangian without prior knowledge of the heavy particles we will have to integrate out. This will require a more general discussion on the principles of constructing EFTs. In explaining some aspects of EFTs, I keep referring to the EFT Lagrangian obtained in Eq. 2.5.

2.2. Constructing an EFT Lagrangian

EFTs allow the computation of experimentally measurable quantities with finite errors. An EFT has an expansion parameter δ, usually referred to as the power counting parameter, in which calculations are done in an expansion to some order n. The

[2] Recall the mass dimensions of the generic fields and tensors in d=4 spacetime dimensions: $[\varphi]$=1, $[\psi]$=3/2, $[A_\mu]$=1, $[X_{\mu\nu}]$=2, for scalar, fermion, and vector fields, and field strength tensors, respectively.

error is then of order δ^{n+1}. The expansion parameter in the Fermi theory example was $\delta \equiv q/m_w$. It is worth mentioning that the EFT Lagrangian of Eq. 2.5 is just a subset of an infinite series of operators with the coefficients designed to absorb divergences arising from loop diagrams, if computations are performed beyond the tree-level. Having mentioned that, like any other QFT, EFTs require regularisation and renormalisation schemes to obtain finite matrix elements.

The number of experimental inputs used to fix the Lagrangian parameters increases with the order in δ. Infinite predictions require an infinite number of terms and, consequently, an infinite number of parameters. However, the power of the power counting argument comes in instructing the calculation about terms to keep at a given order in δ. In the muon decay of the Fermi theory example, the coefficient in Eq. 2.5 (which is historically written in terms of the Fermi constant, G_F) is fixed by the muon lifetime. Given this input, the theory is then able to provide parameter-free predictions, and so it has *predictive* power.

In writing down an EFT Lagrangian, the first step would be to determine the dynamical degrees of freedom, i.e. the field content of the Lagrangian relevant for the problem of interest. In cases where the EFT theory is a weakly coupled low-energy version of a UV theory, like the Fermi theory example, this exercise is "simple", since it just involves retaining the light fields.

2.2.1. EFT expansion

The action S is the integral of the local Lagrangian density, $\mathcal{L}(x)$, (which I have been referring, and will be referring to as just the "Lagrangian"),

$$S = \int d^d x \mathcal{L}(x), \tag{2.7}$$

with the Lagrangian having mass dimension d, and is defined as the sum of local, gauge-invariant and Lorentz invariant operators, $\mathcal{Q}_i$, with coefficients c_i,

$$\mathcal{L}(x) = \sum_i c_i \mathcal{Q}_i(x). \tag{2.8}$$

The operator has dimension D while its coefficient has $d - D$ dimensions (from the condition of dimensionless action; $[S] = 0$[3]), where $D \leq d = 4$. The Lagrangian

[3] For $\hbar \neq 1$; $[S] = \hbar$.

constructed from imposing $D \leq d = 4$ is a renormalisable QFT Lagrangian including the so-called *relevant* and *marginal* operators.

The EFT expansion is manifest in expanding the Lagrangian of Eq. 2.8 *beyond* $D = d$, in powers of operators dimensions,

$$\mathcal{L}_{\text{EFT}}(x) = \sum_i \frac{c_i}{\Lambda^{D-d}} \mathcal{Q}_i^D(x), \tag{2.9}$$

where c_i is a dimensionless coefficient and Λ is an introduced short distance scale at which new physics occurs. This expansion introduces the so-called *irrelevant* operators which are suppressed by a positive power of Λ. The Lagrangian of Eq. 2.9 can be expanded to arbitrarily high dimensions,

$$\mathcal{L}_{\text{EFT}}(x) = \mathcal{L}^{(D\leq 4)} + \frac{\mathcal{L}^{(D=5)}}{\Lambda} + \frac{\mathcal{L}^{(D=6)}}{\Lambda^2} + \dots. \tag{2.10}$$

However, in the rather hopeless attempt of infinitely summing all the terms of the series, not only the theory can not be renormalisable (discussed below), but also it loses its predictive power. Therefore, the EFT series must be treated in terms of power expansion in the δ parameter.

As hinted before, in this thesis context, we will be dealing with the *bottom-up* approach of EFT. That is, we are simply ignorant of the UV theory, more precisely, to the physics lying beyond the validity of the EFT. The coefficients of the higher-dimensional operators are therefore measured from the experiment, the relevant quantity for experimental measurements is c_i/Λ^{D-d}. This is in opposition to the *matching* we have done in the Fermi theory example, in which we had some knowledge about the UV theory; the latter is called the *top-down* approach.

2.2.2. Power counting and renormalisability

Considering a scattering amplitude $\mathcal{A}$ with zero mass dimension, an insertion of an EFT operator of dimension D would give a contribution to the amplitude of $(q/\Lambda)^{D-d}$ requiring the coefficient to have a mass dimension of $1/\Lambda^{D-d}$ according to Eq. 2.9, where q in the expansion parameter is the momentum scale of the process[4]. For a theory in $d = 4$ spacetime dimensions, the insertion of the higher dimension operator leads to an amplitude proportional to $(q/\Lambda)^n$ where $n = \sum_i (D_i - 4)$ and is called the

[4] For the amplitude to remain dimensionless, kinematic factors are assumed to provide the remaining mass dimensions.

EFT power counting formula with i running over all inserted operators. An example would be to add two dimension-five operators, i.e. $i = 1, 2$ and $D_i = 5$ for $i = 1, 2$. The EFT power counting formula can be written as follows:

$$n = (D_1 - 4) + (D_2 - 4) = 2 \rightarrow (q/\Lambda)^2 \tag{2.11}$$

instructing the calculation to corrections up to order $\mathcal{O}(\Lambda^2)$, i.e. $\delta^{n=2}$. Equivalently, we get the same result with one insertion of a dimension-six operator.

Loop diagrams are technically challenging to handle since momentum p is integrated over all values from $-\infty$ to $+\infty$, and obviously, the EFT expansion p/Λ breaks down. Retaining the given example, loop diagrams with two dimension-five insertions are divergent, at the same order, one dimension-six insertion acts like a counter-term. Two insertions of dimension-six operators will require dimension-eight counter-terms, and so-forth.

Using the power counting formula, one can realise that for $\mathcal{L}$ of $D \leq 4$, there are no generation of higher dimensional operators taking place (there are no q/Λ corrections), and so divergences in the theory are already absorbed by new operators generated by loops, but which are *already* included in $\mathcal{L}^{(D\leq 4)}$. In this sense, renormalisable theories are just a special case of EFTs where $\Lambda \rightarrow \infty$. For $D > d$, the theory is non-renormalisable because, in principle, an infinite number of operators are needed to renormalise the theory fully. However, in stressing again that the EFT series must be treated in terms of power expansion, computations must be performed for a maximum order of correction n, then there will be only a limited number of operators that contribute, and the EFT series will be renormalisable for this given order in n, e.g. at $n = 2$ divergent loop diagrams with two dimension-five insertions are renormalised with dimension-six counter-terms which arise at the same order of n.

2.3. Fields redefinition

In QFT, experimentally observable quantities are S-matrix elements. From the functional integral in QFT, one computes the correlation function of the product of quantum fields, Green functions. The relation between S-matrix elements and Green functions is mediated through the LSZ reduction formula. S-matrix elements are on-shell scattering amplitudes of particles. The full S-matrix element contains an infinite number of Feynman diagram, and so each Feynman diagram represents a term in the perturbation theory expansion of the S-matrix element for a given interaction. The relation between

the S-matrix element $\langle p_F|S|p_I\rangle$ and the amplitude $\mathcal{A}$ is given by the following:

$$\langle p_F|S|p_I\rangle = \langle p_F|p_I\rangle + 2\pi\delta(E_F - E_I)\mathcal{A}. \tag{2.12}$$

where S is a scattering operator, and $\langle p_F|$ and $|p_I\rangle$ are some final and initial momentum eigenstates, respectively. The cross-sections as observables for scattering experiments, σ, are proportional to $|\mathcal{A}|^2$. Since S-matrix elements are physics observables depending on particle states not the fields, they do not change under field redefinitions. Such invariance of the S-matrix elements under fields redefinition is a consequence of the equivalence theorem [36, 37].

2.3.1. An example using classical equations of motion

Field redefinition using classical equations of motion (eom) is a special case, and I here attempt to depict it through one simple example. The important aspect is that the S-matrix is invariant under the shifted Lagrangian $\mathscr{L}[\varphi]$, which can be mathematically expressed as follows:

$$\mathscr{L}[\varphi] = \mathcal{L}[\varphi] + \epsilon F[\varphi]\frac{\delta S}{\delta\varphi}, \tag{2.13}$$

where ϵ is some small parameter, i.e. $\epsilon \ll 1$, $F[\varphi]$ constitutes the redefinition of the field φ, and $\delta S/\delta\varphi$ is the classical equation of motion. This procedure then shifts the total Lagrangian $\mathcal{L}$ with a term derived from the equations of motion of the *lower* order Lagrangian.

Considering the following EFT Lagrangian:

$$\mathcal{L} = \frac{1}{2}\partial_\mu\varphi\partial^\mu\varphi - \frac{1}{2}m^2\varphi^2 - \frac{1}{4!}\lambda\varphi^4 + \frac{c_1}{\Lambda^2}\varphi^3\partial^2\varphi + \frac{c_2}{\Lambda^2}\varphi^6, \tag{2.14}$$

where the *lower* order Lagrangian is clearly made of the first three terms on the r.h.s as the last two terms come at a suppression scale $1/\Lambda^2$. The eom of the lower order Lagrangian reads

$$\frac{\delta S}{\delta\varphi} = (-\partial^2 - m^2)\varphi - \frac{\lambda}{3!}\varphi^3. \tag{2.15}$$

Considering the following field transformation:

$$\varphi \to \varphi + F[\varphi] \equiv \varphi + \frac{c_1}{\Lambda^2}\varphi^3, \tag{2.16}$$

one can write the shifted Lagrangian $\mathscr{L}$ as follows:

$$\begin{aligned}\mathscr{L} &= \frac{1}{2}\partial_\mu\varphi\partial^\mu\varphi - \frac{1}{2}m^2\varphi^2 - \frac{1}{4!}\lambda\varphi^4 + \frac{c_1}{\Lambda^2}\varphi^3\partial^2\varphi + \frac{c_2}{\Lambda^2}\varphi^6 \\ &\quad + \frac{c_1}{\Lambda^2}\varphi^3\left[(-\partial^2 - m^2)\varphi - \frac{\lambda}{3!}\varphi^3\right] + \dots \\ &= \frac{1}{2}\partial_\mu\varphi\partial^\mu\varphi - \frac{1}{2}m^2\varphi^2 - \left[\frac{1}{4!}\lambda + \frac{c_1}{\Lambda^2}m^2\right]\varphi^4 + \left[\frac{c_2}{\Lambda^2} - \frac{c_1}{\Lambda^2}\frac{\lambda}{3!}\right]\varphi^6 + \dots .\end{aligned} \tag{2.17}$$

On the significance of the dots The power counting of the EFT has been maintained going from $\mathcal{L}$ to $\mathscr{L}$, i.e. only retained dimension-six terms up to the suppression scale of $\mathscr{O}(\Lambda^2)$. Considering the eom of the *higher* order part of $\mathcal{L}$ would have induced terms of dimension-eight, i.e. $\mathscr{O}(\Lambda^4)$. This is another manifestation of the strenuous role of the power counting formula in organising EFT calculations.

Both $\mathcal{L}$ and $\mathscr{L}$ provide the same S-matrix elements. However, in the latter, the $\varphi^3\partial^2\varphi$ term has been eliminated at the price of redefining the coefficients of the φ^4 and φ^6 fields. The fewer operator of $\mathscr{L}$ makes the EFT computation easier. Equations of motion are usually applied to eliminate operator containing derivatives. In general, field redefinitions are often used to put EFT Lagrangians in canonical forms.

2.4. The SM EFT

SMEFT is a bottom-up approach EFT constructed of SM fields and respecting the SM symmetries and is used to analyse deviation from SM predictions in searching for BSM physics. Higher dimensional operators in SMEFT are generated at the scale Λ, which is the scale of new physics and is unknown a priori. Nevertheless, as seen in the previous discussions, one can still do systematic computations in SMEFT. The SMEFT Lagrangian can be written schematically as follows[5]:

$$\mathcal{L}_{\text{SMEFT}} = \mathcal{L}_{SM} + \sum_i \frac{c_i}{\Lambda^2}\mathcal{Q}_i^{dim-6} + \dots \tag{2.18}$$

[5] Where I have omitted the dimension-five SMEFT terms for them being not relevant to the discussion.

where the $\mathcal{L}_{SM}$ is the renormalisable SM Lagrangian containing dimension-two and dimension-four operators. It is worth noting that the dimension of an operator is usually determined from the field content of the term, ignoring possible dimensionful coupling constants. This section is devoted to discussing some key aspects of SMEFT, focusing on dimension-six operators in particular.

2.4.1. Basis

The fact that dimension-six operators characterise low-energy effects of heavy particles was already realised some time ago [38, 39]. The invariance of the S-matrix under fields redefinition concerted a vigorous effort towards using a complete and *non-redundant* set of operators. Eliminating these redundancies can be achieved using the classical equations of motion (as discussed in the example given in Sec. 2.3.1), integration by parts[6], Fierz identities, or even other methods. Starting from the set of dimension-six operators constructed from the SM fields. The minimal and non-redundant set of operators are referred to as *basis*. One construction of dimension-six operators, excluding flavour structure (assuming one fermion generation) and hermitian conjugates is referred to as the *Warsaw* basis and is given in Fig. 2.1 and Fig. 2.2 [40]. I will adopt this basis convention for the rest of the discussion. Stressing again, not all gauge and Lorentz invariant operators built out of SM fields must be present because some operators were declared redundant and eliminated. This construction of Ref. [40] was further extended in Ref. [41] to the three generations of fermions. Moreover, bases for dimension-seven have been constructed in Refs. [42, 43], and for dimension-eight in Refs. [43–46]. In dimension-five SMEFT, there is a single operator, usually denoted as the *Weinberg* operator [47]. After EWSB, the Weinberg operator generates neutrino masses and mixing, however it violates, the lepton number.

Bosonic operators and two-fermion operators Purely bosonic operators contain an even number of Higgs fields and even number of covariant derivatives D because Lorentz indices must be contracted. This only gives rise to dimension-six bosonic operators of the following forms:

$$\{X^3, X^2\varphi^2, X^2D^2, X\varphi^2D^2, \varphi^6, \varphi^4D^2, \varphi^2D^4\}, \tag{2.19}$$

[6] Terms related by a total derivative can vanish; in perturbation theory, total derivatives do not contribute to the S-matrix element.

X^3		φ^6 and $\varphi^4 D^2$		$\psi^2\varphi^3$	
Q_G	$f^{ABC}G_\mu^{A\nu}G_\nu^{B\rho}G_\rho^{C\mu}$	Q_φ	$(\varphi^\dagger\varphi)^3$	$Q_{e\varphi}$	$(\varphi^\dagger\varphi)(\bar{l}_p e_r \varphi)$
$Q_{\widetilde{G}}$	$f^{ABC}\widetilde{G}_\mu^{A\nu}G_\nu^{B\rho}G_\rho^{C\mu}$	$Q_{\varphi\Box}$	$(\varphi^\dagger\varphi)\Box(\varphi^\dagger\varphi)$	$Q_{u\varphi}$	$(\varphi^\dagger\varphi)(\bar{q}_p u_r \widetilde{\varphi})$
Q_W	$\varepsilon^{IJK}W_\mu^{I\nu}W_\nu^{J\rho}W_\rho^{K\mu}$	$Q_{\varphi D}$	$\left(\varphi^\dagger D^\mu\varphi\right)^\star\left(\varphi^\dagger D_\mu\varphi\right)$	$Q_{d\varphi}$	$(\varphi^\dagger\varphi)(\bar{q}_p d_r \varphi)$
$Q_{\widetilde{W}}$	$\varepsilon^{IJK}\widetilde{W}_\mu^{I\nu}W_\nu^{J\rho}W_\rho^{K\mu}$				
$X^2\varphi^2$		$\psi^2 X\varphi$		$\psi^2\varphi^2 D$	
$Q_{\varphi G}$	$\varphi^\dagger\varphi\, G_{\mu\nu}^A G^{A\mu\nu}$	Q_{eW}	$(\bar{l}_p\sigma^{\mu\nu}e_r)\tau^I\varphi W_{\mu\nu}^I$	$Q_{\varphi l}^{(1)}$	$(\varphi^\dagger i\overleftrightarrow{D}_\mu\varphi)(\bar{l}_p\gamma^\mu l_r)$
$Q_{\varphi\widetilde{G}}$	$\varphi^\dagger\varphi\,\widetilde{G}_{\mu\nu}^A G^{A\mu\nu}$	Q_{eB}	$(\bar{l}_p\sigma^{\mu\nu}e_r)\varphi B_{\mu\nu}$	$Q_{\varphi l}^{(3)}$	$(\varphi^\dagger i\overleftrightarrow{D}_\mu^I\varphi)(\bar{l}_p\tau^I\gamma^\mu l_r)$
$Q_{\varphi W}$	$\varphi^\dagger\varphi\, W_{\mu\nu}^I W^{I\mu\nu}$	Q_{uG}	$(\bar{q}_p\sigma^{\mu\nu}T^A u_r)\widetilde{\varphi}\, G_{\mu\nu}^A$	$Q_{\varphi e}$	$(\varphi^\dagger i\overleftrightarrow{D}_\mu\varphi)(\bar{e}_p\gamma^\mu e_r)$
$Q_{\varphi\widetilde{W}}$	$\varphi^\dagger\varphi\,\widetilde{W}_{\mu\nu}^I W^{I\mu\nu}$	Q_{uW}	$(\bar{q}_p\sigma^{\mu\nu}u_r)\tau^I\widetilde{\varphi}\, W_{\mu\nu}^I$	$Q_{\varphi q}^{(1)}$	$(\varphi^\dagger i\overleftrightarrow{D}_\mu\varphi)(\bar{q}_p\gamma^\mu q_r)$
$Q_{\varphi B}$	$\varphi^\dagger\varphi\, B_{\mu\nu}B^{\mu\nu}$	Q_{uB}	$(\bar{q}_p\sigma^{\mu\nu}u_r)\widetilde{\varphi}\, B_{\mu\nu}$	$Q_{\varphi q}^{(3)}$	$(\varphi^\dagger i\overleftrightarrow{D}_\mu^I\varphi)(\bar{q}_p\tau^I\gamma^\mu q_r)$
$Q_{\varphi\widetilde{B}}$	$\varphi^\dagger\varphi\,\widetilde{B}_{\mu\nu}B^{\mu\nu}$	Q_{dG}	$(\bar{q}_p\sigma^{\mu\nu}T^A d_r)\varphi\, G_{\mu\nu}^A$	$Q_{\varphi u}$	$(\varphi^\dagger i\overleftrightarrow{D}_\mu\varphi)(\bar{u}_p\gamma^\mu u_r)$
$Q_{\varphi WB}$	$\varphi^\dagger\tau^I\varphi\, W_{\mu\nu}^I B^{\mu\nu}$	Q_{dW}	$(\bar{q}_p\sigma^{\mu\nu}d_r)\tau^I\varphi\, W_{\mu\nu}^I$	$Q_{\varphi d}$	$(\varphi^\dagger i\overleftrightarrow{D}_\mu\varphi)(\bar{d}_p\gamma^\mu d_r)$
$Q_{\varphi\widetilde{W}B}$	$\varphi^\dagger\tau^I\varphi\,\widetilde{W}_{\mu\nu}^I B^{\mu\nu}$	Q_{dB}	$(\bar{q}_p\sigma^{\mu\nu}d_r)\varphi\, B_{\mu\nu}$	$Q_{\varphi ud}$	$i(\widetilde{\varphi}^\dagger D_\mu\varphi)(\bar{u}_p\gamma^\mu d_r)$

Figure 2.1.: All dimension-six operators in the Warsaw basis except for the four-fermion operators. The Table is taken from Ref. [40].

$(\bar{L}L)(\bar{L}L)$		$(\bar{R}R)(\bar{R}R)$		$(\bar{L}L)(\bar{R}R)$	
Q_{ll}	$(\bar{l}_p\gamma_\mu l_r)(\bar{l}_s\gamma^\mu l_t)$	Q_{ee}	$(\bar{e}_p\gamma_\mu e_r)(\bar{e}_s\gamma^\mu e_t)$	Q_{le}	$(\bar{l}_p\gamma_\mu l_r)(\bar{e}_s\gamma^\mu e_t)$
$Q_{qq}^{(1)}$	$(\bar{q}_p\gamma_\mu q_r)(\bar{q}_s\gamma^\mu q_t)$	Q_{uu}	$(\bar{u}_p\gamma_\mu u_r)(\bar{u}_s\gamma^\mu u_t)$	Q_{lu}	$(\bar{l}_p\gamma_\mu l_r)(\bar{u}_s\gamma^\mu u_t)$
$Q_{qq}^{(3)}$	$(\bar{q}_p\gamma_\mu\tau^I q_r)(\bar{q}_s\gamma^\mu\tau^I q_t)$	Q_{dd}	$(\bar{d}_p\gamma_\mu d_r)(\bar{d}_s\gamma^\mu d_t)$	Q_{ld}	$(\bar{l}_p\gamma_\mu l_r)(\bar{d}_s\gamma^\mu d_t)$
$Q_{lq}^{(1)}$	$(\bar{l}_p\gamma_\mu l_r)(\bar{q}_s\gamma^\mu q_t)$	Q_{eu}	$(\bar{e}_p\gamma_\mu e_r)(\bar{u}_s\gamma^\mu u_t)$	Q_{qe}	$(\bar{q}_p\gamma_\mu q_r)(\bar{e}_s\gamma^\mu e_t)$
$Q_{lq}^{(3)}$	$(\bar{l}_p\gamma_\mu\tau^I l_r)(\bar{q}_s\gamma^\mu\tau^I q_t)$	Q_{ed}	$(\bar{e}_p\gamma_\mu e_r)(\bar{d}_s\gamma^\mu d_t)$	$Q_{qu}^{(1)}$	$(\bar{q}_p\gamma_\mu q_r)(\bar{u}_s\gamma^\mu u_t)$
		$Q_{ud}^{(1)}$	$(\bar{u}_p\gamma_\mu u_r)(\bar{d}_s\gamma^\mu d_t)$	$Q_{qu}^{(8)}$	$(\bar{q}_p\gamma_\mu T^A q_r)(\bar{u}_s\gamma^\mu T^A u_t)$
		$Q_{ud}^{(8)}$	$(\bar{u}_p\gamma_\mu T^A u_r)(\bar{d}_s\gamma^\mu T^A d_t)$	$Q_{qd}^{(1)}$	$(\bar{q}_p\gamma_\mu q_r)(\bar{d}_s\gamma^\mu d_t)$
				$Q_{qd}^{(8)}$	$(\bar{q}_p\gamma_\mu T^A q_r)(\bar{d}_s\gamma^\mu T^A d_t)$
$(\bar{L}R)(\bar{R}L)$ and $(\bar{L}R)(\bar{L}R)$		B-violating			
Q_{ledq}	$(\bar{l}_p^j e_r)(\bar{d}_s q_t^j)$	Q_{duq}	$\varepsilon^{\alpha\beta\gamma}\varepsilon_{jk}\left[(d_p^\alpha)^T C u_r^\beta\right]\left[(q_s^{\gamma j})^T C l_t^k\right]$		
$Q_{quqd}^{(1)}$	$(\bar{q}_p^j u_r)\varepsilon_{jk}(\bar{q}_s^k d_t)$	Q_{qqu}	$\varepsilon^{\alpha\beta\gamma}\varepsilon_{jk}\left[(q_p^{\alpha j})^T C q_r^{\beta k}\right]\left[(u_s^\gamma)^T C e_t\right]$		
$Q_{quqd}^{(8)}$	$(\bar{q}_p^j T^A u_r)\varepsilon_{jk}(\bar{q}_s^k T^A d_t)$	Q_{qqq}	$\varepsilon^{\alpha\beta\gamma}\varepsilon_{jn}\varepsilon_{km}\left[(q_p^{\alpha j})^T C q_r^{\beta k}\right]\left[(q_s^{\gamma m})^T C l_t^n\right]$		
$Q_{lequ}^{(1)}$	$(\bar{l}_p^j e_r)\varepsilon_{jk}(\bar{q}_s^k u_t)$	Q_{duu}	$\varepsilon^{\alpha\beta\gamma}\left[(d_p^\alpha)^T C u_r^\beta\right]\left[(u_s^\gamma)^T C e_t\right]$		
$Q_{lequ}^{(3)}$	$(\bar{l}_p^j\sigma_{\mu\nu}e_r)\varepsilon_{jk}(\bar{q}_s^k\sigma^{\mu\nu}u_t)$				

Figure 2.2.: All dimension-six four-fermion operators in the Warsaw basis grouped according to their chirality structure. The Table is taken from Ref. [40].

where operators of these forms $\varphi^2 D^4$, $X\varphi^2 D^2$, and $X^2 D^2$ are reduced through eom to operators with two fermions or to the purely bosonic classes,

$$\{X^3, X^2\varphi^2, \varphi^6, \varphi^4 D^2\} \tag{2.20}$$

Moving to the classification of two-fermion operators, Lorentz invariance requires that fermion fields come in pairs. According to the Warsaw basis, the set of two-fermion basis are the following:

$$\{\psi^2\varphi^3, \psi^2 X\varphi, \psi^2\varphi^2 D\}. \tag{2.21}$$

The set of operators belonging to the forms shown in Eq. 2.20 and Eq. 2.21 are all presented in Fig. 2.1.

Four-fermion operators and Fierz identities Four-fermion operators are grouped according to their chirality structure and can be simplified using the so-called Fierz identities. I show a straightforward example of using Fierz identities to remove redundant four-fermion operators.

Considering gauge and Lorentz invariant made from $\bar{l}\gamma_\mu l$ bilinear. Only bilinears with γ_μ will be allowed because both l fields are left-handed. The l field can be SU(2) singlets or triplets, and therefore, the are two ways to write down the invariant;

$$\mathcal{Q}_{ll}^{(prst)} = (\bar{l}_i^{(p)}\gamma^\mu l^{(r)i})(\bar{l}_j^{(s)}\gamma_\mu l^{(t)j}) \tag{2.22}$$

$$\mathcal{Q}_{ll}^{3(prst)} = (\bar{l}_i^{(p)}\gamma^\mu [\tau^a]^i_j l^{(r)j})(\bar{l}_k^{(s)}\gamma_\mu [\tau^a]^k_m l^{(t)m}) \tag{2.23}$$

where i, j, k, m are weak SU(2) indices. Using the SU(2) Fierz identity,

$$[\tau^a]^i_j[\tau^a]^k_m = 2\delta^i_m\delta^k_j - \delta^i_j\delta^k_m, \tag{2.24}$$

the $\mathcal{Q}_{ll}^3$ operators can be written as follows:

$$\begin{aligned}
\mathcal{Q}_{ll}^{3(prst)} &= (\bar{l}_i^{(p)}\gamma^\mu l^{(r)j})(\bar{l}_k^{(s)}\gamma_\mu l^{(t)m})(2\delta^i_m\delta^k_j - \delta^i_j\delta^k_m) \\
&= 2\delta^i_m\delta^k_j(\bar{l}_i^{(p)}\gamma^\mu l^{(r)j})(\bar{l}_k^{(s)}\gamma_\mu l^{(t)m}) - \delta^i_j\delta^k_m(\bar{l}_i^{(p)}\gamma^\mu l^{(r)j})(\bar{l}_k^{(s)}\gamma_\mu l^{(t)m}) \\
&= 2(\bar{l}_i^{(p)}\gamma^\mu l^{(r)k})(\bar{l}_k^{(s)}\gamma_\mu l^{(t)i}) - (\bar{l}_i^{(p)}\gamma^\mu l^{(r)i})(\bar{l}_k^{(s)}\gamma_\mu l^{(t)k}),
\end{aligned} \tag{2.25}$$

and then conveniently ($k \to j$) written as:

$$\mathcal{Q}_{ll}^{3(prst)} = 2(\bar{l}_i^{(p)}\gamma^\mu l^{(r)j})(\bar{l}_j^{(s)}\gamma_\mu l^{(t)i}) - (\bar{l}_i^{(p)}\gamma^\mu l^{(r)i})(\bar{l}_j^{(s)}\gamma_\mu l^{(t)j}). \tag{2.26}$$

Now one can apply the spinor Fierz identity on the first term of Eq. 2.25,

$$(\overline{\psi}_1\gamma^\mu P_L\psi_2)(\overline{\psi}_3\gamma_\mu P_L\psi_4) = (\overline{\psi}_1\gamma^\mu P_L\psi_4)(\overline{\psi}_3\gamma_\mu P_L\psi_2), \tag{2.27}$$

which can be written in terms of the SU(2) singlet as follows:

$$\mathcal{Q}_{ll}^{3} = 2(\bar{l}_i^{(p)}\gamma^\mu l^{(t)i})(\bar{l}_j^{(s)}\gamma_\mu l^{(r)j}) - (\bar{l}_i^{(p)}\gamma^\mu l^{(r)i})(\bar{l}_j^{(s)}\gamma_\mu l^{(t)j}) = 2\mathcal{Q}_{ll}^{(ptsr)} - \mathcal{Q}_{ll}^{(prst)}, \tag{2.28}$$

manifesting $\mathcal{Q}_{ll}^3$ is just a linear combination of $\mathcal{Q}_{ll}$. This is the reason why $\mathcal{Q}_{ll}^3$ is not included in the $(\overline{L}L)(\overline{L}L)$ four-fermion operators of Fig. 2.2, where all the dimension-six four-fermion operators in the Warsaw basis are presented.

2.4.2. Phenomenology of operators

Higher dimensional operators can lead to deviations from the SM interactions in two ways, either through the modification of SM couplings, i.e. corrections to the coupling strength for the SM-like interactions, or through introducing new interactions which are not present in the SM. In this section, I briefly discuss some phenomenology aspects of the different dimension-six operators.

In the Warsaw basis, the are four X^3 operators, two of which are CP-even and two are CP-odd, each containing three field strengths as depicted in Fig. 2.3. Examples of

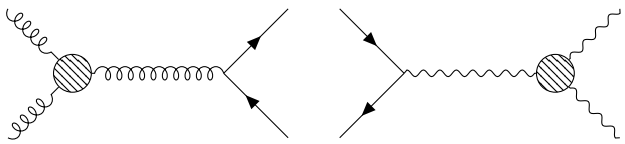

Figure 2.3.: Representative diagrams of the X^3 operators insertions depicted by the shaded blobs.

these operators are ones with three gluon field strengths that can be well constrained in multijet production studies [48, 49]. Moreover, although not as strongly, they can also be well constrained in four top quark production. Operators involving three weak gauge fields strength are constrained in diboson production [50–54].

The φ^6 operator involves six Higgs fields. After EWSB, the structure of these operators leads to introducing an H^6 interaction to the SM.

The $\varphi^4 D^2$ operators modify the Higgs boson coupling to the EW gauge bosons. These operators contribute to the Higgs production via vector boson fusion, where they can potentially modify the HZZ coupling, as depicted in the *left* diagram of Fig. 2.4. It is worth noting that, in general, operators involving Higgs fields, because of the Goldstone degrees of freedom, can potentially connect to amplitudes involving the longitudinally polarised W and Z bosons.

The $X^2\Phi^2$ operators involve gauge field strengths and Higgs fields. This leads to interactions like $gg \to h$, as displayed in the *right* diagram of Fig. 2.4, and $h \to \gamma\gamma$, which in the SM can only take place at the one-loop-level [55, 56].

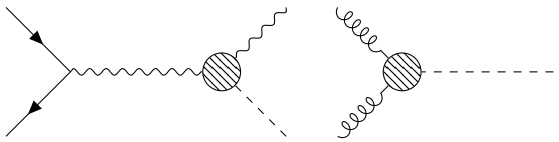

Figure 2.4.: Same as Fig. 2.3 but for the $\varphi^4 D^2$ operator (*left*), and the $X^2\varphi^2$ operator (*right*).

The $\psi^2\varphi^3$ operators violate the relation between the Higgs boson coupling and fermions, i.e. they violate the Yukawa-coupling-mass proportionality. In acquiring vev, the extra term, $(\varphi^\dagger\varphi)$, from the EFT operators, shifts the Yukawa interactions. The top quark pair production in association with the Higgs boson, $t\bar{t}H$ is one primary process where these operators enter, as shown in the *left* diagram of Fig. 2.5. It is also worth mentioning that these operators break the $\mathrm{U}(3)^5$ symmetry (a topic later discussed in Sec. 2.5.1).

The so-called dipole operators $\psi^2 X\varphi$ involve two-fermion fields, a gauge field strength and a Higgs field. These operators enter many different processes, one example is again the $t\bar{t}H$ production where they can affect the initial state gluon interaction to the top quark as depicted in the *right* diagram of Fig. 2.5. Similar to

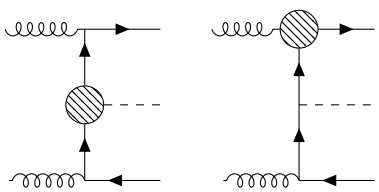

Figure 2.5.: Same as Fig. 2.3 but for the $\psi^2\varphi^3$ operator (*left*) and the $\psi^2 X\varphi$ operator (*right*).

$\psi^2\varphi^3$ operators, this set of operators also violate the $\mathrm{U}(3)^5$ symmetry.

The $\psi^2\varphi^2 D$ operators modify the coupling of EW gauges bosons to fermions, for example they modify interactions like $Z \to ll$ as shown in the *left* diagram of Fig. 2.6.

Finally, four-fermion operators, ψ^4, depicted in Fig. 2.6, from which four are baryon-number-violating, can be highly constrained in proton decay studies (proton decays violate baryon number). Mixed chirality ψ^4 operators also break the $\mathrm{U}(3)^5$ symmetry.

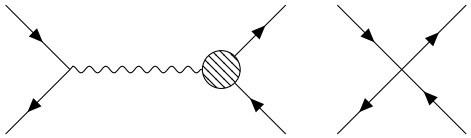

Figure 2.6.: Same as Fig. 2.3 but for the $\psi^2\varphi^2 D$ operator (*left*) and the ψ^4 *contact* operator (*right*).

Moreover, in one flavour assumption of SMEFT, a topic later discussed, these operators can also be highly constrained in four top quark production.

2.5. On constraining the coefficients

The EFT model independence comes at the cost of a large number of SMEFT WCs which are a priori unknown by the EFT bottom-up approach construction. Therefore, these effective coefficients must be determined from experimental measurements. In the dimension-six SMEFT, the total number of operators in the absence of any flavour symmetry, i.e. including the three generations of fermions, are 2499 [41]. This number represents all CP-even and CP-odd $\Delta B = \Delta L = 0$ operators, where $\Delta B = \Delta L = 0$ indicate operators conserving baryon and lepton numbers. In the absence of flavour structure, i.e. assuming only one generation of fermions, this number reduces to a total of 76 CP-even and CP-odd $\Delta B = \Delta L = 0$ operators. In our discussion above, we have used the classification of dimension-six operators according to [40], in which they include a total of 59 CP-even and CP-odd $\Delta B = \Delta L = 0$ operators, split into 15 bosonic operators, 19 single-fermionic current ones, and 25 four-fermion ones. Relaxing the $\Delta B = 0$ constrain increases the number of operators to 63. This classification of Ref. [40] is one widely used in the literature.

Global fits aim to constrain the WCs by fitting them to the data available from the LHC and other particle physics experiments. There is a vigorous effort in the community in performing these global studies [57–62]. The reason for these studies being *global* is that they must consider all available datasets. This is because one WC may contribute to multiple measurements. Moreover, ignoring a subset of coefficients

in simplifying the fitting procedure may spoil the EFT model independence and introduce an inherent scale dependence.

Interlude: on renormalisation group equations As previously mentioned, EFTs are non-renormalisable theories and can only be renormalised order by order in $1/\Lambda$. One convenient choice in QFTs is to use a mass-independent regularisation and renormalisation scheme. In turn, these schemes introduce a scale dependence in the WCs. The example in Sec. 2.2.2 discussed the use of dimension-six counter-terms in renormalising loop diagrams with two dimension-five insertions. In such case, and because of using mass-independent scheme, a $c(\mu)$ dependence is introduced, where μ denotes some relevant scale. This coefficient will evolve with μ according to renormalisation group equations (RGE),

$$\mu \frac{dc_i}{d\mu} = \gamma_{ij} c_j \tag{2.29}$$

where γ_{ij} is the so-called anomalous-dimension matrix. While $c(\mu)$ can vanish at some certain μ (or by symmetry arguments), it is still a scale-dependent coefficient. This renders arbitrarily setting $c = 0$ a scale-dependent statement.

For example, in doing one-loop matching, which requires scale-dependent coefficients for renormalisation, if one is interested in computing observables at lower scales, then RGE should be used to run the coefficients down. Realistically, in having multiple operators, they mix in their running down. The anomalous-dimension matrix in the RGE equation encodes this mixing.

2.5.1. Flavour assumption

The universality of the quarks and fermions flavours can be achieved through respecting the $\mathrm{U}(3)^5$ symmetry assumption,

$$U(3)^5 \equiv SU(3)_q \times SU(3)_u \times SU(3)_d \times SU(3)_l \times SU(3)_e \times U(1)^5, \tag{2.30}$$

where the fermion representations transform under the $\mathrm{SU}(3)$ rotations. Imposing such symmetry is a common approach to practically deal with the enormous number of operators should we consider all the different fermions flavours in the SM. According to the Minimal Flavour Violation (MFV) hypothesis [63, 64], in the SM, no sources of flavour violation exist beyond the SM Yukawa couplings, i.e. *only* Yukawa interactions in the SM break the $\mathrm{U}(3)^5$ symmetry.

SMEFT operators can also be classified according to their $\mathrm{U}(3)^5$ respecting. Imposing the same symmetry in SMEFT reduces the 59 operators of Ref. [40] to 42, since also operators with Yukawa interactions violate $\mathrm{U}(3)^5$.

A more relaxed flavour assumption which is used across the studies presented in this thesis is the following:

$$U(3)_l \times U(3)_e \times U(2)_q \times U(2)_u \times U(3)_d \equiv U(2)^2 \times U(3)^3, \tag{2.31}$$

which singles out the top quark interactions from the global symmetry assumption, and therefore such assumption is mainly used in SMEFT studies with a particular interest in top quark operators. This minimal relaxation give rise to chirality flipping operators, i.e. $\psi^2\varphi^3$ and $\psi^2 X\varphi$, since the latter and even though included in the one-fermion generation SMEFT basis, they break the $\mathrm{U}(3)^5$ symmetry. Furthermore, such relaxation of the symmetry allows the third generation quark doublet and right-handed top quark fields to receive independent modifications to their couplings to gauge bosons via the $\psi^2\varphi^2 D$ operators.

2.5.2. Input schemes

The dynamics of the SM are dependent on 19 parameters whose numerical values are expected to be established only by experiments. The subset of these parameters inherent to the SM EW sector are the masses of the W and Z bosons, m_W and m_Z, the $\mathrm{SU}(2)$ and $\mathrm{U}(1)$ gauge couplings introduced, g and g', respectively, the Fermi constant G_F, and the Higgs field vev, v. After EWSB, the independent $\mathrm{SU}(2)$ and $\mathrm{U}(1)$ gauge couplings are absorbed into the fine structure coupling constant, α. While α is already precisely determined from low-energy processes, the extraction of $\alpha(m_Z)$ is needed for studying EW processes.

In performing a SMEFT fit, theoretical predictions of observables are given in terms of the SM input parameters and the EFT coefficients. Due to this shared dependence, the SM and EFT parameters can be simultaneously determined from fitting to data. Adopting a choice on which input parameters to use in the fit is the so-called *EW input scheme*, see for e.g. [65]. The choice of inputs is already used calculating the theoretical predictions before performing the fit. In SMEFT computations, the complexity arises from the input parameters dependence on the EFT coefficients. This will result in indirect constraints on the corresponding operators even if they are not necessarily relevant to the problem.

Chapter 3.

Examples of top quark studies

This chapter is a brief introduction to top quark physics. It provides introductory discussions on a selection of top-quark-related studies which illustrate some recent improvements in theoretical predictions as well as the interpretation of LHC data in the context of SMEFT. These studies were selected based on their novelty as well as their relation to the original work presented in the following chapters of this thesis. Sec. 3.1 serves as a brief introduction to top quark physics. In Sec. 3.2, the theoretical improvements in the computation of the $t\bar{t}W$ production process and the corresponding most recent measurement by the CMS collaboration are presented. Sec. 3.3 introduces the theoretical basis of top quark spin polarisation measurements, followed by a discussion on the most recent corresponding ATLAS measurement. In Sec. 3.4, the EFT interpretation of CMS measurement of anomalous top quark coupling in the $t\bar{t}\gamma$ production process is presented.

3.1. On the top quark

The top quark is the most massive of all observed elementary particles. In 1995, the top quark was discovered by the CDF and DØ collaborations [66, 67]. The mass of the top quark, m_t, is measured to be around 173 GeV. In the SM, the coupling of the top quark to the Higgs boson, the top-Yukawa coupling, y_t, follows the relation $y_t = \sqrt{2}(m_t/v)$ where $v \simeq 246$ GeV is the vev of the Higgs field. Given the direct measurement of the top quark mass, the coupling y_t is very close to unity; which is, in the SM, the strongest coupling at the scale of the weak interactions and above; hinting at a unique role for the top quark in the EWSB. Since the top quark is heavier than the W boson, it decays semi-weakly, i.e., into a real W boson and a b quark. This contrasts with other SM quarks that decay through a virtual W boson emission. This decay of the top quark allows it a short lifetime of roughly $5\text{x}10^{-25}$ seconds, further allowing it to

decay before hadronising. This feature provides a remarkable opportunity to study a "bare" quark as it is the only known quark not to form bound states. For the reasons mentioned above, the top quark is believed to play a special role in the SM and many of its extensions, making top quark physics a unique avenue where the understanding of the strong interactions and EWSB can be tested.

In hadronic collisions of multi-TeV centre-of-mass energies, the most common top quark production is the QCD top-antitop quark pair production (for short, referred to as "top quark pair" production). At the parton level, the top quark pair production mechanisms are gluon fusion and quark-antiquark annihilation, as depicted by the diagrams in Fig. 3.1. Single top quark production (discussed thoroughly in Sec. 3.3), in contrast, takes place through charged current interactions, as shown in Fig. 3.2. The production rate for single top quarks is suppressed with respect to top quark pair production by a factor of $\sim$ 2-3 corresponding to the ratio of the strong and weak interactions coupling strengths, α_s and α_w, respectively.

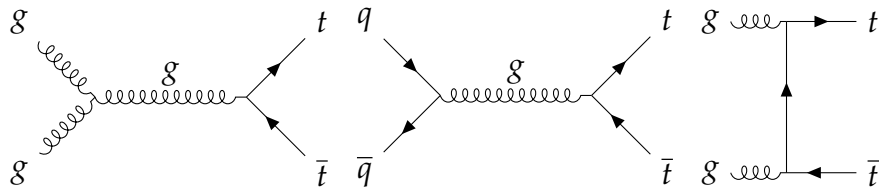

Figure 3.1.: Diagrams for the LO top quark pair production at the LHC.

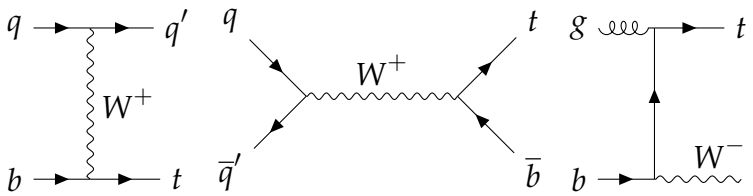

Figure 3.2.: Representative diagrams for the LO single top quark production at the LHC. All modes of single top quark production are presented. From *left* to *right*, the *t*-channel production through the exchange of a space-like W boson, the *s*-channel production through the exchange of a time-like W boson, and the associated production of a top quark with an on-shell W boson.

Through precise measurements of the top quark's properties, e.g. mass and coupling, essential information can be attained on the fundamental interactions at the EWSB scale and beyond. While these extensively studied top quark properties can further test the SM hypothesis, they can also discriminate between competing theories of BSM physics. The different measurements presented in this chapter show that

BSM effects can indirectly affect top quark physics. The EFT approach discussed in Chap. 2 is used to describe such physics, hinting at where potentially indirect effects of BSM physics can be observed. The guiding principles for interpreting top quark measurements at the LHC in the context of SMEFT have been established in Ref. [68].

As previously mentioned, the topics chosen in this chapter are mainly motivated by their relation to the main discussion of the thesis. The $t\bar{t}W$ process is one of the main background contributions to the $t\bar{t}H$ and $t\bar{t}t\bar{t}$ multilepton signals. The improved $t\bar{t}W$ calculation presented in Sec. 3.1, therefore, would potentially aid in the background modelling for the corresponding measurements. Moreover, and while also interesting from a theoretical point of view, the top quark spin polarisation and the $t\bar{t}\gamma$ measurements presented in Sec. 3.3 and Sec. 3.4, respectively, provide complementary bounds on WCs relevant to the $t\bar{t}H$ and the tWZ processes. The studies of both the latter, together with the $t\bar{t}t\bar{t}$ process, are the primary constituents of this thesis.

3.2. Top quark pair production in association with a W boson

The top quark pair production associated with a massive weak vector boson is an ongoing investigation by the ATLAS and CMS collaborations. The inclusive measurements at $\sqrt{s}$ =13 TeV for both $t\bar{t}Z$ and $t\bar{t}W$ are reported in Refs. [69,70]. In both processes, there is an agreement between theoretical predictions and the inclusive measurements; however, with a slightly higher measured cross-section for the $t\bar{t}W$ process. It is worth noting that the contributions from $t\bar{t}W$ and $t\bar{t}Z$ processes are dominant backgrounds to the $t\bar{t}H$ [71] and the $t\bar{t}t\bar{t}$ analyses [72]. This imposes the necessity of precise modelling of such major background for it to be properly subtracted, particularly in the multilepton signatures for which the tension mentioned above has been reported in both the $t\bar{t}H$ and the $t\bar{t}t\bar{t}$ analyses efforts. This observed discrepancy between the theoretical predictions and the measurement has led to using a normalisation factor of $\sim$1.5 for the $t\bar{t}W$ background in the $t\bar{t}H$ analysis of Ref. [71], whereas the $t\bar{t}t\bar{t}$ analysis required a normalisation factor of $\sim$1.6 [72]. This discrepancy also induces significant systematic uncertainties for the experimental analyses in the multilepton signal regions. To that end, several $t\bar{t}W$ theoretical calculations and studies have been performed aiming at a more precise theoretical understanding of the process [73–84].

In the discussion of those theoretical efforts toward the understanding of the $t\bar{t}W$ process, the notation of Refs. [9,73,85] is followed to present the FO multi-coupling

expansion of a generic observable Σ for the process $pp \to t\bar{t}V(+X)$ in the powers of α_s and α_w,

$$\Sigma^{t\bar{t}V}(\alpha_s, \alpha_w) = \sum_{m+n\geq 2} \alpha_s^m \alpha_w^{n+1} \Sigma^{t\bar{t}V}_{m+n+1,n}, \tag{3.1}$$

where X indicates an extra QCD or QED radiation and m and n are positive integers. The contributions at LO constrain the sum of the integers to $m+n=2$ and involve only tree-level diagrams. On the other hand, NLO corrections correspond to terms with $m+n=3$ and are induced by the interference among all the possible one-loop and tree-level Born diagrams as well among all the possible tree-level diagrams involving one additional quark, gluon or photon in the final state. The $t\bar{t}V$ observables at LO, $\Sigma^{t\bar{t}V}_{\text{LO}}$, can be expanded as follows:

$$\begin{aligned}\Sigma^{t\bar{t}V}_{\text{LO}} &= \alpha_s^2\alpha_w \Sigma^{t\bar{t}V}_{3,0} + \alpha_s\alpha_w^2 \Sigma^{t\bar{t}V}_{3,1} + \alpha_w^3 \Sigma^{t\bar{t}V}_{3,2} \\ &\equiv \Sigma_{\text{LO}_1} + \Sigma_{\text{LO}_2} + \Sigma_{\text{LO}_3}.\end{aligned} \tag{3.2}$$

Similarly, the NLO corrections reads

$$\begin{aligned}\Sigma^{t\bar{t}V}_{\text{NLO}} &= \alpha_s^3\alpha_w \Sigma^{t\bar{t}V}_{4,0} + \alpha_s^2\alpha_w^2 \Sigma^{t\bar{t}V}_{4,1} + \alpha_s\alpha_w^3 \Sigma^{t\bar{t}V}_{3,2} + \alpha_w^4 \Sigma^{t\bar{t}V}_{4,3} \\ &\equiv \Sigma_{\text{NLO}_1} + \Sigma_{\text{NLO}_2} + \Sigma_{\text{NLO}_3} + \Sigma_{\text{NLO}_4}.\end{aligned} \tag{3.3}$$

The complete NLO calculation of Ref. [73] has shown that the $t\bar{t}W$ NLO EW ($\alpha_s^2\alpha_w^2$) corrections reduce the LO cross-section by $\sim -4\%$, while the dominant subleading EW corrections ($\alpha_s\alpha_w^3$) increase it by $\sim 12\%$. These large contributions at $\mathcal{O}(\alpha_s\alpha_w^3)$ arise from the $tW \to tW$ scattering diagrams [74] presented in Fig. 3.3, a conclusion that further indicates the complexity of this process and the necessity of a complete understanding of $t\bar{t}W$.

One study on the structure of the higher-order contributions in the $t\bar{t}W$ process suggests a $\sim 10\%$ increase in the cross-section expected from ($\alpha_s^4\alpha_w$), a coupling order which is already at the level of next-to-next-leading order (NNLO) accuracy [86]. Since an NNLO calculation is not yet available due to its complexity, one way of capturing parts of these contributions is using multi-jet merging at NLO. Merging is the procedure of combining matrix elements characterised by different multiplicities in MC simulations, a detailed discussion on the topic is in Ref. [87]. A real emission radiation can be a jet attached to a QCD vertex (j_{QCD}) or one that is attached to an EW vertex to the W boson (j_{weak}), in a collinear (and) or soft limit. The QCD

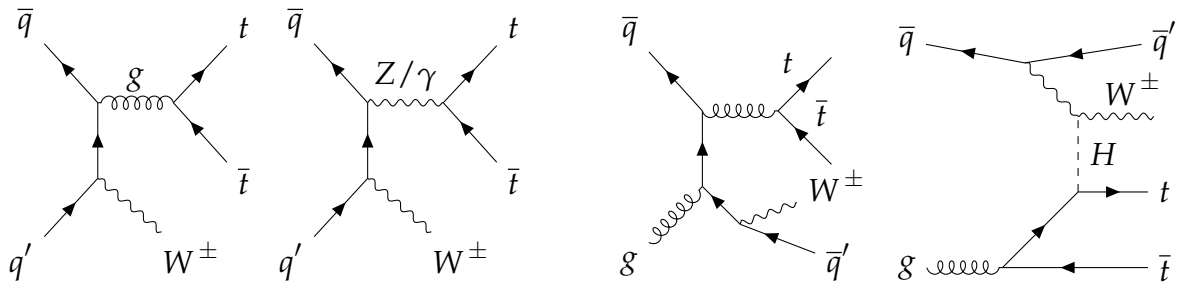

Figure 3.3.: Representative diagrams for two Born $t\bar{t}W$ amplitudes contributing to Σ_{LO_1} and Σ_{LO_3}*(left)*, and two NLO real emission $t\bar{t}W^{\pm}\bar{q}'$ amplitudes contributing to Σ_{NLO_1} and Σ_{NLO_3}, where the latter involves the $tW \to tW$ scattering.

splitting functions[1] of $pp \to t\bar{t}W$ allow the inclusion of j_{QCD} emissions via the parton shower (PS); this is, however not the case for the weak jets configuration. At LO and through `MadGraph5`, the weak jets configuration is excluded from the merging procedure and instead treated as independent finite contributions. The merging procedure has been upgraded within `MadGraph5` for NLO calculations in QCD using the so-called `FxFx` framework [87], at which point these said separations were not yet considered. The `FxFx` framework has been further extended in [88] to correctly account for the separation of weak jets, and thus $t\bar{t}Wj_{\mathrm{weak}}$ contributions hereafter referred to as the "improved merging".

The CMS collaboration has recently measured the $t\bar{t}W$ production cross-section in pp collisions at a centre-of-mass energy $\sqrt{s} = 13$ TeV using a recorded data sample corresponding to 138 fb^{-1} of integrated luminosity [89]. This analysis has been performed for events with two or three leptons, electrons or muons, and additional jets. The measured cross-section amounts to $868 \pm 40(\mathrm{stat})^{+52}_{-50}(\mathrm{syst})$ fb. The Monte-Carlo (MC) simulation used in the analysis included terms corresponding to the Σ_{LO_3} and the Σ_{NLO_3} contributions from Eq. 3.2 and Eq. 3.3, respectively. The cross-section used to normalise the $t\bar{t}W$ prediction is the one of Ref. [77] computed to NLO+next-to-next-leading-log (NNLL) accuracy. In Fig. 3.4 a comparison between the measured $t\bar{t}W$ cross-section and the theoretical prediction used for normalising the number of events in the MC simulation, as well as to the one evaluated using the improved merging of Ref. [88] is presented.

The measured cross-section from the combination of all the investigated leptonic channels still exhibits the previously mentioned tension compared to the theoretical prediction. Nevertheless, the comparison against the prediction using the improved

[1] QCD splitting functions provide the mechanism for handling non-cancelled collinear divergences arising from the radiation of massless partons from one of the incoming partons.

merging procedures suggests the necessity of the correct accounting of weak jet configurations in the NLO merging.

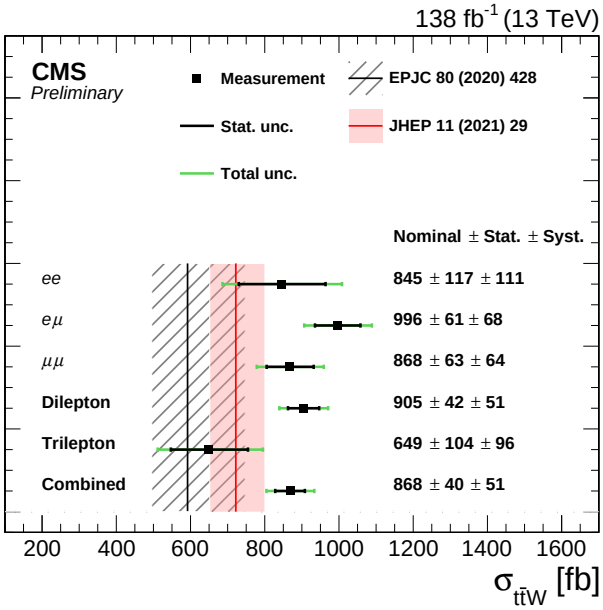

Figure 3.4.: Measured cross-sections for the $t\bar{t}W$ production in different final states compared to theoretical predictions of Refs. [77, 88]. The cross-sections are measured in the ee, $e\mu$, and $\mu\mu$ dilepton final states and in the trilepton channel. The cross-section obtained from the combination of all channels is also presented. The figure is taken from Ref. [89].

Due to the valence quark effects[2] in pp collision, an enhancement of the $t\bar{t}W^+$ cross-section is expected when compared to $t\bar{t}W^-$. This expected feature renders the separate measurement of $t\bar{t}W^+$ and $t\bar{t}W^-$ of particular importance since it provides information on the PDF of the proton. In the same CMS measurement, the cross-section of both processes was measured, and their ratio in a simultaneous fit was calculated. The measured ratio $R_{t\bar{t}W^+/t\bar{t}W^-}$ is reported as $1.61^{+0.15}_{-0.14}(\text{stat})^{+0.07}_{-0.05}(\text{syst})$ whereas the predicted value from Ref. [76] is $R^{\text{TH.}}_{t\bar{t}W^+/t\bar{t}W^-} = 1.94^{+0.37}_{-0.24}$. Therefore, the ratio measurement is found to agree with the SM predictions.

[2] Valence quarks are the quarks constituting the quantum number of a hadron. The proton has three valence quarks, two up and one down quark. Since there are twice more up-quarks than down-quarks in the proton's parton distribution function (PDF), the ttW measurement leads to more ttW^+ measured events compared to ttW^- events.

3.3. Top quark polarisation in the t-channel single production

Three main single top quark production channels are the t-channel production through the exchange of a space-like W boson, the s-channel production through the exchange of a time-like W boson, and the associated production of a top quark with an on-shell W boson, all shown in Fig. 3.2. All single top quark production channels are connected directly to the EW vertex tWb, so they can be used to measure the Cabibbo-Kobayashi-Maskawa (CKM) matrix element, V_{tb}. Moreover, single top quark production can be sensitive to BSM physics; one way is through the modified structure of the Wtb vertex, a topic discussed later in the EFT interpretation section.

3.3.1. Polarisation measurement

The CMS collaboration at the LHC has measured the t-channel single top quark cross-section at $\sqrt{s} = 13$ TeV in pp collisions inclusively [90] and differentially [91]. The top quark polarisation in the t-channel production has also been measured by the ATLAS collaboration [92]. The measurement set bounds on the Wtb SMEFT dipole operator. The theoretical motivation and the measurement results constitute this section's main topic.

At a hadron collider, the dominant mechanism for single top quark production is through t-channel exchange of a W boson. Therefore, it is worth breaking down the t-channel production diagrams into two sub-processes, a dominant sub-process and a sub-dominant one. The dominant sub-process is the scattering of an incoming up type (down type) quark from a bottom quark (antiquark) through the W boson exchange producing a down type (up type) *spectator* quark and a top quark (antiquark) as presented in the two most *left* diagrams of Fig. 3.5. The subdominant process, on the other hand, proceeds with the scattering of a down type (up type) antiquark from a bottom quark (antiquark), producing an up type (down type) spectator antiquark and a top quark (antiquark), as shown in the two most *right* diagrams of Fig. 3.5.

In contrast to QCD top quark pair production, where the top quarks produced are non-polarised due to parity conservation, single top quarks are always produced via the left-handed EW interaction and therefore polarised. This impacts the produced top quark's spin direction and, in turn, the spin of its decay products. Therefore, it is worth introducing the basics of top quark polarisation before presenting the corresponding experimental measurement. The following density matrix can describe the state of an

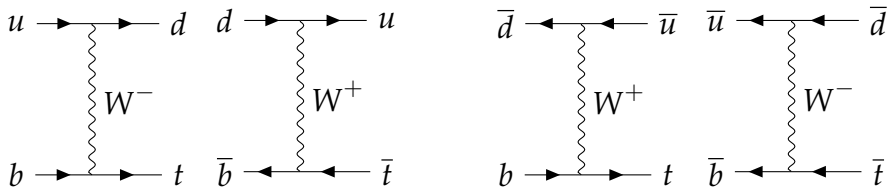

Figure 3.5.: The two *left* diagrams show the dominant sub-process of single (anti) top quark t-channel production at the LHC, while the two *right* show the sub-dominant ones. The diagrams shown are in the five-flavour scheme (5FS), where the b quarks are included in the PDF of the colliding protons. The t-channel production of a single top quark in the four-flavour scheme (4FS) proceeds as $qg \to q' t\bar{b}$ exploiting gluon splitting in the initial state.

ensemble of polarised top quarks,

$$\rho = \frac{1}{2}[\mathrm{I} + \vec{P}.\vec{\sigma}], \tag{3.4}$$

where I is the identity matrix, $\vec{P}$ is a vector in three-dimensional space, and $\vec{\sigma}$ is the Pauli vector[3]. Introducing the reference frame (x, y, z), the density matrix ρ can be written as follows:

$$\rho = \frac{1}{2}\begin{pmatrix} 1 + P_z & P_x - iP_y \\ P_x + iP_y & 1 - P_z \end{pmatrix}, \tag{3.5}$$

with eigenvalues $\lambda_{\pm} = \frac{1}{2}[1 \pm |\vec{P}|]$. The following constraints on $|\vec{P}|$ are in order: $|\vec{P}| \leq 1$, and $|\vec{P}| = 1$ only and only if the top quarks are produced in pure spin states. The vector $\vec{P}$ is a Bloch vector. A Bloch vector indicates the point within a sphere which corresponds to a given state; a Bloch sphere. A Bloch sphere is a geometrical representation of the state space of a two-level quantum mechanical system. The surface of the Bloch sphere represents all the pure states; hence the constraint $|\vec{P}| = 1$ for top quarks produced in pure spin states, whereas the interior of the sphere, $|\vec{P}| < 1$, corresponds to all the mixed states. The components of $\vec{P}$ can be calculated as the expectation value of the Pauli matrices,

$$\vec{P} = \mathrm{Tr}(\rho\vec{\sigma}) = \langle\vec{\sigma}\rangle, \tag{3.6}$$

[3] The Pauli vector is defined as $\vec{\sigma} = \sigma_1\hat{k1} + \sigma_2\hat{k2} + \sigma_3\hat{k3}$ where σ_i with $i = 1, 2, 3$ are the Pauli matrices representing the observable corresponding to spin along the k^{th} coordinate axis in three-dimensional Euclidean space.

where $P_i = 2\langle S_i \rangle$ for $i = x, y, z$ with S representing the the spin operators[4]. The component P_i represents the expectation value of the spin operators, in other words, the polarisation of the top quark along the i^{th} axis coordinate. The definitions of the coordinates in terms of the process of interest are as follows. The $\hat{z}$-direction is taken as the direction of the spectator quark's three-momentum $\vec{p}_s$. The $\hat{y}$-direction is taken to be orthogonal to both $\vec{p}_s$ and the initial quark's three momentum $\vec{p}_i$. The $\hat{x}$-direction is determined such that the coordinate system is right-handed,

$$\hat{z} = \frac{\vec{p}_s}{|\vec{p}_s|}, \qquad \hat{y} = \frac{\vec{p}_s \times \vec{p}_i}{|\vec{p}_s \times \vec{p}_i|}, \qquad \hat{x} = \hat{y} \times \hat{z}, \tag{3.7}$$

where $\vec{p}_s$ and $\vec{p}_i$ in the top quark's rest frame.

The expected values of the polarisation of the top quarks and antiquarks at LO accuracy in the SM were computed to be $P_{\hat{z}}^{(t)} = 0.90$ and $P_{\hat{z}}^{(\bar{t})} = -0.86$ [93] along the direction of the spectator quark. In the NNLO calculation of Ref. [94], the predicted top quark polarisation components were reported to be $P_{\hat{z}}^{(t)} = 0.965$ and $P_{\hat{z}}^{(\bar{t})} = -0.957$. The measurement performed by the ATLAS collaboration in Ref. [92] used $\sqrt{s}$ = 13 TeV pp collision data that amounts to a total integrated luminosity of 139 fb^{-1}. The analysis reports a high polarisation along (against) the direction of the spectator quark in the top quark (antiquark) rest frame. The three measured polarisation components for the top quark and the antitop quark are reported as follows:

$$\vec{P} = (P_{\hat{x}}, P_{\hat{y}}, P_{\hat{z}}) = (0.01, -0.029, 0.91)(t) \tag{3.8}$$

$$\vec{P} = (P_{\hat{x}}, P_{\hat{y}}, P_{\hat{z}}) = (-0.02, -0.007, -0.79)(\bar{t}), \tag{3.9}$$

and presented in Fig. 3.6 in a two-dimensional parameter space $(P_{\hat{z}}, P_{\hat{x}})$ with their statistical-only and statistical-and-systematic contours at 68% CL reported.

3.3.2. Sensitivity to EFT

As previously mentioned, the modified structure of the Wtb vertex can be one way to use single top quark production as a probe for new physics beyond the SM. A systematic approach for testing the presence of effects from a modified Wtb coupling is to exploit the framework SMEFT. Assuming massless b quarks, i.e. the 5FS, in single top quark production, the relevant dimension-six SMEFT operators are the

[4] The spin operators are defined as the Pauli matrices normalised by the factor $\hbar/2$. In using natural units where $\hbar = 1$, $S_i = \frac{1}{2}\sigma_i$ and so $\langle \sigma_i \rangle = 2\langle S_i \rangle$, hence $P_i = 2\langle S_i \rangle$.

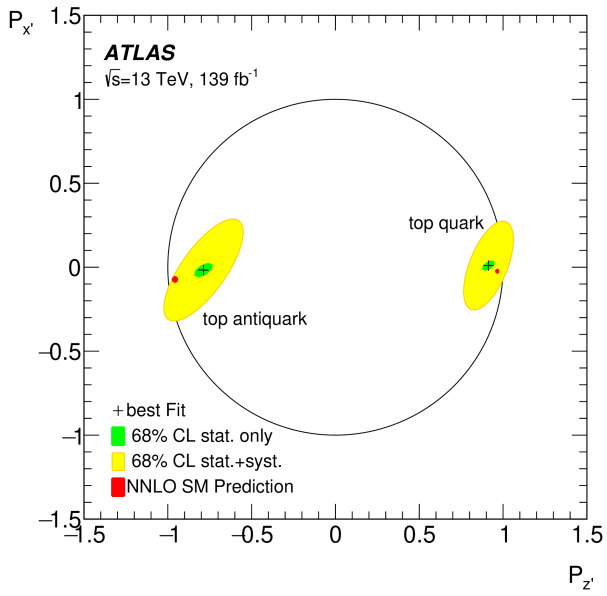

Figure 3.6.: The observed best fit polarisation measurement reported with statistical-only and statistical-and-systematic contours at 68% CL. The results are plotted in the two-dimensional parameter space $(P_{\hat{z}}, P_{\hat{x}})$. The red point represents the NNLO SM prediction based on Ref. [94]. The figure is taken from Ref. [92].

following [40, 95–97]:

$$\begin{aligned}
\mathcal{Q}^{(3)}_{\varphi Q} &= i\frac{1}{2}y_t^2(\varphi^\dagger \overleftrightarrow{D}^I_\mu \varphi)(\overline{Q}\gamma^\mu\tau^I Q),\\
\mathcal{Q}_{tW} &= y_t g_w(\overline{Q}\sigma^{\mu\nu}\tau^I t)\tilde{\varphi}W^I_{\mu\nu},\\
\mathcal{Q}^{(3)}_{qQ^{r,s}} &= (\overline{q}_r\gamma^\mu\tau^I q_s)(\overline{Q}\gamma_\mu\tau^I Q),
\end{aligned} \tag{3.10}$$

with their definitions following that of Refs. [96, 97], and where I use $\mathcal{Q}$ to denote a generic dimension-six SMEFT operator in the Warsaw basis. More SMEFT operators of dimension-eight can contribute to this process. However, it is generally assumed these contributions are sufficiently suppressed by their $1/\Lambda^4$ factor. The interaction Wtb vertex in the SM Lagrangian reads

$$\mathcal{L}^{SM}_{Wtb} = -\sum_{f=d,s,b}^{3}\frac{gV_{tf}}{\sqrt{2}}\overline{q}_f(x)\gamma^\mu P_L t(x)W_\mu(x) + \text{h.c.}, \tag{3.11}$$

where g is the coupling strength, $t(x)$ and $W_\mu(x)$ are the top quark and the W boson fields, respectively. The quark fields are denoted by $q_f(x)$ where $f = d, s, b$ refers to down, strange, and bottom quarks. The coefficient V_{tf} is an element of the CKM matrix, and P_L is the left-hand projection operator. The top (antitop) quark mainly

decays to a W boson and a b quark. This decay is followed by the subsequent one to an antilepton (lepton) and (anti)neutrino. The studies of Refs [98, 99] have shown a near-perfect correlation between the flight direction of the lepton in the top quark rest frame and the top quark spin. Due to the relative easiness of experimental detection of the lepton, this correlation allows the determination of the top quark spin and the coupling handedness from angular distributions. The four-fermion operator $\mathcal{Q}^{(3)}_{qQ^{r,s}}$ has a negligible effect on angular distribution [97], and so in the latest ATLAS measurement [92] was omitted. The other two operators in Eq. 3.10 modify the Wtb interaction as follows:

$$\begin{aligned}\mathcal{L}^{dim6}_{Wtb} = &\frac{-g}{\sqrt{2}}\bar{b}(x)\gamma^{\mu}P_L t(x)W_{\mu}(x)\left(1+\frac{C^{(3)}_{\varphi Q}y_t^2 v^2}{2\Lambda^2}\right)\\ &+\frac{2gvy_t C_{tW}}{\Lambda^2}\bar{b}(x)\sigma^{\mu\nu}P_R t(x)\partial_{\nu}W_{\mu}+\text{h.c.},\end{aligned} \tag{3.12}$$

where V_{tb} is assumed to unity. Comparing Eq. 3.11 and Eq. 3.12, it is clear that the coefficient $C^{(3)}_{\varphi Q}$ only alters the magnitude of the Wtb interaction, and so of a limited relevance to the differential study at hand. Therefore, in the ATLAS analysis, only the effects of the $\mathcal{Q}_{tW}$ operator were considered. WCs are complex ones and so they consist of real and imaginary parts, hereafter the WC of the $\mathcal{Q}_{tW}$ operator will be referred to as $\text{Re}\{C_{tW}\} \equiv C_{tW}$ and $\text{Im}\{C_{tW}\} \equiv C_{itW}$.

In the coordinate system defined in Eq. 3.7, θ_{li} is considered the polar angle of the charged lepton momentum with respect to the i^{th} axis ($i = \hat{x}, \hat{y}, \hat{z}$). Using these polar angles, one can obtain the differential angular distributions associated with the three polarisation components. The ATLAS analysis has used the unfolded[5] normalised distribution of $\cos\theta_{l\hat{x}}$ and $\cos\theta_{l\hat{y}}$ to set bounds on the complex WC of the $\mathcal{Q}_{tW}$ operator. The angular distribution of $\cos\theta_{l\hat{z}}$ has been ignored since it has been shown that it is insensitive to the effects of the $\mathcal{Q}_{tW}$ operator [100]. The data collected by the ATLAS experiment were compared to the effects of the $\mathcal{Q}_{tW}$ operator, which contributes to the production and the decay of the top quark. This comparison was performed in a likelihood fit using the theoretical predictions from the simulated samples as discussed in Sec. 2 of the corresponding ATLAS paper [92]. The results of the fitting are shown in Fig. 3.7 for both the $\cos\theta_{l\hat{x}}$ and the $\cos\theta_{l\hat{y}}$ angular distributions. The C_{tW} mostly affects the polarisation's component along the $\hat{x}$-axis, $P_{\hat{x}}$, whereas C_{itW} affects the $\hat{y}$-axis correspondent, $P_{\hat{y}}$ [92]. The reported best fit values for the coefficients

[5] The finite resolution of the detector smears the measured distributions. The deconvolution of the detector effects aiming to restore the true underlying distribution is called *unfolding*.

are $C_{tW} = 0.3 \pm 0.6(1.1)$ and $C_{itW} = -0.3 \pm 0.2(0.5)$ at 68% CL (95% CL) showing consistency with their SM prediction [92]. The obtained limits for the coefficients when all EFT terms are included up to $\mathcal{O}(\Lambda^{-4})$ and at the 95%CL for C_{tW} are [-0.9,1.4] and for C_{itW} are [-0.8,0.2]. This recent ATLAS measurement has improved the bound on the

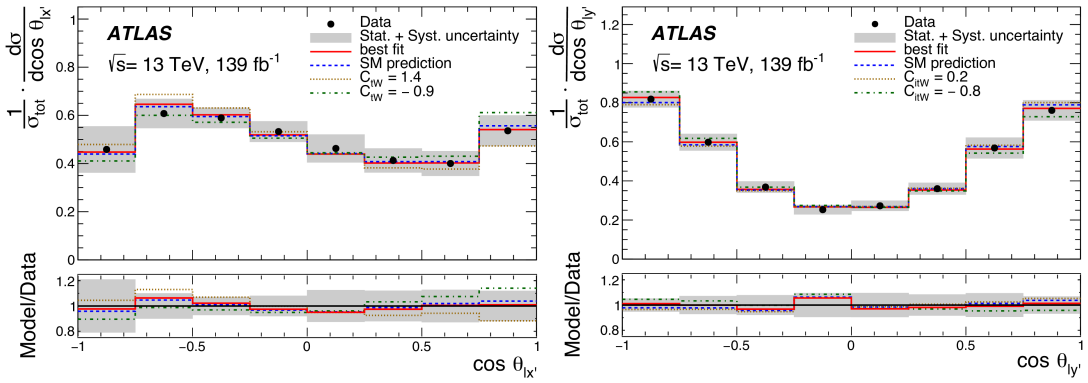

Figure 3.7.: Data to EFT fit for the polarisation angles $\cos\theta_{l\hat{x}}$ *(left)* and $\cos\theta_{l\hat{y}}$ *(right)*. The best fit result in the red line is the EFT prediction using the best fit values for the WC, C_{tW}. The blue line is the SM prediction obtained as described in the ATLAS analysis [92]. The brown (green) line shows the model at its upper (lower) 95%CL bounds for C_{tW} *(left)* and C_{itW} *(right)*. The figure is taken from Ref. [92].

imaginary part of the $\mathcal{Q}_{tW}$ operator, i.e. C_{itW}, compared to the previous corresponding ATLAS results.

3.4. Top quark pair production in association with a photon

The cross-section measurement of a top quark pair production with a photon, γ, is a probe for coupling the top quark to photons. This probe can serve as a test for the SM predictions and provide sensitivity to new physics phenomena beyond the SM. The current large amount of data collected by the CMS detector made the measurements of relatively small cross-sections, like the one of the $t\bar{t}\gamma$ production, feasible. A new analysis by the CMS experiment has measured the cross-section of the $t\bar{t}\gamma$ production process in the decay channel constituting two oppositely charged leptons using 138 fb^{-1} data recorded for pp collisions at $\sqrt{s} = 13$ TeV [101]. The analysis measures the $t\bar{t}\gamma$ cross-section differentially and consequently interprets the results in the context of SMEFT to obtain limits on the relevant WCs. This EFT interpretation constitutes the main discussion of this section.

The CDF collaboration found the first evidence of $t\bar{t}\gamma$ production in pp collisions [102]. The ATLAS collaboration was the first to observe the $t\bar{t}\gamma$ production at LHC at $\sqrt{s} = 7$ TeV [103]. Further measurements were performed by the ATLAS and CMS collaborations at $\sqrt{s} = 8$ [104, 105] and $\sqrt{s} = 13$ TeV [106–108]. The measurement in discussion defines a fiducial phase space for the $t\bar{t}\gamma$ signal process with criteria on the kinematic properties of the photon, leptons, and jets at the particle level. The events considered are the ones in which the photon is radiated from a top quark or an incoming quark, as shown in Fig. 3.8, or any of the charged decay products of the top quarks. The $t\bar{t}\gamma$ SM production has been computed at NLO in QCD and EW

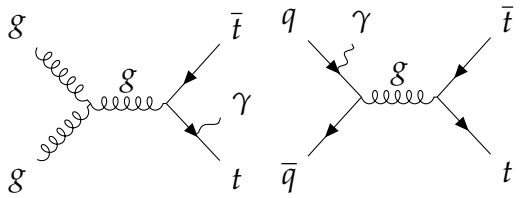

Figure 3.8.: Representative diagrams for the LO $t\bar{t}\gamma$ production where the photon is radiated by a top quark *(left)* and by an incoming quark *(right)*.

theory [78, 109–114]. The top quark decays and photon radiations from the final-state particles at the NLO accuracy have also been performed [115, 116]. The sensitivity to new-physics modifications has been studied in the SMEFT framework in Ref. [117].

Since the measurement of $t\bar{t}\gamma$ production is sensitive to the EW dipole moments of the top quark, the operators $\mathcal{Q}_{tW}$ and $\mathcal{Q}_{tB}$ can be used to modify the $t\bar{t}\gamma$ vertex. The $\mathcal{Q}_{tW}$ operator is presented in Eq. 3.10 while the $\mathcal{Q}_{tB}$ operator is defined as follows [117]:

$$\mathcal{Q}_{tB} = y_t g_Y (\overline{Q}\sigma^{\mu\nu} t)\tilde{\varphi} B_{\mu\nu}. \tag{3.13}$$

Due to the SM gauge symmetries, complementarity arises between the $tt\bar{t}\gamma$ and $t\bar{t}Z$ vertices [118–120] and therefore, a linear combination of the Warsaw basis coefficients of the $\mathcal{Q}_{tW}$ and $\mathcal{Q}_{tB}$ operators can describe the modification of the $t\bar{t}Z$ interaction vertex,

$$c_{tZ} = \mathrm{Re}\{-\sin\theta_W C_{tB} + \cos\theta_W C_{tW}\}, \tag{3.14}$$

$$c_{tZ}^{I} = \mathrm{Im}\{-\sin\theta_W C_{tB} + \cos\theta_W C_{tW}\}, \tag{3.15}$$

and the $t\bar{t}\gamma$ interaction vertex [101],

$$c_{t\gamma} = \mathrm{Re}\{\cos\theta_W C_{tB} - \sin\theta_W C_{tW}\}, \tag{3.16}$$

$$c_{t\gamma}^{I} = \mathrm{Im}\{\cos\theta_W C_{tB} - \sin\theta_W C_{tW}\}, \tag{3.17}$$

where the superscript I indicates the imaginary part of the coefficient. With the assumption that W boson helicity fractions measurements are a better probe for C_{tW} [121], the C_{tW} were set to zero in the CMS analysis [101]. This choice renders $c_{t\gamma}$ and c_{tZ} dependent parameters.

The new physics hypothesis was parameterised in terms of the c_{tZ} and c_{tZ}^{I} coefficients, while all other operator coefficients were set to zero. The effects from possible new physics deviations are then probed in the differential measurement of the photon p_T distribution. The other observables were found to be insensitive to this new-physics effects [101]. The observed 95% CL individual limits were reported as $[-0.53, 0.52]$ and $[-0.58, 0.52]$, for c_{tZ} and c_{tZ}^{I}, respectively. A similar measurement by CMS was performed using final states with one lepton and jets (l+jets) [108]. The more significant number of signal events at large photon p_T values in the measurement of Ref. [108] increases the sensitivity to the SMEFT operators modifications, and thus, a further improvement in the obtained constraints was expected. The combined result from the two measurements are reported at 95%CL as $[-0.36, 0.31]$ and $[-0.38, 0.36]$ for c_{tZ} and c_{tZ}^{I}, respectively, providing the best published limits to date [101].

Chapter 4.

Measurement of the $t\bar{t}H$ production rate at the LHC

As discussed in the previous chapter, top quark interactions can serve as a window to BSM physics. Such potential new physics can be encapsulated as slight deviations from SM predictions, i.e. the SMEFT approach, or as resonances in direct searches, i.e. UV-complete BSM scenarios. Regardless of the particular interpretation of BSM physics, the top-Yukawa coupling remains one of the traditional probes of top quark interactions due to its crucial role in many new physics scenarios. Over the last years, vigorous effort concerted by theoretical and experimental communities has been put into studying the top-Yukawa coupling. An example of one of such experimental efforts is the measurement of the $t\bar{t}H$ production rate at the LHC.

This chapter presents the CMS measurement of the $t\bar{t}H$ process, performed in pp collisions at $\sqrt{s} = 13$ TeV. Two CMS measurements targeted the $t\bar{t}H$ production process; an inclusive measurement [122][1] and a differential one. Both constitute the material presented in this chapter. The inclusive $t\bar{t}H$ measurement is performed in ten different final states, with electrons, muons and taus, referred to as "channels". One of the $t\bar{t}H$ production channels is the two-leptons-same-sign channel, 2lSS+0τ_h, where l denotes light leptons (e, μ) and τ_h denotes hadronically decaying tau leptons. This discussion is focused *only* on the 2lSS+0τ_h channel for it being the one with the highest sensitivity and largest signal yield. This led to the further use of 2lSS+0τ_h in investigating the top–Higgs system's differential behaviour for the differential study, aiming to constrain new physics in the context of SMEFT.

The chapter is organised as follows: following a brief introduction in Sec. 4.1, Sec. 4.2 discusses the data and simulated samples used in the inclusive analysis. Sec. 4.3 covers the event selection followed by a discussion on the signal extraction

[1] The measurement originally targeted both the $t\bar{t}H$ and the tH signals, I focus here on the $t\bar{t}H$ one.

and systematic uncertainties in Sec. 4.4. The results from the inclusive measurement are presented in Sec. 4.5. The prospect of the differential measurement and the EFT interpretation are discussed in Sec. 4.6 and Sec. 4.7, respectively.

Declaration

The discussion constituting Sec. 4.2-Sec. 4.5 is based on the inclusive measurement of the $t\bar{t}H$ production of Ref. [122]. The author's work, however, was primarily focused on measuring the $t\bar{t}H$ process differentially for which the presentation of the inclusive measurement is intended to serve the purpose of setting the stage.

Sec. 4.6 and Sec. 4.7 present the analysis effort put into performing a differential measurement of the $t\bar{t}H$ process. This work was not public by the time of writing, only internally within the CMS collaboration. Therefore, some aspects of those sections could have been already outdated or further improved by the time of reading. This being the effort to which the author of this work mostly contributed, such contributions are as follows:

- Measuring the $t\bar{t}H$ differential cross-section through reconstructing the relevant differential observables in the 2lSS+0τ_h final state.
- Assessing the efficiency of the originally planned-to-use boosted decision tree (BDT)-based discriminant (referred to as the "top-tagger") for targeting hadronically decaying top quarks. An assessment led to more optimal methods to identify top quarks with better efficiency than the top-tagger.
- Computing the response matrices that assess the quality of the differential reconstruction. This computation allowed us to quantify the inefficiencies from imperfect lepton and jet assignments and missing energies in the final state.
- Internal study of the NLO and PS effects on the $t\bar{t}H$ process laying the theoretical foundation of the differential study.
- Parameterisation of the EFT effects induced from the relevant SMEFT operators to the $t\bar{t}H$ process and aiding in the EFT reweighting procedures.
- Contributing to the documentation of the work mentioned above.

4.1. Introduction

The Higgs boson discovery by the CMS and ATLAS experiments in 2012 [5, 6, 123] motivated a profusion of research that focuses on studying the properties of the

newly discovered particle. In the SM, the top quark-Yukawa coupling, y_t, is directly proportional to the top quark's mass. The latter being the heaviest fermion (that we know of) renders its Yukawa coupling at the order of unity. This strength of the top quark coupling to the Higgs boson may allude to a top quark's unique role in the EWSB [124–126]. Furthermore, a measured deviation from the SM prediction of y_t may serve as a shred of evidence for BSM physics [127]. The measurement of the $t\bar{t}H$ differential cross-section can disentangle effects arising due to a modified Higgs self-coupling from other effects such as the presence of anomalous top-Higgs interactions [128]. In the context of SMEFT, the $t\bar{t}H$ process provides a firm handle on the relevant dimension-six coefficients [129]. Moreover, and as will be discussed in Sec. 4.7, the $t\bar{t}H$ process offers valuable insight into the interplay between the top quark and Higgs measurements in constraining new physics. Such interplay emphasises the complementarity between different sectors of the SM in performing global EFT studies. The LO diagrams for $t\bar{t}H$ production are shown in Fig. 4.1.

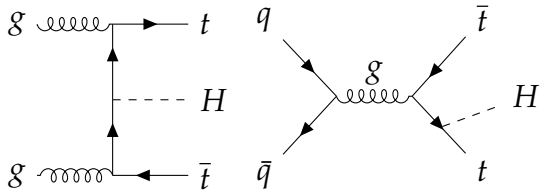

Figure 4.1.: Representative diagrams showing the $t\bar{t}H$ production process at the LHC at the LO accuracy.

The above-mentioned reasons render the theoretical understanding and precise experimental measurement of the $t\bar{t}H$ production process a crucial and an exciting endeavour. An enormous theoretical effort has been done in calculating the SM prediction for the $t\bar{t}H$ process at NLO in QCD [129–137]. In Ref. [138], the SM $t\bar{t}H$ production cross-section at NLO in QCD along with EW corrections at the same order is reported to be $\sigma^{SM}_{t\bar{t}H} = 506.5$ fb. This chapter presents the most recent experimental measurement of $t\bar{t}H$, and its interpretation in the context of the SMEFT.

4.2. Data and Monte Carlo simulation

The data used in the analysis are pp collisions recorded at $\sqrt{s} = 13$ TeV by the CMS detector at the LHC during the years 2016-2018. The total integrated luminosity of the analysed data is 137 fb^{-1}.

The event samples produced using MC simulation were used to calculate signal selection efficiencies, estimate background contributions, and train machine learning algorithms. This inclusive analysis is performed in ten different final state channels. However, as mentioned before, the discussion here is focused on the 2lSS+$0\tau_h$ channel for which the most relevant background contribution is $t\bar{t}$ production in association with a W boson, $t\bar{t}W$. The $t\bar{t}W$ background sample was generated at NLO in QCD using `MadGraph5`. The modelling of $t\bar{t}W$ included additional $\alpha_s\alpha_w^3$ corrections [74,75]. The NLO program `POWHEGv2.0` [139–141] was used to simulate background contributions stemming from diboson production, WZ, ZZ, and from other SM Higgs production processes. The `NNPDF3.0LO` (`NNPDF3.0NLO`) [142–144] set of parton distribution functions (PDFs) were used in simulating the LO (NLO) 2016 samples, while `NNPDF3.1 NNLO` [145] were used for 2017 and 2018 LO and NLO samples. Parton showering, hadronisation, and the construction of the underlying event were modelled using `Pythiav8.2` [146]. The modelling of the $t\bar{t}H$ signal and the backgrounds were further improved by normalising the simulated samples to cross-sections computed at higher order in QCD. These higher-order cross-sections are found in Ref. [138] for the signal and $t\bar{t}W$ processes. Pileup, i.e. the presence of simultaneous pp collisions in the same or nearby bunch crossings, was modelled by superimposing inelastic pp interactions simulated using `Pythiav8.2` to all MC events. All MC events were passed through a detector simulation of the CMS apparatus, based on `GEANT4` [147,148].

4.3. Event selection

This analysis originally targeted $t\bar{t}H$ and tH events where the Higgs boson decays are generally as follows, $H \to W^+W^-$, $H \to \tau^+\tau^-$, or $H \to ZZ$, with the corresponding subsequent decays. The branching fractions of these (125 GeV) Higgs decay modes are $\sim$21%, $\sim$6%, and $\sim$2%, respectively. Furthermore, the branching fraction of the W boson decay into leptonic final states amounts to $\sim$32.5%, while the Z boson branching fraction to charged leptons is $\sim$10.2%. The τ lepton branching fraction to purely leptonic decays is $\sim$35.2% [149].

For the $t\bar{t}H$ signal and in the 2lSS+$0\tau_h$ channel, the Higgs boson is assumed to decay via $H \to W^+W^-$ where one W boson decays to hadrons and the other one to leptons. Moreover, one top quark decays semi-leptonically, i.e. $t \to bW \to bl\nu_l$, and the other decays hadronically, i.e. $t \to bW \to bq\bar{q}'$, and analogously for the antitop quarks. The leptons from the W boson and the top quark should have the same sign for the 2lSS+$0\tau_h$ final state to be achieved. This final state constitutes an experimental

signature consisting of electrons, muons, missing energies caused by the neutrinos stemming from W boson decays, b-jets from the top quark decays, and the light-quark jets originating from the decays of either the Higgs boson or the top quark.

Events were selected at the trigger level using a combination of single- and double-lepton triggers. Even though requiring same-sign leptons reduces the signal yield by about half, it increases the signal-to-background ratio by a large factor since it removes the background arising from $t\bar{t}$ +jets production in which both top quarks decay semi-leptonically. Vetoing events containing opposite-sign pairs of same-flavour leptons suppresses the background contributions from processes like $t\bar{t}Z$ and Drell-Yan (DY). The suppression of background contributions arising from DY production in the 2lSS+$0\tau_h$ channel was further improved by imposing a requirement on the linear discriminant, $L_D > 30$ GeV. The latter is a variant of missing transverse momentum designed for an optimal trade-off between discrimination and sensitivity to pileup. It is defined by $L_D = 0.6p_T^{miss} + 0.4H_T^{miss}$, where p_T^{miss} denotes the magnitude of the missing transverse momentum vector, and H_T^{miss} is a variable generally defined in the same way as p_T^{miss} but with imposing some fiducial cuts[2] on the objects entering into its definition, rendering it less sensitive to soft hadrons which predominantly originate from the pileup. To target the $t\bar{t}H$ signal, events were selected to have at least three central jets of $p_T > 25$ GeV and $|\eta| < 2.4$, of which two must be tagged as b-jets. Tab. 4.1 presents a summary of the event selection criteria applied for the 2lSS+$0\tau_h$ final state.

Selection	**2lSS + $0\tau_H$**
Target $t\bar{t}H$ decays	$t \to bl\nu$, $t \to bq\bar{q}'$ with $H \to WW \to l\nu q\bar{q}'$
Trigger	Single and double-lepton triggers
lepton p_T	$p_T > 25/15$ GeV
lepton η	$\|\eta\| < 2.5(e)$ or $\|\eta\| < 2.4(\mu)$
Charge	2 SS leptons plus charge quality requirements
Number of central jets	≥ 3 plus b-tagging requirements
Missing transverse momentum	$L_D > 30$ GeV

Table 4.1.: Summary of the event selection criteria for the $t\bar{t}H$ signal process in the 2lSS+$0\tau_h$ channel.

[2] Fiducial cross-section is the cross-section of a process defined through a set of *fiducial cuts* so that the distinctive signatures of a given process are detected with the sensitive regions of the detector volume, i.e. the *fiducial volume*.

4.4. Signal extraction and systematic uncertainties

Signal extraction In order to separate the $t\bar{t}H$ signal from the background contributions, a maximum likelihood (ML) fit to the distributions of several discriminating observables was employed. The following expression is the likelihood function:

$$\mathcal{L}(\text{data}|\mu,\theta) = \prod_i \mathcal{P}(n_i|\mu,\theta) \prod_k p(\tilde{\theta}_k|\theta_k), \tag{4.1}$$

where the index i refers to individual bins of the discriminating observables distributions that are included in the fit. The factor $\mathcal{P}(n_i|\mu,\theta)$ represents the Poisson probability to observe n_i events in a given bin i, where $\nu_i(\mu,\theta)$ events are expected from the sum of signal and background contributions in that bin. The number of expected events is a linear function of the parameter of interests (POIs); $\mu_{t\bar{t}H}$ and μ_{tH},

$$\nu_i(\mu,\theta) = \mu_{t\bar{t}H}\nu_i^{t\bar{t}H}(\theta) + \mu_{tH}\nu_i^{tH}(\theta) + \nu_i^{B}(\theta), \tag{4.2}$$

where the symbols $\nu_i^{t\bar{t}H}$, ν_i^{tH}, and ν_i^{B} denote, respectively, the SM expectation for the $t\bar{t}H$ signal contribution, similarly for tH, and the summed contributions expected from background processes in bin i. The notation $\nu_i(\mu,\theta)$ indicates that the number of events expected from signal and background processes in each bin i depends on a set of parameters, denoted by the symbol θ, that represent the systematic uncertainties, and are referred to as nuisance parameters. Individual elements of the set of nuisance parameters θ are denoted by the symbol θ_k, where each k represents a specific source of systematic uncertainty. The function $p(\tilde{\theta}_k|\theta_k)$ represents the probability to observe a value $\tilde{\theta}_k$ in an auxiliary measurement of the nuisance parameter, given that its true value is θ_k. This probability's density function depends on whether the systematic uncertainties affect the distribution's normalisation or shape. A detailed discussion can be found in Sec. 9 of Ref. [122].

The discriminating observables used for the fit were chosen based on different studies performed with simulated samples of signal and background events. They are the outputs of machine learning algorithms that were trained using simulated samples of signal and background and were chosen in line with their discrimination power, aiming at maximising the expected sensitivity of the analysis. The background training was performed on $t\bar{t}W$, $t\bar{t}Z$, $t\bar{t}$ +jets and diboson contributions. For signal extraction in the 2lSS+0τ_h channels, artificial neural networks (ANNs) were employed. Examples of the observables used as input to the ANNs are electron multiplicity,

leptons three-momenta, transverse and invariant mass. All input variables to the ANNs for the analysis ten different channels are presented in Ref. [122].

The ANNs used in the 2lSS+0τ_h have multiple output nodes that allow for the discrimination between the $t\bar{t}H$ and tH signals from backgrounds, accomplish the separation of the tH from the $t\bar{t}H$ signal, and perform a distinction between individual types of backgrounds. The `softmax` [150] function is chosen as an activation function for all output nodes, this permits the interpretation of their activation values as probability for a given event to be either $t\bar{t}H$ signal, tH signal, $t\bar{t}W$ background, or other 2lSS+0τ_h background contribution. The selected events were therefore classified into those four categories according to the output node with the highest corresponding probability value. The four distributions of the probability values were input to the ML fit. The training is performed using the `TENSORFLOW` package [151] with the `KERAS` interface [152].

Systematic uncertainties Several experiment- and theory-related effects can affect the event rates and the previously mentioned distributions of the discriminating observables. These effects are referred to as systematic uncertainties and are modelled by nuisance parameters in the ML fit. Examples of experimental sources are trigger efficiencies and the efficiency of identifying electrons and muons. On the other hand, theoretical uncertainties mainly arise from missing higher-order corrections to the perturbative expansions in cross-section computations, also from uncertainties in the PDFs. MC sample and sideband statistical uncertainty are the uncertainties associated with the limited number of simulated MC events and the amount of data events in the sideband region used for estimating the background contribution due to misidentified leptons. Tab. 4.2 summarises the impact of all systematic and statistical uncertainties on the $t\bar{t}H$ signal rates and the main background contributions. It is worth noting that $t\bar{t}W$ and $t\bar{t}Z$ processes show mostly lower systematic uncertainties impacts since the three-lepton and four-lepton control regions were included in the maximum likelihood fit.

4.5. Inclusive measurement results

An example of the distributions included in the ML fit are shown in Fig. 4.2. These distributions show the activation value of the ANN output node in the 2lSS+0τ_h, and are classified as $t\bar{t}H$ signal and $t\bar{t}W$ background. The expected distributions for signal

Source	$\Delta\mu_{t\bar{t}H}/\mu_{t\bar{t}H}$[%]	$\Delta\mu_{t\bar{t}W}/\mu_{t\bar{t}W}$[%]	$\Delta\mu_{t\bar{t}Z}/\mu_{t\bar{t}Z}$[%]
Trigger efficiency	2.3	1.2	1.9
Leptons reconstruction and identification efficiency	2.9	1.7	3.2
b-tagging efficiency	3.6	1.3	2.9
Misidentified leptons and flips	6.0	2.6	1.4
Jet energy scale and resolution	3.4	1.1	1.2
MC sample and sideband statistical uncertainty	7.1	2.4	2.3
Theory-related sources affecting acceptance and shape of distributions	4.6	2.0	4.2
Normalisation of MC-estimated processes	13.3	13.9	11.3
Integrated Luminosity	2.2	1.8	3.1
Statistical uncertainty	20.9	5.9	5.8

Table 4.2.: The impact of the systematic and statistical uncertainties on the measurement of the $t\bar{t}H$ signal rates as well as the $t\bar{t}W$ and $t\bar{t}Z$ background rates.

and background are shown for the value of the POI and nuisance parameters obtained from the ML fit.

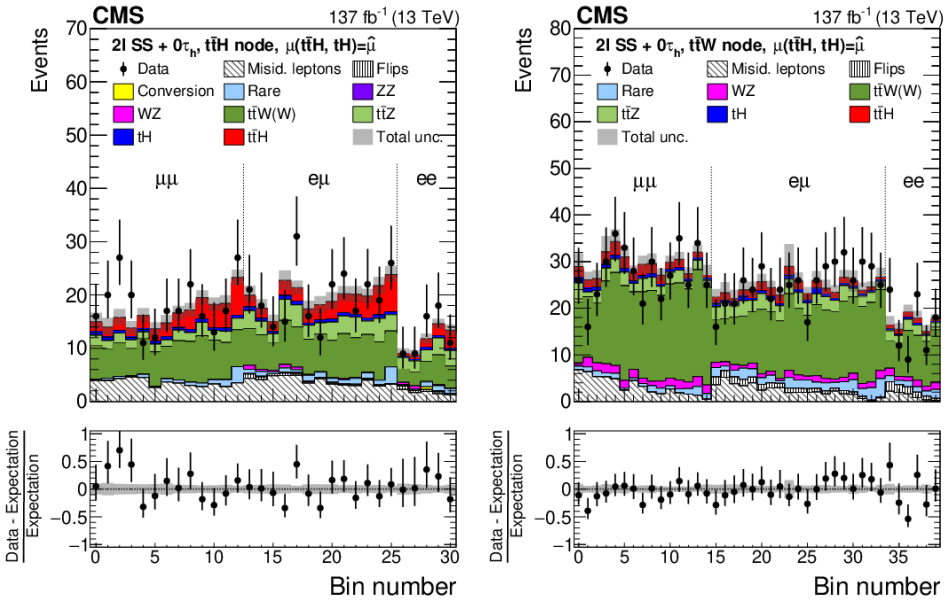

Figure 4.2.: Distributions of the activation value of the ANN output node with the highest activation value for events selected in the 2lSS+0τ_h channel and classified as $t\bar{t}H$ signal *(left)*, and $t\bar{t}W$ background *(right)*. The distributions are shown in the different subcategories based on the leptons flavour.

The production rates of the $t\bar{t}H$ and tH signals were determined through a binned simultaneous ML fit, in which the production rates of $t\bar{t}H$ (and tH) constituted the POIs. The symbol $\mu_{t\bar{t}H}$ (and μ_{tH}) denotes the ratio of the production rate of each signal process to its SM expectation. Assuming the distributions of the discriminating observables for the tH and $t\bar{t}H$ signals agree with their SM expectation, the produc-

tion rate for the $t\bar{t}H$ signal was measured to be $\mu_{t\bar{t}H} = 0.92 \pm 0.19(\text{stat})^{+0.17}_{-0.13}(\text{syst})$ times the SM expectation. This is equivalent to a $t\bar{t}H$ production cross-section of $466 \pm 96(\text{stat})^{+70}_{-56}(\text{syst})$ fb. The corresponding observed (expected) significance of the $t\bar{t}H$ signal amounts to 4.7 (5.2) standard deviations, assuming the tH process to have the SM production rate. The production rates measured in each of the ten individual channels are shown in Fig. 4.3, also rate when all channels are combined.

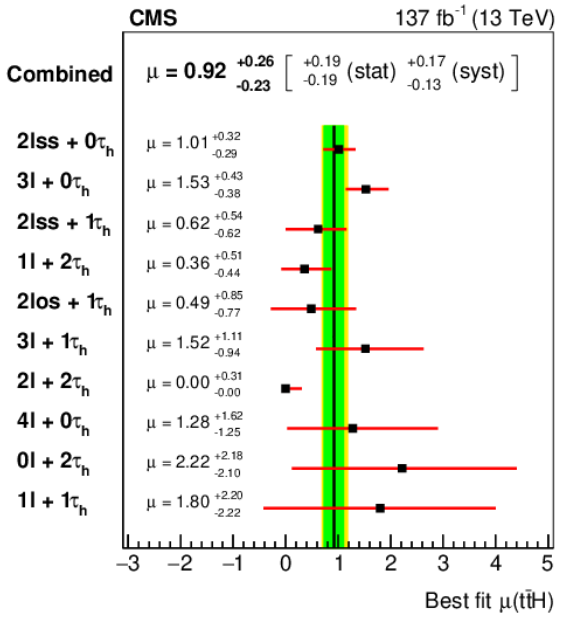

Figure 4.3.: The production rate $\mu_{t\bar{t}H}$ of the $t\bar{t}H$ signal measured in each of the ten channels individually and for the combination of all channels.

The event yields for $t\bar{t}H$, tH, and all the backgrounds are given in Tab. 4.3. The misidentified leptons refer to events with the reconstruction of at least one electron or muon due to misidentifying a non-prompt lepton. The conversion background constitutes events in which one or more electrons are reconstructed due to the conversion of a photon. The flips background in the 2lSS+$0\tau_h$ channel consists of events where the charge of a reconstructed lepton is mismeasured. Finally, rare backgrounds are the sum of background contributions other than those arising from $t\bar{t}W$, $t\bar{t}Z$ $t\bar{t}$ +jets, DY, diboson backgrounds, or from SM Higgs production (ggH, qqH, WH, ZH, $t\bar{t}WH$, and $t\bar{t}ZH$). Example of these rare backgrounds are tW, tZ, and $t\bar{t}t\bar{t}$ production processes.

Process	**2lSS + 0τ_H**
$t\bar{t}H$	222 ± 51
tH	119 ± 85
$t\bar{t}Z$+$t\bar{t}\gamma^*$	322 ± 25
$t\bar{t}W$+$t\bar{t}WW$	1153 ± 64
WZ	296 ± 31
ZZ	31.2 ± 3.3
Misidentified leptons	1217 ± 91
Flips	121 ± 19
Rare backgrounds	222 ± 48
Conversion	42 ± 12
ggH+qqH+VH+$t\bar{t}VH$	35.3 ± 4.0
Total expected background	3517 ± 85
Data	3738

Table 4.3.: The number of events selected in the 2lSS+0τ_h channel compared to the expected events yields from the $t\bar{t}H$ and tH signal processes and the background contributions. Uncertainties represent the sum of statistical and systematic components.

4.6. Towards a differential measurement

The importance of differentially measuring the $t\bar{t}H$ production process was highlighted in Sec. 4.1. Moreover, achieving the differential results within the simplified template cross-section (STXS) framework [153] is also crucial in allowing the integration of the top-Higgs coupling results in the global fits; to study the properties of the 125 GeV Higgs boson. The STXS are physical cross-sections defined in *mutually exclusive* regions of phase space, i.e. "bins". The experimental measurements are unfolded to the STXS bins, which are common for all analyses. This is a crucial feature of STXS and is the reason why it allows for a global combination of all measurements in different decay channels and from ATLAS and CMS.

The 2lSS+0τ_h final state is characterised by the largest expected yields, and so it was further used in performing the differential measurement. Nevertheless, the decision on which final state is to be investigated is yet driven by another primary consideration, which is the possibility of performing a full or approximately-full kinematic reconstruction of the final state in question. Such a possibility is crucial to disentangle the top quark-related portion of the event from the Higgs boson one. The kinematics of the 2lSS+0τ_h final state can be determined by 40 free parameters

through the following constraints:

$$\begin{aligned}
&P(t) = P(b) + P(W), \;\; P(\bar{t}) = P(b) + P(W), \\
&P(H) = P(W) + P(W), \\
&P(W) = P(l_1) + P(\nu_1), \;\; P(W) = P(l_2) + P(\nu_2), \\
&P(W) = P(q_1) + P(q_2), \;\; P(W) = P(q_3) + P(q_4),
\end{aligned} \tag{4.3}$$

where P denotes the four-momenta of a given particle. The 2lSS+0τ_h final state can be determined using 39 measurements and constraints, as outlined in Tab. 4.4. The remaining constraint can be added using experimental hypotheses, for example, splitting the neutrinos missing energies, E_T^{miss}, into components assigned to the two neutrinos in the final state.

Object	Parameter	Type	N$_{pars}$	Incremental total
Charged leptons	$E, \vec{p}$	Measurement	2x4	8
Jets	$E, \vec{p}$	Measurement	6x4	32
Neutrinos	$E_{\hat{x}}^{miss}$,$E_{\hat{y}}^{miss}$	Measurement	2	34
Hadronic W-bosons	on-/off-shell	Constraint	2	36
Top quark mass	$m_t = m_{\bar{t}}$	Constraint	2	38
Higgs boson mass	m_H	Constraint	1	39

Table 4.4.: The 39 measurements and constraints which can be used to determine the 2lSS+0τ_h final state for its kinematic reconstruction.

As previously mentioned, in the 2lSS+0τ_h channel, one top quark decays hadronically, and the other decays semi-leptonically. The Higgs decays to WW, where one W boson decays to hadrons and the other to leptons. This leads to two b-jets and four light jets arising from the hadronic W boson decays. The BDT-based discriminant that targets hadronically decaying top quarks, the so-called "top-tagger", was the first choice in the differential analysis, as had been the case in the inclusive measurement. The top-tagger computes the likelihood of three jets to be originated from a hadronic top decay. Those jets are required not to overlap, within $\Delta R < 0.4$, with an electron or a muon. Input to the BDT-discriminant includes kinematic information on jets arising from W boson decays as well as information on the b-tag discriminators. The BDT is trained using an aggregation of $t\bar{t}H$, $t\bar{t}W$, $t\bar{t}Z$ and $t\bar{t}$+jets MC samples. It is trained for all channels in which $t\bar{t}H$ signal events are expected to contain top quarks that decay

hadronically. However, it was found that in around 50% of the times, the discriminant "mistaken" the two jets arising from the W boson decay in the Higgs decay leg for jets originating from the W boson decay in the top quark decay leg. An alternative method to reconstruct the Higgs boson p_T as the differential observable firstly used in this analysis, which was found to be more optimal, is to reconstruct the W bosons from light jets whose invariant mass is close to that of it. The closest lepton in ΔR to that two jets[3], is assumed to be the one originating from the other W boson in the Higgs decay leg, and it recoils against the $t\bar{t}$ system. Therefore, this lepton, along with the two light jets, were used to reconstruct the transverse momentum of the Higgs boson. This reconstruction method resulted in a 70–75% selection efficiency of $t\bar{t}H$ events, corresponding to the percentage of events in which the Higgs boson p_T was reconstructed.

The initial step in the unfolding procedure and the estimation of the quality of the reconstruction is to compute a response matrix defining the event migration probability between the particle-level and reconstructed quantities. These response matrices were obtained using the generator and reconstruction information in the simulated samples, shown in Figs. 4.4-4.9 and discussed below. At this point, it is worth introducing the notations used in these matrices. The "visible" Higgs boson p_T, denoted as $p_T^{vis.}(H)$, is the reconstructed p_T with no attempts to include the missing energy of the neutrinos. The full generator-level, i.e. the MC truth, p_T is denoted as $p_T^{gen.}(H)$. The generator-level p_T corresponding to $p_T^{vis.}(H)$ is denoted as $p_T^{vis.gen.}(H)$ and is computed as the transverse component of the sum of the four-momenta of the generated lepton and quarks from the Higgs decay. In Fig. 4.4 and Fig. 4.5, $p_T^{vis.}(H)$ is compared to $p_T^{gen.}(H)$. Even though there is a reasonable correlation, there are two main sources of smearing.

The first source is due to estimating only the $p_T^{vis.}(H)$ without considering the missing energies of the neutrinos. The entity of such smearing was further assessed through analysing the response matrices of $p_T^{vis.gen.}(H)$ compared to $p_T^{gen.}(H)$, as displayed in Fig. 4.6 and Fig. 4.7. The second source of smearing is due to the difference between the reconstructed and the generator-level quantities, i.e. $p_T^{vis.gen.}(H)$ and $p_T^{vis.}(H)$. This inefficiency arises from the imperfect lepton and jet assignments used in the reconstruction algorithm, i.e. the two jets coming from the W boson through the Higgs decay leg are not always identified correctly. This smearing was further assessed in the response matrices for the two quantities as shown in Fig. 4.8 and Fig. 4.9.

[3] ΔR is a measure of the distance between two objects in the φ-η space of the detector and is defined as $\Delta R = \sqrt{(\Delta\eta)^2 + (\Delta\varphi)^2}$.

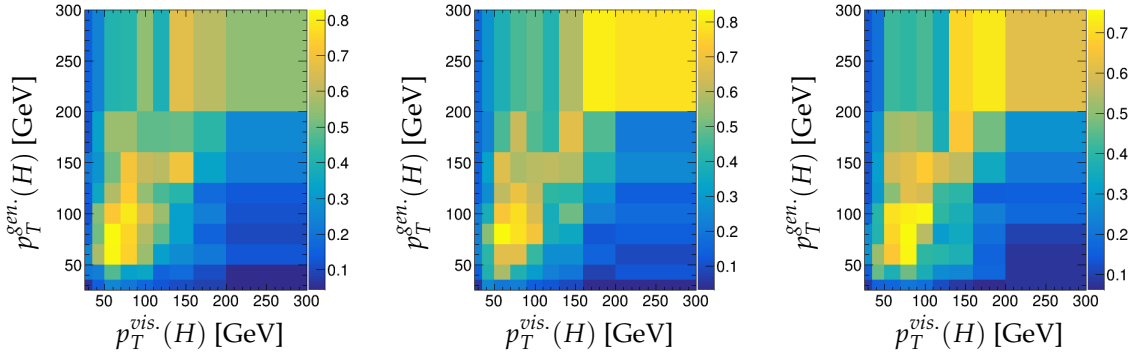

Figure 4.4.: Response matrices showing $p_T^{vis.}(H)$ against $p_T^{gen.}(H)$ for the estimated yields of 2016, 2017, and 2018 data-taking periods, respectively from left to right, in simulated $t\bar{t}H$ events.

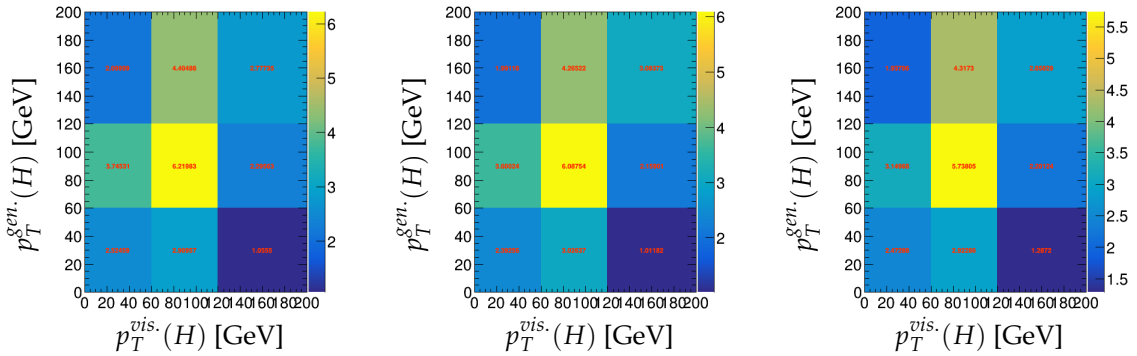

Figure 4.5.: Same as Fig. 4.4 but in the bins of the STXS scheme. The three bins used are [0-60],[60-120], and [120-200] GeV.

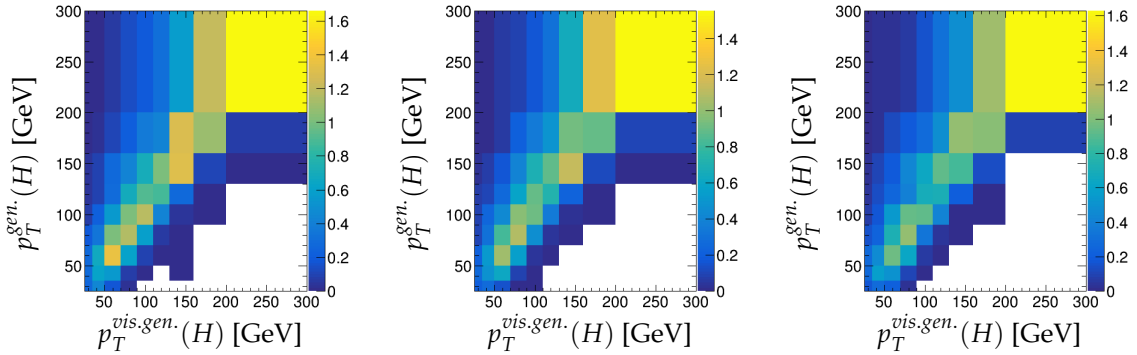

Figure 4.6.: Response matrices showing the $p_T^{vis.gen.}(H)$ against $p_T^{gen.}(H)$ for the estimated yields of 2016, 2017, and 2018 data-taking periods, respectively from left to right, in simulated $t\bar{t}H$ events.

As of the time of writing, an improvement in eliminating both smearing sources is foreseen. The first smearing source can be reduced by including the missing energies

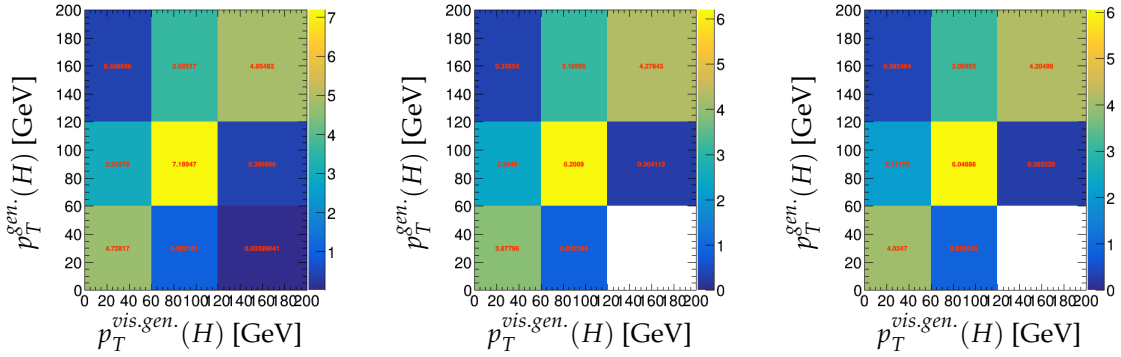

Figure 4.7.: Same as Fig. 4.6 but in the bins of the STXS scheme. The three bins used are [0-60],[60-120], and [120-200] GeV.

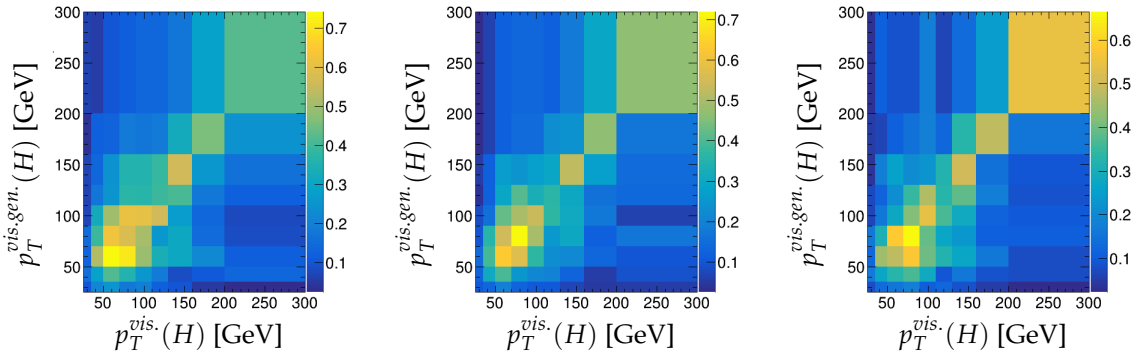

Figure 4.8.: Response matrices showing the $p_T^{vis.}(H)$ against $p_T^{vis.gen.}(H)$ for the estimated yields of 2016, 2017, and 2018 data-taking periods, respectively from left to right, in simulated $t\bar{t}H$ events.

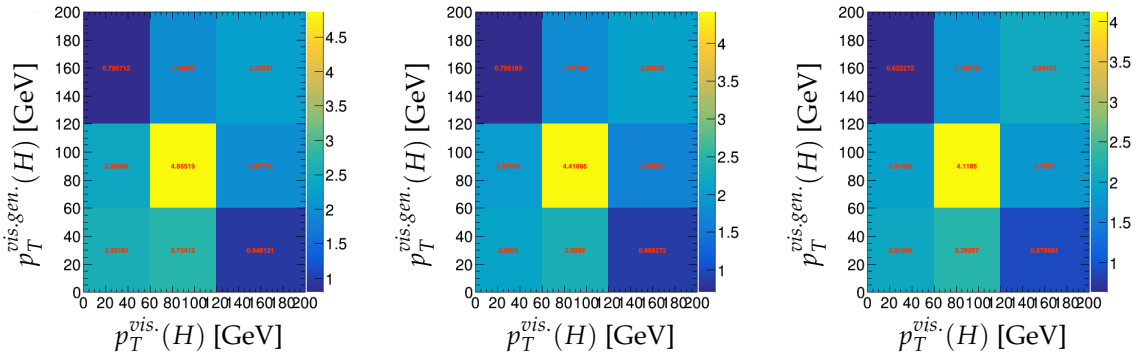

Figure 4.9.: Same as Fig. 4.8 but in the bins of the STXS scheme. The three bins used are [0-60],[60-120], and [120-200] GeV.

of the neutrinos in the reconstruction algorithm with dedicated techniques, whereas smearing due to imperfect lepton and jet assignments can be suppressed through the

use of algorithms that solves the combinatorics problem; identifying the correct jets to be assigned to the W boson from the Higgs decay.

4.7. EFT interpretation

The relevant dimension-six SMEFT operators impacting the $t\bar{t}H$ process are those which modify the $t\bar{t}H$, $t\bar{t}g$ and ggH vertices [129]. These operators establish a connection between the top quark and the Higgs boson sectors in the SMEFT at dimension-six. The EFT interpretation of the $t\bar{t}H$ differential measurement proceeds through considering diagrams with at most one EFT insertion at the production level, as presented in Fig. 4.10. The modification via the $\mathcal{Q}_{t\varphi}$ operator rescales the top-Yukawa coupling in

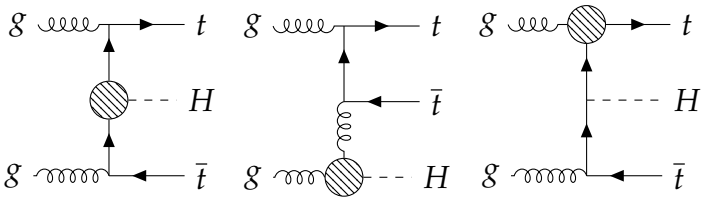

Figure 4.10.: Representative diagrams showing one insertion for each relevant dimension-six SMEFT operator to the $t\bar{t}H$ production process, represented by the blob. The diagrams are for the $\mathcal{Q}_{t\varphi}$, $\mathcal{Q}_{\varphi G}$, and $\mathcal{Q}_{tG}$ operators, from left to right, respectively.

the SM and introduces a new $ttHH$ vertex (*left* diagram of Fig. 4.11). The modification from the chromomagnetic dipole operator $\mathcal{Q}_{tG}$ gives rise to a dipole interaction in the SM $t\bar{t}g$ vertex, and introduces $ggtt$ (*right* diagram of Fig. 4.11), $gttH$, and $ggttH$ vertices. In principle, the modification induced from $\mathcal{Q}_{\varphi G}$ is relevant for $t\bar{t}H$, for it

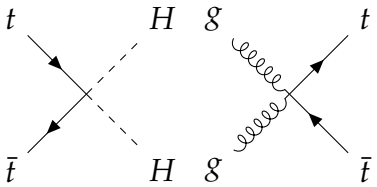

Figure 4.11.: Higher-point vertices induced by SMEFT operators. *Left* is the $ttHH$ vertex induced by $\mathcal{Q}_{t\varphi}$. *Right* is the $ggtt$ vertex induced by $\mathcal{Q}_{tG}$.

being a loop-induced interaction between the gluon and Higgs fields, but it is not included in the SMEFT model used in the analysis, i.e. the `dim6top` model [68], and so it does not take part of the EFT interpretation. The operators $\mathcal{Q}_{t\varphi}$ and $\mathcal{Q}_{tG}$ are defined

as follows [40, 129]:

$$\mathcal{Q}_{t\varphi} = y_t^3(\varphi^\dagger\varphi)(\overline{Q}t)\tilde{\varphi}, \tag{4.4}$$

$$\mathcal{Q}_{tG} = y_t g_s(\overline{Q}\sigma^{\mu\nu}T^A t)\tilde{\varphi}G^A_{\mu\nu}, \tag{4.5}$$

with their definitions follow that of Ref. [129]. The background contributions to the $t\bar{t}H$ process arise mainly from the $t\bar{t}W$ process followed by the $t\bar{t}Z$ one, as shown in Tab. 4.3. Both background processes are also affected by the $\mathcal{Q}_{tG}$ operator as it modifies the $t\bar{t}g$ interaction. It is worth noting that $\mathcal{Q}_{tG}$ is often considered as better constrained in top quark measurements, e.g. $t\bar{t}$ production. However, it has been shown in Ref. [129] that limits obtained on c_{tG} from $t\bar{t}H$ are not so far from their corresponding $t\bar{t}$ ones. This suggests that future Higgs measurements, e.g. at the High Luminosity (HL)-LHC, will become increasingly important in constraining this coefficient. Such observation further emphasises the importance of a differential study in $t\bar{t}H$, as well as the interplay between top quark and Higgs measurements in bounding new physics effects.

Samples for the $t\bar{t}H$, $t\bar{t}W$ and $t\bar{t}Z$ processes were generated with the inclusion of variations induced from the SMEFT operators. The `dim6top` model was used to simulate those effects at LO accuracy in QCD. In this model, the EFT degrees of freedom of top quark processes are defined as linear combinations of Warsaw basis operator coefficients and the $\mathrm{U}(2)_\mathrm{q} \times \mathrm{U}(2)_\mathrm{u} \times \mathrm{U}(2)_\mathrm{d}$ symmetry (among the first two quark generations) is imposed. This symmetry singles out the interactions involving the top and the bottom quark. Simulations using the `dim6top` model are only possible at LO accuracy in QCD and, in the unitary gauge, at tree-level.

4.7.1. EFT parameterisation

Taking into account the additional amplitudes arising from the dimension-six SMEFT insertions, the total matrix element of interest can be schematically written in its SM and EFT components,

$$\mathcal{A} = \mathcal{A}_{SM} + \sum_i^N \mathcal{A}^{(i)}_{EFT}, \tag{4.6}$$

with the index i indicating the sum of all the matrix elements arising from the N operators included in the analysis. The cross-section can therefore be written as

follows:

$$\sigma \propto \sigma_{sm} + \sum_{j}^{N} \frac{C_j}{\Lambda^2}\sigma_j + \sum_{j,k}^{N} \frac{C_j C_k}{\Lambda^4}\sigma_{jk}, \tag{4.7}$$

where C_j is the WC of the j^{th} SMEFT, and σ_j being the corresponding cross-section. This formulation leads to four categories of terms in the expansion of the cross-section σ; the pure SM contributions represented by the term σ_{sm}, the contribution from the SM interference with the EFT amplitudes represented by $(C_j/\Lambda^2)\sigma_j$. The term $(C_j C_k/\Lambda^4)\sigma_{jk}$ represents the interference between different EFT operators in the condition $j \neq k \neq 0$, and also represents the pure quadratic EFT contributions in the condition $j = k$ and $j, k \neq 0$. In Eq. 4.7, the cross-section is given as a function of the WCs and is parameterised as a multidimensional quadratic function. The latter can be fully constrained by $(N+1)(N+2)/2$ terms, allowing the determination of the yields dependence as a function of the WCs at any bin.

4.7.2. EFT reweighting

As a precursor for this discussion, it is worth reminding the reader of the concept of "event weights" in particle physics studies. In working with real data collected by the experiment, one can usually fill a histogram with events, each with a weight of unity. In contrast, filling a histogram with MC events requires using event weights. The reason is that MC simulations do not represent the real number of events we expect in actual data. Therefore, weighting each event with an appropriate weight is necessary to *normalise* the MC distribution such that it represents the real number of expected events.

The reweighting functionality of `MadGraph5` [154] allows the association of events generated under a particular theoretical hypothesis to an additional weight corresponding to a different theoretical hypothesis. Both original and additional weights are based on matrix-element computations. The additional weight can be therefore propagated through the simulation chain without having to perform a full simulation for the new theoretical hypothesis. This approach is very convenient as it only requires generating a single sample per process of interest. However, one limitation of reweighting in `MadGraph5` is that for a reliable reweighting procedure, both the original and the new hypothesis should have non-negligible contributions to the same parts of the phase-space [154]. To validate the reweighting procedure, the generator-level distributions generated under the exact EFT hypotheses (including linear and

quadratic contributions of the EFT) were compared against distributions generated under the SM hypothesis but then reweighted to obtain the EFT one, as shown in Figs. 4.12-4.13. Good agreement was observed between the reweighted and the exact EFT hypotheses for both operators in the $t\bar{t}W$ sample. For the $t\bar{t}H$ sample, $\mathcal{Q}_{tG}$ exhibits a slight disagreement between the original EFT prediction and the one reweighted from the SM. One possible way to mitigate this effect is to use a different baseline scenario for the reweighting rather than using the SM as the original hypothesis. These considerations may be taken into account at the later stages of the analysis.

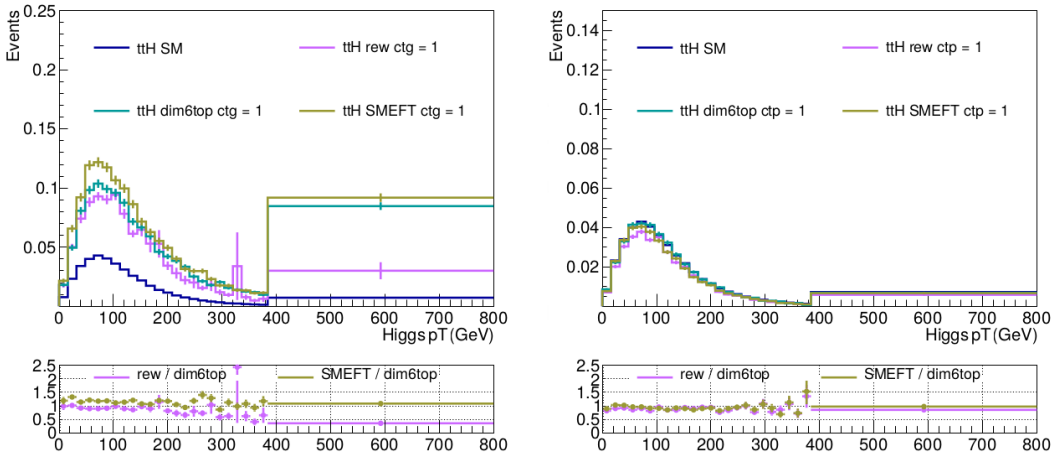

Figure 4.12.: Comparison of the reweighted $t\bar{t}H$ MC signal distribution (magenta) in $p_T(H)$ bins, against exact EFT predictions using the `dim6top` [68] and the `SMEFT@NLO` [155] models, and the SM. The comparison was performed for the $\mathcal{Q}_{tG}$ *(left)* and $\mathcal{Q}_{t\varphi}$ *(right)* operators contributions. The WCs of the operators were individually set to 1 and Λ is fixed to 1 TeV. The inset shows the ratio of the reweighted distribution to the exact one obtained by the `dim6top` model (magenta) and the ratio between the two EFT predictions obtained from both models. The y-axis is the number of events normalised to unity.

4.7.3. Constraining new physics

Constraining the values of the WCs requires the disentanglement of the signal from the various backgrounds and the exploitation of the kinematic variables sensitive to the effects of EFT modifications. In exploiting those kinematic variables, the differential variable m_{ttH}, the reconstructed total invariant mass of the $t\bar{t}H$ system, is, so far, the variable[4] used in fitting the data. A likelihood scan to an Asimov dataset[5] was

[4] The inclusion of the Higgs boson transverse momentum, $p_T(H)$, is foreseen.

[5] At the time of writing, the fit was performed using an Asimov dataset. Therefore, the ML is maximised at exactly zero by construction. The "observed" label of Fig. 4.14 is not to cause confusion.

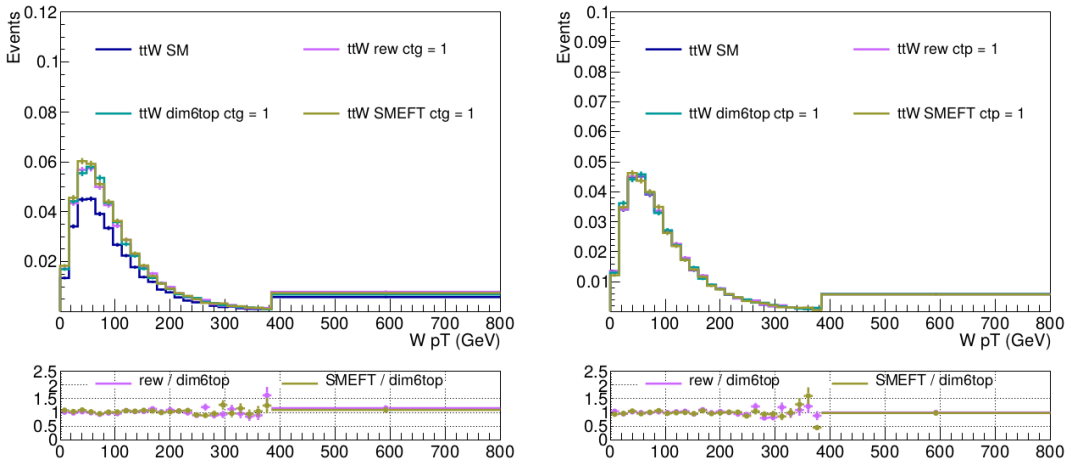

Figure 4.13.: Same as as Fig. 4.12 but for $t\bar{t}W$ process and in the W boson transverse momentum bins.

performed to constrain the values of the WCs, shown in Fig. 4.14. In scanning a given WC, the others coefficients were set to their SM values. The EFT predictions were computed including the linear and the quadratic contributions in SMEFT. The

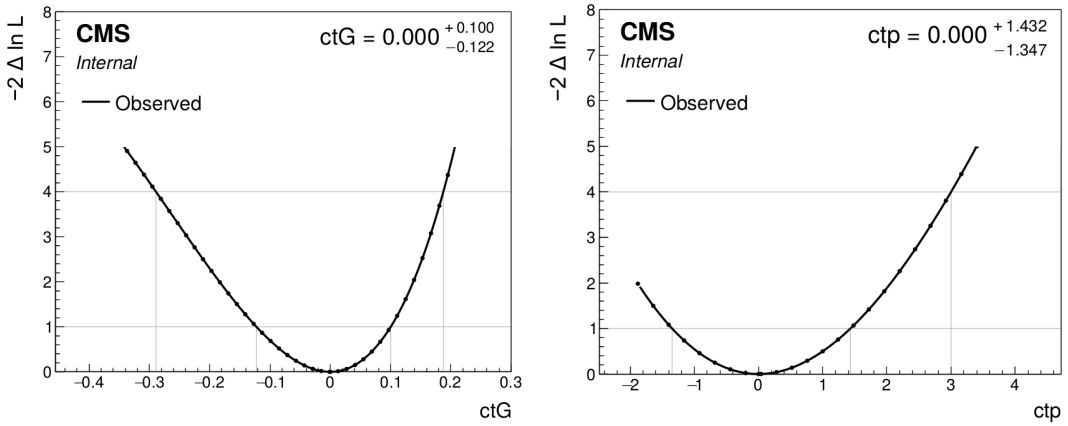

Figure 4.14.: Likelihood one-dimensional scans as a function of the WCs of the $\mathcal{Q}_{tG}$ operator *(left)*, and of the $\mathcal{Q}_{t\varphi}$ operator *(right)*.

preliminary bounds on the effective coefficients obtained from this likelihood scan and reported in the panels of Fig. 4.14 demonstrate the potential of the $t\bar{t}H$ measurement in constraining the relevant effective coefficients. Further optimisations in this analysis are foreseen. The obtained bound on c_{tG} is comparable to the results of a recently published CMS analysis which considered events containing one or more top quarks produced with additional prompt leptons and reporting an individual 2σ interval on c_{tG} of [-1.26,-0.69] $\cup$ [0.08,0.79] [156].

This chapter presented the top-Yukawa coupling as one potential probe of top quark interactions. In the next chapter, we move to a different top quark probe, the top quark coupling with EW gauge bosons, and investigate its potential sensitivity to new physics effects using the SMEFT approach.

Chapter 5.

tWZ production at NLO in QCD at the LHC in the SMEFT

The previous chapter discussed the top-Yukawa coupling as a probe of top quark interactions. In this chapter, I present the top quark couplings with EW gauge bosons as a different probe of the top quark. The tWZ process is a rare top quark EW process which has not yet been measured at the LHC. Its unitarity violating behaviour through modified EW interactions offers a promising sensitivity to new physics, this motivates its study in the context of SMEFT with the aim of having its data included in global EFT studies. Moreover, unlike $t\bar{t}Z$ and tZj processes, tWZ does not receive contributions from four-fermion operators at tree-level, such feature can aid in decorrelating effects from four-fermion operators and top quark EW couplings.

This chapter discusses the study of tWZ at the LHC in the context of the SM and SMEFT [1]. At NLO in QCD, tWZ interferes with $t\bar{t}Z$ and $t\bar{t}$ processes, and a method to meaningfully separate it from these overlapping processes needs to be employed. We found the diagram-removal procedures to provide reliable results for the SM and the SMEFT in a suitably defined phase space region. We provide robust results for total and differential cross-sections for tWZ at $\sqrt{s} = 13$ TeV, including the relevant dimension-six operators, also matching short-distance events to PS.

Declaration

The following is the author's contribution to this work:

- The implementation of the diagram-removal procedure in `MadGraph5`.
- Writing the analysis codes used in obtaining all the predictions.
- Performing all computations and making all plots.

- Obtaining predictions in the different helicity eigenstates, initially to cross-check with what is expected from Ref. [157]
- Matching the NLO computation to PS using `Pythia8`

The author's contribution excludes the helicity amplitudes calculation presented in Tab. A.1.

5.1. Introduction

At the tree-level, tWZ is similar to the tW production process, except for the added emission of one Z boson from any external or internal line, i.e., $gb \to tWZ$. Even though characterised by a relatively small cross-section of $\mathcal{O}(100)$ fb, the advantage of studying the tWZ process is manifested in its unique unitarity-violating behaviour induced in its sub-amplitudes and arising from the modification of the top quark EW interactions [74, 157]. Therefore, tWZ might provide enhanced sensitivity to new physics deviations in the context of SMEFT. Our work aimed to explore whether such a feature could be exploited to constrain or discover new physics. An LO study has confirmed the promising potential [158].

At LO accuracy and in the 5FS (where b quarks are massless), tWZ is easily identified through the tree-level partonic process $gb \to tWZ$ as shown in Fig. 5.1. On the

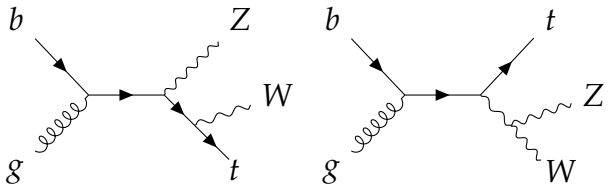

Figure 5.1.: Representative diagrams for the LO tWZ production in the 5FS.

other hand, at NLO, real corrections of the type $gg \to tWbZ$ arise featuring a resonant (anti)top quark in the intermediate state and therefore overlap with $gg \to t\bar{t}$, $\bar{t} \to \bar{b}WZ$, i.e., $t\bar{t}$ production at LO, as well as $gg \to t\bar{t}Z$, $\bar{t} \to \bar{b}W$, i.e. $t\bar{t}Z$ production at LO. Both processes are displayed in Fig. 5.2. This overlap poses an apparent problem. The cross-section of $t\bar{t}Z$ is roughly five times larger than tWZ, while $t\bar{t}$ cross-section is larger by a few orders of magnitude at LO. A "naive" computation would therefore lead to a poorly-behaved perturbative expansion on the one hand, and on the other, to a loss of the overall precision due to the "LO overlap" with other final states whose predictions are currently known at higher accuracy. Therefore, such overlapping

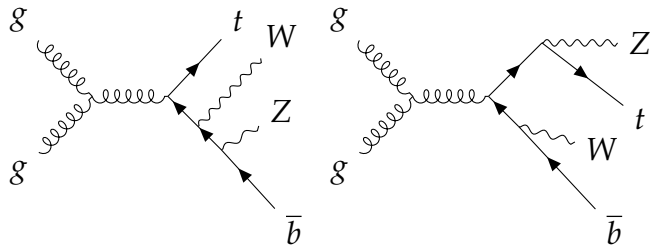

Figure 5.2.: Representative diagrams of the gg-initiated production of $t\bar{t}$ (*left*) and $t\bar{t}Z$ (*right*) processes with a potentially resonant (anti)top quark leading to the $tWZb$ final state.

resonant contributions need to be subtracted to achieve a meaningful operative definition of tWZ. Different methods have been proposed to achieve such subtraction of resonances that is local in phase space [159–168]. For this work, we followed that of Refs. [167, 168]. In subtracting the resonant contributions, the quantum mechanical nature of the process introduces ambiguities whose impact on the analyses needs to be carefully assessed, both for the SM and the SMEFT amplitudes. Such complexity renders achieving a meaningful definition valid at NLO accuracy for tWZ production more complicated than tW or even tWH processes.

5.2. On the nature of the problem

Considering tWZ at NLO, the overlapping processes involve contributions where an intermediate (anti)top quark can be on-shell and thus resonant. Essentially, the complication arises from amplitudes sharing the same $tWZb$ final state; yet are naturally associated with different underlying partonic processes, i.e. $t\bar{t}$ and $t\bar{t}Z$. Even though appearing at the same α_s and α_w order of the perturbative expansion, these terms are enhanced when the top quark is close to being on-shell through a factor of $1/\alpha_w$ induced from top quark width (due to the top quark propagator). Therefore, including these diagrams would potentially lead to substantial corrections spoiling the perturbative convergence of the tWZ cross-section. Moreover, a consistency problem arises: top quarks appear in the same diagram on the one hand as stable asymptotic states and on the other hand as intermediate ones. In the former case, their width should be set to zero to fulfil the local cancellation of IR divergences, whereas, in the latter, a finite top quark width must be kept to regularise the resonant propagator. In general, this violates QCD gauge-invariance.

One possible way to evade such complications is to consider the LO process in terms of (pseudo-)stable final states, i.e., $pp \to b\bar{b}W^+W^-Z$ in the 4FS and treat the top quark width in the complex mass scheme [169, 170]. While this approach has its advantages, it also poses non-trivial challenges. Ignoring the decays of the vector bosons and considering only the leading term ($\alpha_s^2\alpha_w^3$), this process can be easily computed at the tree-level. In doing so, all processes mentioned above, i.e., doubly resonant $t\bar{t}$ and $t\bar{t}Z$ processes, singly resonant tWZ, and non-resonant contributions would be accounted for simultaneously, together with their interference[1].

While the automatic computation at the NLO in QCD accuracy through event generators could also be envisaged, this approach is currently not considered practical for two main reasons. First, such NLO computations are not available and implementing them would entail considerable work, not least in our use case, in which we investigate a vast parameter space of BSM effects in this process. Second, such an approach would encounter complications in the experimental workflow, as some of the processes that would be included in the computation and considered as backgrounds, i.e., $t\bar{t}$, are known at higher accuracy and are currently simulated independently. Finally, at the theoretical level, the reliability of a 4FS for such a high-Q^2 process can be scrutinised, i.e., how to re-sum potentially large logarithms; $\log m_b^2/Q^2$. Therefore, it is more beneficial to consider an alternative approach that is sufficiently accurate to define the *signal* at NLO accuracy, and the experimental studies can directly employ that. To this aim, we developed a procedure to remove the additional resonant contributions appearing at NLO and yield an operative definition of tWZ.

5.3. Methods of resonance removal

Methods to remove resonances appearing in higher-order corrections are reasonably well-established. These methods were successfully applied to similar processes, tW [159] and tWH processes [167]. Resonant overlap removal methods, which can be applied at the differential level, fall into two broad categories, dubbed diagram removal (DR) and diagram subtraction (DS). In the latter, a constructed suitable gauge-invariant subtraction term locally suppresses the contribution of the resonant process. In the former, resonant diagrams are set to zero, thus requiring a much simpler implementation but possibly inducing some gauge dependence of the final result. A variant

[1] The computation of $pp \to b\bar{b}W^+W^-Z$ including the decays of the vector bosons is available at NLO QCD accuracy with massless b quarks [171]. In this case, the b quarks must be resolved in order to obtain a finite prediction; hence the phase space for tWZ cannot be probed.

of the DR scheme, which retains the interference between resonant and non-resonant diagrams, is also possible, often dubbed as DR with interference (DR-I) or DR2 (in this case, the standard DR is referred to as DR1). In this work, we employed the DR schemes. The studies of tW and tWH observed the DS results to lie between DR1 and DR2 [167]. This observation renders the difference between the latter as a measure of the uncertainty associated with these schemes.

So far, DR and DS techniques have been limited to cases where resonant diagrams correspond to $1 \to 2$ decays. These cases are now treated in a fully-automatic manner [168]. However, as previously mentioned, tWZ production has two underlying resonant processes, one of which proceeds through a $1 \to 3$ decay, and so in this work, we implemented the diagram removal procedures by hand. Therefore, we consider it worthwhile to spend some time describing our process structure and establishing the notation.

The general amplitude, $\mathcal{A}$, can be decomposed into a non-resonant and a resonant part,

$$\mathcal{A} = \mathcal{A}_{\text{non-res}} + \sum_i \mathcal{A}_{\text{res},i}, \tag{5.1}$$

where the index i labels different resonant processes (in the case at hand, $t\bar{t}$ and $t\bar{t}Z$). The amplitude squared reads

$$|\mathcal{A}|^2 = |\mathcal{A}_{\text{non-res}}|^2 + 2\Re\mathfrak{e}\left(\mathcal{A}_{\text{non-res}} \sum_i \mathcal{A}_{\text{res},i}\right) + \left|\sum_i \mathcal{A}_{\text{res},i}\right|^2. \tag{5.2}$$

In the case of standard DR procedure (DR1), one discards the resonant terms before squaring the amplitude, i.e.

$$|\mathcal{A}|^2_{\text{DR1}} \equiv |\mathcal{A}_{\text{non-res}}|^2. \tag{5.3}$$

In the case of diagram-removal with interference (DR2), one only discards the squared resonant matrix elements in the squared amplitude but keeps their interference with the non-resonant part, i.e.

$$|\mathcal{A}|^2_{\text{DR2}} \equiv |\mathcal{A}_{\text{non-res}}|^2 + 2\Re\mathfrak{e}\left(\mathcal{A}_{\text{non-res}} \sum_i \mathcal{A}_{\text{res},i}\right). \tag{5.4}$$

It must be noted that, in the case of DR2, one could keep the interference terms between different resonant amplitudes. However, in the following, we will not consider these terms.

5.4. *tWZ* in the SM

We initiated the study by first computing tWZ at NLO in QCD in the SM. In doing such computation, the choice on whether to include the interference between the resonant and the non-resonant amplitudes shall be made. This choice is mainly derived from how the predictions will be employed. Since this work aimed to use the tWZ process in constraining new physics effects via an EFT parameterisation, an operative definition of tWZ as an independent process must be provided, and interference with other processes, including the resonant ones, must be reduced as much as possible. Such reduction can be achieved by designing suitable selections which suppress the resonant contributions. In the case of top quark resonances, a suitable selection is to veto the b-tagged jet (b-jet) that would emerge from the top quark decay [159]. Generally, these b-jets originating from the top quark decay tend to be harder than ones originating from real emission diagrams since the latter are enhanced in the soft and collinear limits. Indeed, imposing such a requirement significantly suppresses the difference between DR1 and DR2. This suppression of the discrepancy between DR1 and DR2 predictions implies a negligible overlap with the resonant processes and a satisfactory level of control on the theoretical uncertainty associated with the subtraction method.

The left panel of Fig. 5.3 shows the differential cross-section predictions in the $W\ell^+\ell^-$ invariant mass bins for the $tW\ell\ell$ process at NLO in QCD in the DR1 and DR2 schemes (where we have considered the decay of the Z boson), both at the inclusive-level and after imposing a veto on central ($|\eta| < 2.5$) or hard ($p_T > 30$ GeV) b quarks. We also applied a minimum threshold on the dilepton invariant mass of 30 GeV to suppress the photon-mediated contributions. The first two insets show the relative scale uncertainties of the DR1 and DR2 predictions for the inclusive and b-veto cases, respectively. The third inset shows the ratio of the DR1 and DR2 differential cross-sections for the two cases. The apparent discrepancy between DR1 and DR2 at the inclusive level (the no b-veto case) indicates that a significant overlap exists in the full phase space, while in the b-veto case, the discrepancy disappears. This is in line with the observed behaviour in previous studies of the tW [159] and tWH [167]. We observed in the inclusive case the discrepancy between DR1 and DR2 and the scale uncertainty of the latter grows significantly as a function of energy,

indicating a pathology in the predictions. This is likely because we are probing regions of phase space where the potentially resonant diagrams are no longer so, causing gauge-invariance issues; the diagrams lose their special status away from the resonant region and should therefore be retained to ensure a well-behaved amplitude.

Looking ahead to the following EFT study, we simplified the definition of the tWZ process by maintaining a stable Z boson *in lieu* of the dilepton pair. We justify this simplification as follows: in imposing the b-veto, effects due to diagrams not involving a $Z \to \ell\ell$ splitting matter only far away from the Z boson peak, where the cross-section is suppressed. If we select only diagrams with resonant Z bosons and compare the cross-section with the case where all diagrams are retained, the dilepton invariant mass distributions depart from each other for less than 10% in the range [70, 150] GeV, as displayed in the right panel of Fig. 5.3. Moreover, the tWZ component of $tW\ell\ell$

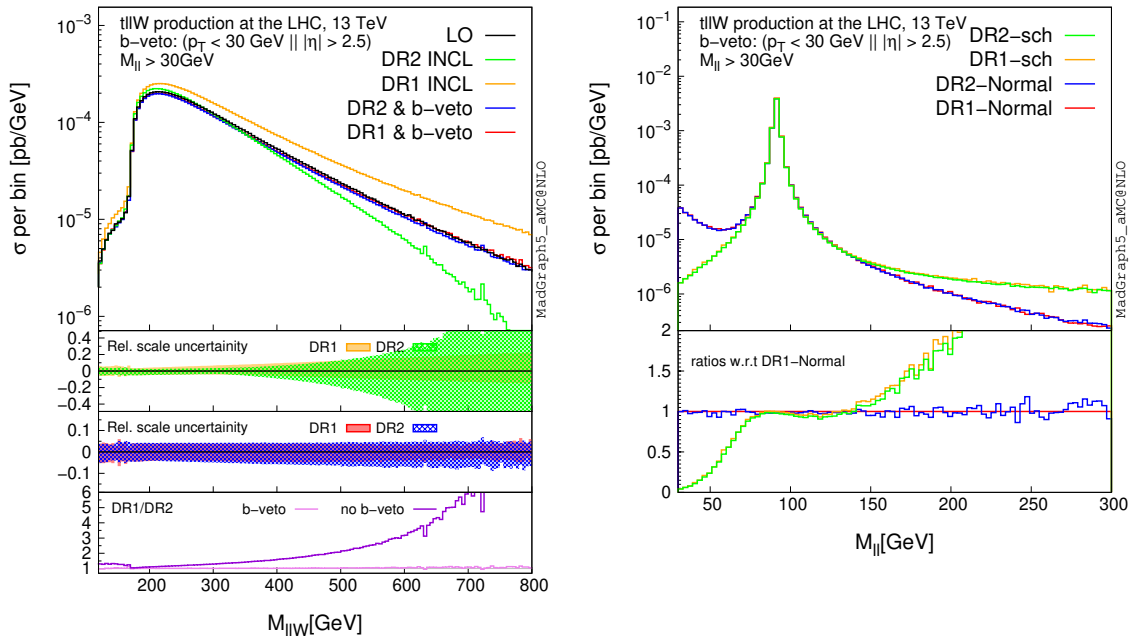

Figure 5.3.: The differential cross-section in the invariant mass bins of the $W\ell^+\ell^-$ system for the $tW\ell\ell$ process at NLO in QCD (*left*). Predictions are given for the DR1 and DR2 overlap removal schemes before and after imposing a veto on central ($|\eta| < 2.5$) or hard ($p_T > 30$ GeV) b quarks. The first two insets depict relative scale uncertainties, and the third one shows the DR1/DR2 ratio. DR1 and DR2 predictions of the invariant mass of the lepton pair, M_{ll} (*right*). Full predictions labelled "Normal" are shown alongside the "sch", the latter only includes diagrams with a Z boson in the s-channel. The inset shows the ratios of the distributions w.r.t to the "Normal" DR1 prediction.

can easily be isolated by requiring the dilepton invariant mass to lie around the Z

boson peak. Moving further with this simplification, we can also safely neglect the $t\bar{t}$, $t \to Wb\ell\ell$ resonant process: inspecting the five-body decay $t \to b\ell^+\ell^-\ell^{+\prime}\nu$ shown in Fig. 5.4, the opposite-charge, same-flavour lepton pair invariant mass peaks at low values showing a suppression at the Z boson mass. Besides, $t \to WZb$ occurs exceptionally close to the top quark threshold and never contributes to the cross-section in practice.

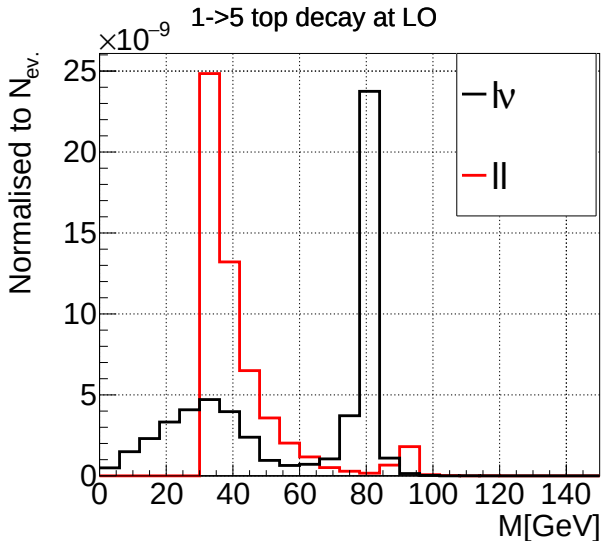

Figure 5.4.: The normalised invariant mass distributions of the $\ell\nu$ and $\ell\ell$ pairs in the five-body, $t \to be^+e^-\mu^+\nu_\mu$ decay, where different lepton flavours were simulated to distinguish those predominantly coming from intermediate neutral and charged gauge bosons. The top quark decay was performed in the 5FS and using the complex mass scheme at LO. A minimum invariant mass threshold of 30 GeV was imposed on the same-flavour, opposite-charge lepton pair.

5.5. *tWZ* in SMEFT

5.5.1. Probing new physics via high-energy top quark scattering

Since tWZ is a rare EW top quark production process, it can serve as a potential probe of the top quark weak couplings that are, to date, relatively poorly measured. Although tWZ cannot compete in terms of total rate with more traditional probes such as $t\bar{t}Z$, it has the significant advantage of being sensitive to unitarity-violating behaviour induced by modified EW interactions. Searching for the expected energy growth in EW top quark scattering amplitudes is a complementary avenue for searching for new physics via new interactions. The relevant sub-amplitude probed by tWZ is

$b\,W \to t\,Z$, whose tree-level SM diagrams are given in Fig. 5.5. The embedding of the sub-amplitude into the tWZ process at a hadron collider is also shown. This scattering

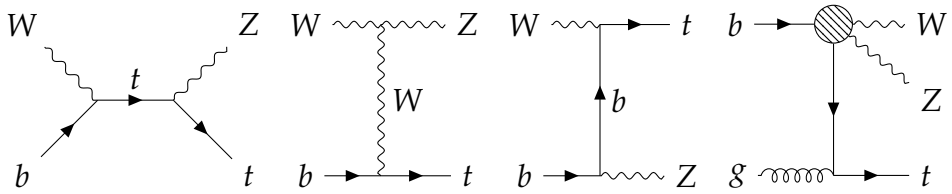

Figure 5.5.: SM diagrams for the $b\,W \to t\,Z$ sub-process. The far right diagram shows the embedding of the $b\,W \to t\,Z$ sub-amplitude, represented by the blob, into $gb \to tWZ$ production at a hadron collider.

is affected by modified weak interactions of the top and bottom quarks and the SU(2) gauge bosons self-interactions. However, it is not immediately evident that such modifications can potentially lead to an unacceptable growth with energy (beyond the maximal E^0 dependence admitted by perturbative unitarity for a $2 \to 2$ scattering amplitude). The feature indicates that the theory has a finite range of validity in energy, beyond which new unitarity-restoring-physics must appear, motivating the use of SMEFT to classify the possible deviations from SM interactions.

The application of this concept to top quark EW scatterings was studied in detail for a wide range of amplitudes and associated collider processes in Refs. [74, 157], highlighting the connection between modified SM interactions and SMEFT operators, as well as the emergence of energy growth via contact interactions between fermion and gauge or Goldstone boson currents. Moving from amplitudes to the observable cross-sections is vital in determining the interference structure of the new physics contributions with the corresponding SM amplitudes. In most cases, when the scattering states involve longitudinal polarisation of gauge bosons, the energy-growing SMEFT helicity configurations coincide with the leading high-energy SM ones, such that their interference also grows with energy, providing an enhanced LO sensitivity to the effective coefficients, and in turn motivating searches that exploit these channels.

5.5.2. Advantages of *tWZ*

EW-induced $t\bar{t}Z/W$ production does embed interesting EW top quark scatterings. However, these production modes are not only dwarfed by their QCD-induced counterparts but also, at LO, they feature an off-shell EW state in the s-channel that suppresses

any interesting energy growth[2]. Moreover, these processes can receive modifications through many four-fermion operators mediating top quark pair production, further diluting sensitivity to EW top quark interactions.

The tWZ process also compares favourably to related EW processes embedding the $b\,W \to t\,Z$ sub-amplitude, namely tWj and tZj. The edge of tWZ comes in realising that while tWj for instance, embeds the $b\,W \to t\,Z$ amplitude, such final state corresponds to a real-radiation contribution to tW production at NLO. This QCD-induced process does not embed $b\,W \to t\,Z$ and, therefore, would likely reduce the sensitivity to several EW top quark couplings. Furthermore, and even at LO, tWj only differs from $t\bar{t}$ production and decay by a single b-tag. This may pose additional challenges in reconstructing the final state; that is, a $t\bar{t}$ event with one b quark mistagged as a light jet will have a final state identical to tWj. Conversely, for tWZ, *only* NLO corrections overlap with $t\bar{t}Z$ and weakly with $t\bar{t}$.

Another possibly competing process is tZj. It was found in Ref. [157] that this process has a significant promise in probing EW top quark couplings. However, due to phase space cancellations, some of the expected energy growth at the interference level was not observed. Finally, tWZ is not affected by any top quark four-fermion operators at the tree-level, contrary to all the other processes discussed. Therefore, it is worth considering tWZ as a complementary probe of new top quark interactions.

5.5.3. SMEFT operators relevant to tWZ

We considered SMEFT contributions to the tWZ process using the flavour symmetry assumption given in Eq. 2.31 and explained in the corresponding chapter. In our analysis, we followed the notation and operators conventions of Ref. [155] where we kept the symbol $\mathcal{O}$ for operators aligning with this convention. On the other hand, the symbol $\mathcal{Q}$ is retained for operators given in the original Warsaw basis. Eq. 5.5 shows all SMEFT operators affecting the $b\,W \to t\,Z$ scattering and/or tWZ full amplitude in our flavour assumption where the simple linear relations between the $\mathcal{O}$ and $\mathcal{Q}$ operators are shown in the same equation.

[2] Part of the NLO EW corrections to $t\bar{t}X$ involve the so-called tX scattering diagrams, which do not suffer the above mentioned s-channel suppression. [73,75]. This renders tX good candidates to study top quark EW interactions when considering NLO EW corrections [74,157].

$$
\begin{aligned}
\mathcal{O}_{\varphi D} &= (\varphi^\dagger D^\mu \varphi)^\dagger (\varphi^\dagger D_\mu \varphi), & \mathcal{O}_{tW} &= \mathcal{Q}_{tW} + (c_W/s_W)\,\mathcal{Q}_{tB},\\
\mathcal{O}_{\varphi WB} &= (\varphi^\dagger \tau_I \varphi)\, B^{\mu\nu} W^I_{\mu\nu}, & \mathcal{O}_{tZ} &= -\mathcal{Q}_{tB}/s_W,\\
\mathcal{O}_W &= \varepsilon_{IJK}\, W^I_{\mu\nu}\, W^{J,\nu\rho}\, W^{K,\mu}_{\rho}, & \mathcal{Q}^{(1)}_{\varphi Q} &= i\big(\varphi^\dagger \overleftrightarrow{D}_\mu \varphi\big)\big(\overline{Q}\,\gamma^\mu\, Q\big),\\
\mathcal{O}_{tG} &= i g_S \big(\overline{Q}\tau^{\mu\nu}\, T_A\, t\big)\, \tilde{\varphi}\, G^A_{\mu\nu} + \text{h.c.}, & \mathcal{Q}^{(3)}_{\varphi Q} &= i\big(\varphi^\dagger \overleftrightarrow{D}_\mu \tau_I \varphi\big)\big(\overline{Q}\,\gamma^\mu\, \tau^I Q\big),\\
\mathcal{Q}_{tW} &= i\big(\overline{Q}\tau^{\mu\nu}\, \tau_I\, t\big)\, \tilde{\varphi}\, W^I_{\mu\nu} + \text{h.c.}, & \mathcal{O}^{(-)}_{\varphi Q} &= \mathcal{Q}^{(1)}_{\varphi Q},\\
\mathcal{Q}_{tB} &= i\big(\overline{Q}\tau^{\mu\nu}\, t\big)\, \tilde{\varphi}\, B_{\mu\nu} + \text{h.c.}, & \mathcal{O}^{(3)}_{\varphi Q} &= \mathcal{Q}^{(3)}_{\varphi Q} + \mathcal{Q}^{(1)}_{\varphi Q},\\
& & \mathcal{O}_{\varphi t} &= i\big(\varphi^\dagger \overleftrightarrow{D}_\mu \varphi\big)\big(\bar{t}\,\gamma^\mu\, t\big).
\end{aligned}
\tag{5.5}
$$

In keeping with the the conventions of Refs. [68, 155], i.e. the "top-basis", the linear rotations between $\mathcal{O}$ and $\mathcal{Q}$ leads to the following rotation of the corresponding WCs:

$$
\begin{aligned}
c_{tW} &= C_{tW},\; c_{tZ} = -\sin\theta_W C_{tB} + \cos\theta_W C_{tW}\\
c^{(3)}_{\varphi Q} &= C^{(3)}_{\varphi Q},\; c^{(-)}_{\varphi Q} = C^{(1)}_{\varphi Q} - C^{(3)}_{\varphi Q}.
\end{aligned}
\tag{5.6}
$$

where c_i are the coefficients corresponding to $\mathcal{O}$ operators, and C_i are the coefficients corresponding to $\mathcal{Q}$ operators (note the rotation to c_{tZ} is the same one used in Eq. 3.14).

In summary, there are eight relevant operators consistent with the flavour symmetry assumption and contributing to tWZ via the $bW \to tZ$ sub-amplitude[3]. Although it does belong to the $bW \to tZ$ scattering, the top quark chromomagnetic moment, $\mathcal{O}_{tG}$, does affect the tWZ process through the coupling of the initial state gluon to the top quark. The first three entries of Eq. 5.5 are of the bosonic type in that they do not contain any fermion fields. They are primarily constrained by non-top quark data, such as EW precision data and diboson production. Interestingly, the typical assumption that these are better constrained than the remaining top quark operators does not hold any longer, particularly at the marginalised level. Nevertheless, we expect improvements in constraints in this sector to continue to be driven by non-top quark data and therefore restrict our analysis to the other operators,

$$
\{\mathcal{O}^{(3)}_{\varphi Q},\, \mathcal{O}^{(-)}_{\varphi Q},\, \mathcal{O}_{\varphi t},\, \mathcal{O}_{tW},\, \mathcal{O}_{tZ},\, \mathcal{O}_{tG}\}.
\tag{5.7}
$$

[3] Note that, in keeping with the assumed flavour symmetry, the right-handed charged current operator, $\mathcal{O}_{\varphi tb} = i\big(\tilde{\varphi}^\dagger D_\mu \varphi\big)\big(\bar{t}\,\gamma^\mu\, b\big)$, and the operator modifying the right-handed $Zb\bar{b}$ coupling, $\mathcal{O}_{\varphi b} = i\big(\varphi^\dagger \overleftrightarrow{D}_\mu \varphi\big)\big(\bar{b}\,\gamma^\mu\, b\big)$ are omitted, even though they contribute to the $bW \to tZ$ amplitude. The interference term of $\mathcal{O}_{\varphi tb}$ and the entire energy-growing contribution from $\mathcal{O}_{\varphi b}$ are suppressed by the b quark mass.

5.5.4. The $bW \to tZ$ sub-amplitude

In this section, we summarise the discussion of Ref. [157] relevant to tWZ. The work of Ref. [157] involved relating new interactions in the top quark EW sectors to the energy growth in the $b\,W \to t\,Z$ scattering. Dimension-six operators contributions to $2 \to 2$ scatterings can maximally have a quadratic dependence on the energy E. The interaction vertices of Fig. 5.5 depict the types of modified interactions that can potentially affect the tWZ process. Starting with modifications of the existing SM interactions, it is apparent that all possible neutral and charged top, and bottom quarks gauge interactions exist, i.e. $t\bar{t}Z$, $b\bar{b}Z$ and Wtb, as well as the W^+W^-Z triple-gauge coupling. In the high-energy (massless) limit, only the gauge couplings of the left-handed top and bottom quarks are relevant.

The energy growth arising from modifications of these vertices is understood to originate from the violation of some delicate unitarity cancellations in the SM. By this logic, one can rule out a shifted Wtb vertex as a possible source of energy growth since it appears in every diagram. Therefore it can only lead to a global rescaling of the amplitude. On the other hand, the remaining interactions participate in said unitarity cancellations. The leading energy growth is found to be in the left-handed, fully longitudinal helicity configuration, $(\lambda_b, \lambda_W, \lambda_t, \lambda_Z) = (-, 0, -, 0)$, and scales as $\sim E^2$;

$$\mathcal{A}(-,0,-,0) \propto \sqrt{s(s+t)}\,(g^Z_{b_L} - g^Z_{t_L} + g_{WZ})\,, \tag{5.8}$$

where $g^Z_{b_L}$, $g^Z_{t_L}$ and g_{WZ} denote generic couplings for the left-handed $b\bar{b}Z$, $t\bar{t}Z$ and the triple-gauge interactions, respectively, and s, t are the Mandelstam variables. Assigning SM values to each coupling leads to an exact cancellation, underlining that the non-abelian gauge-invariance of the theory relates all three couplings. On the other hand, independently modifying the couplings violates gauge symmetry and leads to non-unitary behaviour. Subleading sources of energy growth are also present,

$$\begin{aligned}\mathcal{A}(-,-,-,0) = \mathcal{A}(-,0,-,-) &\propto \sqrt{-t}\,(g^Z_{b_L} - g^Z_{t_L} + g_{WZ})\,,\\ \mathcal{A}(-,0,+,0) &\propto \sqrt{-t}\,(2m_W^2(g^Z_{b_L} - g^Z_{t_R} + g_{WZ}) - g_{WZ}m_Z^2)\,.\end{aligned} \tag{5.9}$$

The first corresponds to a change from longitudinal to a transverse polarisation of the W or Z boson with respect to Eq. 5.8, carrying the same cancellation structure and differing only by a factor of $\sim m_{W,Z}/\sqrt{s}$ associated to the helicity flip. The second has a non-trivial cancellation structure between the gauge couplings of two different

fermion representations, gauge boson self-interactions and the gauge boson masses. The involvement of the gauge coupling alongside the appearance of the gauge boson masses strongly suggests a connection to the EWSB, even though the Higgs boson does not explicitly participate in the scattering.

The helicity amplitudes[4] contributing to the $bW \to tZ$ scattering for the top-quark-specific operators of Eq. 5.7 are summarised in Tab. A.1 of appendix A.

The schematic high-energy behaviour of the corresponding SM helicity amplitudes is also given in the same table, from which one can infer the behaviour of the corresponding SMEFT interference term. The effective theory description can be used to identify the SMEFT origin of the three above mentioned examples. The modification of the interaction can be interpreted as coming from various combinations of the three current operators, $\mathcal{O}_{\varphi Q}^{(3)}$, $\mathcal{O}_{\varphi Q}^{(-)}$ and $\mathcal{O}_{\varphi t}$. The maximal growth from the $\mathcal{O}_{\varphi Q}^{(3)}$ operator can be identified with a dimension-six contact term, in the Feynman gauge, between the charged fermion and Goldstone boson currents,

$$\mathcal{O}_{\varphi Q}^{(3)} \supset (\bar{t}_L \gamma^\mu b_L)(G^0 \overset{\leftrightarrow}{\partial}_\mu G^+) + \text{h.c.} \tag{5.10}$$

In the high-energy limit, the Goldstone equivalence theorem [172] identifies amplitudes involving the Goldstone bosons with those of the longitudinal gauge degrees of freedom. This explains the $\sim E^2$ dependence induced by this operator in the fully longitudinal configuration. It is worth noting that the SMEFT introduces new Lorentz structures which are not present in the SM; this includes the weak dipole interactions. The ones relevant to the tWZ process are the $\mathcal{O}_{tW}$ and $\mathcal{O}_{tZ}$ operators, which couple the right-handed top and the left-handed bottom quarks. They predict maximal energy growth in the mixed transverse-longitudinal configurations with a flipped fermion helicity.

The SM has a constant energy growth in the three configurations (according to the polarisation of the gauge bosons). Of which, the left-hand fully-longitudinal one coincides with the leading energy growth from $\mathcal{O}_{\varphi Q}^{(3)}$, such that one would expect an energy-growing interference term. Other sources of energy growth in the SMEFT have a counter SM energy dependence, such that the interference term is significantly suppressed. This is a consequence of the so-called "non-interference" theorems from helicity selection rules in $2 \to 2$ scattering at dimension-six involving at least one transverse gauge boson [173].

[4] In the helicity amplitude approach, amplitudes are calculated for a given assignment of particle helicities.

5.5.5. Embedding the $bW \to tZ$ sub-amplitude

Before moving on to the SMEFT predictions of tWZ, I present the results from embedding the $b\,W \to t\,Z$ sub-amplitudes into the tWZ process at the high-energy limit. Our aim was to compare the impact of the $b\,W \to t\,Z$ sub-amplitude in the full tWZ process to our expectations from the previous analysis, where we assessed the scaling of $b\,W \to t\,Z$ with $\sqrt{s}$ with different operators insertions. We can then quantify the extent to which the energy growth is retained in realistic collider observables. We simulated the contribution from each operator in Eq. 5.7 with `MadGraph5` using the `SMEFTatNLO` model. Exploiting `MadGraph5` feature of handling the polarisation of initial and final states [174], we split the cross-section in the helicities of the W and Z bosons, where 'T' and '0' denote transverse ($\lambda_i = \pm$) and longitudinal ($\lambda_i = 0$) polarisation, respectively, and appropriately summing/averaging over all others. The polarisation is defined as the projection of the spin component along the particle momentum in the centre-of-mass frame of the partonic collision, not in the lab frame.

The differential cross-sections in the invariant mass bins of the WZ system, m_{WZ}, are presented in Fig. 5.6, where m_{WZ} acts as a proxy for the $b\,W \to t\,Z$ sub-amplitude scattering energy. SMEFT contributions were truncated at interference-level, $\mathcal{O}(\Lambda^{-2})$, with $c_i/\Lambda^2 = 1$ TeV $^{-2}$. The expected high-energy enhancement from the operator contribution is apparent in the fully longitudinal configuration (upper left panel). The inset shows the ratio of each operator interference term to the SM. At low energies, the effect of this operator leads to a net positive shift with respect to the SM, while the new-physics contribution exhibits a sign change at around $m_{WZ} = 500$ GeV. For this coefficient value, the relative impact reaches 100% at around $m_{WZ} = 1$ TeV. Beyond this point, the $\mathcal{O}(\Lambda^{-2})$ truncated prediction is not physical since it predicts a negative cross-section. Moreover, for this configuration, the energy-enhanced effect from $\mathcal{O}_{tG}$ can be understood as follows: at LO, large m_{WZ} involves a recoil against a high-p_T top quark. The recoil is enhanced by the derivative interaction of the chromomagnetic operator. The contribution from $\mathcal{O}_{tW}$ appears relatively mild and enhanced at low energies. This fully longitudinal configuration has no induced energy-growing interference effects for all other operators, in line with the expectations from the energy scaling in Tab. A.1.

In fact, taken at face-value, Tab. A.1 implies that we should not observe any other energy-growing interference effects in any different configuration. Nevertheless, we still observe some of the "non-interfering" operators yielding some energy growth. This observation suggests that finite mass effects remain essential in our studied energy range. In both mixed longitudinal-transverse configurations (upper right and lower left panels), energy growth is evident for $\mathcal{O}_{tW}$ and mildly for $\mathcal{O}_{tZ}$. $\mathcal{O}_{tG}$ exhibits energy

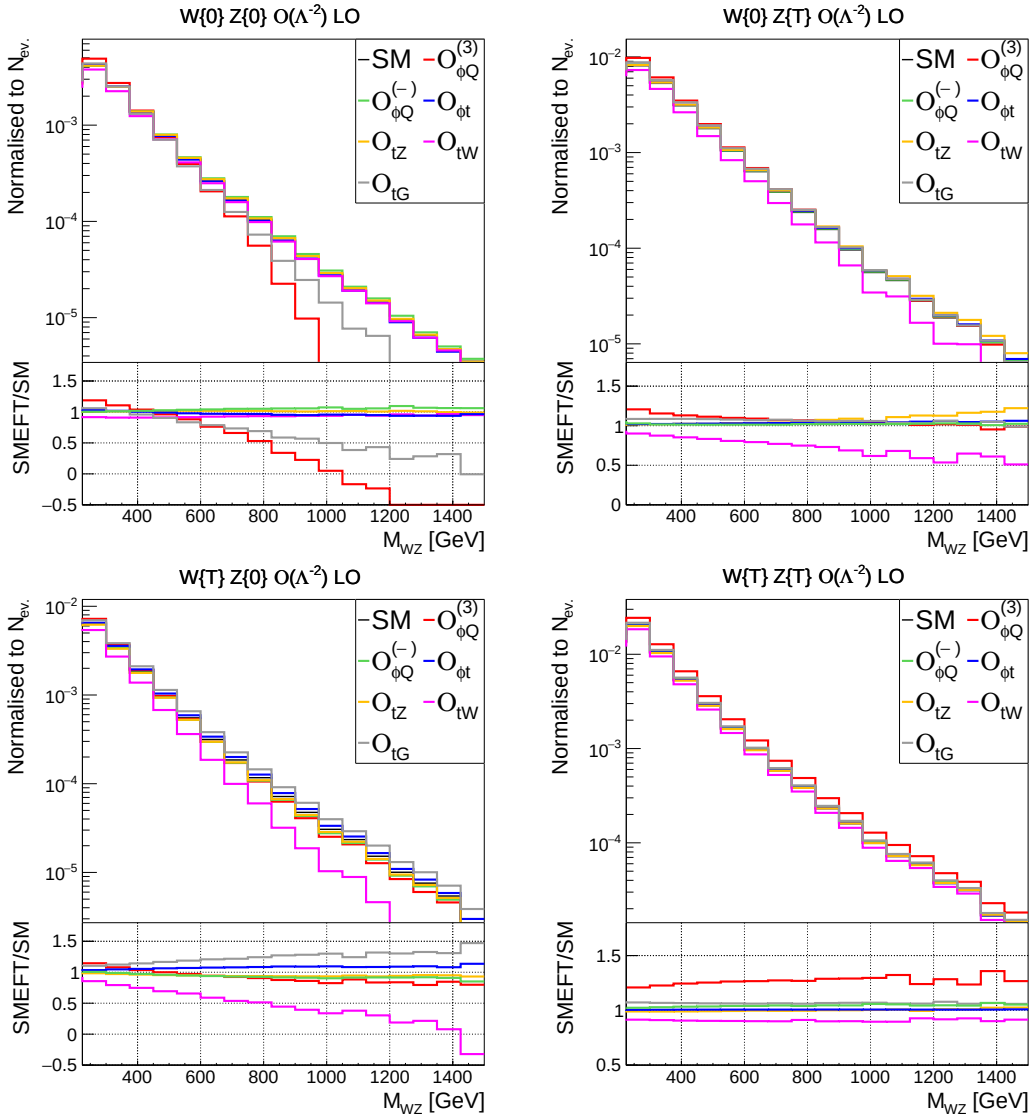

Figure 5.6.: LO SM and SMEFT contributions to the differential cross-section of the tWZ process in the WZ invariant mass bins for different W and Z helicity configurations. SMEFT predictions were computed for $c_i/\Lambda^2 = 1$ TeV $^{-2}$, and truncated at the interference-level, $\mathcal{O}(\Lambda^{-2})$. The curly brackets indicate the helicity eigenstates following the notation of `MadGraph5`, where `{0}` and `{T}` refer to longitudinal and transverse polarisation, respectively. The inset shows the ratio of the SM+EFT contribution to the SM.

growth for $\lambda_W, \lambda_Z = \pm, 0$ but strangely not in the other mixed configuration. The effects from $\mathcal{O}^{(3)}_{\varphi Q}$ persist, albeit at a milder level. The fully transverse configurations (lower right panel) do not show any evidence of enhanced interference effects but do receive energy-constant contributions from $\mathcal{O}^{(3)}_{\varphi Q}$, $\mathcal{O}_{tW}$, and $\mathcal{O}_{tG}$.

It is interesting to note the hierarchy in SM rates among the different configurations, the fully-transverse being the largest (56.20 fb), followed by the mixed transverse-longitudinal (47.64 fb) and finally the fully-longitudinal (12.57 fb). Measurements that are blind to the gauge boson polarisation are weighted by the relative size of each configuration. This dilutes the impact of the rarer configuration modes, which is evident in the *left* panel of Fig. 5.7 showing the interference effects of each operator on the total unpolarised differential cross-section. The contributions from $\mathcal{O}_{\varphi Q}^{(3)}$ and $\mathcal{O}_{tW}$ have a minor relative impact, and the crossing point of the former is shifted to higher m_{WZ} through the positive and constant effect in the fully-transverse configuration. Diluted by their lack of effect on the fully-transverse configuration, the contributions from all other operators are immensely suppressed. The right panel of Fig. 5.7, includes the quadratic $\mathcal{O}(\Lambda^{-4})$ terms in the unpolarised cross-section prediction. For this

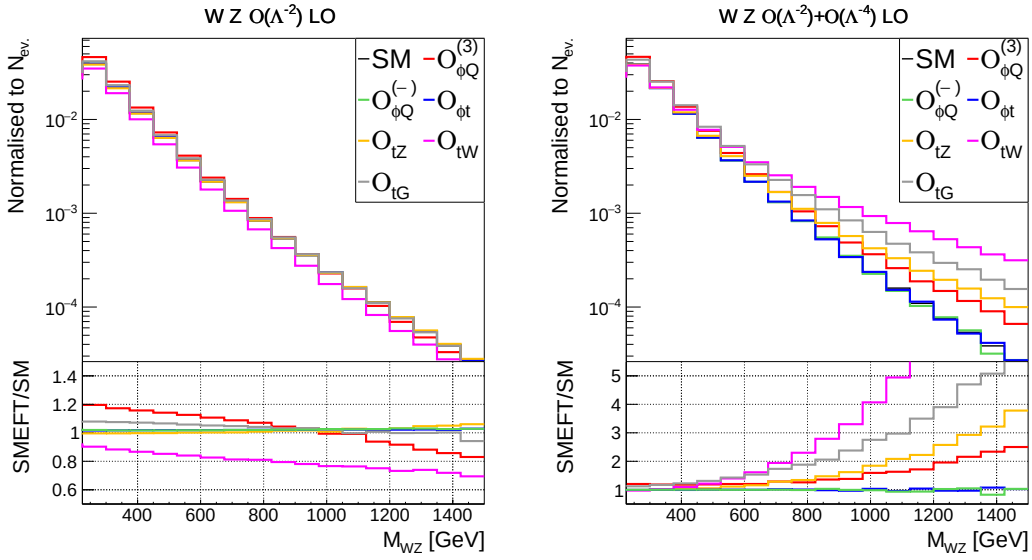

Figure 5.7.: Same as Figs. 5.6 (*left*) and Fig. A.1 (*right*), but showing contributions to the total unpolarised cross-section.

point in parameter space, i.e. $c_i/\Lambda^2 = 1$ TeV $^{-2}$, the quadratic terms start to dominate around $m_{WZ} \sim 350$ GeV, yielding significant energy growth for all operators except for $\mathcal{O}_{\varphi Q}^{(-)}$ and $\mathcal{O}_{\varphi t}$. One can therefore anticipate that the latter two operators are not likely to be significantly constrained by high-energy measurements in tWZ. The polarised breakdown of the full SMEFT contributions are shown in Fig. A.1 in appendix A.2. Ultimately, the relative importance of quadratic terms depends on both the probed energy scales and the data constraining power. It, therefore, should not be used as a measure of the EFT validity until a global fit is performed.

5.6. *tWZ* SMEFT predictions

In this section, I present our tWZ SMEFT predictions using high-energy observables, i.e. m_{WZ}, that maximise sensitivity to the SMEFT by enhancing unitarity-violating effects. As discussed in Sec. 5.4, in the high-energy phase space regions, the contribution of the t overlap becomes non-resonant and should be retained. Therefore, as far as the SMEFT phase space is concerned, it is only the $t\bar{t}Z$ overlap that we should care about. Furthermore, we made the simplifying assumption of keeping the Z boson stable. On one side, this maps better to the discussion on unitarity-violating behaviour in $b\,W \to t\,Z$, and on the other, the approximation was already justified in our study of the SM process.

For our SM predictions, we simulated the tWZ process via `MadGraph5` at NLO in QCD accuracy. The same is true for SMEFT predictions, where we have also used the `SMEFTatNLO` model. In contrast to the SM results, for SMEFT predictions, we used the recommended fixed factorisation, renormalisation scales μ_F, μ_R of 172 GeV $\sim (m_t + m_W + m_Z)/2$, since `MadGraph5` does not evolve operator coefficients[5]. The proton PDFs and their uncertainties are evaluated employing reference sets and error replicas from the `NNPDF3.1 NLO` global fit in the 5FS, in which the bottom quark is taken to be massless. We did not make any parton-level selections. The b-veto method for suppressing the overlapping resonant contributions proved effective for the SM and the SMEFT.

It is worth noting that, in principle, all of the operators contribute to the overlapping processes, which we consider in our simulation. However, in practice, the b-veto should suppress these effects. One should consider this when considering the overlapping processes as backgrounds in a SMEFT interpretation. Finally, some of the operators can also modify the top quark width. Our predictions did not model this effect as we assumed the top quark to be stable, except in the resonant diagrams where in applying DR/DS, the width only acts as a regulator. In these cases, its precise value does not matter as long as it is negligible with respect to all other relevant scales since the resonant squared amplitude is never evaluated.

[5] The EFT renormalisation scale parameter, `mueft`, of `SMEFTatNLO` in `MadGraph5` is not relevant unless the running of the EFT coefficients is included. We did not consider the running of the EFT coefficients in this work.

5.6.1. Fixed order predictions

Tab. 5.1 presents the SM inclusive cross-section predictions as well as predictions in a high-energy region of the phase space at LO and NLO in QCD. The high-energy region was defined by requiring the transverse momenta, p_T, of the W and Z bosons to be greater than 500 GeV. For SMEFT contributions, Tab. 5.2 summarises the inclusive

	Inclusive			High-Energy		
	LO	NLO DR1	NLO DR2	LO	NLO DR1	NLO DR2
SM	$103.36(4)^{+12.76\%}_{-12.82\%}$	$106.70(15)^{+4.97\%}_{-6.28\%}$	$106.80(9)^{+5.04\%}_{-5.62\%}$	$0.073(0)^{+15.92\%}_{-14.23\%}$	$0.048(0)^{+10.86\%}_{-18.35\%}$	$0.036(0)^{+26.82\%}_{-45.63\%}$

Table 5.1.: The SM contributions [fb] to inclusive and high-energy tWZ production at LO and NLO accuracies within their QCD scale uncertainties at $\sqrt{s}$ =13 TeV. These results are for DR1 and DR2 predictions when applying a veto on b quarks with $|\eta| < 2.5$ or $p_T > 30$ GeV. The stability of the SM DR1 and DR2 cross-sections signifies the efficiency of the b-veto.

cross-sections of the linear $\mathcal{O}(\Lambda^{-2})$ and quadratic contributions $\mathcal{O}(\Lambda^{-4})$ for each of the six relevant operators, at LO and NLO at $c_i/\Lambda^2 = 1$ TeV $^{-2}$. The impacts of the SMEFT

c_i	$\mathcal{O}(\Lambda^{-2})$			$\mathcal{O}(\Lambda^{-4})$		
	LO	**NLO DR1**	**NLO DR2**	**LO**	**NLO DR1**	**NLO DR2**
$c_{\varphi Q}^{(3)}$	$19.78(1)^{+12.98\%}_{-13.02\%}$	$21.20(2)^{+5.66\%}_{-6.13\%}$	$21.37(3)^{+5.90\%}_{-6.27\%}$	$4.94(1)^{+10.53\%}_{-10.62\%}$	$4.71(2)^{+4.88\%}_{-6.37\%}$	$4.72(2)^{+4.90\%}_{-6.50\%}$
$c_{\varphi Q}^{(-)}$	$2.19(0)^{+12.65\%}_{-12.72\%}$	$2.69(1)^{+8.92\%}_{-8.18\%}$	$2.74(1)^{+8.52\%}_{-8.17\%}$	$0.44(0)^{+12.18\%}_{-12.29\%}$	$0.48(0)^{+5.89\%}_{-5.89\%}$	$0.48(0)^{+5.86\%}_{-6.03\%}$
$c_{\varphi t}$	$1.77(0)^{+13.11\%}_{-13.13\%}$	$1.81(0)^{+4.81\%}_{-5.53\%}$	$1.84(0)^{+5.08\%}_{-5.74\%}$	$0.19(0)^{+11.44\%}_{-11.61\%}$	$0.18(0)^{+4.45\%}_{-7.08\%}$	$0.17(0)^{+5.09\%}_{-7.54\%}$
c_{tW}	$-11.34(1)^{+12.27\%}_{-12.15\%}$	$-11.49(2)^{+5.84\%}_{-5.57\%}$	$-11.68(1)^{+5.72\%}_{-5.41\%}$	$24.06(3)^{+10.53\%}_{-9.90\%}$	$23.38(5)^{+4.15\%}_{-5.18\%}$	$22.79(3)^{+4.59\%}_{-6.41\%}$
c_{tZ}	$-0.26(0)^{+11.03\%}_{-11.01\%}$	$-0.35(2)^{+4.99\%}_{-6.66\%}$	$-0.34(1)^{+5.47\%}_{-7.06\%}$	$5.23(1)^{+10.53\%}_{-10.05\%}$	$4.90(2)^{+4.59\%}_{-6.69\%}$	$4.94(1)^{+4.64\%}_{-6.57\%}$
c_{tG}	$7.95(0)^{+13.00\%}_{-13.04\%}$	$7.36(1)^{+4.00\%}_{-5.01\%}$	$7.26(1)^{+4.65\%}_{-6.29\%}$	$15.04(3)^{+11.61\%}_{-11.22\%}$	$12.19(8)^{+6.97\%}_{-11.93\%}$	$12.17(7)^{+6.95\%}_{-11.96\%}$

Table 5.2.: The LO and NLO SMEFT contributions [fb] to inclusive tWZ production, at linear and quadratic levels, including QCD scale uncertainties, for the LHC $\sqrt{s} = 13$ TeV and $c_i/\Lambda^2 = 1$ TeV $^{-2}$. These results are for DR1 and DR2 predictions obtained when imposing a veto on b quarks with $|\eta| < 2.5$ or $p_T > 30$ GeV.

operators on the inclusive cross-section and in the high-energy region are presented in Tab. 5.3. Moreover, the radar charts shown in Fig. 5.8 depict the relative impact of each operator with respect to the corresponding SM prediction at NLO. The *Left* and *right* panels show the effect of the interference term and squared term, respectively, for $c_i/\Lambda^2 = 1$ TeV $^{-2}$. Purple (orange) points correspond to the impact on the inclusive (high-energy) phase space.

c_i	Inclusive						High-Energy					
	$\mathcal{O}(\Lambda^{-2})$			$\mathcal{O}(\Lambda^{-4})$			$\mathcal{O}(\Lambda^{-2})$			$\mathcal{O}(\Lambda^{-4})$		
	LO	NLO	K	LO	NLO	K	LO	NLO	K	LO	NLO	K
$c_{\varphi Q}^{(3)}$	0.191	0.200	1.05	0.048	0.044	0.92	-0.870	-0.715	0.82	5.626	7.476	1.33
$c_{\varphi Q}^{(-)}$	0.021	0.026	1.24	0.004	0.004	1.00	0.028	0.056	2.00	0.058	0.057	0.98
$c_{\varphi t}$	0.017	0.017	1.00	0.002	0.002	1.00	0.017	0.023	1.35	0.056	0.054	0.96
c_{tW}	-0.110	-0.109	0.99	0.233	0.213	0.91	-0.528	-0.524	0.99	30.905	40.695	1.32
c_{tZ}	-0.003	-0.003	1.00	0.051	0.046	0.90	0.098	0.076	0.78	7.739	10.482	1.35
c_{tG}	0.077	0.068	0.88	0.145	0.114	0.79	-0.232	-0.354	1.53	7.488	5.242	0.70

Table 5.3.: Relative SMEFT operator contributions (DR2 predictions) to inclusive and high-energy tWZ production, i.e. SMEFT cross-sections normalised by the corresponding LO (NLO) SM predictions in the inclusive and high-energy regions shown in Tab. 5.1. The "K-factors" are defined as the ratio between NLO and LO impacts, these are not traditional K-factors since the NLO process is defined up to the diagram-removal scheme and the b-veto implementation.

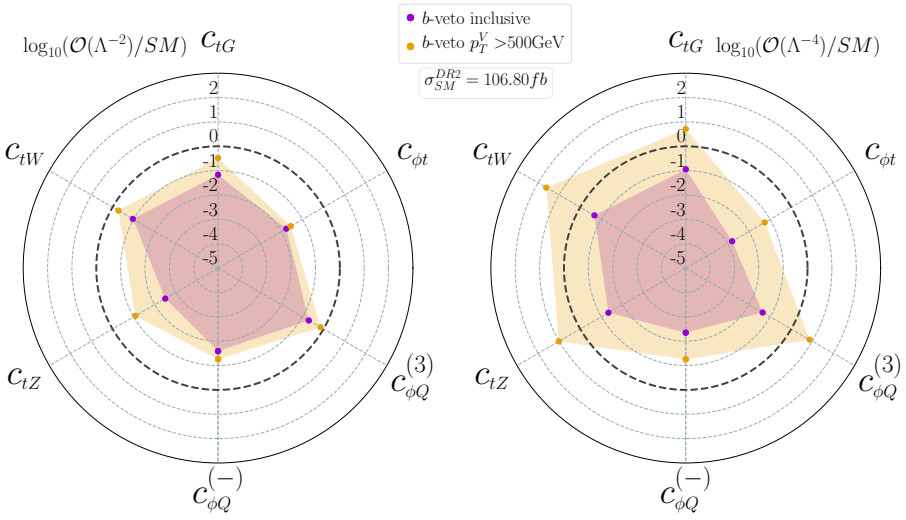

Figure 5.8.: Relative impact of the linear (*left*) and quadratic (*right*) SMEFT contributions to the tWZ process at NLO accuracy in QCD, applying the DR2 overlap removal and a veto on central ($|\eta| < 2.5$) or hard ($p_T > 30$ GeV) b-jets. They were obtained by dividing the cross-section contributions over the inclusive (magenta) and high-energy (orange) phase space regions by the corresponding SM prediction. The high-energy phase space region is defined by requiring the W and Z bosons p_T to be greater than 500 GeV.

In the *left* panel of Fig. 5.8 and as expected from Tab. A.1, the enhancement at high energies of the $\mathcal{O}_{\varphi Q}^{(3)}$ interference term is apparent. Furthermore, a significant

enhancement of $\mathcal{O}_{tZ}$ indicates cancellations at the inclusive level being lifted by the selections. The interfering growth observed for $\mathcal{O}_{tW}$ in the LO differential distribution shown in Fig. 5.7 is confirmed here. Finally, the neutral current operators $\mathcal{O}_{\varphi Q}^{(-)}$ and $\mathcal{O}_{\varphi t}$ do not display significant energy-growing interference, in line with expectations. Moving to the quadratic contributions in the *right* panel, we observed energy growth across the board. The growth here is beyond the one depicted in Fig. 5.7, thanks to the logarithmic scale. As seen from Tab. 5.3, the impacts are broadly found to be stable under QCD corrections, where significant deviations from unity occur in cases where the overall contribution is relatively small. Notable exceptions are the $\mathcal{O}_{\varphi Q}^{(3)}$ and $\mathcal{O}_{tG}$ impacts in the high-energy region. This stability under QCD corrections further confirmed that our DR treatment of the $t\bar{t}Z$ and $t\bar{t}$ overlap has been correctly identifying the phase space of the tWZ process in the SMEFT case.

I now move to the differential SMEFT predictions; for these, we used kinematic observables, namely the transverse momenta of the top quark, W or Z, and the WZ invariant mass, M_{WZ}. Since we already observed that the contributions from $\mathcal{O}_{\varphi t}$ and $\mathcal{O}_{\varphi Q}^{(-)}$ operators are relatively insignificant, we omitted them in the rest of the study. Differential distributions are presented for the remaining operators, $\mathcal{O}_{\varphi Q}^{(3)}$, $\mathcal{O}_{tW}$, $\mathcal{O}_{tZ}$ and $\mathcal{O}_{tG}$ in Figs. 5.9, 5.10, 5.11 and 5.12, respectively. These are DR2 predictions generated for the $\sqrt{s} = 13$ TeV LHC in subtracting only the $t\bar{t}Z$ overlap and applying the b-veto. The main figure shows the NLO prediction in the SM in black, alongside predictions for $c_i/\Lambda^2 = 1$ TeV $^{-2}$. The red and green lines correspond to SMEFT prediction taking only interference into account or both the interference and the squared contributions, respectively. The first inset displays the relative scale uncertainty obtained from a nine-point renormalisation and factorisation scale variation around the 172 GeV central scale. The second and third insets show the ratio of the two coloured lines in the main figure to the SM prediction. For reference, both insets include the same ratio at LO.

The $\mathcal{O}_{\varphi Q}^{(3)}$ distributions in Fig. 5.9 confirmed our expectations formed from the previously discussed helicity amplitudes and LO studies. The energy-growing interference contributions are present in all distributions except for $p_T(t)$; the latter does not capture considerable energy-growing effects. This is expected since the final state top quark is not part of the embedded $b\,W \to t\,Z$ scattering. The energy growth is most pronounced in M_{WZ}, confirming the latter is likely the best proxy for the sub-amplitude centre-of-mass energy.

Figs. 5.10 and 5.11 show the same distributions for both weak dipole operators. Both operators show the expected growth in the quadratic contributions, which is particularly strong for $\mathcal{O}_{tW}$. The latter also exhibits some sub-dominant interference

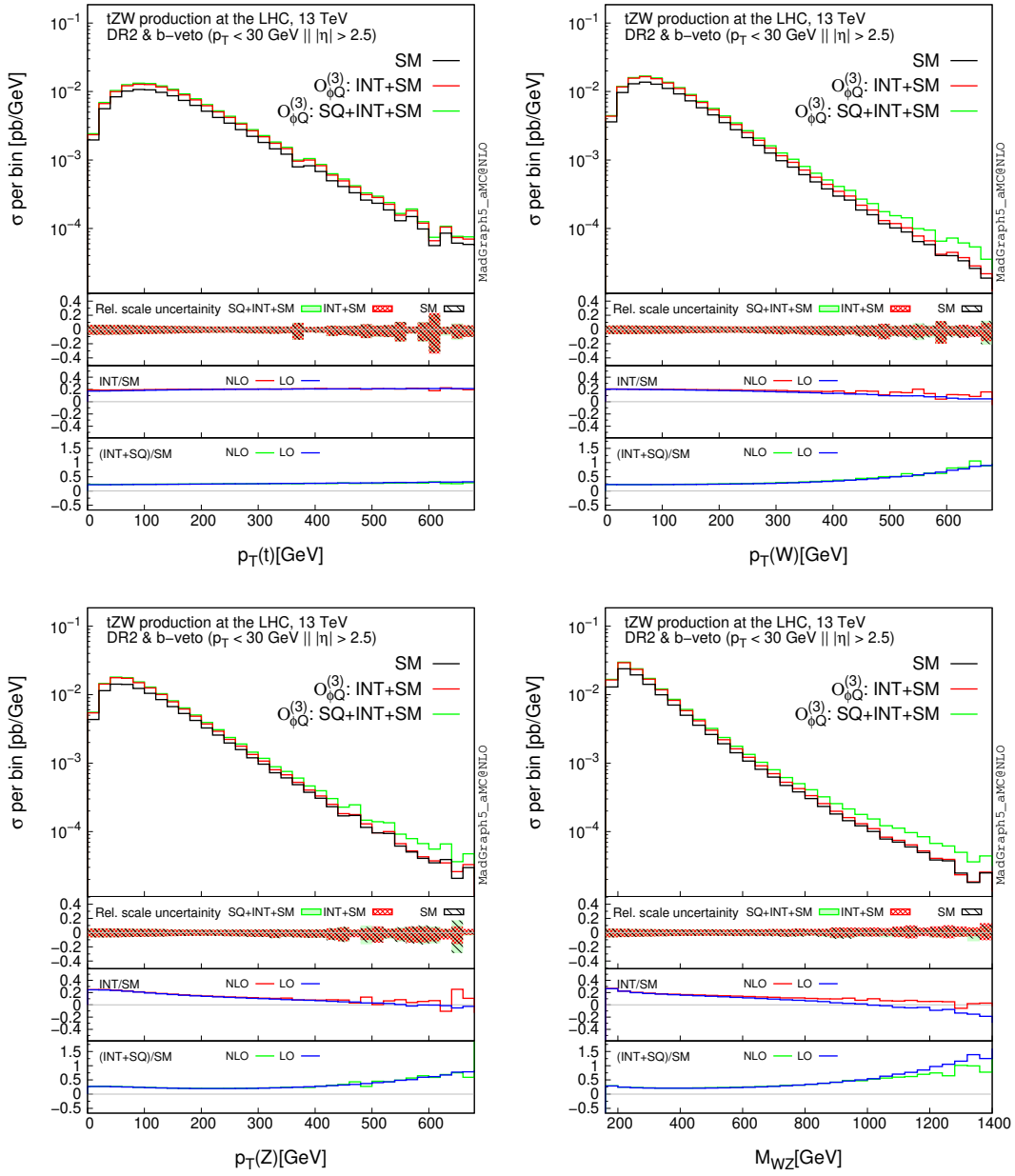

Figure 5.9.: Clockwise from *top left*: the transverse momentum of the (anti)top quark, $p_T(t)$, of the $W^{\pm}$ boson, $p_T(W)$, the invariant mass of the WZ pair, M_{WZ}, and the transverse momentum of the Z boson, $p_T(Z)$ at DR2 for the $\mathcal{O}^{(3)}_{\varphi Q}$ SMEFT operator when the $t\bar{t}Z$ overlap is subtracted and the b-veto is imposed, at FO NLO accuracy. The legends correspond to different computations for different SMEFT contributions. The first inset shows the scale variations in the process. The middle and the last insets show (at LO and NLO) the interference and the full SMEFT contribution relative to the SM, respectively. The relative scale uncertainties are computed on the summed cross-sections and not separately on the interference and the quadratic SMEFT contributions.

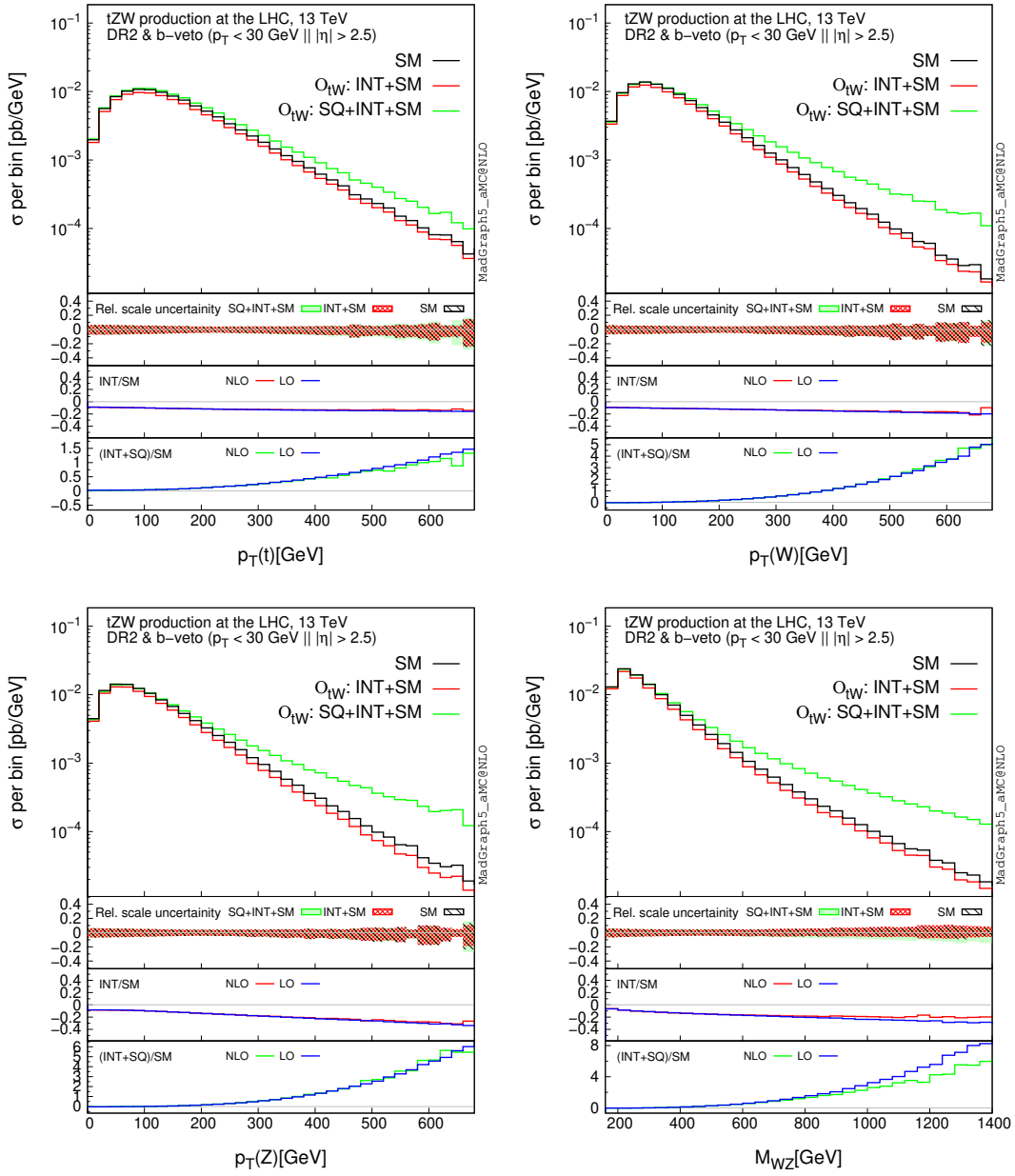

Figure 5.10.: Same as Fig. 5.9 but for the $\mathcal{O}_{tW}$ operator

contributions, in contrast to $\mathcal{O}_{tZ}$ whose interference is highly suppressed. In contrast to the current operator $\mathcal{O}^{(3)}_{\varphi Q}$, both weak dipole operators do impact the $p_T(t)$ distributions, albeit in a milder way than the other kinematic variables.

Fig. 5.12 presents the predictions for the top quark chromomagnetic operator, $\mathcal{O}_{tG}$. This operator does not contribute to $b\,W \to t\,Z$ scattering and therefore has a slightly different behaviour from the previous three operators. As expected from Fig. 5.8, energy growth is evident in all quadratic contributions. The main difference with the

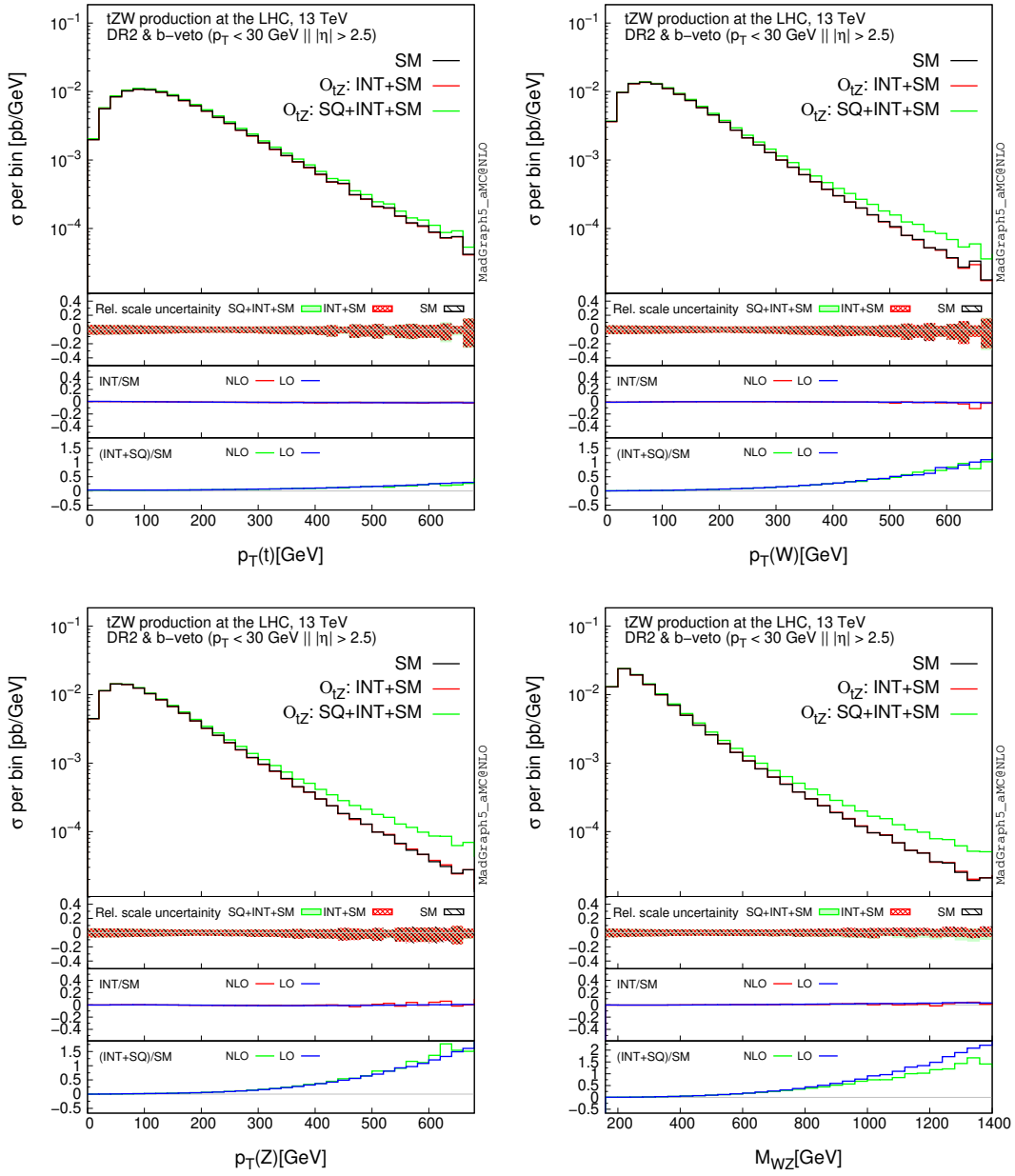

Figure 5.11.: Same as Fig. 5.9 but for the $\mathcal{O}_{tZ}$ operator

other operators is that the relative sensitivity of $p_T(t)$ is about the same as the other kinematic variables. Such observation highlights that the final state gauge bosons that participate in the EW top quark scattering do not have particular importance in this case. Similar to other dipoles, the interference contributions are suppressed due to the helicity flipping structure of this type of effective operator. Finally, in all distributions, the last two insets emphasise the stability of the relative SMEFT impacts under QCD corrections.

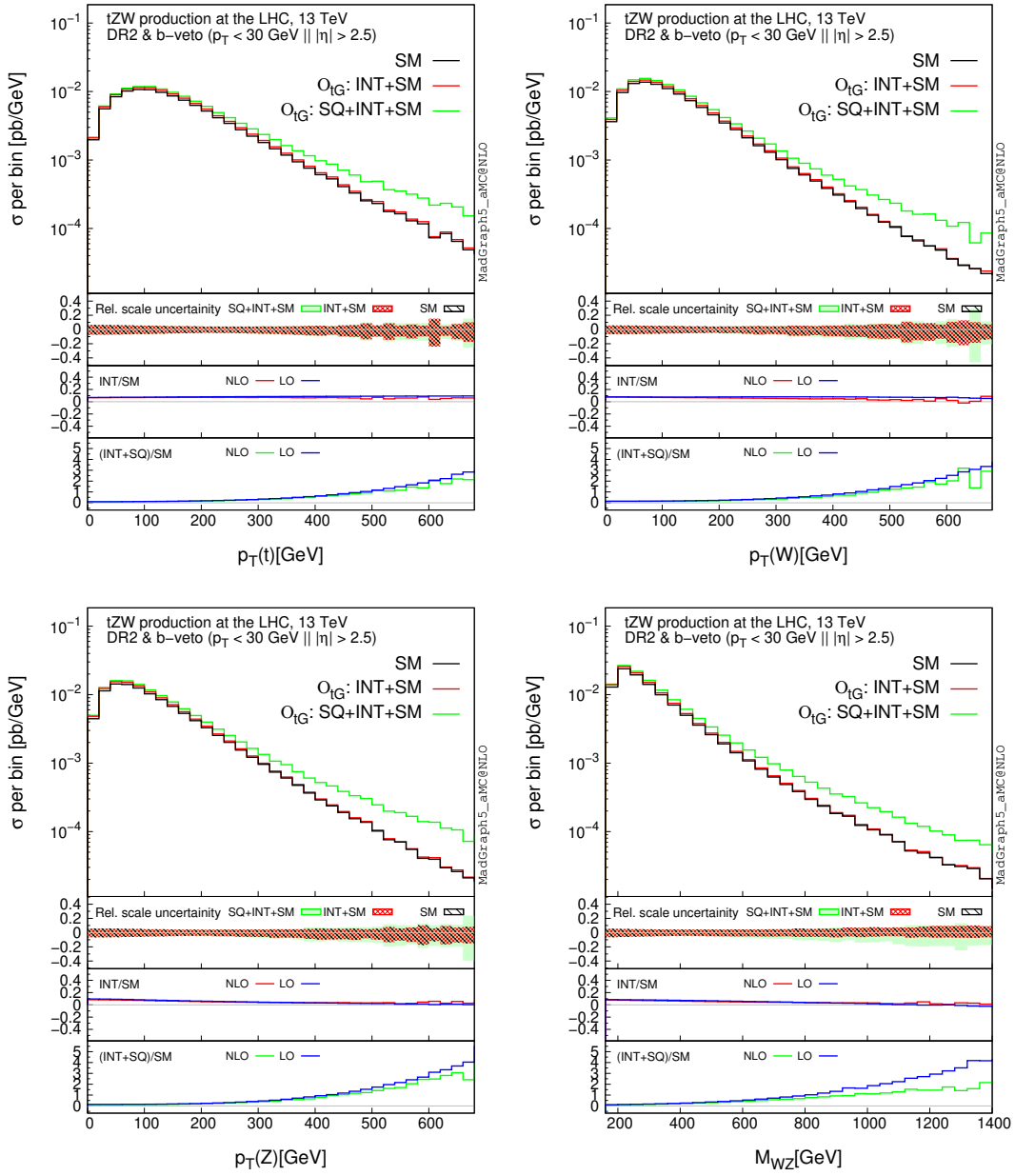

Figure 5.12.: Same as Fig. 5.9 but for the $\mathcal{O}_{tG}$ operator

5.6.2. NLO matched to PS

This section presents SMEFT predictions matched to PS. For this exercise, we used a single EFT operator, $\mathcal{O}^{(3)}_{\varphi Q}$, which best probes unitarity-violation in $b\,W \to t\,Z$. We matched short-distance events with `Pythia8` using the `MC@NLO` method [175] as automated inside `MadGraph5`. The (anti)top quark was allowed to decay in our setup. In contrast, W and Z bosons either appearing in the partonic event or originating

from the decay were kept stable. Jets were defined using the anti-k_T algorithm [176] implemented in `FastJet` [177], with cone radius $R = 0.4$, and the requirement of having $p_T(j) > 30$ GeV and $|\eta(j)| < 4.5$. A jet is b-tagged if a b-hadron appears among its constituents and if $|\eta(j_b)| < 2.5$. The analysis assumed 100% b-tagging efficiency. We selected events with exactly one b-jet and a central W and Z boson, $|\eta(W)| < 2.5$ & $|\eta(Z)| < 2.5$, hereafter referred to as the `1-bjet` scenario. The latter is the equivalent of imposing the b-jet veto we used in obtaining FO predictions, since at NLOPS the top quark decay typically gives rise to an extra b-jet. Most of the time, this jet is the hardest in the event.

The NLOPS predictions are presented in Fig. 5.13, where the transverse momentum distributions of the W boson and of the Z boson are displayed. The former distribution refers to ones of W bosons arising from the hard-scattering event, which is differentiated from the one stemming from the top quark decay using the MC truth. The *top* row of Fig. 5.13 shows the SM distributions in the two diagram removal schemes. From these distributions, the efficacy of the single b-jet requirement in bringing the two predictions together is apparent, thus acting like the parton-level b-veto. Figures in the lower row show the effect of $\mathcal{O}_{\varphi Q}^{(3)}$. The behaviour of higher-dimension operators closely resembles that of FO, shown in Fig. 5.9. A common feature of the NLOPS results is the increased scale uncertainty compared to the FO predictions and the more significant discrepancies between DR1 and DR2 predictions in the distributions tails. This feature was also observed in Ref. [167] in the tWH process, likely occurring due to additional b-jets from the top quark decays. Therefore, the analysis at high-p_T may occasionally select the "wrong" b-jet. Ref. [167] showed that this discrepancy is fully suppressed when using MC truth information on the b-jet origin. In summary, the tWZ process is very stable under PS. This stability is expected because EW interactions primarily drive such process. In general, the results presented prove the principle for the realistic generation of precise SMEFT predictions. Therefore, the methods presented in this work can be used in future measurements and new physics searches. The latter being primarily through precision LHC EFT interpretations of tWZ data in the SMEFT framework.

Since global EFT studies are the ultimate goal of the SMEFT paradigm, more data from different measurements will undoubtedly aid in our understanding of the top quark couplings. This motivates the theoretical studies of different top quark processes in the SMEFT approach. One phenomenologically rich top quark process is the four top quark production, which is the main topic of the next chapter.

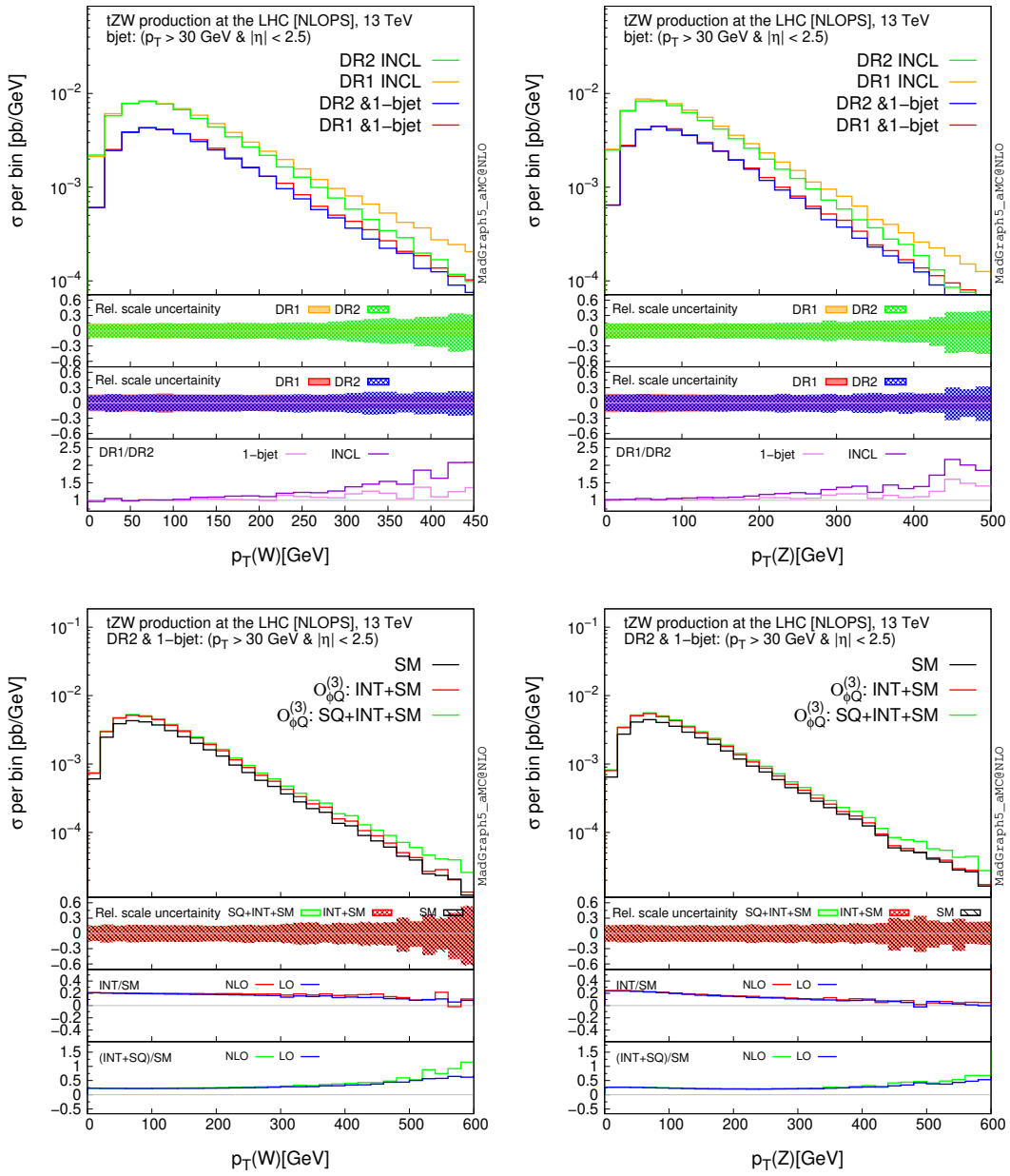

Figure 5.13.: The *top* row shows the NLOPS predictions for the transverse momentum of the $W^{\pm}$ boson, $p_T(W)$ (*left*) and of the Z boson, $p_T(Z)$ (*right*) in the SM at DR1 and DR2 for both inclusive and `1-bjet` scenarios. The insets in the top row are the same as in the left panel of Fig. 5.3. The *bottom* row shows the same observables at DR2 for the $\mathcal{O}^{(3)}_{\varphi Q}$ operator when the selection of one hard b-jet is imposed, at NLOPS. The insets in the *bottom* row are the same as in Fig. 5.9

Chapter 6.

Complete SMEFT predictions for four top quark production

The dimension-six SMEFT compromises many of the so-called four-fermion operators connecting four fermion lines in a contact-interaction term. A subclass of those four-fermion operators is the so-called four heavy, i.e. operators connecting four heavy quarks. The main probe of this subclass of operators is the four top quark production which is an inherently non-trivial process with several interesting subtleties. This renders the study of four top quark production in the context of SMEFT key to future global studies.

In this chapter, I discuss the four top quark production at hadron colliders in the context of SMEFT [2]. This work analysed the tree-level four top quark production, including all possible QCD- and EW-couplings orders and relevant dimension-six operators. We found several cases where formally subleading terms give rise to significant contributions, providing sensitivity to a broad class of operators. We obtained inclusive and differential predictions at the LHC and a future pp circular collider operating at $\sqrt{s} = 100$ TeV. Moreover, we performed a toy fit to set limits on SMEFT Wilson coefficients. We assessed the importance of including subleading terms and differential information in constraining new physics contributions. Finally, we computed the SMEFT predictions for the double insertion of dimension-six operators to scrutinise possible enhancements to the EFT sensitivity induced by higher order terms in the EFT series.

Declaration

The following is the author's contribution to this work:

- Contributing equally with Rafael Aoude in splitting the EW couplings in the simulation.
- Contributing equally with Rafael Aoude in cross-checking the analytical leading order coupling expansion with the one obtained from the simulation.
- Writing the analysis codes used in obtaining all the predictions.
- Performing all computations and making all plots excluding the plot presented in Fig. 6.12.

The author's contribution excludes the writing of the `Mathematica` used for the toy fit. The implementation of the $\mathcal{O}_{\varphi G}$ operator in `SMEFTatNLO` is not a part of the author's contribution.

6.1. On the four top quark process

The third run of the LHC, characterised an increase in collision centre of mass-energy from 13 TeV to 13.6 TeV and a two-fold increase of luminosity, will provide a new handle on rare phenomena. Among the rarest and most spectacular processes at the LHC is the production of four top quarks, $t\bar{t}t\bar{t}$. This process is marked by a tiny SM cross-section at 13 TeV, of about 12 fb [73], i.e., around five orders of magnitude lower than that of $t\bar{t}$ production. Despite the tiny rates, $t\bar{t}t\bar{t}$ signatures are distinctive, leading to a prosperous and energetic final state, which is challenging to mimic through other processes. The very high-Q^2 and low backgrounds offer a unique opportunity for probing new physics [178–191].

NLO corrections of four top quark production in QCD were computed first in Ref. [192] and then included in event generators [9, 78, 193]. The complete NLO predictions of $t\bar{t}t\bar{t}$ production in pp collisions at 13 TeV for the LHC and at 100 TeV for future circular colliders were calculated in Ref. [73]. The latter study revealed a peculiar and unforeseen interplay between EW and QCD contributions, with significant contributions with opposite signs arising from formally subleading terms. Significant subleading contributions were also observed in the case of new physics contributions to $t\bar{t}t\bar{t}$ [155, 190].

In the SM, representative diagrams of the pure-QCD $\mathcal{O}(\alpha_s^2)$ $t\bar{t}t\bar{t}$ production are shown in Fig. 6.1, occurring through gg and $q\bar{q}$ initial states. QCD-induced diagrams typically provide the leading contribution. However, diagrams involving EW couplings insertions can also be significant. Examples of the latter are shown in Fig. 6.2, where top quarks scatter through the exchange of a Higgs boson or Z/γ^*.

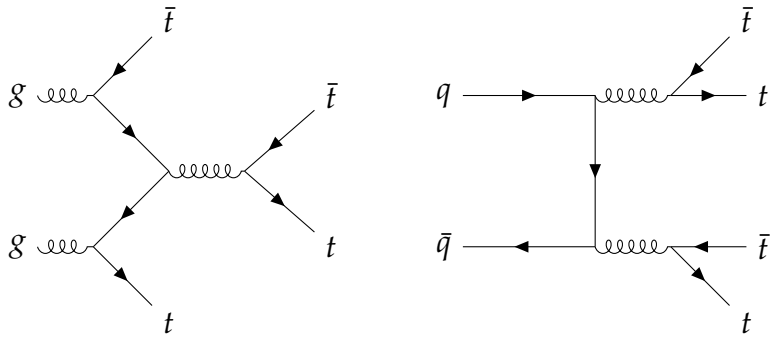

Figure 6.1.: Representative LO diagrams of $\mathcal{O}(\alpha_s^2)$ for the SM four top quark gg-initiated (*left*) and $q\bar{q}$-initiated (*right*) production at the LHC.

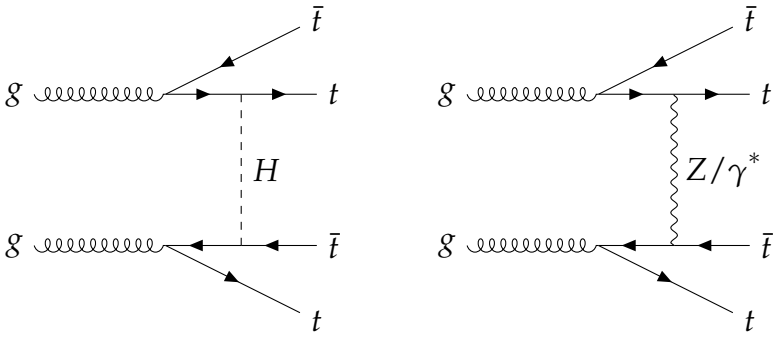

Figure 6.2.: Representative LO diagrams of $\mathcal{O}(\alpha_s\alpha_w)$ for the SM four top quark production at the LHC. The diagrams show the EW $tt \to tt$ scattering involving the exchange of a Higgs boson (*left*) or a Z boson/virtual photon (*right*).

In the SM at $\sqrt{s} = 13$ TeV, it turns out that contributions from the interference of this class of diagrams with the leading QCD amplitudes and from their amplitudes squared are significant, reaching more than a third of the leading tree-level QCD contributions. Nevertheless, these two contributions come with opposite signs, and there is a substantial cancellation between them. This can be seen explicitly in table 7 of Ref. [73].

The peculiar behaviour of the cross-section as a double series in α_s and α_w for the SM process certainly motivates a detailed study in case of inclusion of new physics effects and in particular in the SMEFT framework. In such context, four top quark production is exciting as it is the most straightforward process where top quark self-interactions could be probed at the tree-level. Such interactions are described by a set of dimension-six operators of the form $\overline{\psi}\psi\overline{\psi}\psi$ operators with four top quark fields (left- or right-handed). Other processes at colliders do not directly constrain these operators

at the tree-level. Therefore four top quark production is naively expected to be the first place to see their effects[1].

In this work, we considered all contributions from the SM and the SMEFT, including all the dimension-six CP-even SMEFT operators entering at tree-level. Part of our motivation was that in the SMEFT, the interference $\mathcal{O}(\Lambda^{-2})$ is expected to provide the leading contribution to the cross-section. As the interference projects the kinematic and colour structure of the SM amplitude, its size can change significantly from one operator to another. It is also expected to vary depending on which contributions are included in the SM, as different operators have different colour and chirality structures. We retained all possible tree-level contributions at different orders in QCD and EW couplings in our computations. We further split the EW-induced contributions into the gauge and top-Yukawa ones and determined the inclusive and differential predictions for the LHC and FCC-hh. We organised our predictions in line of α_s, where each term is expanded in the weak parameters, highlighting the potential significance of the formally subleading terms.

6.2. SMEFT framework to four top quark production

6.2.1. Relevant operators

We computed the SMEFT predictions using the same flavour assumption and the notation and operators conventions as in the tWZ study of Chap. 5. We included all dimension-six four quark operators (including an up quark) from the set of four-fermion operators shown in Fig. 2.2. The translation of these operators from the Warsaw basis to the top-basis of is given in Tab. B.1 of appendix B. Moreover, we used the following set of two-fermion (2F) and purely bosonic operators (0F): $\{\mathcal{O}_{t\varphi}, \mathcal{O}_{tZ}, \mathcal{O}_{tW}, \mathcal{O}_{tG}, \mathcal{O}_{\varphi Q}^{(-)}, \mathcal{O}_{\varphi t}, \mathcal{O}_G, \mathcal{O}_{\varphi G}\}$, i.e. the *contributing* operators, all of which are defined in Eq. 5.5 apart from the following ones:

$$\begin{aligned}
\mathcal{O}_{\varphi G} &= \left(\varphi^\dagger\varphi - \frac{v^2}{2}\right) G_A^{\mu\nu} G^A_{\mu\nu}, \\
\mathcal{O}_G &= g_s f_{ABC} G^A_{\mu\nu} G^{B,\nu\rho} G^{C,\mu}_{\rho}, \\
\mathcal{O}_{t\varphi} &= \left(\varphi^\dagger\varphi - \frac{v^2}{2}\right) \overline{Q} t \tilde{\varphi} + \text{h.c.}.
\end{aligned} \tag{6.1}$$

[1] Proposals for constraining four-top-quark operators through loop effects have appeared in Refs. [155, 191, 194, 195].

In the `SMEFTatNLO` model, the operators $\mathcal{O}_{tG}$ and $\mathcal{O}_G$ are defined with an inclusion of an extra g_s factor in their definitions. The consequences of the latter normalisation are later discussed when presenting the inclusive predictions.

The most recent bounds on the effective coefficients of the four-fermion operators from the global study of Ref. [59] are given in Tab. B.2 in appendix B. The bounds on the set of contributing operators are given in Tab. B.3 of the same appendix, apart from the $\mathcal{O}_G$ operator, which is constrained by studies including multi-jet production.

6.2.2. Leading-order coupling expansion

In the presence of SMEFT operators, the scattering amplitude can be expanded as follows:

$$\mathcal{A} = \mathcal{A}_{\text{SM}} + \frac{1}{\Lambda^2}\mathcal{A}_{(\text{d6})} + \frac{1}{\Lambda^4}\left(\mathcal{A}_{(\text{d6})^2} + \mathcal{A}_{(\text{d8})}\right), \tag{6.2}$$

leading to the following decomposition of the partonic differential cross-section up to $\mathcal{O}(\Lambda^{-4})$,

$$d\sigma = d\sigma_{\text{SM}} + \frac{1}{\Lambda^2}d\sigma_{\text{int}} + \frac{1}{\Lambda^4}\left(d\sigma_{\text{quad}} + d\sigma_{\text{dbl}} + d\sigma_{\text{d8}}\right), \tag{6.3}$$

The leading SMEFT contribution, $d\sigma_{\text{int}}$, comes as the linear interference between $\mathcal{A}_{\text{SM}}$ and $\mathcal{A}_{(\text{d6})}$, while the $d\sigma_{\text{quad}}$ and $d\sigma_{(\text{dbl})}$ are the squared single insertion and double insertions contributions, respectively. In terms of the amplitudes, all the $\mathcal{O}(\Lambda^{-4})$ contributions can be schematically written as follows:

$$d\sigma_{\text{quad}} \sim |\mathcal{A}_{(\text{d6})}|^2, \qquad d\sigma_{\text{dbl}} \sim |\mathcal{A}_{\text{SM}}\,\mathcal{A}_{(\text{d6})^2}| \qquad d\sigma_{\text{d8}} \sim |\mathcal{A}_{\text{SM}}\,\mathcal{A}_{\text{d8}}|, \tag{6.4}$$

where the latter is the contribution arising from SMEFT dimension-eight operators interfering with the SM amplitudes. The systematic treatment of dimension-eight operators is beyond the scope of this work.

The differential cross-section for the SM can be expanded in terms of the different strong and weak couplings as follows:

$$d\sigma_{\text{SM}} = \sum_{n,m} \alpha_s^n\,\alpha_w^m\,d\sigma_{\text{SM}}^{(n,m)} = \sum_{i,j,k} \alpha_s^i\,\alpha^j\,\alpha_t^k\,d\sigma_{\text{SM}}^{(i,j,k)}, \tag{6.5}$$

where the couplings are defined as follows:

$$\alpha_s = \frac{g_s^2}{4\pi}, \qquad \alpha = \frac{e^2}{4\pi}, \qquad \alpha_t = \frac{y_t^2}{4\pi}, \tag{6.6}$$

where g_s and e are the strong gauge and electromagnetic coupling, respectively, and α_w collectively represents α or α_t. The $t\bar{t}t\bar{t}$ production occurs via the $gg-$ and $q\bar{q}$-initiated channels. Even though we considered both production modes in all predictions that follow, it is worth noting that contributions induced through quark-initiated amplitudes are at least one order of magnitude smaller than gluon-initiated ones. This is expected since the $t\bar{t}t\bar{t}$ production cross-section is dominated by the gg-initial state. Each of the amplitudes is a six-point diagram; hence, the SM amplitude has four couplings, i.e. $(i+j+k) = 2$, and are expanded in the following way:

$$\mathcal{A}^{(i,j,k)}_{\text{SM},gg} = \alpha_s^2\, \mathcal{A}^{(2,0,0)}_{\text{SM},gg} + \alpha_s \left(\alpha\, \mathcal{A}^{(1,1,0)}_{\text{SM},gg} + \alpha_t\, \mathcal{A}^{(1,0,1)}_{\text{SM},gg} \right), \tag{6.7a}$$

$$\begin{aligned} \mathcal{A}^{(i,j,k)}_{\text{SM},qq} &= \alpha_s^2\, \mathcal{A}^{(2,0,0)}_{\text{SM},qq} + \alpha_s \left(\alpha\, \mathcal{A}^{(1,1,0)}_{\text{SM},qq} + \alpha_t\, \mathcal{A}^{(1,0,1)}_{\text{SM},qq} \right) \\ &\quad + \left(\alpha^2\, \mathcal{A}^{(0,2,0)}_{\text{SM},qq} + \alpha^{3/2}\, \alpha_t^{1/2}\, \mathcal{A}^{(0,3/2,1/2)}_{\text{SM},qq} + \alpha\, \alpha_t\, \mathcal{A}^{(0,1,1)}_{\text{SM},qq} \right), \end{aligned} \tag{6.7b}$$

where the half-integer couplings arise from diagrams containing a Higgs coupling to a top quark via one top-Yukawa vertex and another coupling to two EW bosons via one EW vertex. Each of the two W bosons couples with a fermion line. This structure leads to diagrams at $\mathcal{O}(\alpha^{3/2}\, \alpha_t^{1/2})$ as shown in Eq. 6.7b. Similarly, linear interference cross-section can be decomposed as follows:

$$d\sigma_{\text{int}} = \sum_{n,m} \alpha_s^n\, \alpha_w^m\, d\sigma^{(n,m)}_{\text{int}} = \sum_{i,j,k} \alpha_s^i\, \alpha^j\, \alpha_t^k\, d\sigma^{(i,j,k)}_{\text{int}}, \tag{6.8}$$

Each of the expanded partial cross-sections is a sum of contributions from different WCs,

$$d\sigma^{(n,m)}_{\text{int}} = c_{[r]} d\sigma^{(n,m)}_{\text{int}\,[r]}, \tag{6.9}$$

and similarly for (i,j,k). The label $[r]$ runs over the possible dimension-six operators.

The $t\bar{t}t\bar{t}$ interference cross-section consists of two production channels; the gluon- and the quark-initiated ones [2],

$$d\sigma_{\text{int}} = d\sigma_{\text{int},gg} + d\sigma_{\text{int},qq} \sim 2\Re\left(\mathcal{A}_{\text{SM},gg}\,\mathcal{A}^{\dagger}_{\text{EFT},gg}\right) + 2\Re\left(\mathcal{A}_{\text{SM},qq}\,\mathcal{A}^{\dagger}_{\text{EFT},qq}\right). \tag{6.10}$$

The insertion of a single dimension-six four-fermion operator in the $t\bar{t}t\bar{t}$ amplitude is depicted in Fig. 6.3. The EFT amplitudes for the four-fermion operators read,

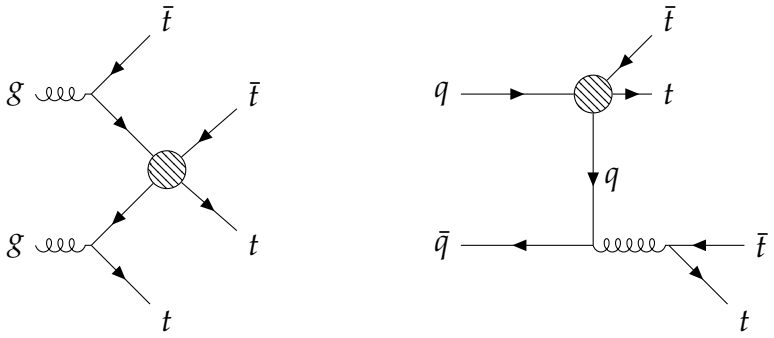

Figure 6.3.: Representative diagrams for the $t\bar{t}t\bar{t}$ amplitudes with blobs representing the one dimension-six EFT insertion, in the gg-initiated production mode (*left*) and in the $q\bar{q}$-initiated production mode (*right*).

$$\mathcal{A}^{(i,j,k)}_{\text{SM},gg,[4\text{F}]} = \alpha_s \mathcal{A}^{(1,0,0)}_{\text{EFT},gg\,[4\text{F}]}, \tag{6.11a}$$

$$\mathcal{A}^{(i,j,k)}_{\text{SM},qq\,[4\text{F}]} = \alpha_s \mathcal{A}^{(1,0,0)}_{\text{SM},qq\,[4\text{F}]} + \alpha \mathcal{A}^{(0,1,0)}_{\text{SM},qq\,[4\text{F}]} + \alpha_t \mathcal{A}^{(0,0,1)}_{\text{SM},qq\,[4\text{F}]}. \tag{6.11b}$$

The cross-section induced by the four-fermion operators[3] can therefore be written as follows:

$$d\sigma_{\text{int},gg,[4\text{F}]} = \alpha_s^3\, d\sigma^{(3,0,0)}_{\text{int},gg} + \alpha_s^2\left(\alpha\, d\sigma^{(2,1,0)}_{\text{int},gg} + \alpha_t\, d\sigma^{(2,0,1)}_{\text{int},gg}\right). \tag{6.12a}$$

$$\begin{aligned} d\sigma_{\text{int},qq,[4\text{F}]} &= \alpha_s^3\, d\sigma^{(3,0,0)}_{\text{int},qq} \\ &+ \alpha_s^2\left(\alpha\, d\sigma^{(2,1,0)}_{\text{int},qq} + \alpha_t\, d\sigma^{(2,0,1)}_{\text{int},qq}\right) \\ &+ \alpha_s\left(\alpha^2\, d\sigma^{(1,2,0)}_{\text{int},qq} + \alpha^{3/2}\,\alpha_t^{1/2}\, d\sigma^{(1,3/2,1/2)}_{\text{int},qq} + \alpha\alpha_t\, d\sigma^{(1,1,1)}_{\text{int},qq} + \alpha_t^2\, d\sigma^{(1,0,2)}_{\text{int},qq}\right) \\ &+ (\alpha^3)\, d\sigma^{(0,3,0)}_{\text{int},qq} + (\alpha^{5/2}\,\alpha_t^{1/2})\, d\sigma^{(0,5/2,1/2)}_{\text{int},qq} \\ &+ (\alpha^2\,\alpha_t)\, d\sigma^{(0,2,1)}_{\text{int},qq} + (\alpha^{3/2}\,\alpha_t^{3/2})\, d\sigma^{(0,3/2,3/2)}_{\text{int},qq} + (\alpha\,\alpha_t^2)\, d\sigma^{(0,1,2)}_{\text{int},qq}. \end{aligned} \tag{6.12b}$$

[2] We have omitted the PDF dependence on the r.h.s.

[3] We performed the same exercise for two-fermion and purely-bosonic operators, however, for simplicity, we omit the presentation of those expansions.

6.3. The hierarchy of inclusive predictions

This section presents the numerical results from the complete LO SMEFT predictions of the $t\bar{t}t\bar{t}$ production process at $\sqrt{s} = 13$ TeV for the LHC, and at $\sqrt{s} = 100$ TeV for future circular pp colliders. The numerical setup here is the same as the one used for the tWZ study described in Sec. 5.6. The only difference is that here we fixed μ_F and μ_R to a relevant scale for $t\bar{t}t\bar{t}$, i.e. 340 GeV $\sim (4m_t)/2$. The decomposition of the $t\bar{t}t\bar{t}$ SM cross-section is given in Tab. 6.1.

$\sqrt{s}$	$\mathcal{O}(\alpha_s^4)$	$\mathcal{O}(\alpha_s^3\alpha)$	$\mathcal{O}(\alpha_s^3\alpha_t)$	$\sum_n \mathcal{O}(\alpha_s^2\alpha_w^n)$	$\sum_n \mathcal{O}(\alpha_s\alpha_w^n)$	$\sum_n \mathcal{O}(\alpha_w^n)$	Inclusive
13 TeV	6.15	-1.44	-0.58	2.33	$\times$	$\times$	6.46
100 TeV	2570	-313	-197	753	$\times$	$\times$	2812

Table 6.1.: The table shows the decomposition of the LO $t\bar{t}t\bar{t}$ SM cross-section at the LHC and the FCC-hh in fb. For $\mathcal{O}(\alpha_s^{<3})$, we summed all possible coupling combinations and present the total cross-section at a given order in α_s. The " $\times$ " denotes negligible contributions.

The strength of the interference between the SM and EFT amplitudes of all dimension-six SMEFT operators belonging to the four-fermion and contributing operators is presented. The interference strength is the interference cross-section in fb when the WC of interest is individually set to unity and the scale of new physics Λ is fixed to 1(3) TeV, for the $\sqrt{s} = 13(100)$ TeV scenario. In presenting the results, the four-fermion operators were categorised into two sub-classes; ones with 4-heavy quarks (4H) and ones with 2-heavy-2-light quarks (2L2H); those insertions are depicted by the blobs shown in the diagrams of Fig. 6.3.

The total inclusive interference cross-section in the four-fermion case can be defined as follows:

$$\sigma_{\text{incl.}} = \sigma_3 + \sigma_2 + \sigma_1 + \sigma_0, \tag{6.13}$$

where σ_i with $i = 3, 2, 1, 0$ denotes the contributions to $\sigma_{\text{incl.}}$ arising from terms with order α_s^i in the cross-section expansion. For example, the σ_2 term denotes the interference cross-section arising *only* from the formally subleading terms in α_s, i.e. $\mathcal{O}(\alpha_s^2\alpha)$ and $\mathcal{O}(\alpha_s^2\alpha_t)$ in Eq. 6.12a and Eq. 6.12b, which can be collectively written as follows:

$$\sigma_2 \equiv \alpha_s^2 \left(\alpha\, \sigma_{\text{int}}^{(2,1,0)} + \alpha_t\, \sigma_{\text{int}}^{(2,0,1)} \right). \tag{6.14}$$

The interference strength is depicted in the heatmaps presented in Figs. 6.4-6.9, the columns correspond to the operator coefficients. The *top* row shows the total inclusive interference cross-section σ_{incl} labelled `INCL`, while subsequent rows correspond to the separate contributions arranged in order of α_s, in line with the example of Eq. 6.14.

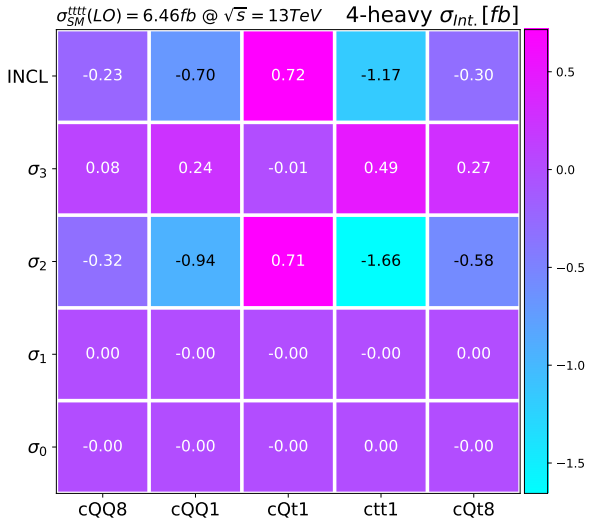

Figure 6.4.: Depiction of the interference strength of the 4-heavy operators. The columns denote the WCs in their UFO notation. The *top* row shows the total inclusive predictions, i.e. summing all the QCD and EW-induced contributions. The subsequent rows are in order of α_s indicating the summation of terms including the given order of α_s. The predictions are obtained at $c = 1$, $\sqrt{s} = 13$ TeV, $\Lambda = 1$ TeV.

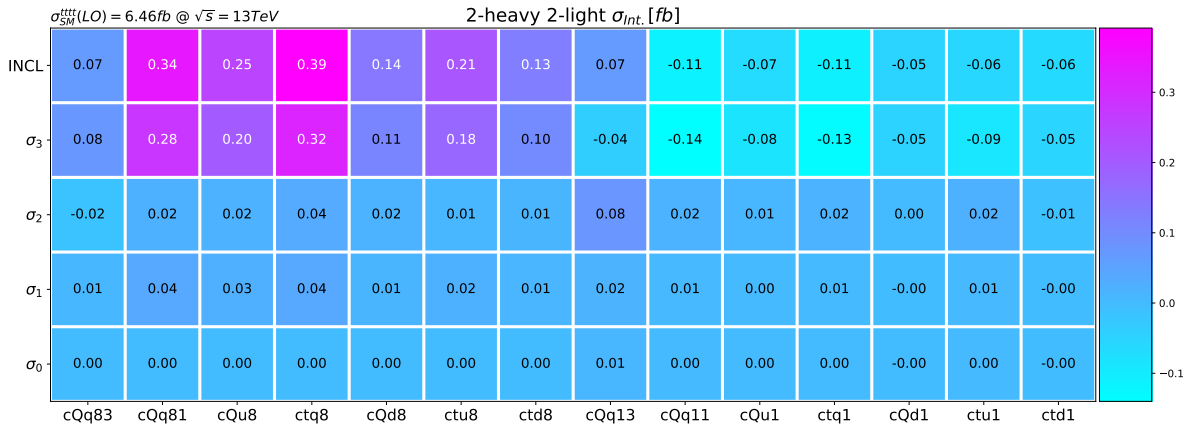

Figure 6.5.: Same as Fig. 6.4 but for the 2-heavy 2-light operators

$\sqrt{s} = 13$ TeV Starting with the 4-heavy operators in Fig. 6.4, we observed that for *all* of them, the dominant interference is the one arising from formally subleading

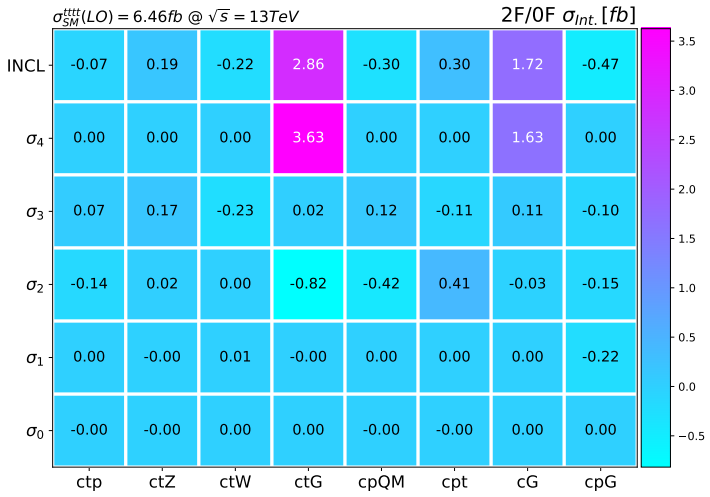

Figure 6.6.: Same as Fig. 6.4 but for the set of contributing operators.

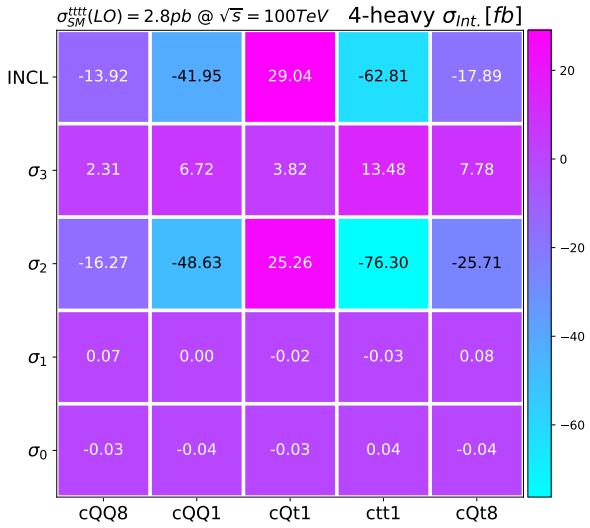

Figure 6.7.: Same as Fig. 6.4 but for the FCC-hh scenario. The predictions are obtained at $\Lambda = 3$ TeV.

orders, σ_2. This contrasts the naive expectation where the leading term in QCD is expected to provide the highest contribution to the cross-section through σ_3. Such observation highlights the significance of the EW scattering of $tt \to tt$, present in the $t\bar{t}t\bar{t}$ production at LO and depicted in Fig. 6.2. The significance of such EW scattering in $t\bar{t}t\bar{t}$ was pointed out in the NLO SM computation of Ref. [73]. It is worth noting that such naive expectation not only underestimates the interference strength of the 4-heavy operators but also generates the "wrong" sign of the interference structure. That is, σ_2 for all the 4-heavy operators has the opposite sign of σ_3. The former dictates the overall sign of the inclusive predictions. Furthermore, the lower-order-α_s cross-

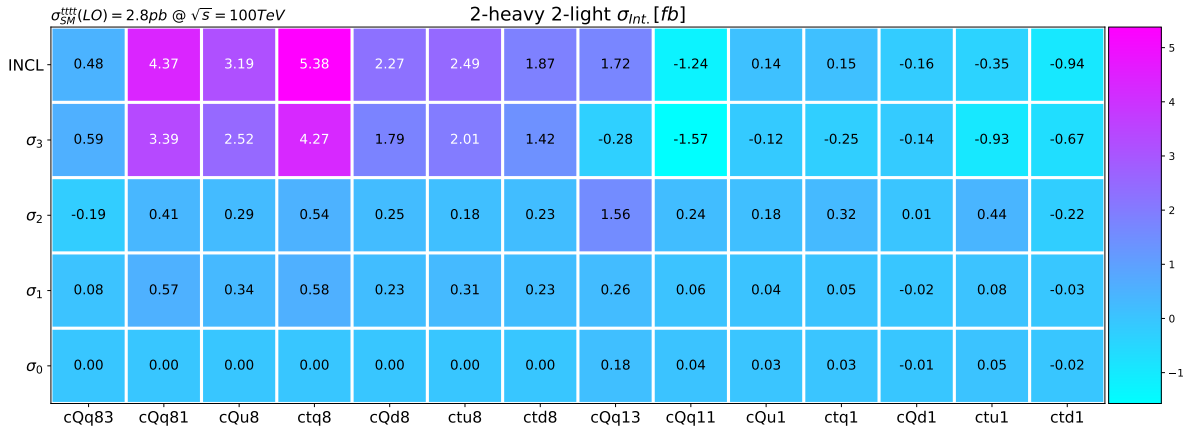

Figure 6.8.: Same as Fig. 6.7 but for the 2-heavy 2-light operators.

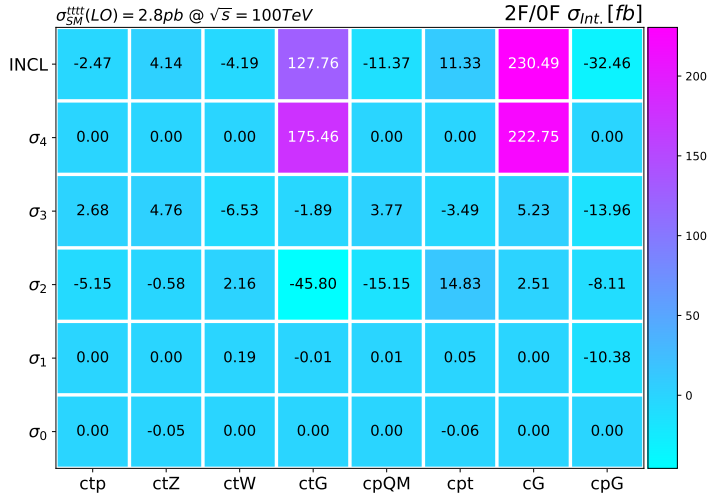

Figure 6.9.: Same as Fig. 6.7 but for the set of contributing operators.

sections, i.e. σ_n where $n < 2$, are heavily suppressed, rendering the consideration of cross-section contributions only down to σ_2 enough to attain reliable predictions for this set of operators. Finally, for the 4-heavy operators, the singlet operators, i.e. $\mathcal{O}^1_{QQ}$, $\mathcal{O}^1_{Qt}$, and $\mathcal{O}^1_{tt}$, were observed to have a "stronger" interference compared to the octet ones, $\mathcal{O}^8_{QQ}$ and $\mathcal{O}^8_{Qt}$, we analysed this effect which will be presented later in the discussion of differential predictions.

Moving on to the 2-heavy-2-light operators presented in Fig. 6.5, we observed, except for the $\mathcal{O}^{3,1}_{Qq}$ operator, that the interference strength of all the operators in this class is dominated by the formally leading σ_3 cross-section. This hints at the electroweak scattering effects being less critical in the interference with $q\bar{q}$-initiated EFT amplitudes. The insertions of the 2-heavy-2-light operators are only present in the $q\bar{q}$-initiated production shown in Fig. 6.3.

Finally, the interference strength of the set of contributing two-fermion and purely-bosonic operators is presented in Fig. 6.6. Due to the model normalisation, i.e. the inclusion of g_s for $\mathcal{O}_{tG}$ shown in Eq. 5.5 and for $\mathcal{O}_G$ as shown in Eq. 6.1, it is immediately apparent those have a non-vanishing σ_4 cross-section. This is expected because a contribution to the cross-section at this order in α_s is not available for the other contributing operators; therefore, their leading cross-sections are σ_3. In contrast to the $\mathcal{O}_{tW}$ and $\mathcal{O}_{tZ}$ dipoles, the contributing two-fermion operators, $\mathcal{O}_{t\varphi}$, $\mathcal{O}^{(-)}_{\varphi Q}$, and $\mathcal{O}_{\varphi t}$, have formally subleading dominant cross-sections, i.e. σ_2. The $\mathcal{O}_{tG}$ operator even though dominating at σ_4, has a non-negligible σ_2 cross-section. Finally, and in complete contrast to $\mathcal{O}_G$, the interference strength of the $\mathcal{O}_{\varphi G}$ operator tends to be inversely proportional to orders in α_s, in other words, proportional to the number of electroweak propagators.

$\sqrt{s} = 100$ TeV The only difference between the numerical simulation performed at $\sqrt{s} = 100$ TeV for future pp colliders, and the one of $\sqrt{s} = 13$ TeV for the LHC, is that for the former, we fixed the scale of new physics Λ to 3 TeV. This is intended to ensure a reliable expansion of the EFT series given the high collision energy of FCC-hh. The interference strength at the FCC-hh scenario from the 4-heavy, 2-heavy-2-light, and the contributing operators are presented in Fig. 6.7, Fig. 6.8, and Fig. 6.9, respectively. Apart from the expected up-scaling of the cross-sections in the FCC-hh scenario, we saw a similar pattern across the board when comparing to the LHC study, albeit with some slight differences: the σ_3 interference of $\mathcal{O}^1_{Qt}$ has an opposite sign in the 100 TeV scenario. The $\mathcal{O}^1_{Qu}$ and $\mathcal{O}^1_{tq}$ operators have a slightly dominant σ_2 in contrast to the LHC case where the dominant cross-section is σ_3. Finally, for the $\mathcal{O}_{\varphi G}$ operator, and while σ_1 is still significant in parallel to the LHC scenario, the σ_3 interference is slightly stronger in the 100 TeV scenario.

In summarising this section, Tab. 6.2 shows the operators aligned with their most dominant cross-section contributions. Furthermore, we put together all operators featuring an unexpected enhancement to their cross-sections from formally subleading terms;

$$\textit{all}\ \text{4-heavy} \qquad \text{and} \qquad \{\mathcal{O}^{3,1}_{Qq}, \mathcal{O}_{t\varphi}, \mathcal{O}_{tG}, \mathcal{O}^{(-)}_{\varphi Q}, \mathcal{O}_{\varphi t}, \mathcal{O}_{\varphi G}\}. \tag{6.15}$$

We coined this group of operators the **non-naive** ones. More precisely, we defined non-naive operators as ones for which *any* of their formally non-leading terms is significant in estimating their total interference cross-section.

	4H	2L2H	2F	0F
σ_4	$\times$	$\times$	c_{tG}	c_G
σ_3	-	$c_{Qq}^{83}, c_{Qu}^{8}, c_{tq}^{8}, c_{Qd}^{8}, c_{tu}^{8}, c_{td}^{8}, c_{Qq}^{81}$ $c_{Qq}^{11}, c_{Qu}^{1}, c_{tq}^{1}, c_{Qd}^{1}, c_{tu}^{1}, c_{td}^{1}$	$c_{t\varphi}, c_{tZ}, c_{tW}$	-
σ_2	$c_{QQ}^{8}, c_{QQ}^{1}, c_{Qt}^{8}, c_{Qt}^{1}, c_{tt}^{1}$	c_{Qq}^{31}	$c_{\varphi t}, c_{\varphi Q}^{(-)}$	-
σ_1	-	-	-	$c_{\varphi G}$
σ_0	-	-	-	-

Table 6.2.: Indication of the most significant contribution to the total cross-section of each operator at $\sqrt{s} = 13$ TeV. Entries labelled $\times$ denote such coupling order is not allowed for the given class of operators. The blue colour indicates operators with contributions not only dominant at this given order in α_s, but also other (higher or lower) orders in α_s are significant enough that they can alter the total rate if not considered.

6.4. Differential predictions

This section presents the LHC and FCC-hh differential predictions for the set of non-naive operators of Eq. 6.15. The rest of the operator differential predictions at the LHC and the FCC-hh are given in appendix C. We obtained the differential distributions in the invariant mass bins of the four top quark system, $m_{tttt} \sim \sqrt{s}$, for which we also included the SMEFT diagonal quadratic contributions at the $\mathcal{O}(\Lambda^{-4})$. The input parameters are the same as the ones used for the inclusive predictions. Predictions for non-naive operators are given in Figs. 6.10-6.14, and split into pure SM predictions, SM predictions summed to the linear EFT interference, and SM predictions summed to the linear EFT interference and the diagonal quadratic contributions. Moreover, the results are presented in every order of α_s, e.g. `INT201` indicates the interference contribution (`INT`) induced from $\mathcal{O}(\alpha_s^2\alpha_t)$ terms, where the first, second and third digits denote the orders of α_s, α, and α_t, respectively. For orders "below" the formal subleading order in α_s, we summed all EW-induced contributions at this given α_s-order. For example, `1XX` indicates summing all possible EW-induced contributions with one α_s coupling, in parallel to the notation used in Sec. 6.3; `1XX` $\equiv \sigma_1$. The relative scale uncertainties were computed individually for each EFT contribution. Contrary to inclusive predictions, the differential computations are performed for WCs values extracted approximately from the global fit of Ref. [59]. An exception is $\mathcal{O}_G$, for which the value of its coefficient is specified in the corresponding plot.

$\sqrt{s} = 13$ TeV One clear pattern in all of the 4-heavy operators predictions is the sizeable interference cross-section arising from the $\mathcal{O}(\alpha_s^2\alpha)$ term, and depicted by the blue line in the second inset. This observation corroborated what we observed in

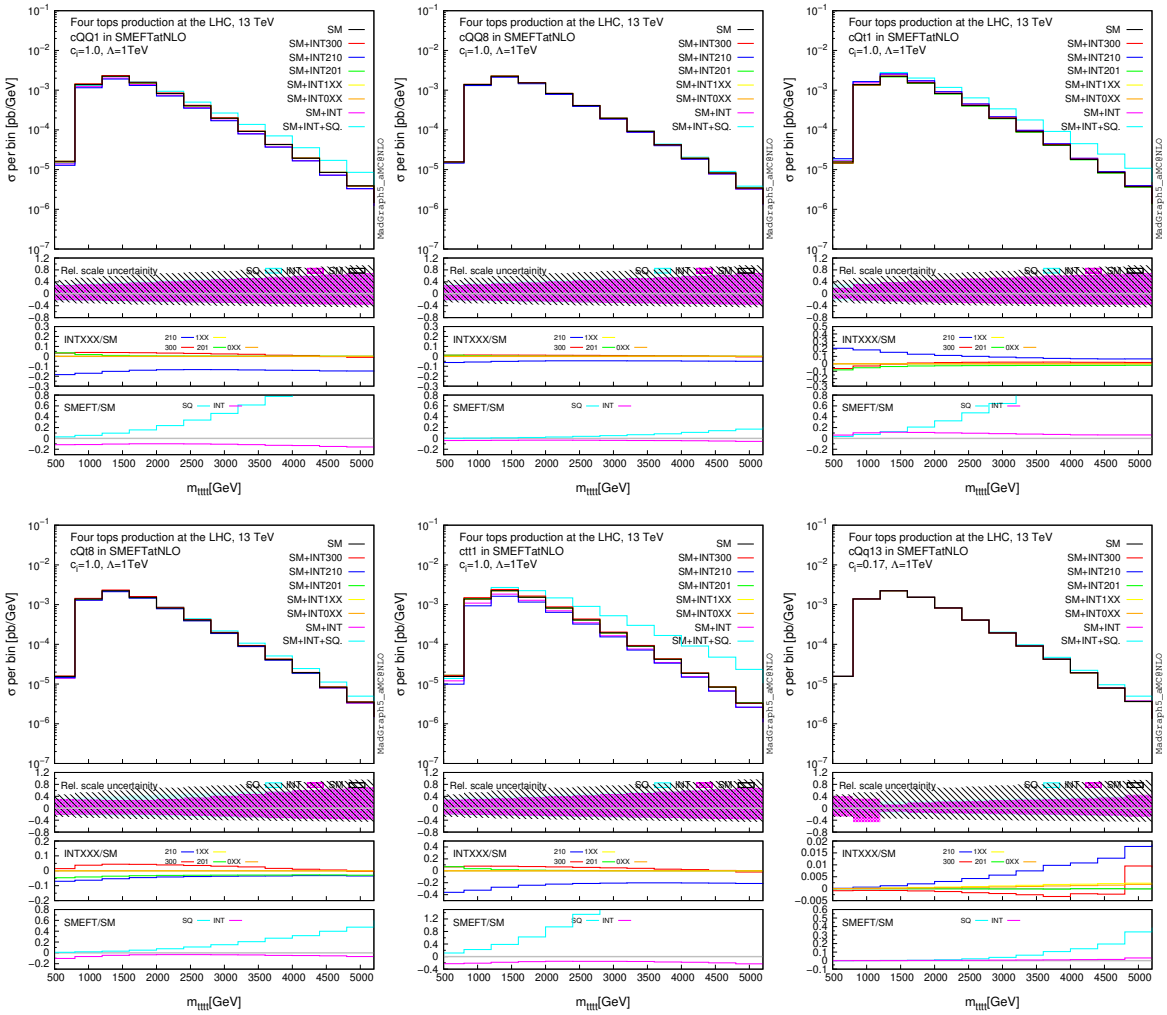

Figure 6.10.: Differential predictions at $\sqrt{s} = 13$ TeV in the m_{tttt} for the set of non-naive 4F operators. The values of the coefficients were approximately extracted from the global fit study of Ref. [59]. The first inset displays the relative scale uncertainties individually calculated for the SM, the interference and the quadratic EFT contributions. The second inset shows the impact of the EFT interference to the SM. The last inset shows the ratio of the total EFT contributions to the SM.

the inclusive predictions; formally subleading contributions are significant. For σ_2 we found that the dominant contribution comes from the $\mathcal{O}(\alpha_s^2\alpha)$ terms rather than those of $\mathcal{O}(\alpha_s^2\alpha_t)$. Moreover, similar to the inclusive predictions, singlet operators were observed to interfere with the SM comparatively stronger than octet operators.

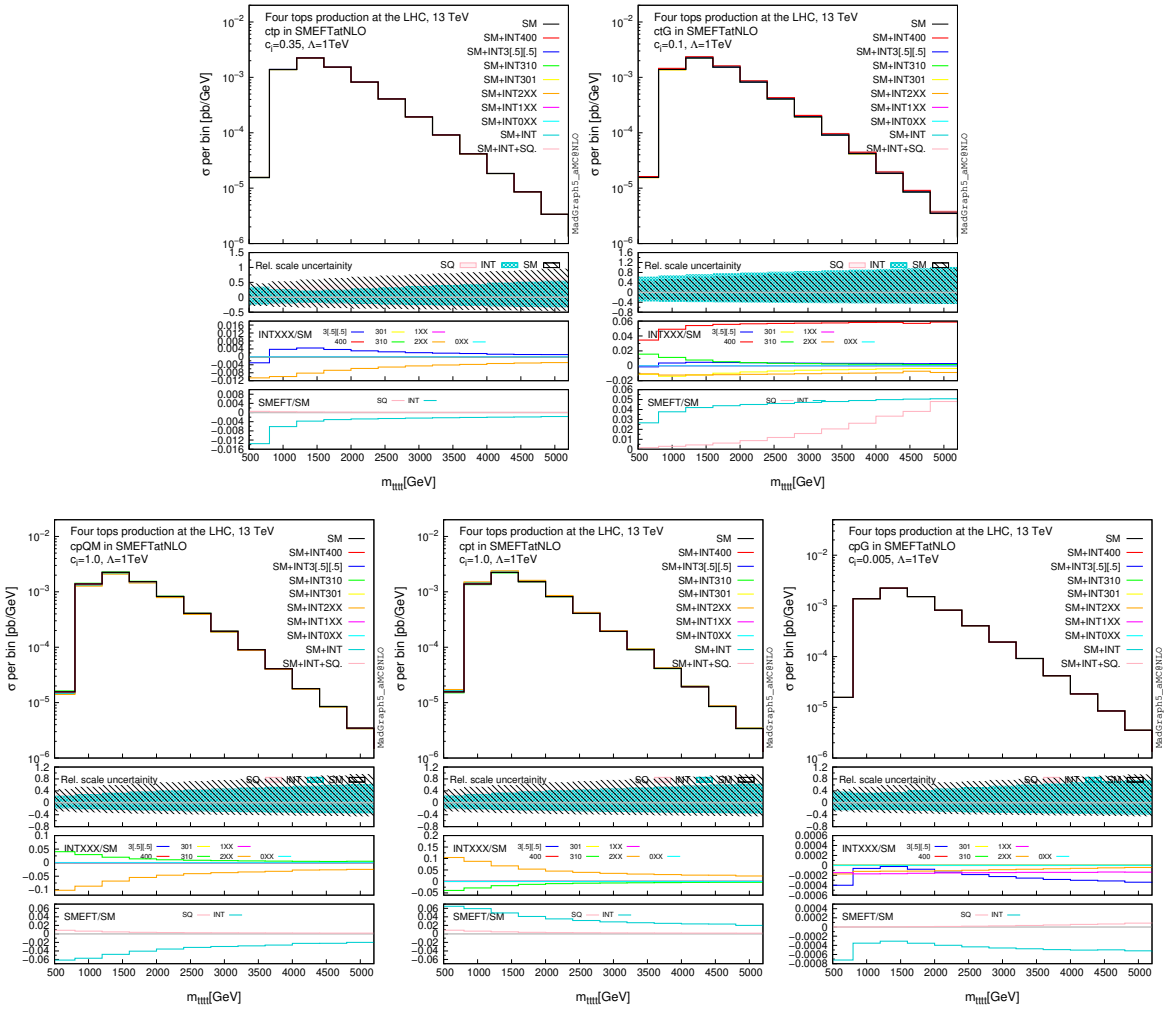

Figure 6.11.: Same as Fig. 6.10 but for the non-naive two-fermion and purely-bosonic operators.

I had already mentioned this pattern in Sec. 6.3. However, I relegated the detailed discussion to this section.

Interlude: on singlets and octets interference pattern It is expected that in formally QCD-dominated production processes, e.g. top quark pair production, amplitudes with colour octet insertions exhibit a "stronger" interference pattern with the SM compared to colour singlets, in $t\bar{t}$ for instance, colour singlets contributions vanish at the tree-level when considering only purely-QCD induced SM amplitudes [57]. In four top quark production, the interference between colour singlet operators and the QCD SM amplitude is non-zero due to the presence of more complicated colour structures, which allow the top-antitop quark pair to be in a colour singlet state. This is evident at the σ_3-level, where the colour singlets interference is comparable to the colour

octet ones. In addition, and as discussed previously, the EW scattering effects in the $gg \to \bar{t}t\bar{t}t$ born-level amplitudes, depicted in Fig. 6.2, provide significant contributions to the cross-section, in the SM and in the SMEFT. This explains the weaker interference strength of colour octets compared to colour singlets in the set of 4-heavy operators at the σ_2-level. The reason comes from the different colour flow in the tt s-channel scattering sub-amplitude; EFT amplitudes with a colour octet insertion would interfere with the formally-leading SM amplitudes where a gluon is the mediator of the $tt \to tt$ scattering. On the other hand, amplitudes with the insertion of a colour singlet operator are expected to interfere with the formally subleading SM amplitudes where the $tt \to tt$ scattering is facilitated via an electroweak mediator.

In contrast to the 4-heavy operators, the previously mentioned insignificance of EW scattering effects in the $q\bar{q}$-initiated production channel explains the "typical" stronger interference strength of the 2-heavy-2-light colour octets compared to colour singlets. The only exception to this is the $\mathcal{O}_{Qq}^{3,1}$ operator. Interestingly enough, $\mathcal{O}_{Qq}^{3,1}$ is also the *only* 2-heavy 2-light operator in the set of non-naive operators. This suggests that the enhancement from formally subleading terms is indeed intertwined with the "unusual" stronger interference arising from EFT amplitudes with colour singlets. The interference pattern of colour octets and singlets in the set of 4-heavy operators is summarised in Fig. 6.12.

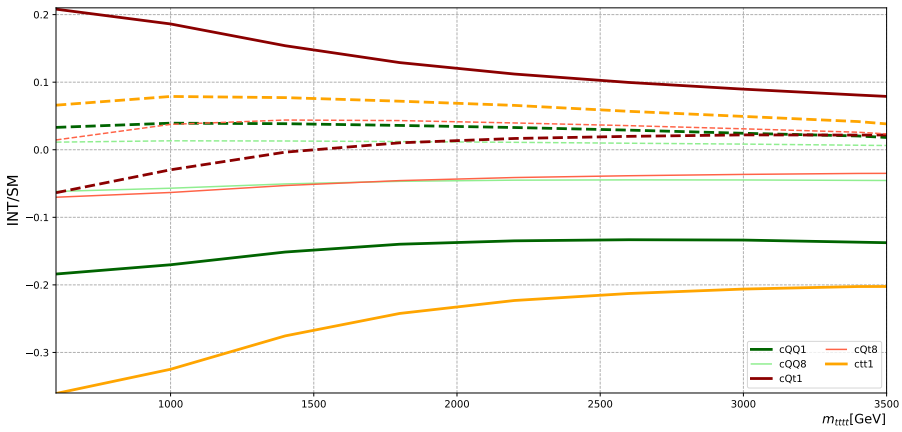

Figure 6.12.: The ratio of the linear EFT interference to the SM prediction for the non-naive 4-heavy operators. Solid lines depict the $\mathcal{O}(\alpha_s^2\alpha)$ contribution, while dashed lines depict the $\mathcal{O}(\alpha_s^3)$ one. Thick (thin) lines represent colour-singlets (-octets).

Moving to the non-naive two-fermion and purely-bosonic operators, we observed a different EFT structure compared to 4-heavy ones. EFT amplitudes with insertions of

four-fermion operators have effective contact terms as depicted in Fig. 6.3. The energy scaling of such amplitudes leads to consistent growth of the quadratic contribution as a function of $\sqrt{s}$. This is seen in the third inset of the distributions of all four-fermion operators in Fig. 6.10. On the other hand, two-fermion operators exhibit suppression of their quadratic contributions and, in most cases, a decaying interference. Such effect is apparent in the third insets of Fig. 6.11, with a notable exception of the $\mathcal{O}_{tG}$ operator. The latter receives enhancement in its energy scaling from their gluon field strength derivatives, hence its different EFT structure: the linear contribution scales as $\sim 1/E^3$, while the quadratic one scales as $\sim 1/E^2$. Such EFT structure is also evident for $\mathcal{O}_G$ in Fig. C.3.

We concluded that the 4-heavy operators are the most sensitive probes to four top quark production. This can be deduced from their sizeable interference magnitude compared to the 2-heavy-2-light operators and the two-fermion and purely-bosonic ones.

$\sqrt{s} = 100$ TeV Despite the high collision energy used in simulating the FCC-hh scenario, the increased value of Λ, i.e. $\Lambda = 3$ TeV, significantly suppresses the magnitude of the EFT contributions compared to the ones from the LHC study. It is worth reminding that changing Λ from 1 to 3 TeV suppresses the interference contribution by a factor of 9 and the squared one by 81. Nevertheless, and in exploiting the predictions of m_{tttt} at higher energies, we observed the expected energy growth of EFT contributions as a function of $\sqrt{s}$; inherently due to the contact term nature of those operators. Again, we observed the colour singlet interfering with the SM more strongly than colour octets, drawing parallels to the LHC predictions. However, in contrast to the LHC predictions, for almost all 2-heavy-2-light colour octets presented in Fig. C.2 for the FCC-hh scenario with its corresponding choice of Λ, we observed the linear interference contributions dominating quadratic ones. For two-fermion and purely bosonic operators, albeit with a milder quadratics growth for $\mathcal{O}_G$ at FCC-hh in Fig. C.4, we saw a similar pattern between the LHC and FCC-hh predictions.

6.5. Sensitivity projections at hadron colliders

Given the current evidence of four top quark production amounting to 4.7σ significance [196], $t\bar{t}t\bar{t}$ is expected to be discovered at the LHC with the Run III data. Four top quark production is primarily induced by gluons in the initial state rendering the

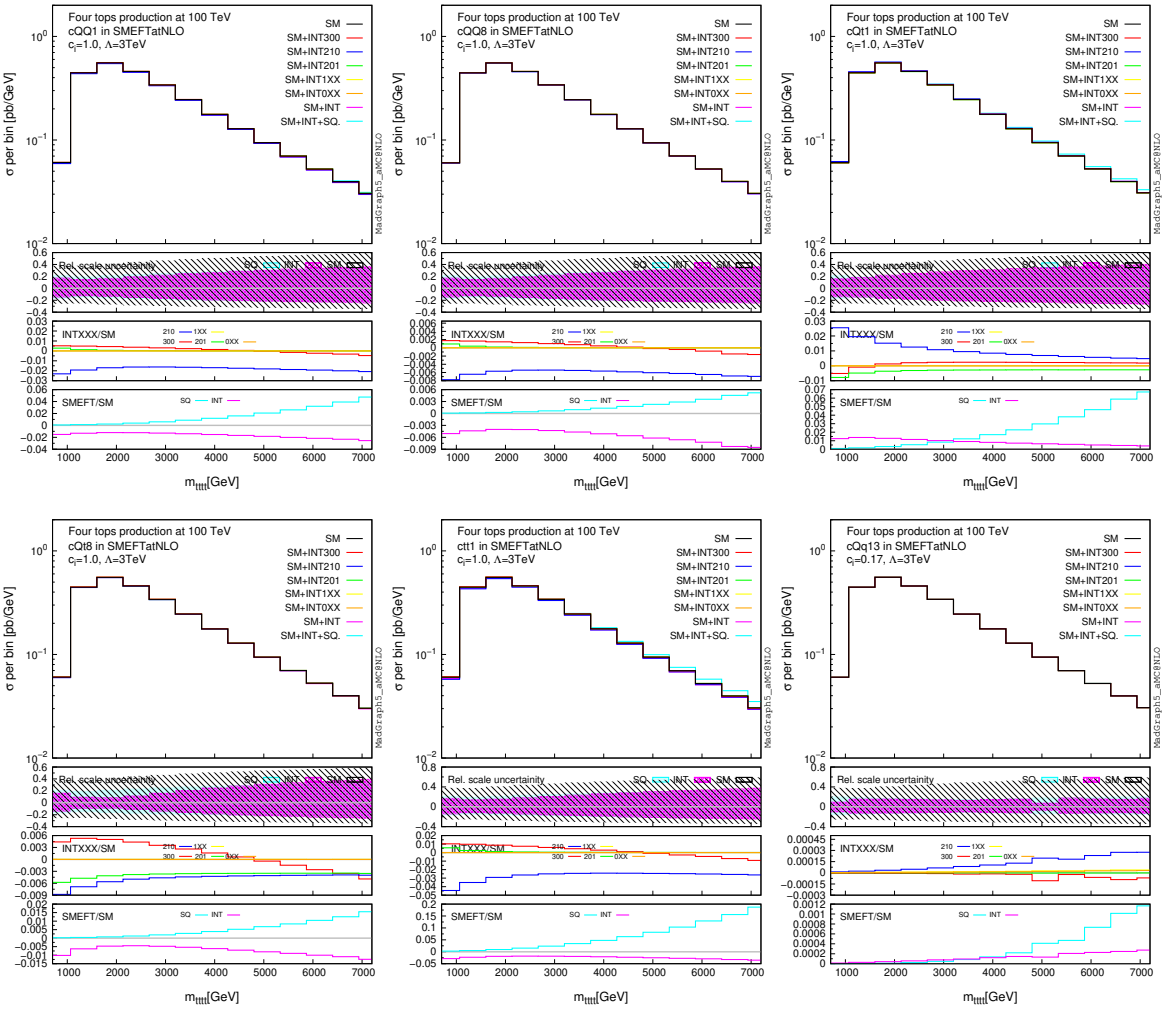

Figure 6.13.: Same as Fig. 6.10 but for $\sqrt{s} = 100$ TeV.

gg-initiated production dominating $\sim$87% of the SM $t\bar{t}t\bar{t}$ cross-section at 13 TeV and $\sim$99% at 100 TeV. Since the main background contribution to the $t\bar{t}t\bar{t}$ signal comes from $t\bar{t}W$ production [197], which proceeds only in the $q\bar{q}$-initiated mode, an increase in the collision energy can lead to an improvement of the signal-to-background of the $t\bar{t}t\bar{t}$ production. On the other hand, systematic uncertainties polluting the experimental measurement can be progressively reduced as a function of an increasingly integrated luminosity. The study of Ref. [198] combined the expected $t\bar{t}t\bar{t}$ experimental sensitivity at future LHC runs and the state-of-art theoretical calculations [73] to predict the total uncertainty by which the $t\bar{t}t\bar{t}$ cross-section can be determined. The reported expected uncertainty on the $t\bar{t}t\bar{t}$ cross-section are 102%, 58%, and 40%, at 95% CL, for 13, 14, and 27 TeV runs respectively with a corresponding integrated luminosities of 300 fb^{-1}, 3 ab^{-1}, and 15 ab^{-1} [198]. In this section, and using these estimated uncertainties, we

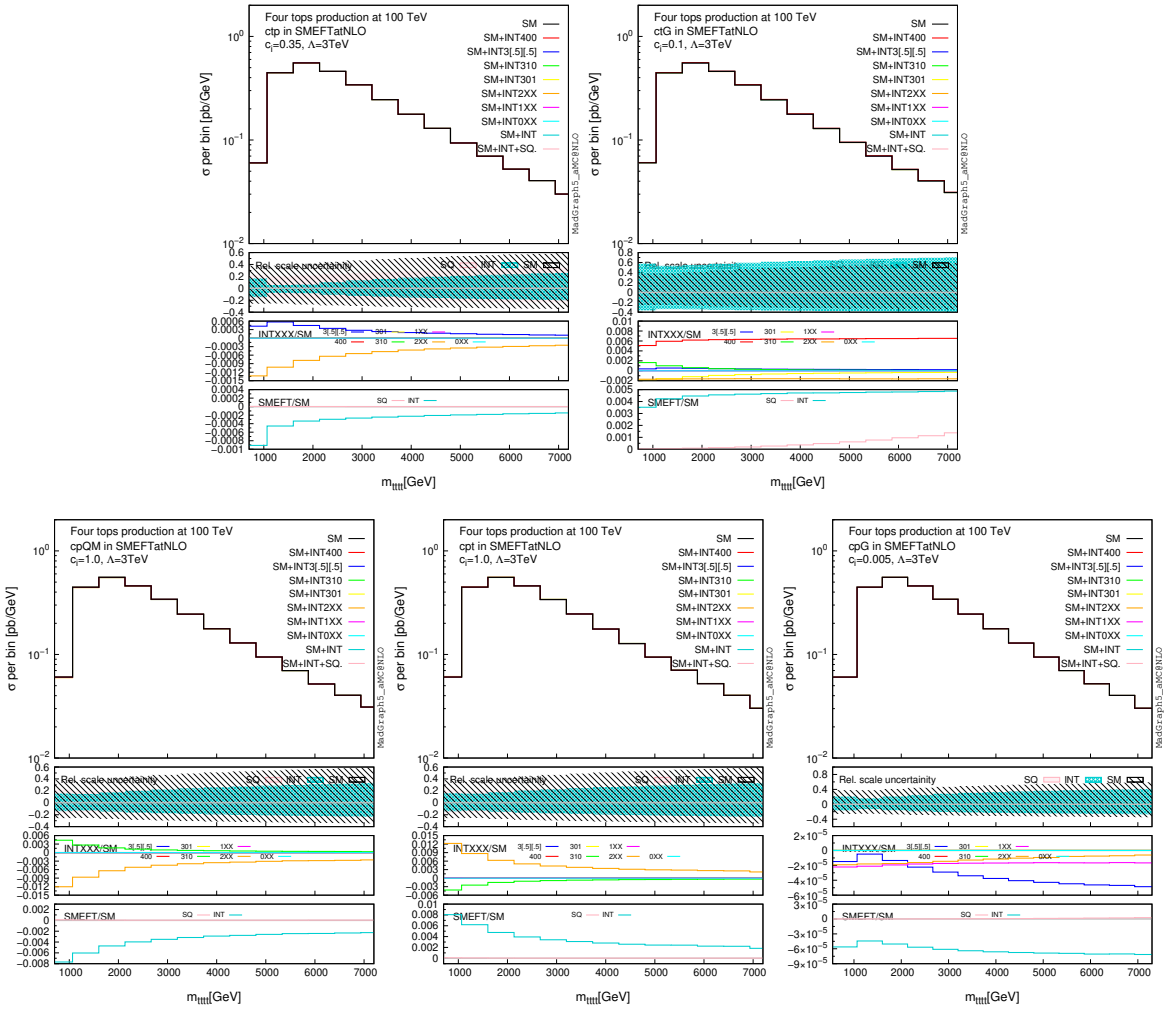

Figure 6.14.: Same as Fig. 6.11 but for $\sqrt{s} = 100$ TeV.

reproduced the study of Ref [198], and subsequently added predictions from FCC-hh for comparison. It is worth noting that this study assumed the sensitivity of the effective operators to be mainly induced from inclusive measurements. We imposed an EFT validity cut on the invariant mass of the four top quark system so the SMEFT predictions can be matched to UV models with higher energy scales, i.e. $m_{tttt} < 3$ TeV. The EFT validity cut is assumed not significantly to alter the projected sensitivity.

To attain the projected sensitivity, we scanned different values of the WCs, computing the $t\bar{t}t\bar{t}$ signal strength, μ_{tttt} at each point. The signal strength is defined as $\mu_{tttt} = \sigma^{tttt}_{\text{obs.}}/\sigma^{tttt}_{\text{exp.}}$, where $\sigma^{tttt}_{\text{obs.}}$ is the obtained SMEFT cross-section including the interference and the quadratic contributions at each value of the WCs, and the $\sigma^{tttt}_{\text{exp.}}$ is the $t\bar{t}t\bar{t}$ cross-section assuming no EFT contributions. The WC scans for all the 4-heavy operators presented in Fig. 6.15 showed a significant EFT sensitivity enhancement at

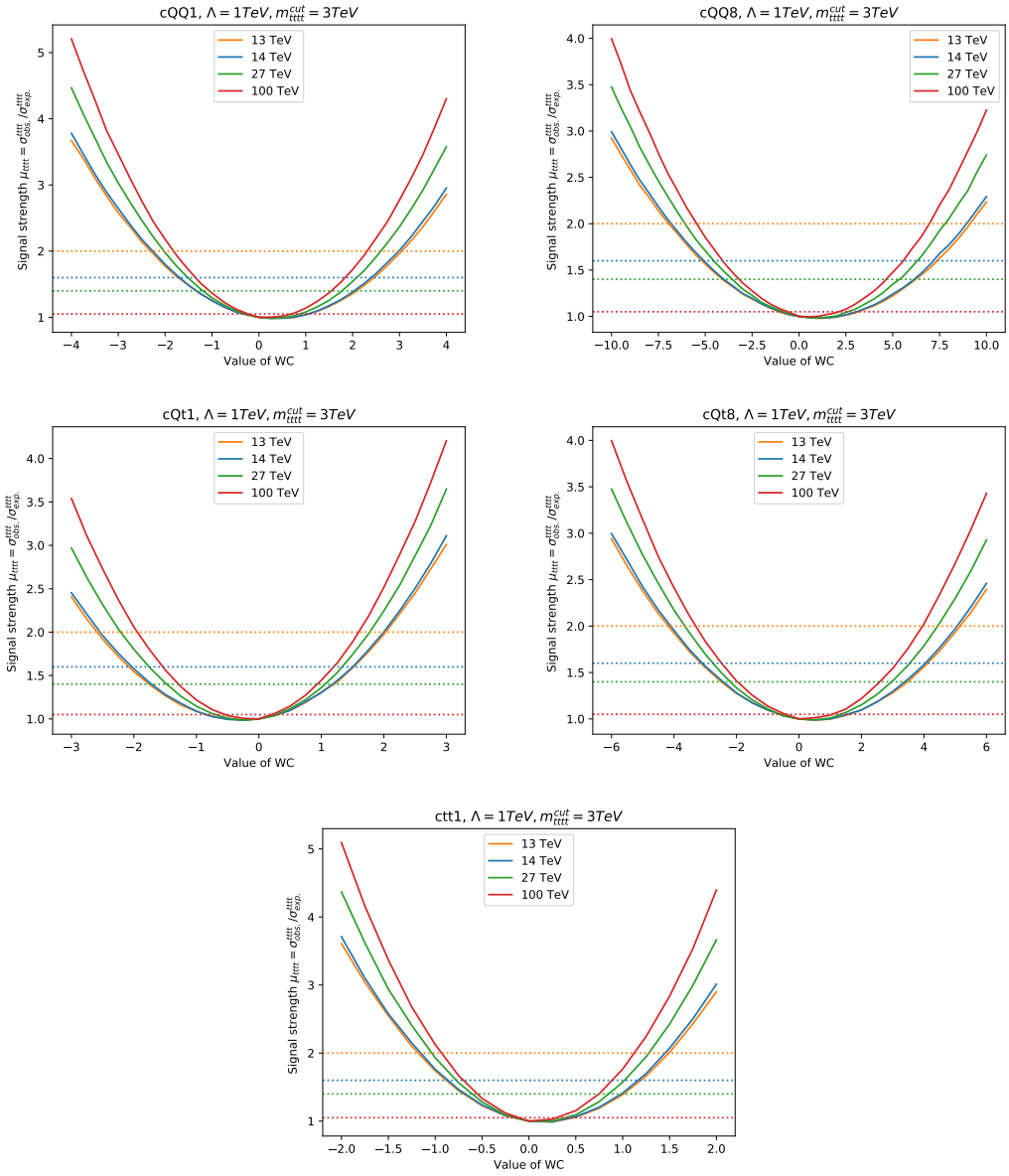

Figure 6.15.: Four top quark production signal strength as a function of the coefficients of all the 4-heavy operators. The EFT predictions include both linear interference and quadratic contributions. The horizontal lines represent the expected measurement at each collision energy derived from the corresponding total uncertainty.

high collision energies, in contrast to the 2-heavy-2-light operators, of which the $\mathcal{O}^{3,1}_{Qq}$ operator projection is presented in Fig. 6.16[4].

The reduced sensitivity of 2-heavy-2-light operators at high energies is because the gg-initiated production dominates over the $\bar{q}q$ one as the collision energy increases.

[4] One can consult Ref. [198] for the obtained WCs limits of all the 2-heavy-2-light operators at future LHC runs.

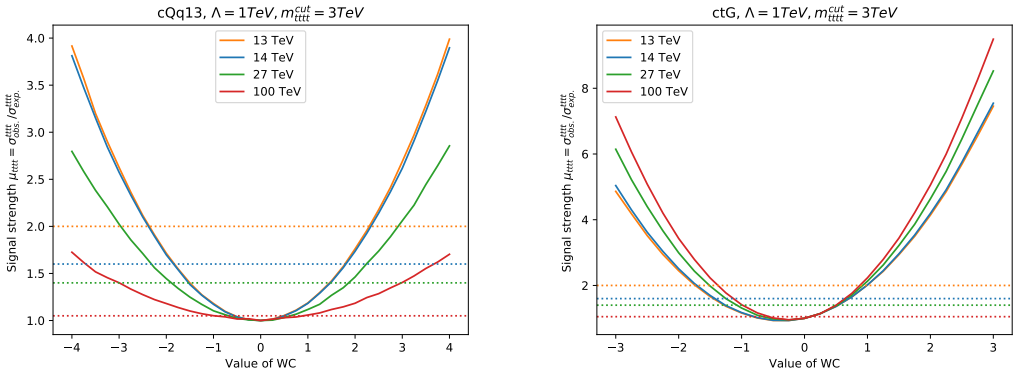

Figure 6.16.: Same as Fig. 6.15 but for the $\mathcal{O}^{3,1}_{Qq}$ operator (*left*) and the $\mathcal{O}_{tG}$ operator (*right*).

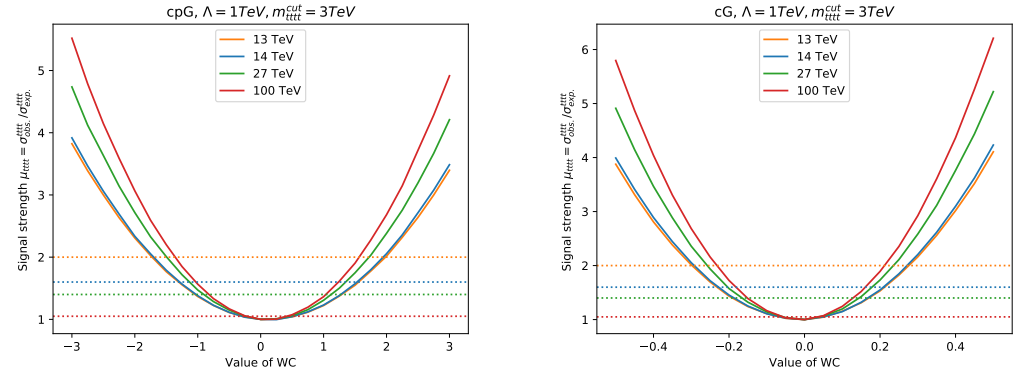

Figure 6.17.: Same as Fig. 6.15 but for the $\mathcal{O}_{\varphi G}$ operator (*left*) and the $\mathcal{O}_{G}$ operator (*right*).

This effect subsequently leads to a marginal improvement in the obtained limits at higher energies. Furthermore, even though all the two fermion operators can be better constrained in different measurements, in Fig. 6.16, we also showed the scan of the $\mathcal{O}_{tG}$ operator's WC. The latter is the most collision-energy-sensitive two-fermion operator in the contributing operators. Finally, the projections for the purely bosonic operators $\mathcal{O}_{\varphi G}$ and $\mathcal{O}_{G}$ are shown in Fig. 6.17. We summarised the expected individual limits on the WCs of the 4-heavy operators in Tab. 6.3.

In obtaining the limits, we used the previously mentioned expected total uncertainties at future LHC runs (represented by the horizontal dashed line in the plots). We kept an estimate of 5% total uncertainty in the $t\bar{t}t\bar{t}$ cross-section measurement at FCC-hh. Our results showed that high collision energies will undoubtedly aid in constraining the 4-heavy effective coefficients through the $t\bar{t}t\bar{t}$ production. On the other hand, we expect other top quark processes to be more sensitive to the rest of the operators.

c_i	13 TeV	14 TeV	27 TeV	100 TeV
c_{QQ}^1	[-2.2,3]	[-1.8,2.2]	[-1.2,1.8]	[-0.25,0.7]
c_{QQ}^8	[-6.75,9]	[-5,7]	[-3.75,5.1]	[-1.0,2.25]
c_{Qt}^1	[-2.6,2]	[-2,1.4]	[-1.4,1.1]	[-0.6,0.3]
c_{Qt}^8	[-4.2,5.3]	[-3.2,4]	[-2.1,2.7]	[-0.45,1.05]
c_{tt}^1	[-1.2,1.4]	[-0.7,1.2]	[-0.6,0.8]	[-0.15,0.35]

Table 6.3.: Theoretical limits on the five 4-heavy operator coefficients expected at the 13, 14, 27, and 100 TeV scenarios, at the 95% CL level.

6.6. Toy fits

In this section, we present limits on effective operators' coefficients from simplified χ^2 individual fits in various collider scenarios: the LHC, FCC-hh and the HL-LHC. We explore the impact of (*i*) subleading EW terms, (*ii*) differential information and (*iii*) the collider energy on the WCs bounds.

Impact of subleading EW terms We start by considering the relevance of the subleading terms in the interference cross-section expansion of the 4-heavy operators. In Fig. 6.18, the individual limits on the 4-heavy coefficients at the FCC-hh are presented in two cases: (I) with only QCD-induced (leading) terms taken into account, and (II) when contributions to the cross-section from all tree-level terms in the mixed QCD-EW expansion are included. For the SM prediction at the FCC-hh, we use the results of Tab. 6.1 with a 20% theoretical (systematic) uncertainty. EFT predictions include only the linear interference contributions. For simplicity, we assume the experimental measurement to be that of the SM cross-section reported in Tab. 6.1 with a 5% total (statistical and systematic) uncertainty. The importance of the subleading terms is evident when considering *only* the contributions from linear interference. However, and since quadratic contributions of four-heavy operators are *only* QCD-induced, including them in the fit would reduce the sensitivity to the subleading terms.

Impact of differential information The HL-LHC will run at $\sqrt{s} = 14$ TeV with 3 ab^{-1} of integrated luminosity; therefore, it is expected to obtain differential information for the four-top process experimentally. Motivated by the larger impact of the EFT operators in the tails of distributions, as illustrated in Fig. 6.10, we examine the impact of adding the invariant mass distribution of the four-top in our toy fit for the HL-LHC. Fig. 6.19 displays the individual limits for the same two cases used

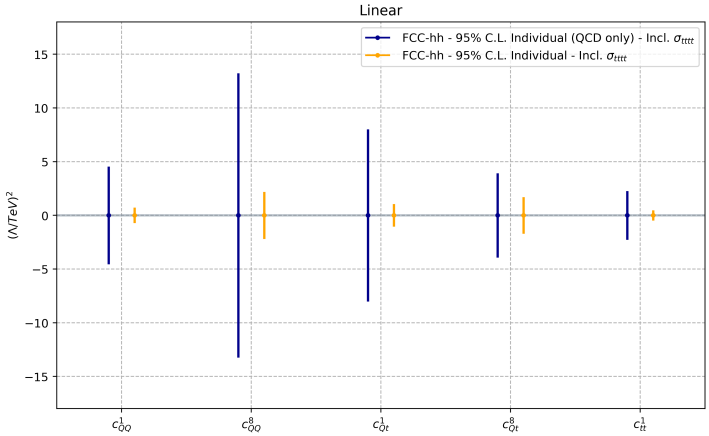

Figure 6.18.: 95%CL limits on the 4-heavy operators' coefficients at the FCC-hh scenario from a χ^2 fit. The limits are shown when only considering leading QCD terms and when considering all the terms in the mixed QCD-EW cross-section expansion. The fit uses the inclusive $t\bar{t}t\bar{t}$ cross-section, σ_{tttt}. EFT predictions were obtained at the interference level.

previously (QCD-only and mixed QCD-EW) and compares the use of only inclusive information from σ_{tttt} to when also adding differential information in the fit from m_{tttt}. We use the HL-LHC SM prediction calculated at LO, $\sigma_{tttt}^{\text{HL}} = 9.0$ fb, with a 20% theoretical uncertainty. The EFT predictions include the linear and quadratic contributions. We assume the experimental measurement to be that of the SM within the expected 28% experimental total uncertainty [198]; $\sigma_{tttt}^{\text{HL}} = 9.0 \pm 2.52$ fb. The m_{tttt}

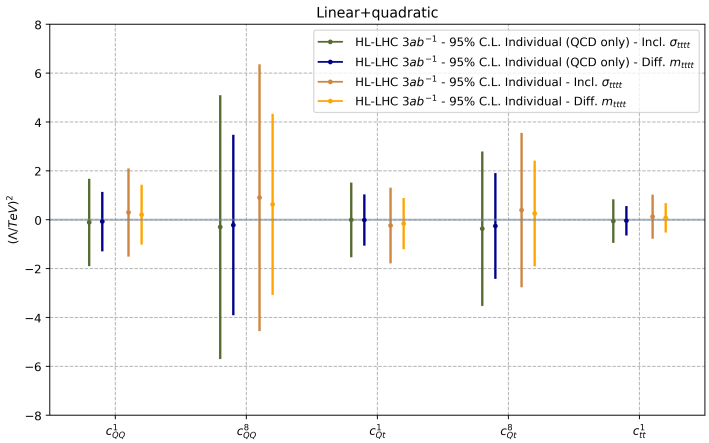

Figure 6.19.: 95%CL limits on the 4-heavy operators' coefficients at the HL-LHC scenario from a χ^2 fit. The limits are shown for when only considering leading QCD terms and when considering all the terms, in using only inclusive information from σ_{tttt} and when adding differential information from m_{tttt}. EFT predictions were obtained for the linear and quadratic contributions.

distribution is organised in three bins: [600-1500], [1500-2500], [2500-6000] GeV, with total experimental uncertainties amounting to 28% for each of the first two bins, and 60% for the latter to account for the degradation of the statistical uncertainty based on the number of events expected in each bin. Even though very much simplified and not based on a detailed analysis of how observables could provide most of the sensitivity, our results indicate that differential information improves the sensitivity and should be used whenever possible.

Comparison of different collider setups To fully appreciate the impact of collider energy in constraining the relevant coefficients, we compare the results from current LHC measurements with the FCC-hh bounds. For simplicity, we only use the inclusive cross-section. The limits obtained from the fit are presented in Fig. 6.20. For both scenarios, EFT predictions include the linear and quadratic contributions. For the LHC, we use the SM prediction at NLO in QCD of Ref. [73], and we fit the theoretical predictions to the inclusive ATLAS [72] and CMS [199] measurements. For the FCC-hh, we use the same theoretical and experimental inputs used for the previous case of Fig. 6.18. The results from this fit show the significant constraining power that

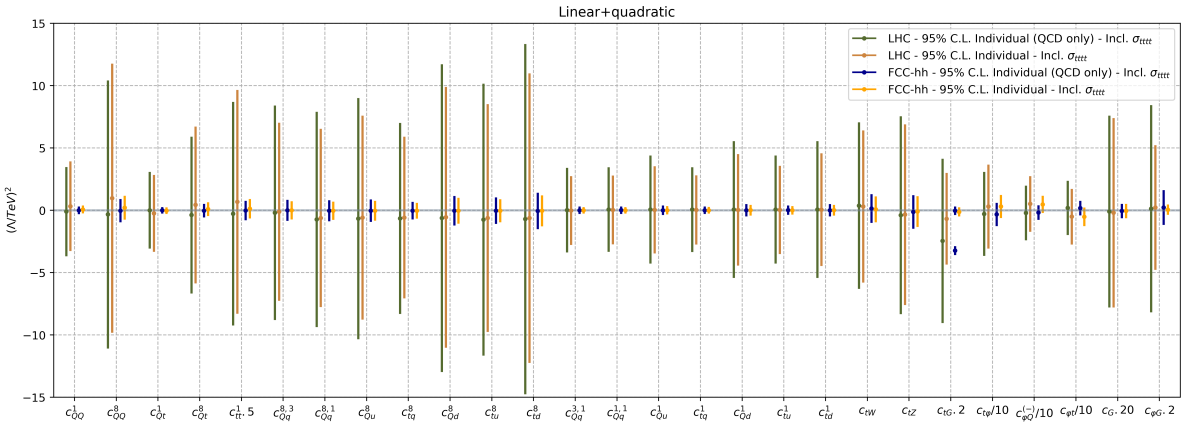

Figure 6.20.: Limits on all four-fermion and relevant operators used in this study obtained from the χ^2 fit to the ATLAS [72] and CMS [199] inclusive measurements and using the SM prediction of Ref. [73] as well as FCC-hh projections.

the FCC-hh will be able to provide for the SMEFT coefficients. Again, the effects from the subleading terms are diluted by including the quadratic contributions in the predictions. Finally, we note that it is expected that with the high-energy reach of the FCC-hh, differential distributions extending well into the multi-TeV range will become available and further improve the bounds beyond those expected from the inclusive cross-section.

6.7. Double insertions

In this work, we critically assessed the study of Ref. [200], where it was suggested that 2-heavy-2-light operators could be better (or comparably) constrained in four top quark production than in $t\bar{t}$. Such suggestion was spurred from Ref. [201] reporting an upper limit on $t\bar{t}t\bar{t}$ cross-section to be 4.6 times that of the SM. Due to the high energy scale related to $t\bar{t}t\bar{t}$ production, E, the cross-section of $t\bar{t}t\bar{t}$ depending on the fourth power of the operator coefficients scales like $\sim (CE^2/\Lambda^2)^4$. The latter is an order probed by the double insertions of dimensions six operators. Ref. [200] argued these terms enhance the EFT sensitivity of the 2-heavy-2-light operators to a level at which $t\bar{t}t\bar{t}$ production can compete with $t\bar{t}$ production in constraining said operators.

In our study, we investigated the strength of the double insertions contributions described in Sec. 6.2. In particular, we compared the EFT sensitivity of double insertions to that of the squared contribution from all the 2-heavy-2-light operators, i.e.,

$$d\sigma_{\text{dbl}} \sim |\mathcal{A}_{\text{SM}}\, \mathcal{A}_{(\text{d6})^2}| \qquad \text{vs.} \qquad d\sigma_{\text{quad}} \sim |\mathcal{A}_{(\text{d6})}|^2. \tag{6.16}$$

The Feynman diagrams depicting the amplitudes with two dimension-six EFT insertions are shown in Fig. 6.21.

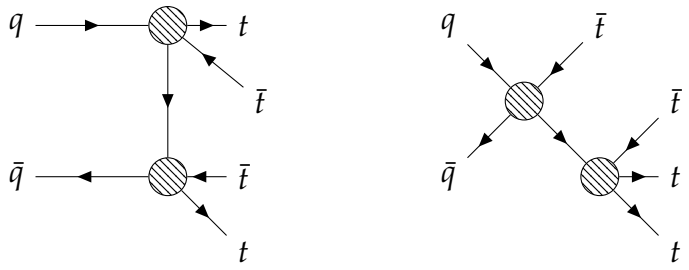

Figure 6.21.: Leading order Feynman diagrams of four top quark production with two EFT insertions represented by the blobs.

As a first step, we proceeded by reproducing the predictions of Ref. [200]. We observed that, indeed, the double insertion contributions provide enhancement to the cross-section compared to the squared ones. However, this is only true given the somewhat loose constraints on WCs, of order $\mathcal{O}(5-10)$, that Ref. [200] considered. Given the current comparatively stringent bounds from the global study of Ref. [59], we did not find an enhanced EFT sensitivity due to double insertions. Our results are presented in Tab. 6.4 where we fixed the value of c to unity and denoted amplitudes

with one EFT insertions with $\mathcal{A}_1$ and those with two insertions with $\mathcal{A}_2$. We fixed Λ to 1(3) TeV for the 13(100) TeV predictions. We summed all contributions arising from double insertions up to $\mathcal{O}(\Lambda^{-8})$. We observed that for all of the 2-heavy-2-light four-fermion operators, the contributions from the double insertions are negligible compared to the dimension-six squared ones, namely $\mathcal{O}(10)$ smaller. We also saw a similar pattern for the FCC-hh scenario.

2-heavy 2-light at c_i=1						
	$\sqrt{s} = 13$ TeV			$\sqrt{s} = 100$ TeV		
$\mathcal{O}_i$	$\lvert\mathcal{A}_1\rvert^2$ [fb]	$\sum_k \mathcal{O}(\mathcal{A}_2)_k$ [fb]	ratio	$\lvert\mathcal{A}_1\rvert^2$ [fb]	$\sum_k \mathcal{O}(\mathcal{A}_2)_k$ [fb]	ratio
$\mathcal{O}_{Qq}^{3,8}$	0.27	0.01	0.04	6.40	0.40	0.06
$\mathcal{O}_{Qq}^{1,8}$	0.28	0.05	0.18	6.36	0.63	0.10
$\mathcal{O}_{Qu}^{8}$	0.21	0.03	0.14	5.34	0.50	0.09
$\mathcal{O}_{tq}^{8}$	0.34	0.06	0.18	8.44	0.76	0.09
$\mathcal{O}_{Qd}^{8}$	0.13	0.03	0.23	3.13	0.35	0.11
$\mathcal{O}_{tu}^{8}$	0.17	0.03	0.18	3.97	0.41	0.10
$\mathcal{O}_{td}^{8}$	0.10	0.02	0.20	2.18	0.27	0.12
$\mathcal{O}_{Qq}^{3,1}$	1.84	0.15	0.08	46.98	5.49	0.12
$\mathcal{O}_{Qq}^{1,1}$	1.84	0.08	0.04	47.35	0.81	0.02
$\mathcal{O}_{Qu}^{1}$	1.14	0.06	0.05	29.94	2.83	0.09
$\mathcal{O}_{tq}^{1}$	1.80	0.14	0.08	46.54	6.33	0.14
$\mathcal{O}_{Qd}^{1}$	0.70	0.08	0.11	17.55	2.15	0.12
$\mathcal{O}_{tu}^{1}$	1.11	0.04	0.04	29.10	2.48	0.09
$\mathcal{O}_{td}^{1}$	0.68	0.05	0.07	17.44	1.79	0.10

Table 6.4.: Cross-section contributions arising from the diagonal quadratic SMEFT contributions at $\mathcal{O}(\Lambda^{-4})$ and denoted by $\lvert\mathcal{A}_1\rvert^2$ compared to the sum of all double insertions contributions up to $\mathcal{O}(\Lambda^{-8})$ and denoted by $\mathcal{A}_2$. The ratio column is that of double insertions contributions to quadratic ones.

It is worth mentioning that while the squared dimension-six term in the EFT expansion is invariant under field transformation, the double insertion contributions arising at the order $\mathcal{O}(\Lambda^{-4})$ are not unless the terms corresponding to dimension-eight SMEFT operators are included. This renders the leading double insertion contribution at $\mathcal{O}(\Lambda^{-4})$ together with the dimension-eight insertion at the same order to be separately invariant under field redefinitions from the rest of the terms. Given the current bounds on the set of 2-heavy-2-light operators, we found that their sensitivity is not enhanced from multiple insertions. Such a conclusion supports the idea that 2-heavy- 2-light operators might be better constrained elsewhere than in four top

quark production. This maintains the status of the set of 4-heavy operators being the ones expected to derive the most robust constraints on their coefficients through the four top quark production.

Chapter 7.

Summary and conclusions

Chap. 1 of this thesis discussed the Standard Model of particle physics (SM) as one of the most successful theories in particle physics, despite its inherent shortcomings. Many theories have tried to extend the SM, aiming to explain the new physics needed to evade the "incompleteness" of the SM. The widespread expectation is that beyond the SM, new physics would manifest itself as new particles that we did not observe before. However, while high-energy experiments have verified the SM to incredible precision, they could not find indications for BSM particles. One explanation for such hindrance is that our current experimental reach has not yet reached the kinematic range that can produce those new particles; reasoning led to the exploitation of effective field theory approaches in search of new physics.

Chap. 2 aimed at addressing the EFTs, particularly the SMEFT, and its ability to systematically parameterise new physics deviations due to the presence of new particles we can not directly measure. I discussed how the SMEFT augments the SM Lagrangian with higher-dimensions operators built out of the SM fields and respecting the SM gauge symmetries. These higher dimensional operators can modify SM interactions that we already know or even introduce new interactions which do not exist in the SM. Precise experimental measurements from the relatively low-energy probes can set constraints on the possible effects of these operators. Such constraints are essentially constraints on new physics. SMEFT studies at the LHC have been an ongoing effort by the experimental and theoretical communities in all the SM sectors: the electroweak, the Higgs, the flavour, and the top quark sectors. Moreover, global fits combining a broad set of publicly available data have also appeared.

Chap. 3 discussed top quark physics as a notable artery for understanding the strong interactions and EWSB and as a potential guide to where the indirect effects of potential new physics may appear. I started with a SM study concerning the improvement in the theoretical calculation of the $t\bar{t}W$ production process to resolve

the tension observed between the experimental measurement and the expected value. While such tension is still a feature of this measurement, the study showed that these improved techniques are necessary for understanding the $t\bar{t}W$ process. I also presented the most recent single top quark polarisation measurement. The measurement pointed out the favourite direction in which top quarks are highly polarised. This measurement also set stringent limits on the effective coefficients of the SMEFT operator modifying the Wtb interaction of the SM. I concluded this chapter by presenting the anomalous $t\bar{t}\gamma$ coupling measurement, which was able to set the best-published limits to date on the coefficients of operators modifying the $t\bar{t}Z$ and the $t\bar{t}\gamma$ interactions in the SM.

In Chap. 4, I presented the CMS measurement of $t\bar{t}H$ in multilepton final states. I discussed how the $t\bar{t}H$ process is crucial for our understanding of the top-Yukawa coupling, and also its capability to constrain relevant SMEFT operators. Regarding the experimental measurement, I started with presenting the latest CMS inclusive one reporting the $t\bar{t}H$ signal production rate, then further discussed the efforts to extend it to the differential level, in particular, the attempts of reconstructing the differential cross-section in the Higgs boson transverse momentum bins. As performing an EFT interpretation of the $t\bar{t}H$ process was the main drive behind these efforts, I also showed the potential SMEFT constraints this measurement could offer. This was shown in likelihood scans for the relevant EFT coefficients, particularly the dipole operator modifying the gluon-top quark interaction of the SM and the one rescaling the top-Yukawa coupling.

Chap. 5 presented a dedicated study of the tWZ process, highlighting its sensitivity to indirect new physics effects via the SMEFT, also discussing the general advantages of tWZ in contributing to our global understanding of top quark EW interactions. In doing so, we constructed an operative definition of the tWZ process, valid beyond LO in perturbation theory. Such operation was necessary due to the overlap of tWZ at NLO with resonant contributions from processes such as $t\bar{t}Z$ and $t\bar{t}$. We performed the overlap removal using the so-called diagram removal (DR) procedures. Our fixed order NLO results proved stable under such procedures. Having defined the phase space region for tWZ at NLO, we studied how SMEFT deformations affected the process. Considering the underlying $b\,W \to t\,Z$ scattering sub-amplitude in our first step, we identified potential energy-growing effects that future collider searches could exploit. We found one operator, namely, $\mathcal{O}^{(3)}_{\varphi Q}$, with such feature appearing in the fully longitudinal configuration of the sub-amplitude. Moving forward, we obtained differential NLO predictions for tWZ in the SM and for each relevant operator contribution at linear and quadratic order of the EFT. Finally, both for the SM and

$\mathcal{O}^{(3)}_{\varphi Q}$, we went beyond the fixed order predictions by matching the latter to PS. The relative effect of $\mathcal{O}^{(3)}_{\varphi Q}$ was practically unchanged compared to the fixed order case. Such a conclusion suggests our predictions can be used as inputs to future analyses, eventually improving our understanding of top quark EW interactions.

Finally, Chap. 6 presented a complete analysis of four top quark production at hadron colliders within the SMEFT framework. In this work, our studies were based on predictions at the tree-level, yet included all the possible QCD and EW coupling order contributions, keeping gauge and top-Yukawa couplings separate. We computed observables in the SMEFT by considering linear interference and quadratic contributions. Within the large set of SMEFT operators possibly contributing to four top quark production, we have identified a subclass, which we called the "non-naive", consisting of all the four heavy operators and a subset of two-fermion and bosonic ones. We coined these operators non-naive since their leading contributions to the linear interference cross-section is primarily induced by formally subleading terms in the mixed QCD-EW expansion. We were able to draw three main conclusions from a thorough analysis of the relevant operators contributions at the LHC and the FCC-hh colliders. First, the 4-heavy operators provide their most significant contribution through the $\mathcal{O}(\alpha_s^2\alpha_w)$ terms. The same happens for the remaining six operators in the non-naive set. Second, $\mathcal{O}(\alpha_s^2\alpha)$ is dominant compared to $\mathcal{O}(\alpha_s^2\alpha_t)$ for the 4-heavy operators. Third, from $t\bar{t}$ production, one could naively expect that octet operators would dominate. However, we observed the opposite: the singlet operators have larger linear interference cross-sections than their octet counterparts. Looking ahead, we studied the sensitivity of future colliders of four top quark production. We found that all the 4-heavy operators exhibit a sensitivity enhancement at high collision energies, in contrast to the 2-heavy-2-light operators. We, therefore, concluded that 4-heavy operators are the ones with the highest potential to be strongly constrained in four top quark production. The importance of our study comes in summarising the four top quark SMEFT predictions and analysing them in each order of the mixed QCD-EW expansion. Our analysis motivates an effort towards systematically studying subleading effects in other processes, such as e.g. $t\bar{t}Z$ and, in particular, $t\bar{t}$ +jets.

Appendix A.

On the $b\,W \to t\,Z$ sub-amplitude

A.1. Helicity amplitudes for the $b\,W \to t\,Z$ scattering

λ_b,	λ_W,	λ_t,	λ_Z	SM	$\mathcal{O}_{tW}$	$\mathcal{O}_{tZ}$	$\mathcal{O}_{\varphi Q}^{(-)}$	$\mathcal{O}_{\varphi Q}^{(3)}$	$\mathcal{O}_{\varphi t}$
$-$,	0,	$-$,	0	s^0	$-s^0$	–	–	$2\sqrt{2}\sqrt{s(s+t)}$	–
$-$,	0,	$+$,	0	$s^{-\frac{1}{2}}$	$4m_W\left(\frac{s}{\sqrt{-t}}-2\sqrt{-t}\right)$	$2m_Z\sqrt{-t}$	$\sqrt{2}m_t\sqrt{-t}$	$2\sqrt{2}m_t\sqrt{-t}$	$-\sqrt{2}m_t\sqrt{-t}$
$-$,	$-$,	$-$,	0	$s^{-\frac{1}{2}}$	–	–	–	$4m_W\sqrt{-t}$	–
$-$,	$-$,	$+$,	0	s^{-1}	$2\sqrt{2}\sqrt{s(s+t)}$	s^0	s^0	s^0	s^0
$-$,	$+$,	$-$,	0	$s^{-\frac{1}{2}}$	–	–	–	–	–
$-$,	$+$,	$+$,	0	s^0	s^0	–	–	s^0	–
$-$,	0,	$-$,	$-$	$s^{-\frac{1}{2}}$	–	$-2\sqrt{2}m_t\sqrt{-t}$	–	$-4m_Z\sqrt{-t}$	–
$-$,	0,	$-$,	$+$	$s^{-\frac{1}{2}}$	–	–	–	–	–
$-$,	0,	$+$,	$-$	s^0	s^0	–	s^0	s^0	–
$-$,	0,	$+$,	$+$	s^{-1}	$-4\sqrt{2}c_W\sqrt{s(s+t)}$	$2\sqrt{2}\sqrt{s(s+t)}$	s^0	–	s^0
$-$,	$-$,	$-$,	$-$	s^0	s^0	s^0	s^0	s^0	–
$-$,	$-$,	$-$,	$+$	s^{-1}	–	–	–	–	–
$-$,	$-$,	$+$,	$-$	$s^{-\frac{1}{2}}$	$8m_Wc_W\frac{s}{\sqrt{-t}}-4m_Z\left(1-\frac{4}{3}s_W^2\right)\sqrt{-t}$	–	–	–	–
$-$,	$-$,	$+$,	$+$	–	$8m_Z\left(\frac{1}{3}s_W^2-1\right)\sqrt{-t}$	$4m_W\sqrt{-t}$	–	–	–
$-$,	$+$,	$-$,	$-$	s^{-1}	–	–	–	–	–
$-$,	$+$,	$-$,	$+$	s^0	–	–	s^0	s^0	–
$-$,	$+$,	$+$,	$-$	$s^{-\frac{1}{2}}$	–	–	–	–	–
$-$,	$+$,	$+$,	$+$	$s^{-\frac{1}{2}}$	$8m_Wc_W\left(\frac{s}{\sqrt{-t}}-\sqrt{-t}\right)$	–	–	–	–
$+$,	·,	·,	·	–	–	–	–	–	–

Table A.1.: Operators contributions to the helicity amplitudes of $b\,W \to t\,Z$ scattering in the high-energy limit, i.e. $s, -t \gg v$. λ_i denotes the helicity/polarisation of the external leg i and the contribution of each operator $\mathcal{O}_j$ omits an overall factor of c_i/Λ^2. "$-$" entries denote SMEFT contributions that decrease with energy. The energy dependence of the corresponding SM helicity amplitude is given in a schematic form. All amplitudes with a right-handed b-quark are not generated since $m_b = 0$ is enforced by our flavor symmetry assumption.

A.2. Embedding $b\,W \to t\,Z$ amplitudes and including quadratic EFT contributions

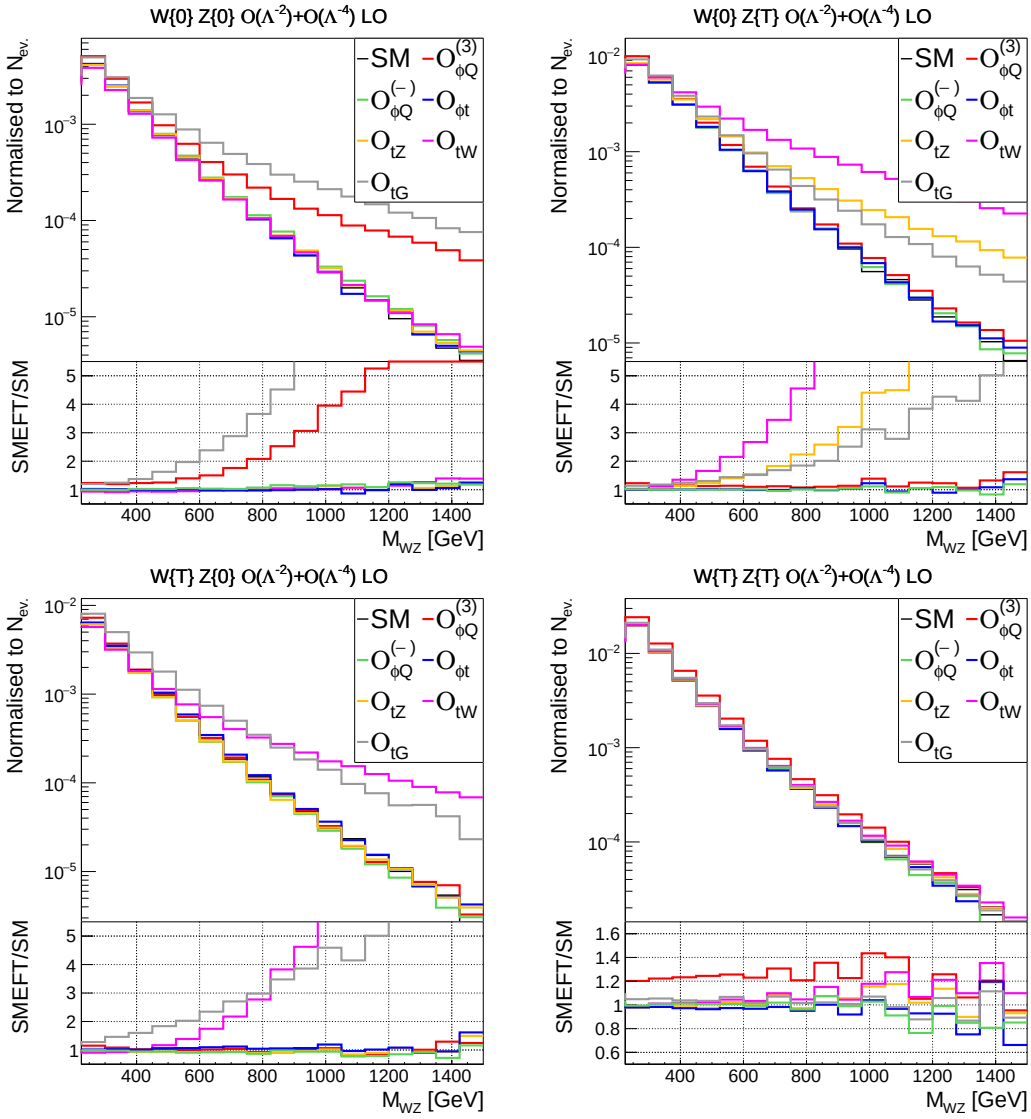

Figure A.1.: Same as Fig. 5.6 but for the SMEFT predictions truncated at the quadratic-level, $\mathcal{O}(\Lambda^{-4})$.

Appendix B.

Translation and constraints relevant to four-top production

2-heavy 2-light					
$\mathcal{O}_i$	UFO	Translation	$\mathcal{O}_i$	UFO	Translation
$\mathcal{O}_{Qq}^{1,1}$	cQq11	$\sum_{i=1,2}[C_{qq}^{(1)}]^{ii33}+\frac{1}{6}[C_{qq}^{(1)}]^{i33i}+\frac{1}{2}[C_{qq}^{(3)}]^{i33i}$	$\mathcal{O}_{Qq}^{1,8}$	cQq18	$\sum_{i=1,2}[C_{qq}^{(1)}]^{i33i}+3[C_{qq}^{(3)}]^{i33i}$
$\mathcal{O}_{Qq}^{3,1}$	cQq31	$\sum_{i=1,2}[C_{qq}^{(3)}]^{ii33}+\frac{1}{6}[C_{qq}^{(1)}]^{i33i}-\frac{1}{6}[C_{qq}^{(3)}]^{i33i}$	$\mathcal{O}_{Qq}^{3,8}$	cQq38	$\sum_{i=1,2}[C_{qq}^{(1)}]^{i33i}-[C_{qq}^{(3)}]^{i33i}$
$\mathcal{O}_{tu}^{1}$	ctu1	$\sum_{i=1,2}[C_{uu}]^{ii33}+\frac{1}{3}[C_{uu}]^{i33i}$	$\mathcal{O}_{tu}^{8}$	ctu8	$\sum_{i=1,2}2[C_{uu}]^{i33i}$
$\mathcal{O}_{td}^{1}$	ctd1	$\sum_{i=1,2(,3)}[C_{ud}^{(1)}]^{33ii}$	$\mathcal{O}_{td}^{8}$	ctd8	$\sum_{i=1,2(,3)}[C_{ud}^{(8)}]^{33ii}$
$\mathcal{O}_{tq}^{1}$	ctq1	$\sum_{i=1,2}[C_{qu}^{(1)}]^{ii33}$	$\mathcal{O}_{tq}^{8}$	ctq8	$\sum_{i=1,2}[C_{qu}^{(8)}]^{ii33}$
$\mathcal{O}_{Qu}^{1}$	cQu1	$\sum_{i=1,2}[C_{qu}^{(1)}]^{33ii}$	$\mathcal{O}_{Qu}^{8}$	cQu8	$\sum_{i=1,2}[C_{qu}^{(8)}]^{33ii}$
$\mathcal{O}_{Qd}^{1}$	cQd1	$\sum_{i=1,2,(3)}[C_{qd}^{(1)}]^{33ii}$	$\mathcal{O}_{Qd}^{8}$	cQd8	$\sum_{i=1,2,(3)}[C_{qd}^{(8)}]^{33ii}$
4-heavy					
$\mathcal{O}_{QQ}^{1}$	cQQ1	$2[C_{qq}^{(1)}]^{3333}-\frac{2}{3}[C_{qq}^{(3)}]^{3333}$	$\mathcal{O}_{QQ}^{8}$	cQQ8	$8[C_{qq}^{(3)}]^{3333}$
$\mathcal{O}_{Qt}^{1}$	cQt1	$[C_{qu}^{(1)}]^{3333}$	$\mathcal{O}_{Qt}^{8}$	cQt8	$[C_{qu}^{(8)}]^{3333}$
$\mathcal{O}_{tt}^{1}$	ctt1	$[C_{uu}^{(1)}]^{3333}$			

Table B.1.: The translation of four-fermion operators from Warsaw basis to top-basis. The UFO column shows the notation of the WCs in the SMEFTatNLO model.

2-heavy 2-light									
UFO	$\mathcal{O}(\Lambda^{-2})$		$\mathcal{O}(\Lambda^{-4})$		UFO	$\mathcal{O}(\Lambda^{-2})$		$\mathcal{O}(\Lambda^{-4})$	
	Individual	Marginalised	Individual	Marginalised		Individual	Marginalised	Individual	Marginalised
cQq11	[-3.603,0.307]	[-8.047,9.400]	[-0.303,0.225]	[-0.354,0.249]	cQq18	[-0.273,0.509]	[-2.258,4.822]	[-0.373,0.309]	[-0.555,0.236]
cQq31	[-0.099,0.155]	[-0.163,0.296]	[-0.088,0.166]	[-0.167,0.197]	cQq38	[-1.813,0.625]	[-3.014,7.365]	[-0.470,0.439]	[-0.462,0.497]
ctu1	[-6.046,0.424]	[-15.565,15.379]	[-0.380,0.293]	[-0.383,0.331]	ctu8	[-0.774,0.607]	[-16.952,0.368]	[-0.911,0.347]	[-1.118,0.260]
ctd1	[-9.504,-0.086]	[-27.673,11.356]	[-0.449,0.371]	[-0.474,0.347]	ctd8	[-1.458,1.365]	[-5.494,25.358]	[-1.308,0.638]	[-1.329,0.643]
ctq1	[-0.784,2.771]	[-12.382,6.626]	[-0.205,0.271]	[-0.222,0.226]	ctq8	[-0.396,0.612]	[-4.035,4.394]	[-0.483,0.393]	[-0.687,0.186]
cQu1	[-0.938,2.462]	[-16.996,1.072]	[-0.281,0.371]	[-0.207,0.339]	cQu8	[-1.508,1.022]	[-12.745,13.758]	[-1.007,0.521]	[-1.002,0.312]
cQd1	[-0.889,6.459]	[-3.239,34.632]	[-0.332,0.436]	[-0.370,0.384]	cQd8	[-2.393,2.042]	[-24.479,11.233]	[-1.615,0.888]	[-1.256,0.715]
4-heavy									
cQQ1	[-6.132,23.281]	[-190,189]	[-2.229,2.019]	[-2.995,3.706]	cQQ8	[-26.471,57.778]	[-190,170]	[-6.812,5.834]	[-11.177,8.170]
cQt1	[-195,159]	[-190,189]	[-1.830,1.862]	[-1.391,1.251]	cQt8	[-5.722,20.105]	[-190,162]	[-4.213,3.346]	[-3.040,2.202]
ctt1	[-2.782,12.114]	[-115,153]	[-1.151,1.025]	[-0.791,0.714]					

Table B.2.: Bounds on four-fermion effective coefficients from the global analysis of Ref. [59].

Contributing operators									
UFO	$\mathcal{O}(\Lambda^{-2})$		$\mathcal{O}(\Lambda^{-4})$		UFO	$\mathcal{O}(\Lambda^{-2})$		$\mathcal{O}(\Lambda^{-4})$	
	Individual	Marginalised	Individual	Marginalised		Individual	Marginalised	Individual	Marginalised
ctp	[-1.331,0.355]	[-5.739,3.435]	[-1.286,0.348]	[-2.319,2.797]	ctZ	[-0.039,0.099]	[-15.869,5.636]	[-0.044,0.094]	[-1.129,0.856]
ctW	[-0.093,0.026]	[-0.313,0.123]	[-0.084,0.029]	[-0.241,0.086]	ctG	[0.007,0.111]	[-0.127,0.403]	[0.006,0.107]	[0.062,0.243]
cpQM	[-0.998,1.441]	[-1.690,11.569]	[-1.147,1.585]	[-2.250,2.855]	cpt	[-2.087,2.463]	[-3.270,18.267]	[-3.028,2.195]	[-13.260,3.955]
cpG	[-0.002,0.005]	[-0.043,0.012]	[-0.002,0.005]	[-0.019,0.003]					

Table B.3.: Bounds on the contributing two-fermion and purely-bosonic effective coefficients from the global analysis of Ref. [59], except for the $\mathcal{O}_G$ operator.

Appendix C.

Additional four-top predictions

$\mathcal{O}_i$	$\left(\frac{1}{\Lambda}\right)^2 : \sigma_3[\sigma_2]$[fb]	$\sum\left(\frac{1}{\Lambda}\right)^2$[fb]	$\sum\left(\frac{1}{\Lambda}\right)^4$[fb]
$\mathcal{O}^8_{QQ}$	0.081 [-0.317]$^{+54\%}_{-32\%}$	-0.235$^{+37\%}_{-25\%}$	0.121$^{+45\%}_{-29\%}$
$\mathcal{O}^8_{Qt}$	0.273 [-0.577]$^{+54\%}_{-32\%}$	-0.303$^{+29\%}_{-22\%}$	0.354$^{+45\%}_{-29\%}$
$\mathcal{O}^1_{QQ}$	0.242 [-0.948]$^{+54\%}_{-33\%}$	-0.706$^{+37\%}_{-25\%}$	1.086(1)$^{+46\%}_{-29\%}$
$\mathcal{O}^1_{Qt}$	-0.005 [0.725]$^{+67\%}_{-61\%}$	0.720$^{+41\%}_{-27\%}$	1.471(2)$^{+46\%}_{-29\%}$
$\mathcal{O}^1_{tt}$	0.485 [-1.670]$^{+54\%}_{-33\%}$	-1.185(1)$^{+36\%}_{-24\%}$	4.339(2)$^{+46\%}_{-29\%}$

Table C.1.: Inclusive predictions within relative scale uncertainties for 4-heavy operators (scales are given on σ_3 in the first column).

$\mathcal{O}_i$	$\left(\frac{1}{\Lambda}\right)^2 : \sigma_3[\sigma_2]$[fb]	$\sum\left(\frac{1}{\Lambda}\right)^2$[fb]	$\sum\left(\frac{1}{\Lambda}\right)^4$[fb]
$\mathcal{O}^{3,8}_{Qq}$	0.077 [-0.02]$^{+42\%}_{-27\%}$	0.070$^{+41\%}_{-27\%}$	0.274(1)$^{+29\%}_{-21\%}$
$\mathcal{O}^{1,8}_{Qq}$	0.278 [0.023]$^{+43\%}_{-28\%}$	0.339$^{+40\%}_{-26\%}$	0.275(1)$^{+30\%}_{-21\%}$
$\mathcal{O}^8_{Qu}$	0.202 [0.022]$^{+43\%}_{-28\%}$	0.249$^{+40\%}_{-26\%}$	0.211(1)$^{+30\%}_{-21\%}$
$\mathcal{O}^8_{tq}$	0.315 [0.036]$^{+43\%}_{-28\%}$	0.391$^{+40\%}_{-26\%}$	0.335(1)$^{+30\%}_{-21\%}$
$\mathcal{O}^8_{Qd}$	0.115 [0.016]$^{+44\%}_{-28\%}$	0.144$^{+40\%}_{-26\%}$	0.129(1)$^{+31\%}_{-21\%}$
$\mathcal{O}^8_{tu}$	0.178 [0.011]$^{+43\%}_{-28\%}$	0.212$^{+40\%}_{-26\%}$	0.167(1)$^{+30\%}_{-21\%}$
$\mathcal{O}^8_{td}$	0.101 [0.015]$^{+44\%}_{-28\%}$	0.129$^{+40\%}_{-26\%}$	0.103(1)$^{+30\%}_{-21\%}$
$\mathcal{O}^{3,1}_{Qq}$	-0.038 [0.079]$^{+41\%}_{-27\%}$	0.071$^{+20\%}_{-16\%}$	1.841(4)$^{+30\%}_{-21\%}$
$\mathcal{O}^{1,1}_{Qq}$	-0.140 [0.016]$^{+43\%}_{-28\%}$	-0.113$^{+47\%}_{-30\%}$	1.839(4)$^{+30\%}_{-21\%}$
$\mathcal{O}^1_{Qu}$	-0.083 [0.010]$^{+41\%}_{-27\%}$	-0.066$^{+45\%}_{-29\%}$	1.137(1)$^{+30\%}_{-21\%}$
$\mathcal{O}^1_{tq}$	-0.131 [0.017]$^{+41\%}_{-27\%}$	-0.106$^{+44\%}_{-29\%}$	1.799(1)$^{+30\%}_{-21\%}$
$\mathcal{O}^1_{Qd}$	-0.048 [0.002]$^{+42\%}_{-27\%}$	-0.049$^{+41\%}_{-27\%}$	0.695(1)$^{+31\%}_{-21\%}$
$\mathcal{O}^1_{tu}$	-0.089 [0.022]$^{+42\%}_{-27\%}$	-0.056$^{+52\%}_{-32\%}$	1.110(4)$^{+30\%}_{-21\%}$
$\mathcal{O}^1_{td}$	-0.051 [-0.011]$^{+43\%}_{-28\%}$	-0.065$^{+40\%}_{-26\%}$	0.684(1)$^{+31\%}_{-21\%}$

Table C.2.: Same as Tab. C.1 but for the 2-heavy 2-light operators.

$\mathcal{O}_i$	$\left(\frac{1}{\Lambda}\right)^2 : \sigma_3[\sigma_2]$[fb]	$\sum\left(\frac{1}{\Lambda}\right)^2$[fb]	$\sum\left(\frac{1}{\Lambda}\right)^4$[fb]
$\mathcal{O}_{tW}$	$\times$ [-0.233]	$-0.220^{+53\%}_{-32\%}$	$0.373^{+37\%}_{-24\%}$
$\mathcal{O}_{tZ}$	$\times$ [0.176]	$0.187^{+50\%}_{-31\%}$	$0.264^{+37\%}_{-24\%}$
$\mathcal{O}_{tG}$	$3.642(1)\ [0.024]^{+68\%}_{-38\%}$	$2.861(1)^{*+75\%}_{-40\%}$	$4.244(2)^{+53\%}_{-32\%}$
$\mathcal{O}_{t\varphi}$	$\times$ [0.072]	$-0.074^{+26\%}_{-20\%}$	$0.012^{+40\%}_{-26\%}$
$\mathcal{O}^{(-)}_{\varphi Q}$	$\times$ [0.123]	$-0.302^{*+35\%}_{-24\%}$	$0.030^{+39\%}_{-26\%}$
$\mathcal{O}_{\varphi t}$	$\times$ [-0.114]	$0.307^{*+35\%}_{-24\%}$	$0.030^{+40\%}_{-26\%}$
$\mathcal{O}_G$	$1.633(2)\ [0.113]^{+75\%}_{-40\%}$	$1.715(2)^{+75\%}_{-40\%}$	$94.5(33)^{+75\%}_{-39\%}$
$\mathcal{O}_{\varphi G}$	$\times$ [-0.107]	$-0.480^{*+41\%}_{-27\%}$	$2.229(1)^{+28\%}_{-20\%}$

Table C.3.: Same as Tab. C.1 but for the set of contributing operators. The $\times$ denotes zero cross-section. The asterisk indicates the operator receives non-negligible contributions at α_s-orders lower than σ_2.

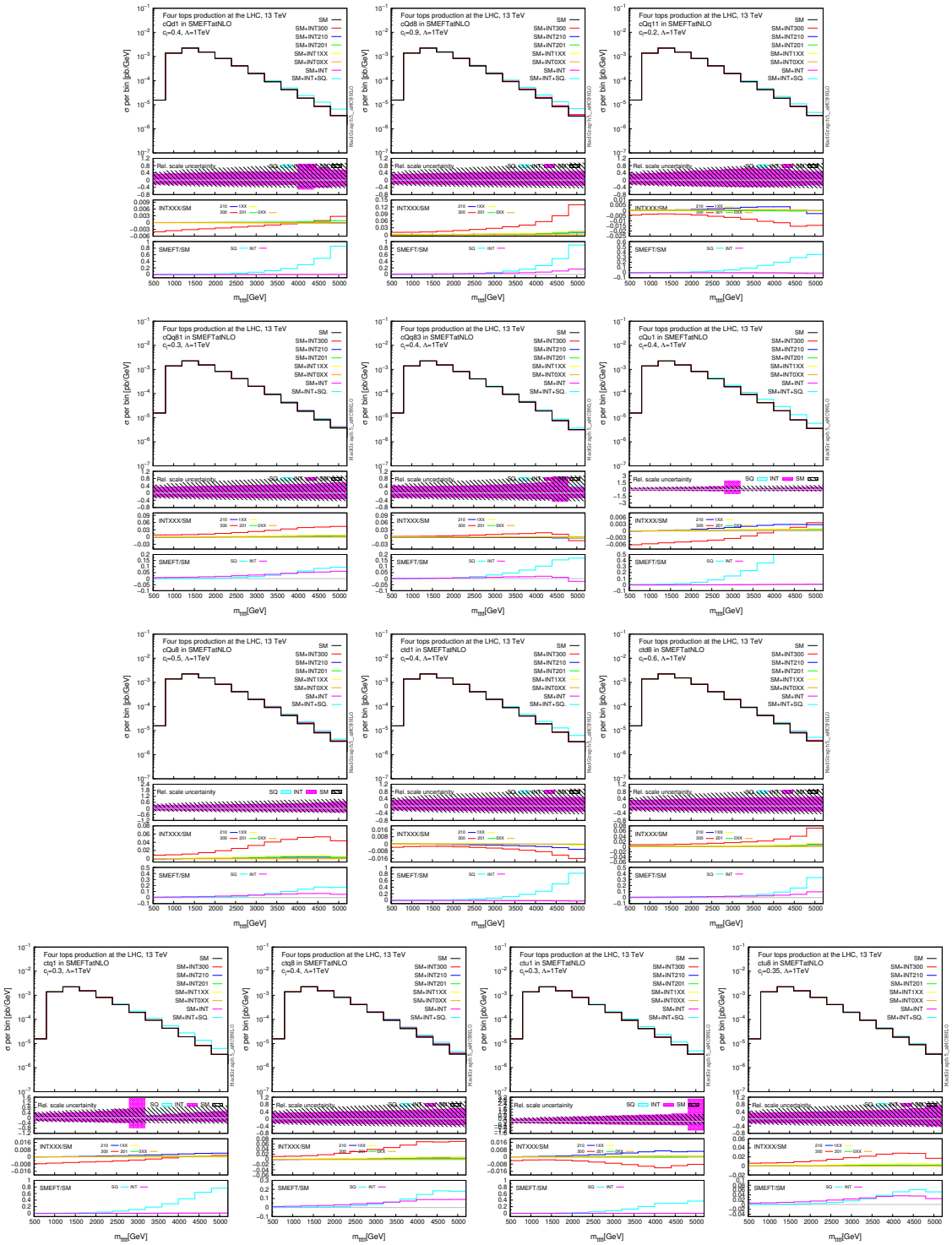

Figure C.1.: Same as Fig. 6.10 but for the rest of the four-fermion operators.

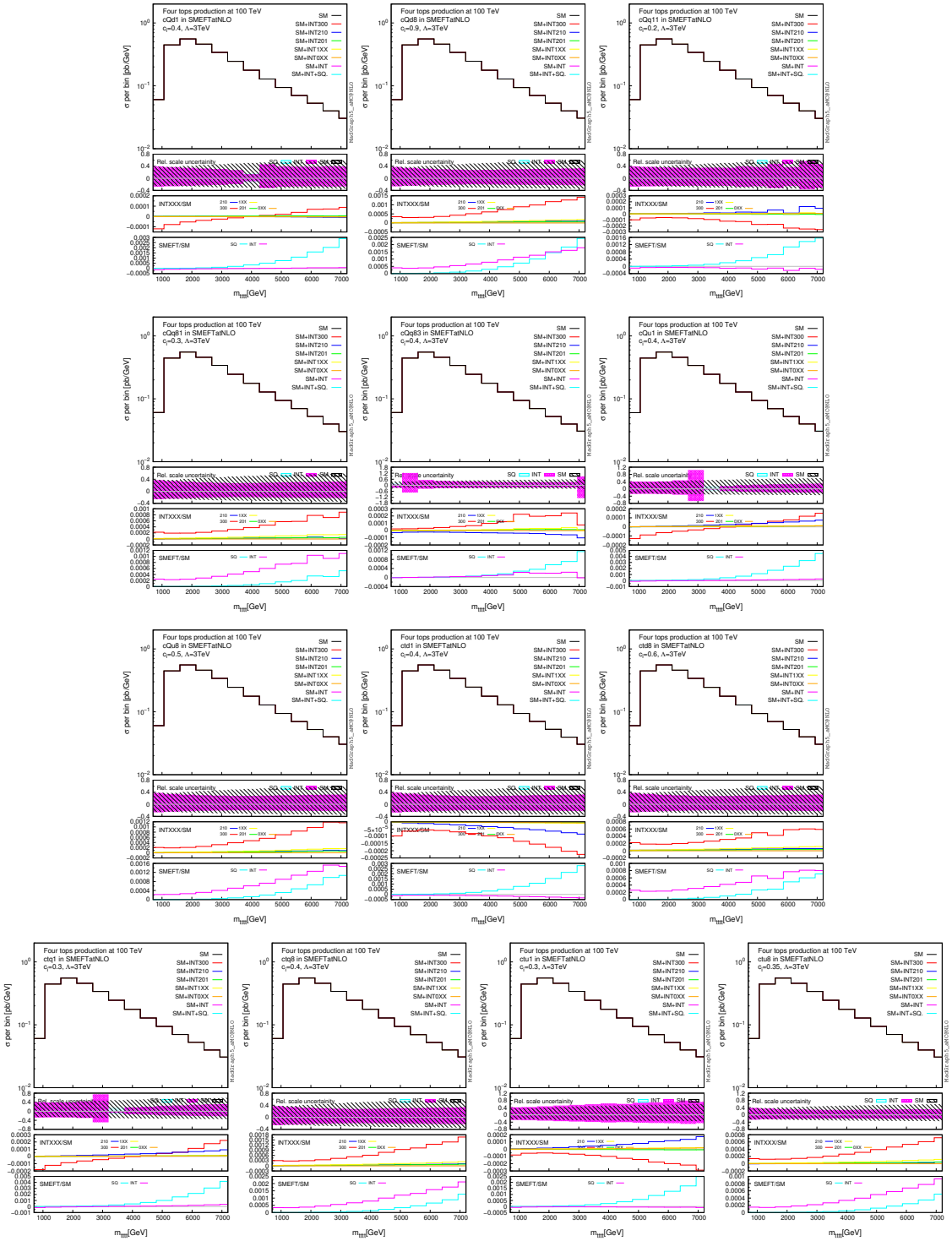

Figure C.2.: Same as Fig. 6.13 but for the rest of the four-fermion operators.

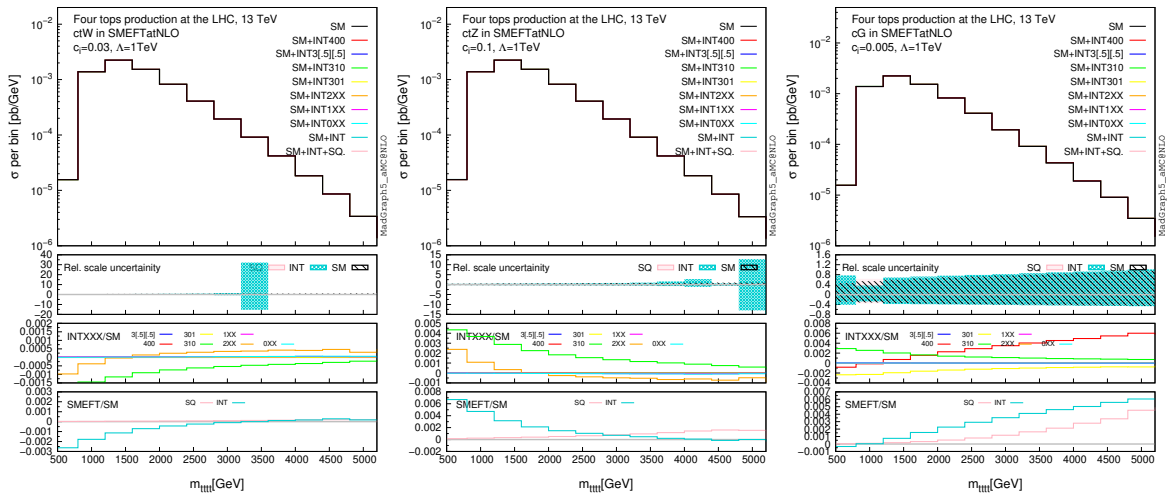

Figure C.3.: Same as Fig. 6.11 but for the rest of the contributing two-fermion and purely-bosonic operators.

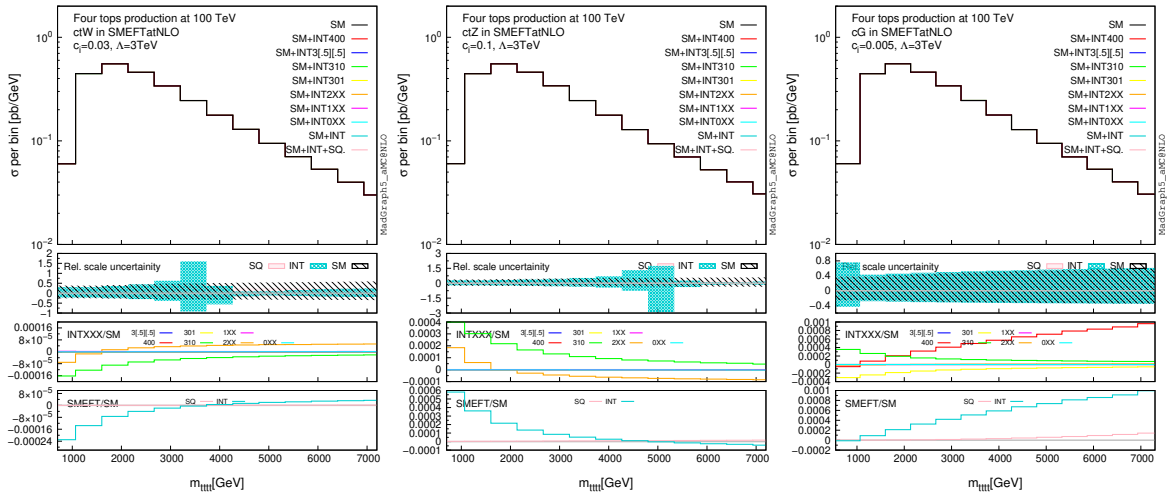

Figure C.4.: Same as Fig. 6.14 but for the rest of the contributing two-fermion and purely-bosonic operators.

Colophon

This thesis was made in LaTeX 2_ε using the "hepthesis" class [202].

Bibliography

[1] *Single top production in association with a WZ pair at the LHC in the SMEFT*, H. E. Faham, F. Maltoni, K. Mimasu, and M. Zaro, JHEP **0**1, 100 (2022), 2111.03080.

[2] *Complete SMEFT predictions for four top quark production at hadron colliders*, R. Aoude, H. El Faham, F. Maltoni, and E. Vryonidou, (2022), 2208.04962.

[3] P. Skands, Introduction to QCD, in *Theoretical Advanced Study Institute in Elementary Particle Physics: Searching for New Physics at Small and Large Scales*, pp. 341–420, 2013, 1207.2389.

[4] M. E. Peskin and D. V. Schroeder, *An Introduction to quantum field theory* (Addison-Wesley, Reading, USA, 1995).

[5] ATLAS, *Observation of a new particle in the search for the Standard Model Higgs boson with the ATLAS detector at the LHC*, G. Aad *et al.*, Phys. Lett. B **7**16, 1 (2012), 1207.7214.

[6] CMS, *Observation of a New Boson at a Mass of 125 GeV with the CMS Experiment at the LHC*, S. Chatrchyan *et al.*, Phys. Lett. B **7**16, 30 (2012), 1207.7235.

[7] *Spin and Unitary Spin Independence in a Paraquark Model of Baryons and Mesons*, O. W. Greenberg, Phys. Rev. Lett. **1**3, 598 (1964).

[8] *Three Triplet Model with Double SU(3) Symmetry*, M. Y. Han and Y. Nambu, Phys. Rev. **1**39, B1006 (1965).

[9] *The automated computation of tree-level and next-to-leading order differential cross sections, and their matching to parton shower simulations*, J. Alwall *et al.*, JHEP **0**7, 079 (2014), 1405.0301.

[10] *The automation of next-to-leading order electroweak calculations*, R. Frederix *et al.*, JHEP **0**7, 185 (2018), 1804.10017, [Erratum: JHEP 11, 085 (2021)].

[11] *CalcHEP 2.3: MSSM, structure functions, event generation, batchs, and generation of matrix elements for other packages*, A. Pukhov, (2004), hep-ph/0412191.

[12] CompHEP, *CompHEP 4.4: Automatic computations from Lagrangians to events*, E. Boos *et al.*, Nucl. Instrum. Meth. A **5**34, 250 (2004), hep-ph/0403113.

[13] *HELAC: A Package to compute electroweak helicity amplitudes*, A. Kanaki and C. G. Papadopoulos, Comput. Phys. Commun. **1**32, 306 (2000), hep-ph/0002082.

[14] *AMEGIC++ 1.0: A Matrix element generator in C++*, F. Krauss, R. Kuhn, and G. Soff, JHEP **0**2, 044 (2002), hep-ph/0109036.

[15] *O'Mega: An Optimizing matrix element generator*, M. Moretti, T. Ohl, and J. Reuter, p. 1981 (2001), hep-ph/0102195.

[16] *WHIZARD: Simulating Multi-Particle Processes at LHC and ILC*, W. Kilian, T. Ohl, and J. Reuter, Eur. Phys. J. C **7**1, 1742 (2011), 0708.4233.

[17] *Helac-Phegas: A Generator for all parton level processes*, A. Cafarella, C. G. Papadopoulos, and M. Worek, Comput. Phys. Commun. **1**80, 1941 (2009), 0710.2427.

[18] *Herwig++ Physics and Manual*, M. Bahr *et al.*, Eur. Phys. J. C **5**8, 639 (2008), 0803.0883.

[19] *Comix, a new matrix element generator*, T. Gleisberg and S. Hoeche, JHEP **1**2, 039 (2008), 0808.3674.

[20] *Parton Distribution and Decay Functions*, J. C. Collins and D. E. Soper, Nucl. Phys. B **1**94, 445 (1982).

[21] *Partial Symmetries of Weak Interactions*, S. L. Glashow, Nucl. Phys. **2**2, 579 (1961).

[22] *A Model of Leptons*, S. Weinberg, Phys. Rev. Lett. **1**9, 1264 (1967).

[23] *Weak and Electromagnetic Interactions*, A. Salam, Conf. Proc. C **6**80519, 367 (1968).

[24] *Broken Symmetries and the Masses of Gauge Bosons*, P. W. Higgs, Phys. Rev. Lett. **1**3, 508 (1964).

[25] *Broken Symmetry and the Mass of Gauge Vector Mesons*, F. Englert and R. Brout, Phys. Rev. Lett. **1**3, 321 (1964).

[26] *Experimental Test of Parity Conservation in β Decay*, C. S. Wu, E. Ambler, R. W. Hayward, D. D. Hoppes, and R. P. Hudson, Phys. Rev. **1**05, 1413 (1957).

[27] *Theory of Fermi interaction*, R. P. Feynman and M. Gell-Mann, Phys. Rev. **1**09, 193 (1958).

[28] *Broken Symmetries*, J. Goldstone, A. Salam, and S. Weinberg, Phys. Rev. **1**27, 965 (1962).

[29] CDF, *High-precision measurement of the W boson mass with the CDF II detector*, T. Aaltonen *et al.*, Science **3**76, 170 (2022).

[30] Particle Data Group, *Review of Particle Physics*, P. A. Zyla *et al.*, PTEP **2**020, 083C01 (2020).

[31] *An Improved experimental limit on the electric dipole moment of the neutron*, C. A. Baker *et al.*, Phys. Rev. Lett. **9**7, 131801 (2006), hep-ex/0602020.

[32] *The Standard Model as an Effective Field Theory*, I. Brivio and M. Trott, Phys. Rept. **7**93, 1 (2019), 1706.08945.

[33] *Introduction to Effective Field Theories*, A. V. Manohar, (2018), 1804.05863.

[34] *Lectures on Effective Field Theories*, A. Falkowski, (2020).

[35] *Infrared Singularities and Massive Fields*, T. Appelquist and J. Carazzone, Phys. Rev. D **1**1, 2856 (1975).

[36] *Change of variables and equivalence theorems in quantum field theories*, S. Kamefuchi, L. O'Raifeartaigh, and A. Salam, Nucl. Phys. **2**8, 529 (1961).

[37] *Structure of phenomenological Lagrangians. 1.*, S. R. Coleman, J. Wess, and B. Zumino, Phys. Rev. **1**77, 2239 (1969).

[38] *Effective Lagrangian Analysis of New Interactions and Flavor Conservation*, W. Buchmüller and D. Wyler, Nucl. Phys. B **2**68, 621 (1986).

[39] *Low-energy effects of new interactions in the electroweak boson sector*, K. Hagiwara, S. Ishihara, R. Szalapski, and D. Zeppenfeld, Phys. Rev. D **4**8, 2182 (1993).

[40] *Dimension-Six Terms in the Standard Model Lagrangian*, B. Grzadkowski, M. Iskrzynski, M. Misiak, and J. Rosiek, JHEP **1**0, 085 (2010), 1008.4884.

[41] *Renormalization Group Evolution of the Standard Model Dimension Six Operators III: Gauge Coupling Dependence and Phenomenology*, R. Alonso, E. E. Jenkins, A. V. Manohar, and M. Trott, JHEP **0**4, 159 (2014), 1312.2014.

[42] *Extending the Standard Model Effective Field Theory with the Complete Set of Dimension-7 Operators*, L. Lehman, Phys. Rev. D **9**0, 125023 (2014), 1410.4193.

[43] *2, 84, 30, 993, 560, 15456, 11962, 261485, ...: Higher dimension operators in the SM EFT*, B. Henning, X. Lu, T. Melia, and H. Murayama, JHEP **0**8, 016 (2017), 1512.03433, [Erratum: JHEP 09, 019 (2019)].

[44] *Low-derivative operators of the Standard Model effective field theory via Hilbert series methods*, L. Lehman and A. Martin, JHEP **0**2, 081 (2016), 1510.00372.

[45] *Dimension-8 operators in the Standard Model Eective Field Theory*, C. W. Murphy, JHEP **1**0, 174 (2020), 2005.00059.

[46] *Complete set of dimension-eight operators in the standard model effective field theory*, H.-L. Li *et al.*, Phys. Rev. D **1**04, 015026 (2021), 2005.00008.

[47] *Baryon- and Lepton-Nonconserving Processes*, S. Weinberg, Phys. Rev. Lett. **4**3, 1566 (1979).

[48] *LHC multijet events as a probe for anomalous dimension-six gluon interactions*, F. Krauss, S. Kuttimalai, and T. Plehn, Phys. Rev. D **9**5, 035024 (2017), 1611.00767.

[49] *Constraining anomalous gluon self-interactions at the LHC: a reappraisal*, V. Hirschi, F. Maltoni, I. Tsinikos, and E. Vryonidou, JHEP **0**7, 093 (2018), 1806.04696.

[50] *Studies of Dimension-Six EFT effects in Vector Boson Scattering*, R. Gomez-Ambrosio, Eur. Phys. J. C **7**9, 389 (2019), 1809.04189.

[51] *Standard model EFT effects in vector-boson scattering at the LHC*, A. Dedes, P. Kozów, and M. Szleper, Phys. Rev. D **1**04, 013003 (2021), 2011.07367.

[52] CMS, *W^+W^- boson pair production in proton-proton collisions at $\sqrt{s} = 13$ TeV*, A. M. Sirunyan *et al.*, Phys. Rev. D **1**02, 092001 (2020), 2009.00119.

[53] ATLAS, *Measurement of fiducial and differential W^+W^- production cross-sections at $\sqrt{s} = 13$ TeV with the ATLAS detector*, M. Aaboud *et al.*, Eur. Phys. J. C **7**9, 884 (2019), 1905.04242.

[54] *A sensitivity study of VBS and diboson WW to dimension-6 EFT operators at the LHC*, R. Bellan *et al.*, JHEP **0**5, 039 (2022), 2108.03199.

[55] *Renormalization Group Scaling of Higgs Operators and $\Gamma(h- > \gamma\gamma)$*, C. Grojean, E. E. Jenkins, A. V. Manohar, and M. Trott, JHEP **0**4, 016 (2013), 1301.2588.

[56] *Modifications to the properties of the Higgs boson*, A. V. Manohar and M. B. Wise, Phys. Lett. B **6**36, 107 (2006), hep-ph/0601212.

[57] *O new physics, where art thou? A global search in the top sector*, I. Brivio *et al.*, JHEP **0**2, 131 (2020), 1910.03606.

[58] *A Monte Carlo global analysis of the Standard Model Effective Field Theory: the top quark sector*, N. P. Hartland *et al.*, JHEP **0**4, 100 (2019), 1901.05965.

[59] SMEFiT, *Combined SMEFT interpretation of Higgs, diboson, and top quark data from the LHC*, J. J. Ethier *et al.*, JHEP **1**1, 089 (2021), 2105.00006.

[60] *Top, Higgs, Diboson and Electroweak Fit to the Standard Model Effective Field Theory*, J. Ellis, M. Madigan, K. Mimasu, V. Sanz, and T. You, JHEP **0**4, 279 (2021), 2012.02779.

[61] *Constraining top quark effective theory in the LHC Run II era*, A. Buckley *et al.*, JHEP **0**4, 015 (2016), 1512.03360.

[62] *The top quark electro-weak couplings after LHC Run 2*, V. Miralles *et al.*, JHEP **0**2, 032 (2022), 2107.13917.

[63] *Composite Technicolor Standard Model*, R. S. Chivukula and H. Georgi, Phys. Lett. B **1**88, 99 (1987).

[64] *Minimal flavor violation: An Effective field theory approach*, G. D'Ambrosio, G. F. Giudice, G. Isidori, and A. Strumia, Nucl. Phys. B **6**45, 155 (2002), hep-ph/0207036.

[65] *Electroweak input parameters*, I. Brivio *et al.*, (2021), 2111.12515.

[66] CDF, *Evidence for top quark production in $\bar{p}p$ collisions at $\sqrt{s} = 1.8$ TeV*, F. Abe *et al.*, Phys. Rev. Lett. **7**3, 225 (1994), hep-ex/9405005.

[67] CDF, *Observation of top quark production in $\bar{p}p$ collisions*, F. Abe *et al.*, Phys. Rev. Lett. **7**4, 2626 (1995), hep-ex/9503002.

[68] *Interpreting top-quark LHC measurements in the standard-model effective field theory*, D. Barducci *et al.*, (2018), 1802.07237.

[69] ATLAS, *Measurement of the $t\bar{t}Z$ and $t\bar{t}W$ cross sections in proton-proton collisions at $\sqrt{s} = 13$ TeV with the ATLAS detector*, M. Aaboud *et al.*, Phys. Rev. D **9**9, 072009 (2019), 1901.03584.

[70] CMS, *Measurement of the cross section for top quark pair production in association with a W or Z boson in proton-proton collisions at $\sqrt{s} = 13$ TeV*, A. M. Sirunyan *et al.*, JHEP **0**8, 011 (2018), 1711.02547.

[71] ATLAS, *Analysis of $t\bar{t}H$ and $t\bar{t}W$ production in multilepton final states with the ATLAS detector*, ATLAS-CONF-2019-045 (2019).

[72] ATLAS, *Evidence for $t\bar{t}t\bar{t}$ production in the multilepton final state in proton–proton collisions at $\sqrt{s} = 13$ TeV with the ATLAS detector*, G. Aad *et al.*, Eur. Phys. J. C **8**0, 1085 (2020), 2007.14858.

[73] *Large NLO corrections in $t\bar{t}W^{\pm}$ and $t\bar{t}t\bar{t}$ hadroproduction from supposedly subleading EW contributions*, R. Frederix, D. Pagani, and M. Zaro, JHEP **0**2, 031 (2018), 1711.02116.

[74] *Strong tW Scattering at the LHC*, J. A. Dror, M. Farina, E. Salvioni, and J. Serra, JHEP **0**1, 071 (2016), 1511.03674.

[75] *Subleading EW corrections and spin-correlation effects in $t\bar{t}W$ multi-lepton signatures*, R. Frederix and I. Tsinikos, Eur. Phys. J. C **8**0, 803 (2020), 2004.09552.

[76] *Top-quark pair hadroproduction in association with a heavy boson at NLO+NNLL including EW corrections*, A. Broggio *et al.*, JHEP **0**8, 039 (2019), 1907.04343.

[77] *Associated top quark pair production with a heavy boson: differential cross sections at NLO+NNLL accuracy*, A. Kulesza, L. Motyka, D. Schwartländer, T. Stebel, and V. Theeuwes, Eur. Phys. J. C **8**0, 428 (2020), 2001.03031.

[78] *Associated production of a top-quark pair with vector bosons at NLO in QCD: impact on* $t\bar{t}H$ *searches at the LHC*, F. Maltoni, D. Pagani, and I. Tsinikos, JHEP **0**2, 113 (2016), 1507.05640.

[79] *Top-quark charge asymmetry and polarization in* $t\bar{t}W$ *production at the LHC*, F. Maltoni, M. L. Mangano, I. Tsinikos, and M. Zaro, Phys. Lett. B **7**36, 252 (2014), 1406.3262.

[80] *The simplest of them all:* $t\bar{t}W^{\pm}$ *at NLO accuracy in QCD*, G. Bevilacqua, H.-Y. Bi, H. B. Hartanto, M. Kraus, and M. Worek, JHEP **0**8, 043 (2020), 2005.09427.

[81] *NLO QCD corrections to off-shell* $t\bar{t}W^{+}$ *production at the LHC*, A. Denner and G. Pelliccioli, JHEP **1**1, 069 (2020), 2007.12089.

[82] *Combined NLO EW and QCD corrections to off-shell* $t\bar{t}W$ *production at the LHC*, A. Denner and G. Pelliccioli, Eur. Phys. J. C **8**1, 354 (2021), 2102.03246.

[83] *NLO QCD corrections to off-shell* $t\bar{t}W^{\pm}$ *production at the LHC: correlations and asymmetries*, G. Bevilacqua *et al.*, Eur. Phys. J. C **8**1, 675 (2021), 2012.01363.

[84] *Top-quark pair production in association with a* $W^{\pm}$ *gauge boson in the POWHEG-BOX*, F. Febres Cordero, M. Kraus, and L. Reina, Phys. Rev. D **1**03, 094014 (2021), 2101.11808.

[85] *Weak corrections to Higgs hadroproduction in association with a top-quark pair*, S. Frixione, V. Hirschi, D. Pagani, H. S. Shao, and M. Zaro, JHEP **0**9, 065 (2014), 1407.0823.

[86] *Anatomy of inclusive* $t\bar{t}W$ *production at hadron colliders*, S. von Buddenbrock, R. Ruiz, and B. Mellado, Phys. Lett. B **8**11, 135964 (2020), 2009.00032.

[87] *Merging meets matching in MC@NLO*, R. Frederix and S. Frixione, JHEP **1**2, 061 (2012), 1209.6215.

[88] *On improving NLO merging for* $t\bar{t}W$ *production*, R. Frederix and I. Tsinikos, JHEP **1**1, 029 (2021), 2108.07826.

[89] CMS, *Measurement of the cross section of top quark-antiquark pair production in association with a W boson in proton-proton collisions at* $\sqrt{s} = 13\,TeV$, submitted to JHEP (2022), 2208.06485.

[90] CMS, *Measurement of the single top quark and antiquark production cross sections in the t channel and their ratio in proton-proton collisions at $\sqrt{s} = 13$ TeV*, A. M. Sirunyan *et al.*, Phys. Lett. B **8**00, 135042 (2020), 1812.10514.

[91] CMS, *Measurement of differential cross sections and charge ratios for t-channel single top quark production at 13 TeV*, CMS-PAS-TOP-17-023 (2019).

[92] ATLAS, *Measurement of the polarisation of single top quarks and antiquarks produced in the t-channel at $\sqrt{s} = 13$ TeV and bounds on the tWb dipole operator from the ATLAS experiment*, G. Aad *et al.*, (2022), 2202.11382.

[93] *New directions for top quark polarization in the t-channel process*, J. A. Aguilar-Saavedra and S. Amor Dos Santos, Phys. Rev. D **8**9, 114009 (2014), 1404.1585.

[94] *Differential Distributions for t-channel Single Top-Quark Production and Decay at Next-to-Next-to-Leading Order in QCD*, E. L. Berger, J. Gao, and H. X. Zhu, JHEP **1**1, 158 (2017), 1708.09405.

[95] *A Minimal set of top anomalous couplings*, J. A. Aguilar-Saavedra, Nucl. Phys. B **8**12, 181 (2009), 0811.3842.

[96] *Single Top Production at Next-to-Leading Order in the Standard Model Effective Field Theory*, C. Zhang, Phys. Rev. Lett. **1**16, 162002 (2016), 1601.06163.

[97] *Effective operators in t-channel single top production and decay*, M. de Beurs, E. Laenen, M. Vreeswijk, and E. Vryonidou, Eur. Phys. J. C **7**8, 919 (2018), 1807.03576.

[98] *Improved spin basis for angular correlation studies in single top quark production at the Tevatron*, G. Mahlon and S. J. Parke, Phys. Rev. D **5**5, 7249 (1997), hep-ph/9611367.

[99] *Single top quark production at the LHC: Understanding spin*, G. Mahlon and S. J. Parke, Phys. Lett. B **4**76, 323 (2000), hep-ph/9912458.

[100] *Single top polarisation as a window to new physics*, J. A. Aguilar-Saavedra, C. Degrande, and S. Khatibi, Phys. Lett. B **7**69, 498 (2017), 1701.05900.

[101] CMS, *Measurement of the inclusive and differential $\mathrm{t\bar{t}}\gamma$ cross sections in the dilepton channel and effective field theory interpretation in proton-proton collisions at $\sqrt{s}$ =13 TeV*, A. Tumasyan *et al.*, JHEP **0**5, 091 (2022), 2201.07301.

[102] CDF, *Evidence for $t\bar{t}\gamma$ Production and Measurement of $\sigma_t\bar{t}\gamma/\sigma_t\bar{t}$*, T. Aaltonen *et al.*, Phys. Rev. D **8**4, 031104 (2011), 1106.3970.

[103] ATLAS, *Observation of top-quark pair production in association with a photon and measurement of the $t\bar{t}\gamma$ production cross section in pp collisions at $\sqrt{s} = 7$ TeV using the ATLAS detector*, G. Aad *et al.*, Phys. Rev. D **9**1, 072007 (2015), 1502.00586.

[104] ATLAS, *Measurement of the $t\bar{t}\gamma$ production cross section in proton-proton collisions at $\sqrt{s} = 8$ TeV with the ATLAS detector*, M. Aaboud *et al.*, JHEP **11**, 086 (2017), 1706.03046.

[105] CMS, *Measurement of the semileptonic $t\bar{t} + \gamma$ production cross section in pp collisions at $\sqrt{s} = 8$ TeV*, A. M. Sirunyan *et al.*, JHEP **10**, 006 (2017), 1706.08128.

[106] ATLAS, *Measurements of inclusive and differential fiducial cross-sections of $t\bar{t}\gamma$ production in leptonic final states at $\sqrt{s} = 13$ TeV in ATLAS*, M. Aaboud *et al.*, Eur. Phys. J. C **79**, 382 (2019), 1812.01697.

[107] ATLAS, *Measurements of inclusive and differential cross-sections of combined $t\bar{t}\gamma$ and $tW\gamma$ production in the $e\mu$ channel at 13 TeV with the ATLAS detector*, G. Aad *et al.*, JHEP **09**, 049 (2020), 2007.06946.

[108] CMS, *Measurement of the inclusive and differential $t\bar{t}\gamma$ cross sections in the single-lepton channel and EFT interpretation at $\sqrt{s}$ = 13 TeV*, A. Tumasyan *et al.*, JHEP **12**, 180 (2021), 2107.01508.

[109] *QCD corrections to associated production of $t\bar{t}\gamma$ at hadron colliders*, P.-F. Duan *et al.*, Phys. Rev. D **80**, 014022 (2009), 0907.1324.

[110] *QCD corrections to top quark pair production in association with a photon at hadron colliders*, K. Melnikov, M. Schulze, and A. Scharf, Phys. Rev. D **83**, 074013 (2011), 1102.1967.

[111] *Next-to-leading order QCD corrections to $t\bar{t}\gamma$ production at the 7 TeV LHC*, P.-F. Duan *et al.*, Chin. Phys. Lett. **28**, 111401 (2011), 1110.2315.

[112] *Hadroproduction of t anti-t pair in association with an isolated photon at NLO accuracy matched with parton shower*, A. Kardos and Z. Trócsányi, JHEP **05**, 090 (2015), 1406.2324.

[113] *Electroweak corrections to top quark pair production in association with a hard photon at hadron colliders*, P.-F. Duan, Y. Zhang, Y. Wang, M. Song, and G. Li, Phys. Lett. B **766**, 102 (2017), 1612.00248.

[114] *Automated EW corrections with isolated photons: $t\bar{t}\gamma$, $t\bar{t}\gamma\gamma$ and $t\gamma j$ as case studies*, D. Pagani, H.-S. Shao, I. Tsinikos, and M. Zaro, JHEP **09**, 155 (2021), 2106.02059.

[115] *Precise predictions for $t\bar{t}\gamma/t\bar{t}$ cross section ratios at the LHC*, G. Bevilacqua, H. B. Hartanto, M. Kraus, T. Weber, and M. Worek, JHEP **01**, 188 (2019), 1809.08562.

[116] *Off-shell vs on-shell modelling of top quarks in photon associated production*, G. Bevilacqua, H. B. Hartanto, M. Kraus, T. Weber, and M. Worek, JHEP **03**, 154 (2020), 1912.09999.

[117] *Probing top quark neutral couplings in the Standard Model Effective Field Theory at NLO in QCD*, O. Bessidskaia Bylund, F. Maltoni, I. Tsinikos, E. Vryonidou, and C. Zhang, JHEP **0**5, 052 (2016), 1601.08193.

[118] *Probing electroweak top quark couplings at hadron colliders*, U. Baur, A. Juste, L. H. Orr, and D. Rainwater, Phys. Rev. D **7**1, 054013 (2005), hep-ph/0412021.

[119] *Electromagnetic dipole moments of the Top quark*, A. O. Bouzas and F. Larios, Phys. Rev. D **8**7, 074015 (2013), 1212.6575.

[120] *Pinning down electroweak dipole operators of the top quark*, M. Schulze and Y. Soreq, Eur. Phys. J. C **7**6, 466 (2016), 1603.08911.

[121] CMS, ATLAS, *Combination of the W boson polarization measurements in top quark decays using ATLAS and CMS data at $\sqrt{s} = 8$ TeV*, G. Aad *et al.*, JHEP **0**8, 051 (2020), 2005.03799.

[122] CMS, *Measurement of the Higgs boson production rate in association with top quarks in final states with electrons, muons, and hadronically decaying tau leptons at $\sqrt{s} = 13$ TeV*, A. M. Sirunyan *et al.*, Eur. Phys. J. C **8**1, 378 (2021), 2011.03652.

[123] CMS, *Observation of a New Boson with Mass Near 125 GeV in pp Collisions at $\sqrt{s} =$ 7 and 8 TeV*, S. Chatrchyan *et al.*, JHEP **0**6, 081 (2013), 1303.4571.

[124] *Electroweak symmetry breaking via top condensation seesaw*, B. A. Dobrescu and C. T. Hill, Phys. Rev. Lett. **8**1, 2634 (1998), hep-ph/9712319.

[125] *Top Quark Seesaw Theory of Electroweak Symmetry Breaking*, R. S. Chivukula, B. A. Dobrescu, H. Georgi, and C. T. Hill, Phys. Rev. D **5**9, 075003 (1999), hep-ph/9809470.

[126] *Is the standard Higgs scalar elementary?*, D. Delepine, J. M. Gerard, and R. Gonzalez Felipe, Phys. Lett. B **3**72, 271 (1996), hep-ph/9512339.

[127] *Why should we care about the top quark Yukawa coupling?*, F. Bezrukov and M. Shaposhnikov, J. Exp. Theor. Phys. **1**20, 335 (2015), 1411.1923.

[128] *Trilinear Higgs coupling determination via single-Higgs differential measurements at the LHC*, F. Maltoni, D. Pagani, A. Shivaji, and X. Zhao, Eur. Phys. J. C **7**7, 887 (2017), 1709.08649.

[129] *Higgs production in association with a top-antitop pair in the Standard Model Effective Field Theory at NLO in QCD*, F. Maltoni, E. Vryonidou, and C. Zhang, JHEP **1**0, 123 (2016), 1607.05330.

[130] *Higgs radiation off top quarks at the Tevatron and the LHC*, W. Beenakker *et al.*, Phys. Rev. Lett. **8**7, 201805 (2001), hep-ph/0107081.

[131] *NLO QCD corrections to t anti-t H production in hadron collisions*, W. Beenakker *et al.*, Nucl. Phys. B **6**53, 151 (2003), hep-ph/0211352.

[132] *Next-to-leading order results for t anti-t h production at the Tevatron*, L. Reina and S. Dawson, Phys. Rev. Lett. **8**7, 201804 (2001), hep-ph/0107101.

[133] *QCD corrections to associated t anti-t h production at the Tevatron*, L. Reina, S. Dawson, and D. Wackeroth, Phys. Rev. D **6**5, 053017 (2002), hep-ph/0109066.

[134] *Associated top quark Higgs boson production at the LHC*, S. Dawson, L. H. Orr, L. Reina, and D. Wackeroth, Phys. Rev. D **6**7, 071503 (2003), hep-ph/0211438.

[135] *Associated Higgs production with top quarks at the large hadron collider: NLO QCD corrections*, S. Dawson, C. Jackson, L. H. Orr, L. Reina, and D. Wackeroth, Phys. Rev. D **6**8, 034022 (2003), hep-ph/0305087.

[136] *Scalar and pseudoscalar Higgs production in association with a top–antitop pair*, R. Frederix *et al.*, Phys. Lett. B **7**01, 427 (2011), 1104.5613.

[137] *Standard Model Higgs boson production in association with a top anti-top pair at NLO with parton showering*, M. V. Garzelli, A. Kardos, C. G. Papadopoulos, and Z. Trocsanyi, EPL **9**6, 11001 (2011), 1108.0387.

[138] LHC Higgs Cross Section Working Group, *Handbook of LHC Higgs Cross Sections: 4. Deciphering the Nature of the Higgs Sector*, D. de Florian *et al.*, **2**/2017 (2016), 1610.07922.

[139] *A New method for combining NLO QCD with shower Monte Carlo algorithms*, P. Nason, JHEP **1**1, 040 (2004), hep-ph/0409146.

[140] *Matching NLO QCD computations with Parton Shower simulations: the POWHEG method*, S. Frixione, P. Nason, and C. Oleari, JHEP **1**1, 070 (2007), 0709.2092.

[141] *A general framework for implementing NLO calculations in shower Monte Carlo programs: the POWHEG BOX*, S. Alioli, P. Nason, C. Oleari, and E. Re, JHEP **0**6, 043 (2010), 1002.2581.

[142] NNPDF, *Unbiased global determination of parton distributions and their uncertainties at NNLO and at LO*, R. D. Ball *et al.*, Nucl. Phys. B **8**55, 153 (2012), 1107.2652.

[143] NNPDF, *Parton distributions with QED corrections*, R. D. Ball *et al.*, Nucl. Phys. B **8**77, 290 (2013), 1308.0598.

[144] NNPDF, *Parton distributions for the LHC Run II*, R. D. Ball *et al.*, JHEP **0**4, 040 (2015), 1410.8849.

[145] NNPDF, *Parton distributions from high-precision collider data*, R. D. Ball *et al.*, Eur. Phys. J. C **7**7, 663 (2017), 1706.00428.

[146] *An introduction to PYTHIA 8.2*, T. Sjöstrand *et al.*, Comput. Phys. Commun. **1**91, 159 (2015), 1410.3012.

[147] *GEANT4-a simulation toolkit*, S. Agostinelli *et al.*, Nuclear Instruments and Methods in Physics Research Section A Accelerators Spectrometers Detectors and Associated Equipment **5**06, 250 (2003).

[148] *Recent developments in Geant4*, J. Allison *et al.*, Nucl. Instrum. Meth. A **8**35, 186 (2016).

[149] Particle Data Group, *Review of Particle Physics*, M. Tanabashi *et al.*, Phys. Rev. D **9**8, 030001 (2018).

[150] J. S. Bridle, Training stochastic model recognition algorithms as networks can lead to maximum mutual information estimation of parameters, in *Proceedings of the 2nd International Conference on Neural Information Processing Systems*, NIPS'89, p. 211–217, Cambridge, MA, USA, 1989, MIT Press.

[151] *TensorFlow: Large-Scale Machine Learning on Heterogeneous Distributed Systems*, M. Abadi *et al.*, CoRR **a**bs/1603.04467 (2016), 1603.04467.

[152] *Keras*, F. C. et al., GitHub (2015), https://github.com/fchollet/keras.

[153] S. Amoroso *et al.*, Les Houches 2019: Physics at TeV Colliders: Standard Model Working Group Report, in *11th Les Houches Workshop on Physics at TeV Colliders: PhysTeV Les Houches*, 2020, 2003.01700.

[154] *On the maximal use of Monte Carlo samples: re-weighting events at NLO accuracy*, O. Mattelaer, Eur. Phys. J. C **7**6, 674 (2016), 1607.00763.

[155] *Automated one-loop computations in the standard model effective field theory*, C. Degrande *et al.*, Phys. Rev. D **1**03, 096024 (2021), 2008.11743.

[156] CMS, *Search for new physics in top quark production with additional leptons in proton-proton collisions at $\sqrt{s} = 13$ TeV using effective field theory*, T. C. Collaboration *et al.*, JHEP **0**3, 095 (2021), 2012.04120.

[157] *Top-quark electroweak interactions at high energy*, F. Maltoni, L. Mantani, and K. Mimasu, JHEP **1**0, 004 (2019), 1904.05637.

[158] *Constraining the SMEFT with a differential cross section measurement of tWZ production at the HL-LHC*, J. Keaveney, (2021), 2107.01053.

[159] *Single-top hadroproduction in association with a W boson*, S. Frixione, E. Laenen, P. Motylinski, B. R. Webber, and C. D. White, JHEP **0**7, 029 (2008), 0805.3067.

[160] *Isolating Wt production at the LHC*, C. D. White, S. Frixione, E. Laenen, and F. Maltoni, JHEP **1**1, 074 (2009), 0908.0631.

[161] *Charged Higgs boson production in association with a top quark in MC@NLO*, C. Weydert *et al.*, Eur. Phys. J. C **6**7, 617 (2010), 0912.3430.

[162] *Single-top Wt-channel production matched with parton showers using the POWHEG method*, E. Re, Eur. Phys. J. C **7**1, 1547 (2011), 1009.2450.

[163] *Automized Squark-Neutralino Production to Next-to-Leading Order*, T. Binoth *et al.*, Phys. Rev. D **8**4, 075005 (2011), 1108.1250.

[164] *Automated Squark and Gluino Production to Next-to-Leading Order*, D. Gonçalves-Netto, D. López-Val, K. Mawatari, T. Plehn, and I. Wigmore, Phys. Rev. D **8**7, 014002 (2013), 1211.0286.

[165] *Matching Squark Pair Production at NLO with Parton Showers*, R. Gavin *et al.*, JHEP **1**0, 187 (2013), 1305.4061.

[166] *Squark Production and Decay matched with Parton Showers at NLO*, R. Gavin *et al.*, Eur. Phys. J. C **7**5, 29 (2015), 1407.7971.

[167] *tWH associated production at the LHC*, F. Demartin, B. Maier, F. Maltoni, K. Mawatari, and M. Zaro, Eur. Phys. J. C **7**7, 34 (2017), 1607.05862.

[168] *Automated simulations beyond the Standard Model: supersymmetry*, S. Frixione *et al.*, JHEP **1**2, 008 (2019), 1907.04898.

[169] *Predictions for all processes e+ e- —> 4 fermions + gamma*, A. Denner, S. Dittmaier, M. Roth, and D. Wackeroth, Nucl. Phys. B **5**60, 33 (1999), hep-ph/9904472.

[170] *Electroweak corrections to charged-current e+ e- —> 4 fermion processes: Technical details and further results*, A. Denner, S. Dittmaier, M. Roth, and L. H. Wieders, Nucl. Phys. B **7**24, 247 (2005), hep-ph/0505042, [Erratum: Nucl.Phys.B 854, 504–507 (2012)].

[171] *Towards constraining Dark Matter at the LHC: Higher order QCD predictions for* $t\bar{t} + Z(Z \to \nu_\ell \bar{\nu}_\ell)$, G. Bevilacqua, H. B. Hartanto, M. Kraus, T. Weber, and M. Worek, JHEP **1**1, 001 (2019), 1907.09359.

[172] *Derivation of Gauge Invariance from High-Energy Unitarity Bounds on the s Matrix*, J. M. Cornwall, D. N. Levin, and G. Tiktopoulos, Phys. Rev. D **1**0, 1145 (1974), [Erratum: Phys.Rev.D 11, 972 (1975)].

[173] *Helicity selection rules and noninterference for BSM amplitudes*, A. Azatov, R. Contino, C. S. Machado, and F. Riva, Phys. Rev. D **9**5, 065014 (2017), 1607.05236.

[174] *Automated predictions from polarized matrix elements*, D. Buarque Franzosi, O. Mattelaer, R. Ruiz, and S. Shil, JHEP **0**4, 082 (2020), 1912.01725.

[175] *Matching NLO QCD computations and parton shower simulations*, S. Frixione and B. R. Webber, JHEP **0**6, 029 (2002), hep-ph/0204244.

[176] *The anti-k_t jet clustering algorithm*, M. Cacciari, G. P. Salam, and G. Soyez, JHEP **0**4, 063 (2008), 0802.1189.

[177] *FastJet User Manual*, M. Cacciari, G. P. Salam, and G. Soyez, Eur. Phys. J. C **7**2, 1896 (2012), 1111.6097.

[178] *Top Compositeness at the Tevatron and LHC*, B. Lillie, J. Shu, and T. M. P. Tait, JHEP **0**4, 087 (2008), 0712.3057.

[179] *Top Quark Compositeness: Feasibility and Implications*, A. Pomarol and J. Serra, Phys. Rev. D **7**8, 074026 (2008), 0806.3247.

[180] *Manifestations of Top Compositeness at Colliders*, K. Kumar, T. M. P. Tait, and R. Vega-Morales, JHEP **0**5, 022 (2009), 0901.3808.

[181] *Multi-tops at the LHC*, A. Deandrea and N. Deutschmann, JHEP **0**8, 134 (2014), 1405.6119.

[182] *Boosted Tops from Gluino Decays*, J. Berger, M. Perelstein, M. Saelim, and A. Spray, (2011), 1111.6594.

[183] *Four tops and the $t\bar{t}$ forward-backward asymmetry*, J. A. Aguilar-Saavedra and J. Santiago, Phys. Rev. D **8**5, 034021 (2012), 1112.3778.

[184] *Probing top-philic sgluons with LHC Run I data*, L. Beck *et al.*, Phys. Lett. B **7**46, 48 (2015), 1501.07580.

[185] *Maximally Symmetric Two Higgs Doublet Model with Natural Standard Model Alignment*, P. S. Bhupal Dev and A. Pilaftsis, JHEP **1**2, 024 (2014), 1408.3405, [Erratum: JHEP 11, 147 (2015)].

[186] *Identifying Multi-Top Events from Gluino Decay at the LHC*, B. S. Acharya *et al.*, (2009), 0901.3367.

[187] *Four top quarks in extensions of the standard model*, T. Gregoire, E. Katz, and V. Sanz, Phys. Rev. D **8**5, 055024 (2012), 1101.1294.

[188] *Non-resonant New Physics in Top Pair Production at Hadron Colliders*, C. Degrande, J.-M. Gerard, C. Grojean, F. Maltoni, and G. Servant, JHEP **0**3, 125 (2011), 1010.6304.

[189] *Probing top-philic new physics via four-top-quark production*, Q.-H. Cao, J.-N. Fu, Y. Liu, X.-H. Wang, and R. Zhang, Chin. Phys. C **4**5, 093107 (2021), 2105.03372.

[190] *Top-philic heavy resonances in four-top final states and their EFT interpretation*, L. Darmé, B. Fuks, and F. Maltoni, JHEP **0**9, 143 (2021), 2104.09512.

[191] *The Present and Future of Four Top Operators*, G. Banelli, E. Salvioni, J. Serra, T. Theil, and A. Weiler, JHEP **0**2, 043 (2021), 2010.05915.

[192] *Constraining BSM Physics at the LHC: Four top final states with NLO accuracy in perturbative QCD*, G. Bevilacqua and M. Worek, JHEP **0**7, 111 (2012), 1206.3064.

[193] *Hadroproduction of four top quarks in the powheg box*, T. Ježo and M. Kraus, Phys. Rev. D **1**05, 114024 (2022), 2110.15159.

[194] *Higgs probes of top quark contact interactions and their interplay with the Higgs self-coupling*, L. Alasfar, J. de Blas, and R. Gröber, JHEP **0**5, 111 (2022), 2202.02333.

[195] *Flavorful electroweak precision observables in the Standard Model effective field theory*, S. Dawson and P. P. Giardino, Phys. Rev. D **1**05, 073006 (2022), 2201.09887.

[196] ATLAS, *Measurement of the $t\bar{t}t\bar{t}$ production cross section in pp collisions at $\sqrt{s} = 13$ TeV with the ATLAS detector*, ATLAS-CONF-2021-013 (2021).

[197] ATLAS, *Search for four-top-quark production in the single-lepton and opposite-sign dilepton final states in pp collisions at $\sqrt{s}$ = 13 TeV with the ATLAS detector*, M. Aaboud *et al.*, Phys. Rev. D **9**9, 052009 (2019), 1811.02305.

[198] *Report from Working Group 1: Standard Model Physics at the HL-LHC and HE-LHC*, P. Azzi *et al.*, CERN Yellow Rep. Monogr. **7**, 1 (2019), 1902.04070.

[199] CMS, *Search for production of four top quarks in final states with same-sign or multiple leptons in proton-proton collisions at $\sqrt{s} = 13$ TeV*, A. M. Sirunyan *et al.*, Eur. Phys. J. C **8**0, 75 (2020), 1908.06463.

[200] *Constraining qqtt operators from four-top production: a case for enhanced EFT sensitivity*, C. Zhang, Chin. Phys. C **4**2, 023104 (2018), 1708.05928.

[201] CMS, *Search for physics beyond the standard model in events with two leptons of same sign, missing transverse momentum, and jets in proton–proton collisions at $\sqrt{s} = 13$ TeV*, A. M. Sirunyan *et al.*, Eur. Phys. J. C **7**7, 578 (2017), 1704.07323.

[202] A. Buckley, The hepthesis LaTeX class.

List of figures

List of tables